Grid Supporting Controllers for Enabling 100% Penetration of Inverter-Based Resources

Final Project Report

S-90

Power Systems Engineering Research Center
Empowering Minds to Engineer
the Future Electric Energy System

Grid Supporting Controllers for Enabling 100% Penetration of Inverter-Based Resources

Final Project Report

Project Team
Maryam Saeedifard, Project Leader
Sakis Meliopoulos
Georgia Institute of Technology

Saeed Lotfifard
Washington State University

Graduate Students
Araz Bagherzadeh Karimi
Siyao Cai
Kaiyu Liu
Syed Sohail Feroz Syed
Georgia Institute of Technology

Ali Maleki
Washington State University

PSERC Publication 23-03

November 2023

For information about this project, contact:

Maryam Saeedifard
Georgia Institute of Technology
School of Electrical and Computer Engineering
777 Atlantic Dr.
Atlanta, GA 30332-0250
Phone: 404 894 4834
Email: Maryam@ece.gatech.edu

Power Systems Engineering Research Center

The Power Systems Engineering Research Center (PSERC) is a multi-university Center conducting research on challenges facing the electric power industry and educating the next generation of power engineers. More information about PSERC can be found at the Center's website: http://www.pserc.wisc.edu.

For additional information, contact:

Power Systems Engineering Research Center
Arizona State University
527 Engineering Research Center
Tempe, Arizona 85287-5706
Phone: 480-965-1643
Fax: 480-727-2052

Notice Concerning Copyright Material

Acknowledgments

This is the final report for the Power Systems Engineering Research Center (PSERC) research project titled "Grid Supporting Controllers for Enabling 100% Penetration of Inverter-Based Resources" (project S-90).

The authors wish to thank the industry collaborators:
Deepak Konka (GE Renewable Energy, deepak.konka@ge.com),
Harvey Scribner (SPP, hscribner@spp.org),
Kwok Cheung (GE Renewable Energy, kwok.cheung@ge.com),
Mehmet Cintuglu (ABB, mehmet.contuglu@us.abb.com),
Melvin Schoech (CNP, Melvin.schoech@centerpointenergy.com),
Miaolei Shao (GE Power, mialoei.shao@ge.com),
Evangelos Farantatos (EPRI, efarantatos@epri.com),
Deepak Ramasubramanian (EPRI, dramasubramanian@epri.com),
Wenzong Wang (EPRI, wwang@epri.com),
Doug Bowman (SPP, dbowman@spp.org),
Mahesh Morjaria (First Solar, Mahesh.morjaria@firstsolar.com),
Alan Engelmann (Exelon, alan.engelmann@ConEd.com),
Mohit Singh (ComEd, mohit.singh@ComEd.com).

Executive Summary

Amid the optimism surrounding the benefits of massive integration of renewables, incidents such as loss of a large amount of PV generation in Southern California in 2016 due to faults on transmission lines have raised concerns over resiliency of the future power system grid with 100% renewables. Renewable energy sources are typically the so-called Inverter-Based Resources (IBRs), meaning that they are interfaced to the grid through power converters, whose fault characteristics are influenced by control strategies. In addition, control system of an inverter is sensitive to grid disturbances such as unbalanced faults. In summary, operation and control of power systems with 100% IBRs pose a number of technical challenges, which are mainly due to: i) lack of a set of reliable methods to achieve desired voltage and frequency supports of the future grid by introducing synthetic inertia to the future grid, ii) insufficient investigation of comprehensive methods enabling the stability analysis of a system with high penetration level of IBRs, and iii) insufficient investigation of fault-ride-through capability and post-fault recovery control strategies to avoid massive dropouts of renewables following a disturbance. The goal of this proposal is to address the aforementioned challenges. This research focuses on three core areas: (1) development of small-signal models for stability analysis of Grid-ForMing (GFM) and Grid FoLlowing (GFL) inverters, (2) development of supplementary predictive inverter control to ensure robust operation of GFM inverters during disturbances, and (3) studying the influential factors on fault-ride-through and post-fault recovery of grid connected inverters. The report is presented in three parts.

Part I: Parametric Small-Signal Modeling of Grid Forming and Grid Following Inverters in 100% Renewable-Based Grids

Part I of this report is focused on small-signal models for the latest inverter control strategies including the GFM and GFL. This involves constructing a parametric model for the inverter by utilizing matrix formulations and linearizing specific blocks in the small-signal domain through the application of computational algebraic equation solvers. Various GFM and GFL control strategies are encompassed within this modeling approach. To this end, the matrix formulation for inverter modeling is detailed, with theoretical derivations of small-signal equations for each inverter control function and circuit component. These blocks are solved computationally and the resulting equivalent impedance/admittance transfer functions are deduced and presented. Then, a comparison of various GFM and GFL controls is undertaken in terms of the number of poles (eigenvalues analysis) and frequency responses. The eigenvalue analysis results show that certain GFM control methods present the highest level of complexity while the GFL represents the minimum number of poles. Another note-worthy point is that the number of poles exhibits notable variation across control strategies, frequently featuring diverse matrix elements with varying degrees of complexity. The frequency-domain analyses show that, depending on the adopted GFM control, the Bode diagram may show pronounced magnitude and/or phase angle shift within a specific frequency range, signifying an oscillatory behavior in response to disturbances. Since the developed models and analysis method are parametric, they can be expanded to multi-inverter systems with a blend of GFL and GFM and used a basis for inter-area oscillation damping for future work.

Project Publications:

Student Theses:

[1] Araz Bagherzadeh Karimi. Parametric Small-Signal Modeling of Grid Forming and Grid Following Inverters in 100% Renewable-Based Grids, Master's thesis, Georgia Institute of Technology, December 2022.

Part II: Grid Forming Inverters

As the number of Distributed Energy Resources (DERs) connected to the power system has been increasing rapidly, the power systems are now operating at a higher penetration level of Inverter-Based Resources (IBRs). In the foreseeable future, states like California and Minnesota have more ambitious plans of fully renewable power supply. Currently, the reliability and stability of the power system still relies on the conventional synchronous generators in the system. Due to the high mechanical inertia nature of the rotating machinery-based synchronous generators, the system dynamic changes at a lower speed, which allows the GFL inverters to track the phase angle and voltages using phase-locked loop (PLL). However, at high penetration levels of IBRs, the rate of change of frequency (RoCoF) increases significantly and makes it difficult for the PLL to track the system dynamics. Therefore, new challenges emerge as the instantaneous penetration of IBRs in the power system increases with forecast of 100% penetration. While the trend is obvious, it is also important to recognize that even at lower penetration levels in terms of installed capacities, operationally, the system may move into operating points that most of the produced electricity is coming from IBRs. It has happened already in the US that for certain periods of time, the system was operating at 100% of IBR generation. We can refer to this as operational penetration level. The reality is that for periods of time the present system operates at 100% IBR penetration level. The trend is that these periods of time will be increasing as we move into the future.

In inverter-dominated power systems, GFM inverters are considered a necessity to ensure synchronous operation of the system, control of frequency and voltages, and avoid disturbances. The alternative to keep using GFL inverters will not work well in a IBR dominated power system, as GFL cannot guarantee frequency and voltage control in these systems; in addition, their design is to drop out when a disturbance occurs.

There is a plethora of information and research on GFM inverters. We have performed a literature survey and reported the work of other researchers in this important issue of designing and controlling grid forming inverters. The literature discussion is provided in Section 3. The literature is rich. Yet, much work remains to be done.

The shortcomings of present inverter designs as far as grid forming is concerned, have been taking into account bin the design of the proposed GFM inverters. The proposed design is provided in Section 4 in terms of the model of GFM inverters. We propose an inverter model that is quadratized to facilitate robust simulation and allow flexible control strategies. Example results are provided to compare the proposed GFM with other software, in this case PSCAD. This comparison was focused on systems with smooth transitions from one operating condition to another. At times of fast transients and/or system oscillations, additional controls must be added to ensure the proper operation of the GFM inverters. For this purpose, we propose supplementary predictive inverter control to ensure robust operation of GFM inverters during disturbances. This work is described in Section 5.

In Section 6 we provide performance results of GFM operating in a hybrid system. The hybrid system is defined as one that has sections of synchronous machine-based systems and inverter based system. The example test system has been designed to operate as a hybrid system or it can island into two subsystems, (a) a 100% IBR system, and (b) a 100% synchronous machine system. The results demonstrate that GFM inverters provide good performance for 100% IBR power systems.

Finally, in Section 7, we performed a comparison of the proposed modeling and design of GFM inverter systems to the analysis results using industry accepted software, in this particular case, PSCAD. An identical test system was constructed and presented in Appendix B to validate the results obtained with the proposed modeling of GFM inverters. The model in Appendix B has been developed for PSCAD so that the proposed models can be compared with PSCAD. The simulation results from the model of Appendix B matches the results from the model of Appendix A (proposed GFM inverter models) despite minor differences in the RMS value of the current and voltage at the load caused by the different parameter settings. At this point in time, we have not identified the root cause of the differences between the described simulation results, i.e. between the proposed models and methods and the industry established PSCAD. We plan to continue this work.

The design and modeling of GFM inverters and the impact of these designs on the performance of the power system of the future is a very complex issue. Research work in this area will continue, so that the challenges generated by IBR dominated power systems can be addressed. This project addressed only a small part of the overall problem.

Project Publications:

[1] Yu Liu, Abhinav Kumar Singh, Junbo Zhao, A. P. Meliopoulos, Bikash Pal, M. A. M. Ariff, Thierry Van Cutsem, Mevludin Glavic, Zhenyu Huang, Innocent Kamwa, Lamine Mili, Saleem Mir, Ahmad Taha, Vladimir Terzija, and Shenglong Yu, "Dynamic State Estimation for Power System Control and Protection," IEEE Transactions on Power Systems, volume: 36, issue: 6, pp. 5909-5921, Nov. 2021, DOI: 10.1109/TPWRS.2021.3079395.

[2] Thomas E. McDermott, Sakis Meliopoulos, M. Ramesh, G. Cokkinides, J. Doty, J. Kolln, N. Shepard, G. Kou, F. Velez, R. Johnson, D. Duke, J. Hambrick and R. Fan, "Protection of Radial Circuits with High Penetration Distributed Photovoltaics", *Proceedings of the 2021 Georgia Tech Protective Relaying Conference*, Atlanta, Georgia, April 28-30, 2021..

Student Theses:

[1] Liu Kaiyu: Spring 2022, Thesis Title: "Dynamic State Estimation Based protection of power electornic systems"

Part III: Fault Ride Through and Post-Fault Recovery of Inverter Based Resources

A key grid code requirement for IBRs such as PV power plants is low voltage ride through capability. Based on the grid code, PV plants should remain connected during voltage sags and inject reactive power to the grid to support the voltage of the grid. In this project we focused on studying the influential factors on fault ride through and post fault recovery of grid connected inverter. The main results of the projects are as follows:

- We studied the impacts of different PLLs and control structures on the response of inverters during different types of faults. The simulation results show that decoupled double synchronous reference frame-PLL (DDSRF PLL) and dual current controller provide desirable results during balanced and unbalanced faults as they can handle unsymmetrical components in the voltage and current signals and can eliminate the output power oscillations during unbalanced faults.
- The results show that addressing the saturation of the controllers is essential to enable seamless transition from the during fault condition to the post-fault condition.
- We demonstrated the saturation of the PI controller of DC capacitor voltage of the inverter is influential on the overall response of the inverter during transitioning to the post-fault condition.
- We simulated different anti-windup controllers as well as a controller called proxy based sliding mode controller (PBSMC). The results show the effectiveness of anti-windup methods in enhancing the transitioning to the post-fault condition. However, the tuning of anti-windup methods is heuristic and may not provide desirable results under certain conditions.
- PBSMC combines nonlinear controller, sliding mode control, and conventional PID controllers. It provides accurate and fast tracking feature during normal condition similar to PID controllers and smooth resuming to the desired reference value after large disturbances that may lead the saturation of the controller. The simulation results demonstrated PBSMC is a promising method with desirable performance and systematic tuning of the control parameters.

Project Publications:

[1] Ali Maleki, Saeed Lotfifard, "Impact analysis of controller saturations on post fault recovery of PV power plants" to be submitted IEEE PES General Meeting, 2024.

Student Theses:

[1] Ali Maleki, Expected Ph.D thesis title "Fault Resilience Enhancement of Inverter Based Resources", Washington State University.

Part I

Parametric Small-Signal Modeling of Grid Forming and Grid Following Inverters in 100% Renewable-Based Grids

Maryam Saeedifard
Araz Bagherzadeh Karimi, Graduate Student

Georgia Institute of Technology

For information about this project, contact

Maryam Saeedifard
Georgia Institute of Technology
School of Electrical and Computer Engineering
777 Atlantic Dr.
Atlanta, GA 30332-0250
Phone: 404 894 4834
Email: Maryam@ece.gatech.edu

Power Systems Engineering Research Center

The Power Systems Engineering Research Center (PSERC) is a multi-university Center conducting research on challenges facing the electric power industry and educating the next generation of power engineers. More information about PSERC can be found at the Center's website: http://www.pserc.wisc.edu.

For additional information, contact:

Power Systems Engineering Research Center
Arizona State University
527 Engineering Research Center
Tempe, Arizona 85287-5706
Phone: 480-965-1643
Fax: 480-727-2052

Notice Concerning Copyright Material

Table of Contents

List of Figures

List of Tables

1. Introduction and Background

In contrast to synchronous generator-based power systems, which benefit from well-established theoretical frameworks concerning dynamics and stability, theoretical analysis of inverter-based AC grids remains unexplored. The foundational requirement for formulating such theoretical explanations is the accurate modeling of inverters within power systems. This modeling needs to be comprehensive, encompassing all potential phenomena that may occur within a system. However, to facilitate analysis, this modeling can be deconstructed into distinct components, each elucidating various phenomena. These phenomena can be categorized based on different attributes such as magnitude and frequency. A noteworthy phenomenon in power system operation that warrants further investigation within the realm of inverter-based grids is stability and inter-area oscillation damping. This phenomenon can be classified into the realm of small-signal analysis and low-frequency dynamics. An essential precondition for delving into the small-signal and low-frequency characteristics of inverter-based grids is the precise modeling of individual inverters within the context of small-signal analysis. The primary goal is to validate the stability of the nonlinear system at operational points and to facilitate the identification and mitigation of inter-area oscillations.

This project is specifically focused on development of small-signal models for the latest inverter control strategies. This involves constructing a parametric model for the inverter by utilizing matrix formulations and linearizing specific blocks in the small-signal domain through the application of computational algebraic equation solvers. Various Grid-Forming (GFM) and Grid-Following (GFL) control strategies are encompassed within this modeling approach.

In the following sections, the report progresses as follows: First, an overview of the existing methods for inverter modeling is provided in Section 1.1. Then, the matrix formulation for inverter modeling is detailed in Section 2, with theoretical derivations of small-signal equations for each inverter block. These blocks are solved computationally and the resulting equivalent impedance/admittance transfer functions are deduced and presented. Moving forward to Section 3, a comparison of various GFM and GFL controls is undertaken in terms of the number of poles and frequency responses. Finally, the report concludes in Section 3.5, offering a summary of findings and pointing toward potential avenues for future research.

1.1 Literature Review

1.2 Power System Phenomena Classification

Figure 1.1 shows different power system phenomena along with their corresponding time scales. In the realm of power system modeling and analysis, selecting an apprropiate time scale which captures the desired phenomena and meanwhile is computationally efficient is of paramount importance. Two predominant categories of power system modeling methods are Electromagnetic

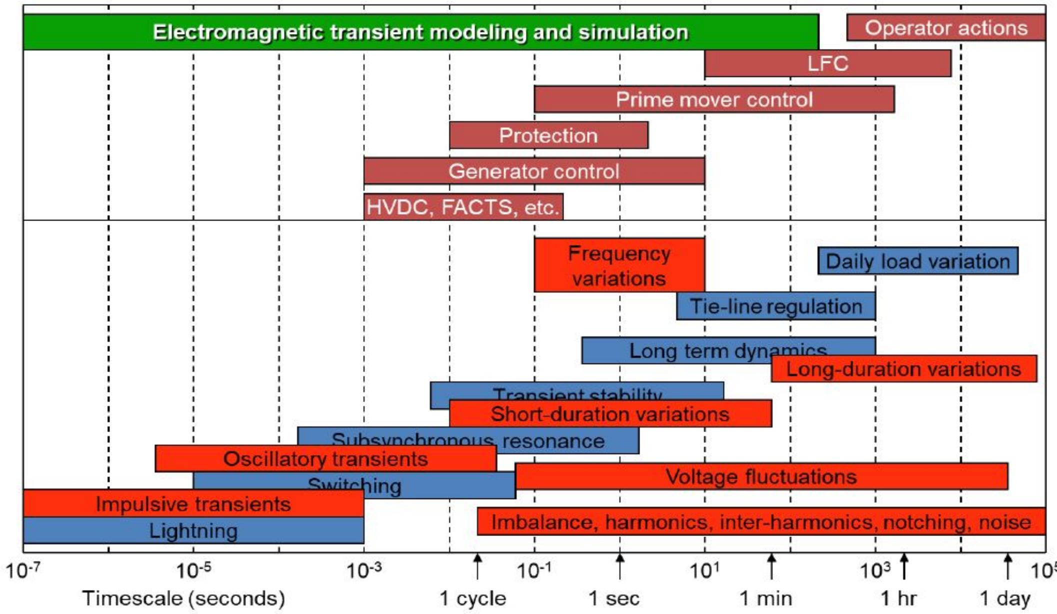

Figure 1.1: Power system phenomena and required accuracy of modeling [1].

Transiet Simulation (EMT) and Root Mean Square (RMS). The spectrum of other modeling approaches generally falls under one of these two overarching methods.

1.2.1 EMT-Based Model

Dommel's Method

The EMT model, regarded as the most accurate representation of an electrical device, encompasses time-domain differential equations for all circuit components, which are solved within the time domain. The first computationally viable approach was introduced by Domell in the late 1960s [2] [3]. Dommel's technique involves modeling every linear and nonlinear circuit element as a current source in parallel with a linear circuit element within a designated time interval. This approach, known as Dommel's method, continues to be employed in software tools like PSCAD (EMTDC) and EMTP. However, the methods based on this approach are computationally intensive and are typically utilized when capturing very high-frequency phenomena is essential, or when quantifying the maximum short-circuit current caused by a high-frequency component in a waveform is required.

Piece-wise Average Model

Semiconductor devices, prevalent in all inverters, stand as a notable source of nonlinearity within power system components. However, incorporating an exact model of these switches can lead to exorbitantly long simulation times. To expedite EMT simulations involving Pulse Width Modulation (PWM) converters, the piece-wise average model was introduced, which integrates an enhanced averaged model of PWM inverters into the EMT framework [4]. While this approach is effective in examining specific scenarios encompassing switching and short circuits that involve PWM inverters, the integration of the averaged model compromises accuracy for faster phenomena such as lightning events.

Dynamic Phasor Modeling

Dynamic phasors offer another avenue that seeks to bridge the gap between EMT and RMS methods. For example, a dynamic phasor model of a Modular Multilevel Converter (MMC) an with extended frequency range for direct interfacing to an EMT simulator is introduced in [5]. The dynamic phasor approach entails modeling the internal dynamics of the MMC by considering the dominant harmonic components of each variable. For the external dynamics of the converter, a novel concept known as base-frequency is introduced and [6]. This concept enables the modeling of any number of frequency components of external variables without incurring a significant increase in computational complexity [6].

1.2.2 RMS-Based Models

Given that slower phenomena can be adequately captured through less intricate methods, resorting to time-consuming EMT modeling for every phenomenon might be excessive. Consequently, strategies like RMS have emerged as solutions to address the computational speed challenges. The RMS models are designed using the phasor model of components, resulting in lighter models compared to the EMT models. These RMS models find extensive application in software tools like MATLAB Simulink and DIgSILENT. This modeling approach forms the foundation for certain inverter models, as elucidated below.

Average Model

The average model linearizes the inverter switching behavior by considering an average value derived from two on-off cycles [7]. This approximation facilitates the incorporation of inverters into RMS simulations. The average model is widely used for various aspects of inverter analysis encompassing design, stability assessment, and control and is a basis for development of other inverter RMS models.

Eigenvalue Based Method

In conventional power systems, eigenvalue analysis is a well-established method to capture specific phenomena like inter-area oscillations and ensure small-signal stability [8]. However, applying this method to inverter-based systems is relatively new. In [9], a modal analysis is conducted for coupled GFM and GFL inverters using global eigenvalue analysis. The results are accurate for a two-inverter system, but the approach lacks modularity and scalability.

In [10], the complex transfer function formulation for a benchmark system for small-signal studies is introduced. A comprehensive model is subsequently presented in [11]. Moreover, [12] adds a dq/abc transformation block to the small-signal model. In the realm of GFM inverters, [13] introduces a small-signal model for placing a specific GFM inverter in a power system. This leaves an unexplored gap in analyzing other GFM inverters alongside GFL ones. Furthermore, in this paper, GFM inverters are typically treated as constant angle devices, without considering the intricacies of GFM angle generation loops.

In this project, the primary objective revolves around incorporating diverse inverter control strategies including the GFM and GFL while encompassing all conceivable block diagrams in a comprehensive manner. Subsequently, the emphasis lies in numerically deriving explicit small-signal parametric equations. The intent is to develop a scalable approach that accommodates a wide range of scenarios and configurations.

2. Methodology

This section begins by elucidating the underlying theory and assumptions governing the small-signal analysis of the inverter shown in Fig. 2.1. Subsequently, it delves into the process of mathematically linearizing and deriving the small-signal matrix form for each control function of the inverter and each circuit component in Fig. 2.1. Ultimately, it synthesizes the comprehensive small-signal model by showcasing a block diagram representation in matrix form.

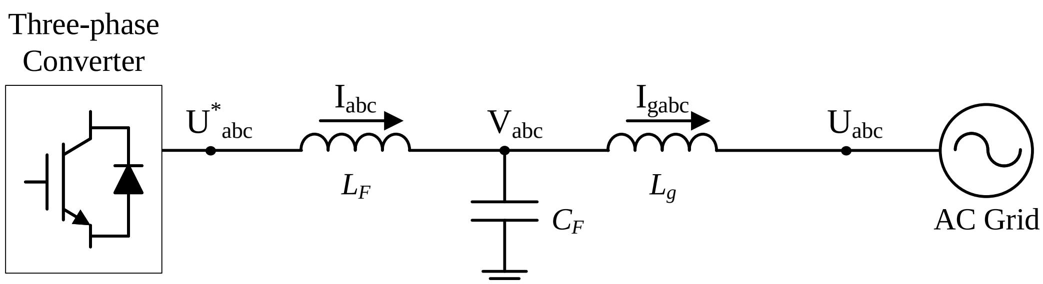

Figure 2.1: Circuit diagram of the two-level inverter.

2.1 Background Theory and Procedure

In a prospective 100% inverter-based power system, the inherent low system inertia raises concerns about prolonged undamped interarea oscillations. The primary objective of this project is to construct a comprehensive small-signal model for inverter-based resources. This model will serve as a tool for scrutinizing system stability and addressing inter-area oscillation damping challenges. The overarching approach for tackling inter-area oscillations encompasses three sequential steps:

- Deriving an equivalent small-signal output inductance model for an individual inverter.
- Streamlining the resultant equivalent small-signal output inductance by reducing its order, facilitating computational and visual analysis of inter-area oscillations.
- Integrating the order-reduced equivalent small-signal output inductance model to deduce small-signal modes and fine-tuning them to enhance overall system damping.

this report, the primary focus centers on the modeling aspect of the aforementioned procedure (first bullet point). Consequently, an equivalent impedance/admittance matrix approach is adopted, diverging from the commonly used state-space model. This approach substantially simplifies the process of inverter-level order reduction and allows seamless integration of various circuit elements into multiple inverter sets in a modular fashion.

Certain assumptions underpin the system's reliance on the small-signal model for specific phenomena. Notably, protection systems such as current limiting and fault ride-through controls are disregarded during small-signal oscillations. Dynamics of the input energy source are considered negligible, assuming a constant input current and treating the DC side as an equivalent capacitor. Perturbations in the magnitude of the reference of the PWM input are assumed to have negligible impact on the high-frequency terms of the output perturbations, enabling the omission of switching frequencies. It is posited that V_{ref} and Q_{ref} are determined by system-level optimal power flow studies, which occur at a slower pace than system dynamics.

Importantly, frequency perturbations are treated as dependent variables linked to output voltages or currents, rather than independent variables subject to change.

The fundamental theory underlying equivalent impedance/admittance modeling posits that the poles of these transfer functions mirror the inverter's eigenvalues.

Given the three-phase balanced nature of the considered inverter in Fig. 2.1, transformation into the dq frame is employed for control purposes. This entails representing complex signals like voltage, current, and modulation index as a 2×1 matrix encompassing both d and q axis components. System signals like angles and DC voltage are similarly reformulated into matrix format to establish a comprehensive formulation for each block. Due to interdependencies between d and q frames on the controller side, the corresponding impedance/admittance or block equivalent gain must be structured as a 2×2 matrix. For example, the transformation for impedance formulation unfolds as follows:

$$\Delta V = Z_{out} \Delta I, \tag{2.1}$$

where,

$$Z_{out} = \begin{bmatrix} Z_{out}^{dd} & Z_{out}^{dq} \\ Z_{out}^{qd} & Z_{out}^{qq} \end{bmatrix}, \tag{2.2}$$

$$\Delta V = \begin{bmatrix} V_d \\ V_q \end{bmatrix}, \tag{2.3}$$

and

$$\Delta I = \begin{bmatrix} I_d \\ I_q \end{bmatrix}. \tag{2.4}$$

Subsequently,

$$\begin{aligned} \Delta V_d &= Z_{out}^{dd} \Delta I_d + Z_{out}^{dq} \Delta I_q, \\ \Delta V_q &= Z_{out}^{qd} \Delta I_d + Z_{out}^{qq} \Delta I_q. \end{aligned} \tag{2.5}$$

2.2 Small-Signal Approximation

In this section, small-signal formulation of each component within the inverter model is presented based on the theory mentioned in Section 2.1.

The variables with prime-suffices denote the measured quantities within the local dq frame. It is important to discern the distinction between the local and global dq frames, as explicitly delineated in Section 2.2.8.

2.2.1 Output Filter

The L filter

For the L filter, the matrix form equation in the dq frame is:

$$\Delta V_o - U = \begin{bmatrix} sL & -L\omega \\ L\omega & sL \end{bmatrix} \Delta I, \tag{2.6}$$

where L represents the inductance of the inductor, s is the Laplace variable, and ω is the system frequency. The variables encompass ΔV_o denoting the output voltage, ΔU representing the inverter's voltage, and ΔI corresponding to the inverter's current perturbations. Equation (2.6) can be written in matrix form as:

$$\Delta V_o - U_c = \mathbf{Z_L} \Delta I_o, \tag{2.7}$$

where $\mathbf{Z_L}$ denotes the impedance of the inductor in matrix form.

The LCL filter

The matrix form euation for the LCL filter in the dq frame is given by:

$$\Delta V_o - V_c = \begin{bmatrix} sL_2 & -L_2\omega \\ L_2\omega & sL_2 \end{bmatrix} \Delta I_o, \tag{2.8}$$

$$\Delta I_o - \Delta I = \begin{bmatrix} sC & -C\omega \\ C\omega & sC \end{bmatrix} \Delta V_c, \tag{2.9}$$

$$\Delta U - \Delta V_c = \begin{bmatrix} sL_1 & -L_1\omega \\ L_1\omega & sL_1 \end{bmatrix} \Delta I, \tag{2.10}$$

which can be represented by:

$$\Delta V_o - V_c = \mathbf{Z}_{L_2} \Delta I_o, \tag{2.11}$$

$$\Delta I_o - \Delta I = \mathbf{Z_c} \Delta V_c, \tag{2.12}$$

$$\Delta U - \Delta V_c = \mathbf{Z}_{L_1} \Delta I. \tag{2.13}$$

2.2.2 The PWM Block

In practice, the PWM block represents the inverter itself, which takes the inputs from the control system and transformes them into duty cycles for the switching devices. Through modulating the DC voltage with varying duty cycles, the PWM process generates a controlled output AC voltage following low-pass filtering. In this context, it is assumed that high-frequency components can be neglected for the small-signal analysis, and the average model for the switching devices is used. The main equation for the PWM block is:

$$U = INV * V_{DC}D, \tag{2.14}$$

where D represents the modulation index and U stands for the output voltage. Both D and U are represented in the dq frame as matrices $D = \begin{bmatrix} D_d \\ D_q \end{bmatrix}$ and $U = \begin{bmatrix} U_d \\ U_q \end{bmatrix}$. Equation (2.14) is nonlinear and must be linearized for small-signal analysis. The $*$ operator denotes simple matrix multiplication.

$$U + \Delta U = INV * (V_{DC} + \Delta V_{DC})(D + \Delta D), \tag{2.15}$$

where $INV = \begin{bmatrix} \frac{1-0.5T_{del}s}{1+0.5T_{del}s} & 0 \\ 0 & \frac{1-0.5T_{del}s}{1+0.5T_{del}s} \end{bmatrix}$ is the switching delay transfer function in the matrix form and

$$U + \Delta U = INV * ((V_{DC})(D) + (V_{DC})(\Delta D) + (\Delta V_{DC})(D) + (\Delta V_{DC})(\Delta D)). \tag{2.16}$$

By neglecting steady-state and double incremental terms, we obtain:

$$\Delta U = INV * ((V_{DC})(\Delta D) + (\Delta V_{DC})(D)). \tag{2.17}$$

Finally,

$$\Delta U = Delv * \Delta D + Deld * \Delta V_{DC} \tag{2.18}$$

in which $Delv = INV * V_{DC}$ and $Deld = INV * D$

2.2.3 Current Loop

The inner current loop is a block that controls the input of the PWM. It achieves this by utilizing the reference current as:

$$\Delta D' = \begin{bmatrix} PI_c & 0 \\ 0 & PI_c \end{bmatrix} (\Delta I_{ref} - \Delta I') + \begin{bmatrix} 0 & -L_1\omega \\ L_1\omega & 0 \end{bmatrix} \Delta I' + \begin{bmatrix} fv & 0 \\ 0 & fv \end{bmatrix} V_c', \tag{2.19}$$

with the final matrix form equation derived as:

$$\Delta D' = PIC(\Delta I_{ref} - \Delta I') + L1w * \Delta I' + FV * V_c'. \tag{2.20}$$

2.2.4 Voltage/Power Loop

Power Loop in GFL: The power loop in GFL is used to ensure constant active and reactive powers:

$$\Delta I_{ref} = \begin{bmatrix} PI_p & 0 \\ 0 & PI_q \end{bmatrix} (\Delta S_{ref} - \Delta S), \tag{2.21}$$

which can be rewritten in the matrix form as:

$$\Delta I_{ref} = PIS * (\Delta S_{ref} - \Delta S). \tag{2.22}$$

Voltage Loop in GFM: The voltage loop in GFM is used to regulate and maintain the system voltage at a desired level:

$$\Delta I_{ref} = \begin{bmatrix} PI_v & 0 \\ 0 & PI_v \end{bmatrix} (\Delta V_{ref} - \Delta V_c') + \begin{bmatrix} 0 & -C\omega \\ C\omega & 0 \end{bmatrix} \Delta V_c' + \begin{bmatrix} fc & 0 \\ 0 & fc \end{bmatrix} \Delta I'. \tag{2.23}$$

By assuming that the $V_{ref} = constant$, (2.23) can be reduced to:

$$\Delta I_{ref} = -\begin{bmatrix} PI_v & 0 \\ 0 & PI_v \end{bmatrix} \Delta V_c' + \begin{bmatrix} 0 & -C\omega \\ C\omega & 0 \end{bmatrix} \Delta V_c' + \begin{bmatrix} fc & 0 \\ 0 & fc \end{bmatrix} \Delta I'. \tag{2.24}$$

Therefore, the matrix form of (2.23) becomes:

$$\Delta I_{ref} = -PIV * \Delta V_c' + Cw * \Delta V_c' + F_{I_I} * \Delta I'. \tag{2.25}$$

2.2.5 Power Measurement

Power measurements in terms of I_d', I_q', V_d', and V_q' are:

$$P = \frac{\omega_c}{s + \omega_c}(V_d' I_d' + V_q' I_q'), \tag{2.26}$$

$$Q = \frac{\omega_c}{s + \omega_c}(V_q' I_d' - V_d' I_q'), \tag{2.27}$$

where $pfilter = \frac{\omega_c}{s+\omega_c}$ represents a low-pass filter applied to the measurements. This element is nonlinear and needs to be linearized for the small-signal analysis. The linearization is as follows:

$$P+\Delta P = pfilter((V'_d+\Delta V'_d)(I'_d+\Delta I'_d)+(V'_q+\Delta V'_q)(I'_q+\Delta I'_q)), \tag{2.28}$$

$$Q+\Delta Q = pfilter((V'_q+\Delta V'_q)(I'_d+\Delta I'_d)-(V'_d+\Delta V'_d)(I'_q+\Delta I'_q)). \tag{2.29}$$

Equations (2.28) and (2.29) can be elaborated as:

$$\begin{aligned} P+\Delta P = pfilter(&(V'_d)(I'_d)+(V'_q)(I'_q)+(\Delta V'_d)(I'_d)+(\Delta V'_q)(I'_q)+(V'_d)(\Delta I'_d) \\ &+(V'_q)(\Delta I'_q)+(\Delta V'_d)(\Delta I'_d)+(\Delta V'_q)(\Delta I'_q)), \end{aligned} \tag{2.30}$$

$$\begin{aligned} Q+\Delta Q = pfilter(&(V'_q)(I'_d)-(V'_d)(I'_q)+(\Delta V'_q)(I'_d)-(\Delta V'_d)(I'_q)+(V'_q)(\Delta I'_d) \\ &-(V'_d)(\Delta I'_q)+(\Delta V'_q)(\Delta I'_d)-(\Delta V'_d)(\Delta I'_q)). \end{aligned} \tag{2.31}$$

If the large signal and double incremental terms are dropped, the equations simplify to:

$$\Delta P' = pfilter((I'_d)(\Delta V'_d)+(I'_q)(\Delta V'_q)+(V'_d)(\Delta I'_d)+(V'_q)(\Delta I'_q)), \tag{2.32}$$

$$\Delta Q' = pfilter((I'_d)(\Delta V'_q)-(I'_q)(\Delta V'_d)+(V'_q)(\Delta I'_d)-(V'_d)(\Delta I'_q)), \tag{2.33}$$

which can be rewritten as:

$$\Delta P' = pfilter(\begin{bmatrix} I'_d & I'_q \end{bmatrix}\begin{bmatrix} \Delta V'_d \\ \Delta V'_q \end{bmatrix}+\begin{bmatrix} V'_d & V'_q \end{bmatrix}\begin{bmatrix} \Delta I'_d \\ \Delta I'_q \end{bmatrix}), \tag{2.34}$$

$$\Delta Q' = pfilter(\begin{bmatrix} -I'_q & I'_d \end{bmatrix}\begin{bmatrix} \Delta V'_d \\ \Delta V'_q \end{bmatrix}+\begin{bmatrix} V'_q & -V'_d \end{bmatrix}\begin{bmatrix} \Delta I'_d \\ \Delta I'_q \end{bmatrix}). \tag{2.35}$$

Finally,

$$\Delta S = \begin{bmatrix} pfilter & 0 \\ 0 & pfilter \end{bmatrix}(\begin{bmatrix} I'_d & I'_q \\ -I'_q & I'_d \end{bmatrix}\begin{bmatrix} \Delta V'_d \\ \Delta V'_q \end{bmatrix}+\begin{bmatrix} V'_d & V'_q \\ V'_q & -V'_d \end{bmatrix}\begin{bmatrix} \Delta I'_d \\ \Delta I'_q \end{bmatrix}). \tag{2.36}$$

We assume $Io = \begin{bmatrix} I'_d & I'_q \\ -I'_q & I'_d \end{bmatrix}$, $Vo = \begin{bmatrix} V'_d & V'_q \\ V'_q & -V'_d \end{bmatrix}$ and $Pfilter = \begin{bmatrix} pfilter & 0 \\ 0 & pfilter \end{bmatrix}$ to derive the matrix form:

$$\Delta S = Pfilter(Io\Delta V' + Vo\Delta I'). \tag{2.37}$$

2.2.6 DC-side Dynamics

Applying the law of conservation of energy, i.e., $W_{DC} = W_{AC}$, we can deduce:

$$\Delta W_{DC} = \Delta W_{AC}, \tag{2.38}$$

$$\Delta W_{DC} = \Delta(\frac{1}{2}(C_{DC})V_{DC}^2). \tag{2.39}$$

By linearization of (2.39), we come up with:

$$\Delta W_{DC} = C_{DC}V_{DC}\Delta V_{DC}. \tag{2.40}$$

In the time domain:

$$\Delta W_{DC} = \Delta W_{AC} = \int \Delta P_{AC} dt, \tag{2.41}$$

and in the frequency domain:

$$\Delta W_{DC} = \frac{\Delta P_{AC}}{s}, \tag{2.42}$$

$$C_{DC}V_{DC}\Delta V_{DC} = \frac{\Delta P_{AC}}{s}. \tag{2.43}$$

By assuming that $\Delta P'_{AC} = \Delta P'$ and also $\Delta V_{dc} = \begin{bmatrix} \Delta V_{DC} \\ 0 \end{bmatrix}$, we obtain:

$$C_{DC}V_{DC}\Delta V_{DC} = \frac{\Delta P'}{s}, \tag{2.44}$$

$$\Delta V_{DC} = \frac{\Delta P'}{C_{DC}V_{DC}s}, \tag{2.45}$$

$$\Delta V_{dc} = \begin{bmatrix} \Delta V_{DC} \\ 0 \end{bmatrix}, \tag{2.46}$$

$$\Delta V_{dc} = \begin{bmatrix} \frac{1}{C_{DC}V_{DC}s} & 0 \\ 0 & 0 \end{bmatrix} \Delta S, \tag{2.47}$$

$$\Delta V_{dc} = DC\Delta S. \tag{2.48}$$

By plugging (2.36) into (2.48):

$$\Delta V_{dc} = pfilter(Kdc\Delta V' + Zdc\Delta I'), \tag{2.49}$$

where $Kdc = DC * Io$ and $Zdc = DC * Vo$.

2.2.7 Angle Reference Generation

Angle reference serves as a necessary input for abc/dq and dq/abc transformation blocks within an inverter and can be generated through different methods for various GFM and GFL inverters. Figure 2.2 shows control blocks of different GFM strategies for angle generation. This subsection derives the small-signal model of these angle generation blocks.

GFL-Conventional

In the conventional basic GFL in which $\theta = Constant$, we have:

$$\Delta\theta = 0. \tag{2.50}$$

In order to have a consistant model, a new complex variable named $\Delta\theta$ is introduced instead of $\Delta\theta$

$$\Delta T = \begin{bmatrix} 0 \\ \Delta\theta \end{bmatrix}. \tag{2.51}$$

Therefore, for the conventional GFL, we have:

$$\Delta T = \begin{bmatrix} 0 \\ 0 \end{bmatrix}. \tag{2.52}$$

GFL-PLL

In most of the GFLs, the angle reference used in the dq/abc or the abc/dq blocks is generated by a Phase-Locked Loop (PLL). The PLL equation is:

$$\Delta\theta = (PI_{pll}/s)\Delta V_q'. \tag{2.53}$$

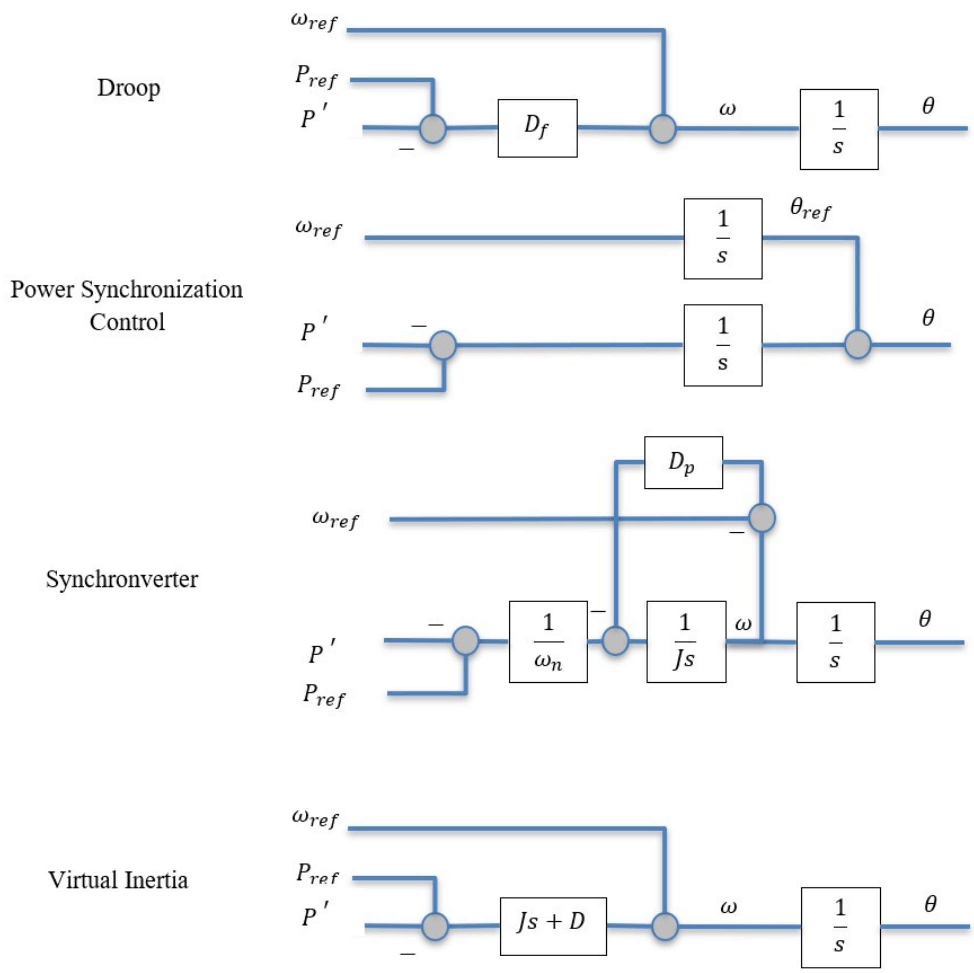

Figure 2.2: GFM control strategies for angle generation.

The following equations convert the PLL equation into ΔT form:

$$\Delta\theta = \left[(0 \quad PI_{pll}/s)\right] \Delta V'_q, \tag{2.54}$$

$$\Delta T = \begin{bmatrix} 0 & 0 \\ 0 & PI_{pll}s \end{bmatrix} \Delta V', \tag{2.55}$$

$$\Delta T = PLL * \Delta V'. \tag{2.56}$$

GFM - Droop Control

Droop control resembles the speed droop characteristic of a governor and trades off the deviations of the power injection and frequency from their nominal values [14]:

$$\Delta\theta = \frac{D_f}{s}\Delta P, \tag{2.57}$$

$$\Delta T = \begin{bmatrix} 0 & 0 \\ \frac{D_f}{s} & 0 \end{bmatrix} \Delta S, \tag{2.58}$$

$$\Delta T = DroopGFM * \Delta S. \tag{2.59}$$

GFM - Syn

Synchronverter (Syn) is a well-known strategy that satisfies the need for a synchronization unit for pre-synchronization purposes, as well as during normal operation [15]:

$$\Delta\theta = \frac{1}{sJ\omega_n(s + \frac{D_p}{J(1+D_pPI_ps)})}\Delta P, \tag{2.60}$$

$$\Delta T = \begin{bmatrix} 0 & 0 \\ \frac{1}{sJ\omega_n(s + \frac{D_p}{J(1+D_pPI_ps)})} & 0 \end{bmatrix} \Delta S, \tag{2.61}$$

$$\Delta T = SYN * \Delta S. \tag{2.62}$$

GFM - Virtual Inertia (VI)

The Virtual Inertia (VI) is a control strategy designed to prevent the transition from self-synchronization mode to PLL mode during grid faults. To ensure consistent performance, a PLL is employed even during regular operations. This approach maintains a continuous output frequency estimation through the PLL, while the angle θ is determined using a specific equation as outlined in [15]. This equation can be transformed into the small-signal domain as:

$$\Delta\theta = \frac{1}{Js^2 + Ds}\Delta P, \tag{2.63}$$

$$\Delta T = \begin{bmatrix} 0 & 0 \\ \frac{1}{JS^2+Ds} & 0 \end{bmatrix} \Delta S, \tag{2.64}$$

$$\Delta T = VI * \Delta S. \tag{2.65}$$

GFM - PSC

The Power Synchronization Control (PSC) is another control strategy wherein a second-order transfer function is implemented in the inner frequency loop, acting on the deviation between power setpoint and measured power [15]:

$$\Delta\theta = \frac{K_i}{s}\Delta P, \tag{2.66}$$

$$\Delta T = \begin{bmatrix} 0 & 0 \\ \frac{K_i}{s} & 0 \end{bmatrix} \Delta S, \tag{2.67}$$

$$\Delta T = PSC * \Delta S. \tag{2.68}$$

2.2.8 abc/dq and Its Inverse Transformation

For closed-loop control of an inverter, abc/dq transformation is imperative. When addressing interactions among multiple inverters, a global dq frame must be considered. Both voltage and current signals are converted into a local dq frame for control purposes. During transients, these two frames may not be exactly the same because of the angle dynamics. In addition, because of the large grid assumption, there is also a steady-state angle difference between both voltage and current global and local dq frames. To differentiate between these frames, the local dq frame signals are denoted with a prime symbol in this report.

abc/dq transformation

abc/dq transformation in a global dq frame is:

$$A' = e^{j\theta} A. \tag{2.69}$$

Both θ and A values can be perturbed. Therefore, small-signal perturbation of the transferred value must consist of both terms. The linear approximation is derived as follows:

$$A' + \Delta A' = e^{j(\theta + \Delta\theta)}(A + \Delta A), \tag{2.70}$$

$$A' + \Delta A' \approx e^{j\theta}(1 + \Delta\theta)(A + \Delta A), \tag{2.71}$$

$$A' + \Delta A' \approx e^{j\theta}(A + \Delta\theta A + \Delta A + \Delta\theta\Delta A). \tag{2.72}$$

By dropping the steady-state and double incremental terms, (2.72) becomes:

$$\Delta A' \approx e^{j\theta}(A\Delta\theta + \Delta A), \tag{2.73}$$

$$e^{j\theta} A' \Delta\theta = (cos\theta + jsin\theta)(A_d + jA_q)\Delta\theta, \tag{2.74}$$

$$e^{j\theta} A' \Delta\theta = ((cos\theta A_d - A_q sin\theta) + j(sin\theta A_d + cos\theta A_d))\Delta\theta, \tag{2.75}$$

$$e^{j\theta} A' \Delta\theta = \begin{bmatrix} (cos\theta A_d - A_q sin\theta) \\ (sin\theta A_d + cos\theta A_d) \end{bmatrix} \Delta\theta, \tag{2.76}$$

$$
\begin{bmatrix}\Delta A_d' \\ \Delta A_q'\end{bmatrix} \approx \begin{bmatrix}(cos\theta A_d - A_q sin\theta) \\ (sin\theta A_d + cos\theta A_d)\end{bmatrix} \Delta\theta + \begin{bmatrix}cos\theta & -sin\theta \\ sin\theta & cos\theta\end{bmatrix} \begin{bmatrix}\Delta A_d \\ \Delta A_q\end{bmatrix}. \tag{2.77}
$$

Considering (2.50), the matrix conversion of (2.77) becomes:

$$
\begin{bmatrix}\Delta A_d' \\ \Delta A_q'\end{bmatrix} \approx \begin{bmatrix}0 & (cos\theta A_d - A_q sin\theta) \\ 0 & (sin\theta A_d + cos\theta A_d)\end{bmatrix} \begin{bmatrix}0 \\ \Delta\theta\end{bmatrix} + \begin{bmatrix}cos\theta & -sin\theta \\ sin\theta & cos\theta\end{bmatrix} \begin{bmatrix}\Delta A_d \\ \Delta A_q\end{bmatrix}, \tag{2.78}
$$

$$
\Delta A' \approx T_A \Delta T + T_{main} \Delta A. \tag{2.79}
$$

Finally, the A variable can be replaced with the output voltage and currrent variables:

$$
\Delta V_o' = T_V \Delta T + T_{main} \Delta V, \tag{2.80}
$$

$$
\Delta I_o' = T_I \Delta T + T_{main} \Delta I, \tag{2.81}
$$

$$
\Delta V_c' = T_{V_c} \Delta T + T_{main} \Delta V_c. \tag{2.82}
$$

dq/abc **transformation:**

Similarly, for the inverse transformation, we have

$$
A = e^{-j\theta} A', \tag{2.83}
$$

$$
A + \Delta A = e^{-j(\theta+\Delta\theta)}(A' + \Delta A'), \tag{2.84}
$$

$$
A + \Delta A \approx e^{-j\theta}(1 - \Delta\theta)(A' + \Delta A'), \tag{2.85}
$$

$$
A + \Delta A \approx e^{-j\theta}(A' - \Delta\theta A' + \Delta A' - \Delta\theta \Delta A'). \tag{2.86}
$$

By dropping the steady-state and double incremental terms, (2.86) becomes:

$$
\Delta A \approx e^{-j\theta}(\Delta A' - A' \Delta\theta), \tag{2.87}
$$

$$
e^{-j\theta} A \Delta\theta = (cos\theta - jsin\theta)(A_d' + jA_q')\Delta\theta, \tag{2.88}
$$

$$e^{-j\theta}A\Delta\theta = ((cos\theta A'_d + A'_q sin\theta) + j(-sin\theta A'_d + cos\theta A'_d))\Delta\theta, \tag{2.89}$$

$$e^{j\theta}A\Delta\theta = \begin{bmatrix} (cos\theta A'_d + A'_q sin\theta) \\ (-sin\theta A'_d + cos\theta A'_d) \end{bmatrix} \Delta\theta, \tag{2.90}$$

$$\begin{bmatrix} \Delta A_d \\ \Delta A_q \end{bmatrix} \approx \begin{bmatrix} (cos\theta A'_d + A'_q sin\theta) \\ (-sin\theta A'_d + cos\theta A'_d) \end{bmatrix} \Delta\theta + \begin{bmatrix} cos\theta & sin\theta \\ -sin\theta & cos\theta \end{bmatrix} \begin{bmatrix} \Delta A'_d \\ \Delta A'_q \end{bmatrix}. \tag{2.91}$$

Considering (2.50), the matrix conversion of (2.91)becomes:

$$\begin{bmatrix} \Delta A_d \\ \Delta A_q \end{bmatrix} \approx \begin{bmatrix} 0 & (cos\theta A'_d + A'_q sin\theta) \\ 0 & (-sin\theta A'_d + cos\theta A'_d) \end{bmatrix} \begin{bmatrix} 0 \\ \Delta\theta \end{bmatrix} + \begin{bmatrix} cos\theta & sin\theta \\ -sin\theta & cos\theta \end{bmatrix} \begin{bmatrix} \Delta A'_d \\ \Delta A'_q \end{bmatrix}, \tag{2.92}$$

$$\Delta A \approx T'_A \Delta T + 1/T_{main}\Delta A. \tag{2.93}$$

Finally, the actual modulation index formula can be obtained in the matrix form as:

$$\Delta D = T'_D \Delta T + 1/T_{main}\Delta D'. \tag{2.94}$$

2.2.9 GFL - Droop

Certain GFL inverters may contribute to voltage and frequency support within the system through a GFL droop block which adjusts active and reactive power references based on the frequency and voltage magnitude, respectively. The corresponding equations are as follows:

$$\Delta P_{ref} = \Delta\theta/m_p, \tag{2.95}$$

$$\Delta Q_{ref} = \Delta V_m/n_p, \tag{2.96}$$

$$\Delta S_{ref} = \begin{bmatrix} P_{ref} \\ Q_{ref} \end{bmatrix}, \tag{2.97}$$

where V_m is the output voltage magnitude, which can be written as $V_m = \sqrt{(V_d^2 + V_q^2)}$ and can be linearized as:

$$\Delta V_m = (V_d/V_m)\Delta V'_d + (V_q/V_m)\Delta V'_q. \tag{2.98}$$

The prime indices are incorporated into ΔV_m to signify its derivation from voltage measurements. Furthermore, $\Delta\theta$ is calculated as presented in (2.53). The resultant ΔP_{ref}, ΔQ_{ref}, and ΔS_{ref} can be determined as follows:

$$\Delta P_{ref} = \begin{bmatrix} 0 & PI_{pll}/sm_p \end{bmatrix} \Delta V', \tag{2.99}$$

$$\Delta Q_{ref} = \begin{bmatrix} V_d/V_m n_p & V_q/V_m n_p \end{bmatrix} \Delta V', \tag{2.100}$$

$$\Delta S_{ref} = \begin{bmatrix} 0 & PI_{pll}/sm_p \\ V_d/V_m n_p & V_q/V_m n_p \end{bmatrix} \Delta V', \tag{2.101}$$

$$\Delta S_{ref} = DroopGFL * \Delta V'. \tag{2.102}$$

Figure 2.3 shows a block diagram representation of both GFM and GFL inverter models. In Fig 2.3, each signal is a 2×1 matrix (for example $\begin{bmatrix} \Delta V_d \\ \Delta V_q \end{bmatrix}, \begin{bmatrix} \Delta I_d \\ \Delta I_q \end{bmatrix}, \begin{bmatrix} \Delta P \\ \Delta Q \end{bmatrix}, and \begin{bmatrix} \Delta\theta \\ 0 \end{bmatrix}$) and each transfer block is a 2×2 matrix of transfer functions, $\begin{bmatrix} X_{dd} & X_{dq} \\ X_{qd} & X_{qq} \end{bmatrix}$ or a linear function of two 2×2 matrices when there are two inputs ($A \begin{bmatrix} X_{dd} & X_{dq} \\ X_{qd} & X_{qq} \end{bmatrix} + B \begin{bmatrix} Y_{dd} & Y_{dq} \\ Y_{qd} & Y_{qq} \end{bmatrix}$). In Fig. 2.3, the red parts are only for GFL inverters while blue characters are only for GFM converters. The linearized block diagrams are shown in Fig. 2.4.

As shown in the Fig. 2.3, the small-signal model of the GFL inverter is built considering the abc/dq effect. Under voltage disturbance, this block generates an error between the converter and global dq frames. The effect of ΔT on the measured small-signal currents and voltages in both GFL and GFM inverters is shown. The noticeable point in Fig. 2.3 is how the generation of ΔT is different in GFL and GFM. The figure shows that the GFM ΔT is generated using both ΔI and ΔV signals, whereas the GFL ΔT is only made from ΔV. Therefore, complexity doubles in the GFM, and more poles will be added to the final small-signal impedance. The difference between GFM and GFL modes is the existence of ΔI alongside ΔV in reference angle generation.

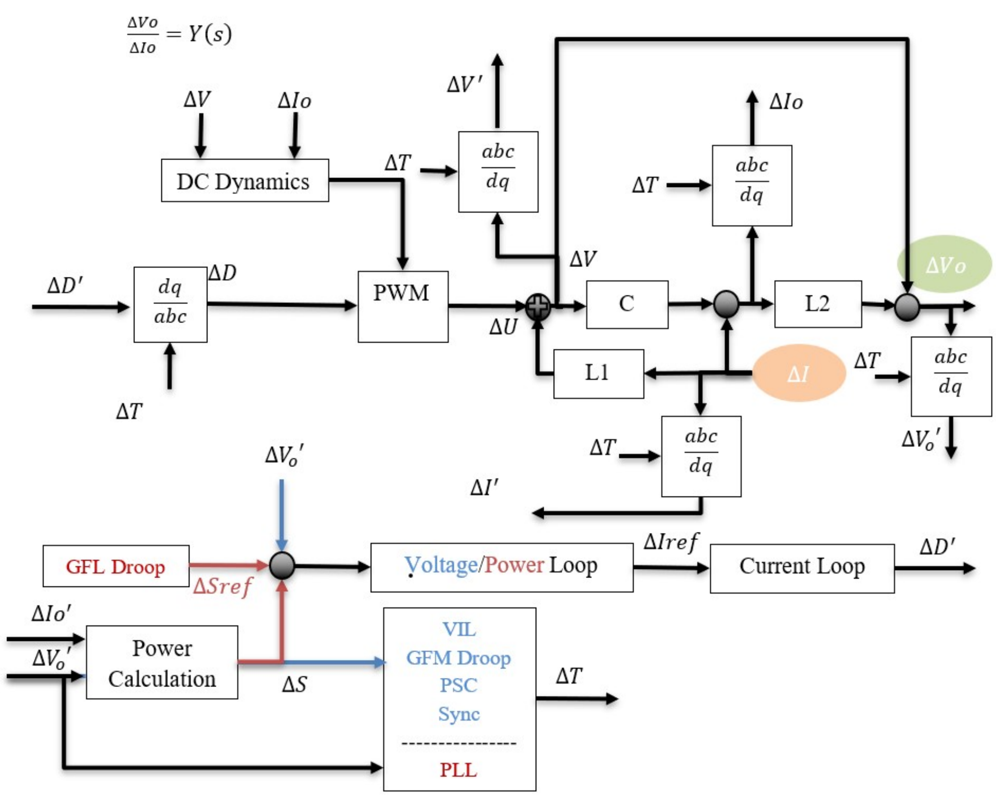

Figure 2.3: Exact inverter small-signal model in matrix form. Black lines and text are for both GFM and GFL, blue lines and text are only for GFM, and red lines and text are only for GFL.

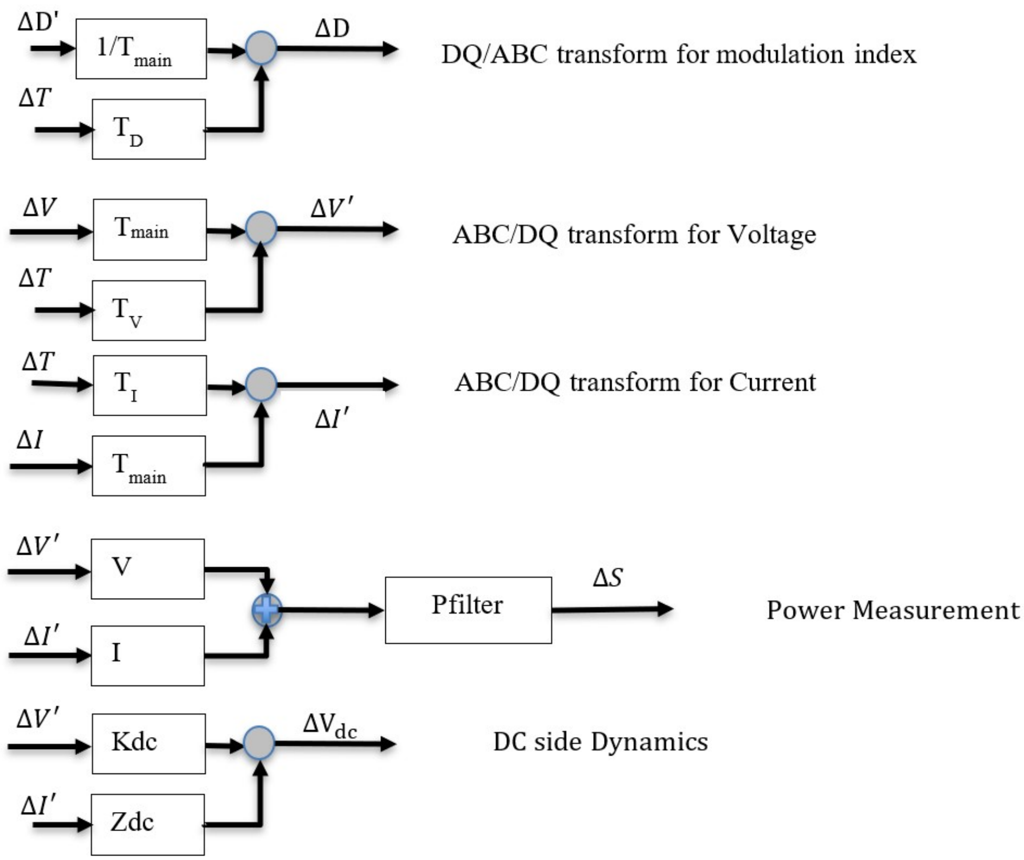

Figure 2.4: Linearized block diagrams of the inverters.

3. Results and Discussion

3.1 Computational Procedure

In Section 2.2, all block equations are eventually transformed into a matrix form involving 2×2 parameters and 1×2 variables. Through this mapping and without loss of generality, all blocks can be expressed as a set of algebraic equations involving scalar parameters and scalar variables. These equations can then be solved using scalar equation solvers. This approach offers computational efficiency, as the results can be computed once and stored for subsequent use, obviating the need for repeated equation solving. After saving the results, the variables can be eliminated, and 2×2 parameters are integrated to yield a conclusive admittance/impedance 2×2 parameter. Following this calculation, the outcomes for each component, namely dd, dq, qd, and qq, for each inverter are stored separately, preferably as a character data class in the computer. Ultimately, these formulas can be used for each set of parameters to derive the numerical transfer functions. The algebraic solutions for matrix equations of each inverter is carried out in Matlab, with their nominator and denominators being calculated parametrically.

3.2 Matrix Substitution

In the next step, each term of the matrix equations from Matlab is replaced with its corresponding complex matrix. A list of all terms with their complex form is presented in Tables 3.1 and 3.2.

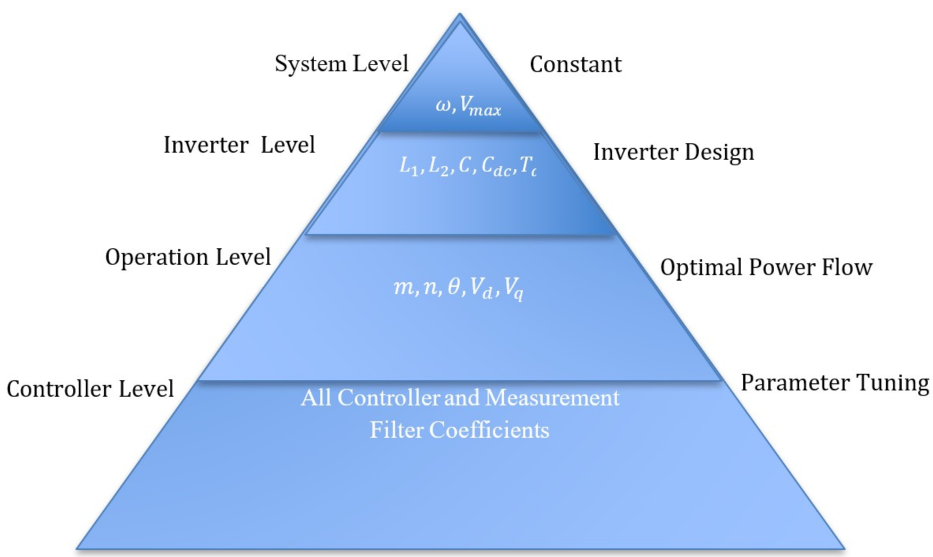

Figure 3.1: Hierarchy of small-signal derivation.

Table 3.1: Matrix Arrays of Parameters

Parameter	dd	dq	qd	qq
Vo	V_{do}	V_{qo}	V_{qo}	$-V_{do}$
Io	I_{do}	I_{qo}	$-I_{qo}$	I_{do}
Z_{L_1}	sL_1	$-\omega L_1$	ωL_1	sL_1
$L1w$	0	$-\omega L_1$	ωL_1	0
Z_{L_2}	sL_2	$-\omega L_2$	ωL_2	sL_2
$L2w$	0	$-\omega L_1$	ωL_1	0
Z_c	sC	$-\omega C$	ωC	sC
Cw	0	$-\omega C$	ωC	0
PIC	$KP_c + KI_c/s$	0	0	$KP_c + KI_c/s$
Fv	$K_{vf}/(1+T_{vf}s)$	0	0	$K_{vf}/(1+T_{vf}s)$
FII	$K_{vii}/(1+T_{vii}s)$	0	0	$K_{vii}/(1+T_{vii}s)$
PIS	$KP_p + KI_p/s$	0	0	$KP_q + KI_q/s$
PIV	$KP_pV + KI_pV/s$	0	0	$KP_qV + KI_qV/s$
$PFilter$	$\omega_c/s+\omega_c$	0	0	$\omega_c/s+\omega_c$
PLL	0	0	0	$KP_{pll} + KI_{pll}/s$
$Droop$	0	$KP_{pll} + KI_{pll}/s$	$V_d/n\sqrt{V_d^2+V_q^2}$	$V_q/n\sqrt{V_d^2+V_q^2}$

3.3 Parameters Substitution and Tuning

Upon matrix substitution, four parametric transfer functions will be generated for each of the inverter controls mentioned in Section 2.2.7. Some of these parameters, such as system frequency ω are dictated by the system. On the other hand, semiconductor, LCL, and DC elements (L_1, L_2, C, and C_{DC} and T_{del}), are determined through the inverter hardware design process. In addition, voltage magnitude and angle reference, which are not dependent variables and the coeeficeincts of Grid Forming Inverter (GFM) droop control are established based on grid operation. The remaining coefficients are implemented locally on a control board. In the design hierarchy shown in Fig. 3.1, the primary objective is to achieve optimal performance with the given parameters derived from an upper-level study. However, adjustments at the upper level might be required if the desired performance cannot be attained. While systematic methods like those outlined in [16] exist to search for optimal parameters, they often have limitations tied to specific types of inverters and are tailored for more constratined inverter models. Tables 3.1 and 3.2 provide the list parameters involved in small-signal modeling and their corresponding contribution to various matrix arrays.

3.4 Comparison of Small-Signal Characteristics for Various GFM Inverters

In this section, the inverter control strategies mentioned in Section 2 are compared in terms of eigenvalues, as well as their frequency domain characteristics.

Table 3.2: Matrix Arrays of Parameters

Parameter	*dd*	*dq*	*qd*	*qq*
$DroopGFL$	D_f/s	D_f/s	0	0
VI	$1/(Js^2+D_{vil}s)$	$1/(Js^2+D_{vil}s)$	0	0
SYN	$\frac{1}{sJ\omega_n(s+\frac{D_p}{J(1+D_pPI_ps)})}$	$\frac{1}{sJ\omega_n(s+\frac{D_p}{J(1+D_pPI_ps)})}$	0	0
PSC	K_pSC/s	K_pSC/s	0	0
K_{DC}	$I_d/C_{DC}V_{DC}$	$I_q/C_{DC}V_{DC}$	0	0
Y_{DC}	$V_d/C_{DC}V_{DC}$	$V_q/C_{DC}V_{DC}$	0	0
$DelD$	$D(\frac{1-0.5T_{del}s}{1+0.5T_{del}s})$	0	0	$D(\frac{1-0.5T_{del}s}{1+0.5T_{del}s})$
$Delv$	$Vdc(\frac{1-0.5T_{del}s}{1+0.5T_{del}s})$	0	0	$Vdc(\frac{1-0.5T_{del}s}{1+0.5T_{del}s})$
$TETA$	$cos(\theta)$	$sin(\theta)$	$-sin(\theta)$	$cos(\theta)$
T_v	0	$-sin(\theta)V_d+cos(\theta)V_q$	0	$-cos(\theta)I_d-sin(\theta)I_q$
T_{io}	0	$-sin(\theta)Io_d+cos(\theta)Io_q$	0	$-cos(\theta)Io_d-sin(\theta)Io_q$
T_i	0	$-sin(\theta)I_d+cos(\theta)I_q$	0	$-cos(\theta)I_d-sin(\theta)I_q$
T_d	0	$cos(\theta)D_d+sin(\theta)D_q$	0	$-sin(\theta)D_d+cos(\theta)D_q$

Table 3.3: Number of Eigenvalues for Each Strategy

Inverter Strategy	GFL basic	GFL	GFM_{PSC}	GFM_{droop}	GFM_{syn}	GFM_{VIL}
Number of *dd* poles	12	12	17	17	21	16
Number of *dq* poles	17	17	16	16	20	16
Number of *qd* poles	19	19	13	13	17	19
Number of *qq* poles	13	17	15	15	19	20

3.4.1 Eigenvalue Analysis

The number of poles, which is equivalently expressed as the number of eigenvalues, for various inverter control strategies is detailed in Table 3.3. The results in Table 3.3 show that GFM_{syn} presents the highest level of complexity in terms of eigenvalues, while GFL_{basic}, a conventional GFL model, boasts the minimum number of poles. Another note-worthy point is that the number of poles exhibits notable variation across control strategies, frequently featuring diverse matrix elements with varying degrees of complexity.

3.4.2 Frequency Domain Analysis

In this subsection, the frequency response of the inverters is presented through Bode diagrams. The optimal parameters are determined through extensive trials and errors with consideration of parameter dependencies in power flow and also complying with the cascaded controller design strategy obtained from [16].

Figure 3.2 depicts the Bode response of the droop GFM. The results show that all gains are negative,

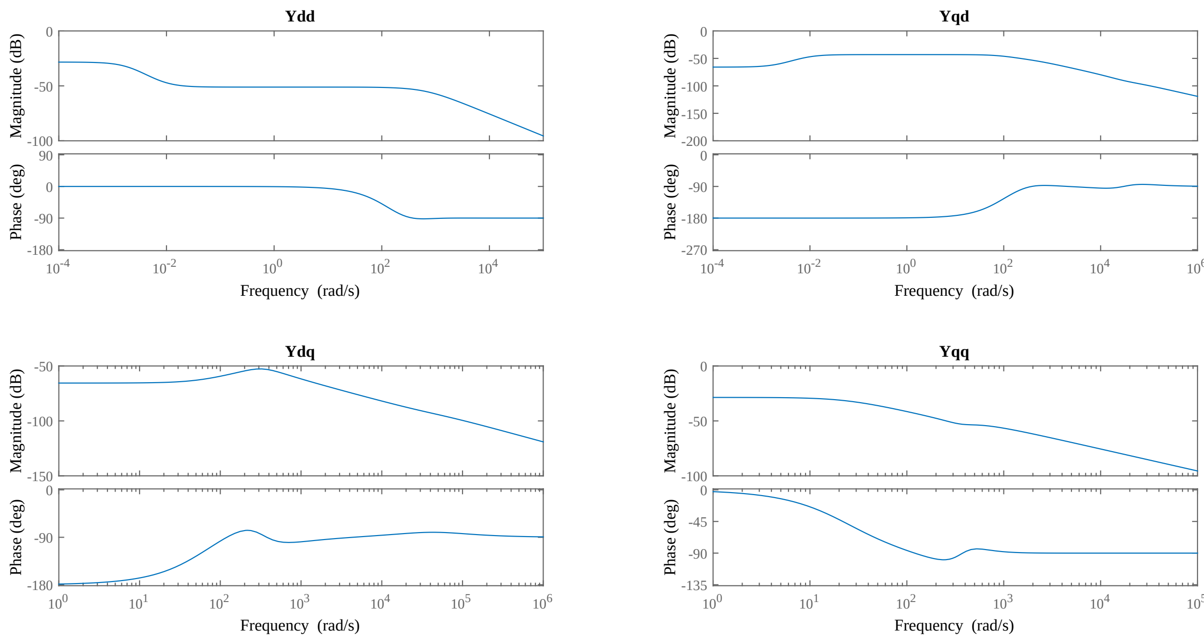

Figure 3.2: Bode diagram of droop inverter.

implying optimal parameters result in lower magnitude and dampening of disturbances across all frequencies. Furthermore, all Y_{dd}, Y_{qd}, Y_{dq}, and Y_{qq} function as low-pass filters, indicating that high-frequency oscillations do not significantly impact inverter performance.

Figure 3.3 shows the Bode diagram of the VI inverter. Notably, due to the presence of an additional term in ΔT generation, a new pole emerges at a frequency of approximately 10^2 rad/s. This addition introduces a higher level of complexity in the response compared to the droop control. This implies that any oscillation within the system will lead to a transient with a frequency of 10^2 rad/s circulating throughout the system. This specific pole has the effect of elevating the gain in Y_{qd} and Y_{dd} beyond 0 dB if an oscillation near 10^2 (rad/s) occures.

Figure 3.4 shows the Bode results of the PSC inverter. The outcomes demonstrate a stable behavior in Y_{dq} and Y_{qd}. However, in the proximity of a specific pole, the magnitude exceeds $0(dB)$. Notably, all four transfer functions of the PSC can be characterized as low-pass filters, akin to the droop controller.

Turning to Fig. 3.5, the Bode results of the Syn inverter are depicted. As indicated in Fig. 3.5, the Syn inverter exhbits the most intricate Bode diagram among various GFM controls. Notably, a highly distinctive feature of the Syn inverter is the pronounced magnitude and angle shift within a specific frequency range. This Bode diagram signifies an oscillatory behavior in response to disturbances. Similar to the PSC, Y_{dq} and Y_{qd} can attenuate disturbances in this case.

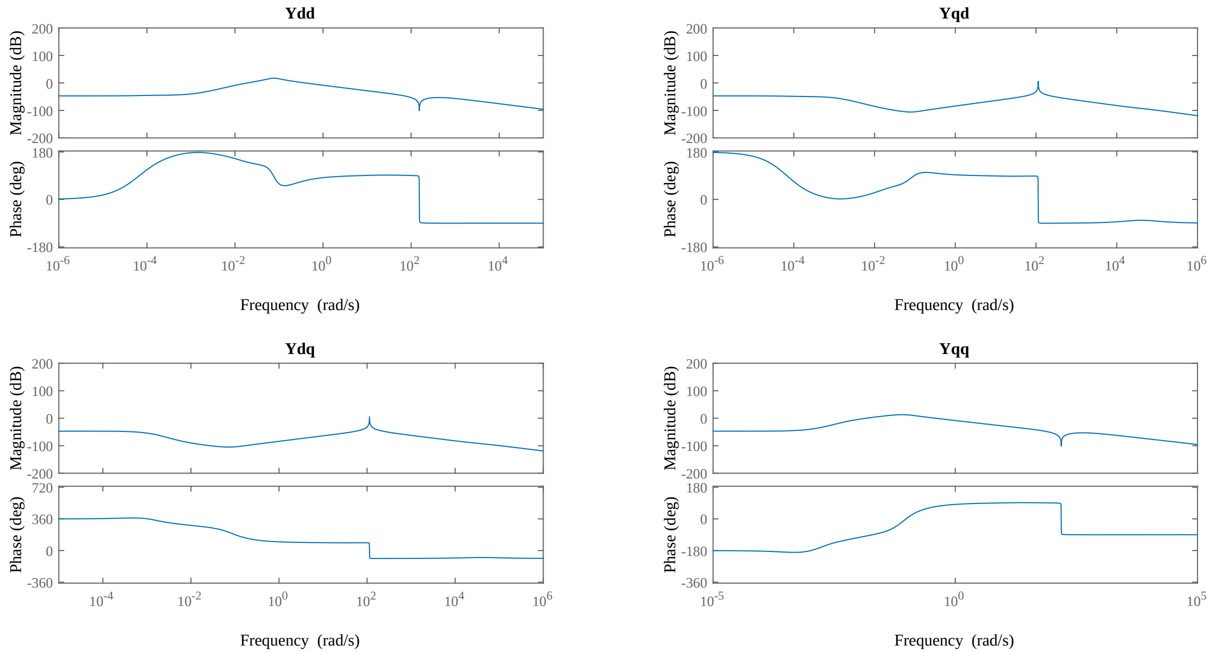

Figure 3.3: Bode diagram of VI inverter.

3.5 Conclusions

This project is focused on small-signal stability analysis of GFM and GFL inverters. To this end, parametric models are developed to incorporate various control strategies. Within the realm of GFM inverters, the Synchronvertor strategy presents particular complexity and challenges in the context of model reduction. While droop control strategies exhibit stable behavior, others struggle to achieve stability using identical parameters. For GFL inverters, the transfer function Y_{dq} is more susceptible to instability compared to the other three transfer functions. The outcomes and results of this project can be extended to a multi-converter system and used for inter-area oscillation damping.

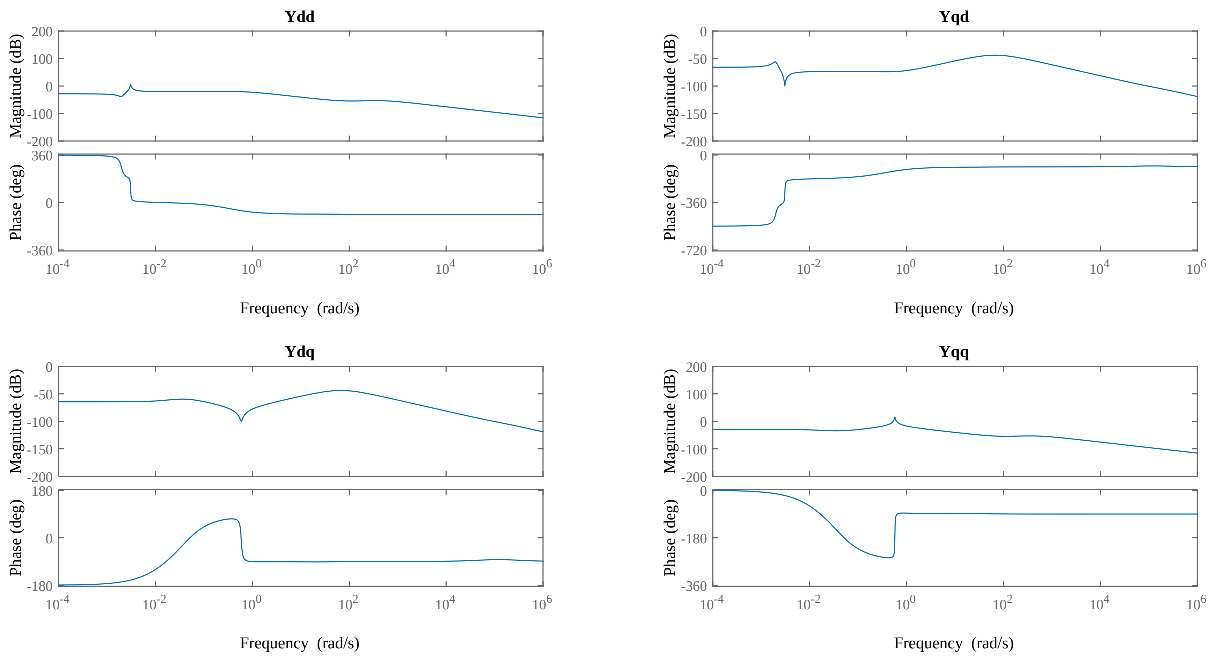

Figure 3.4: Bode diagram of PSC inverter.

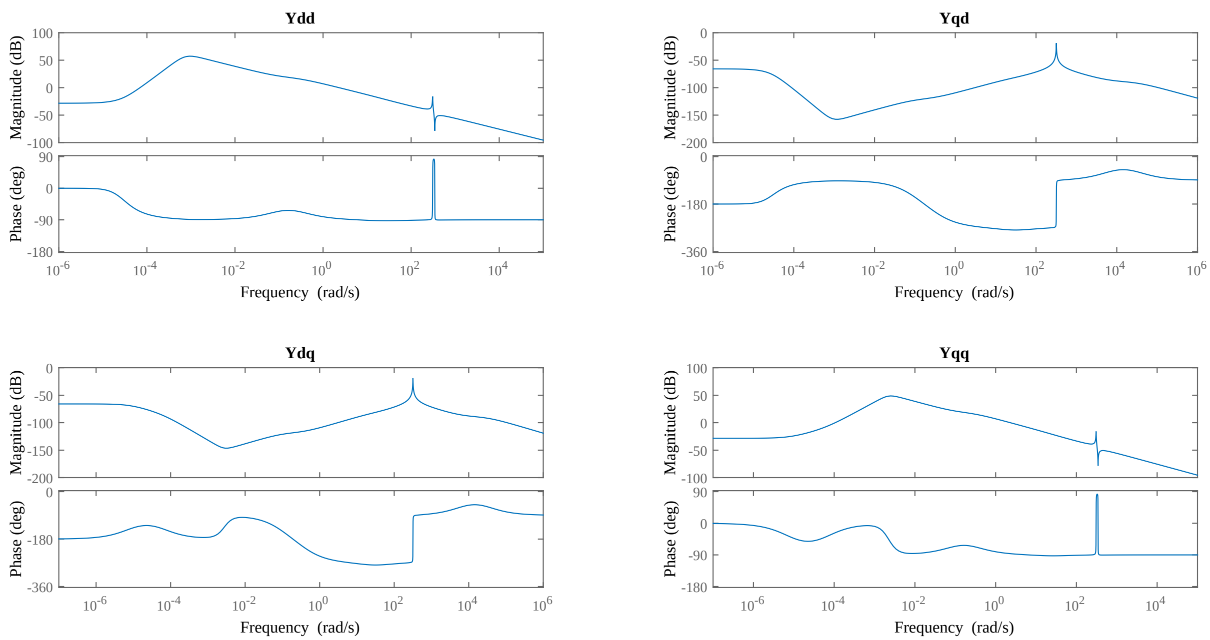

Figure 3.5: Bode diagram of Syn inverter.

References

[1] D. Muthumuni, "General introduction to electromagnetic transient simulations - mathematical background and common applications," *PSCAD Webinar*, p. 30, 2020.

[2] H. W. Dommel, "Digital computer solution of electromagnetic transients in single-and multi-phase networks," *IEEE Transactions on Energy Conversion*, vol. PAS-88, no. 4, pp. 388–399, 1969.

[3] ——, "Nonlinear and time-varying elements in digital simulation of electromagnetic transients," *IEEE Transactions on Power Apparatus and Systems*, vol. PAS-90, no. 6, pp. 2561–2567, 1971.

[4] Y. Xu, Y. Chen, L. Chen, and S. Mei, "Integrating an improved averaged model for PWM converters into EMTP," *IEEE Transactions on Power Delivery*, vol. 29, no. 1, pp. 291–293, 2014.

[5] J. Rupasinghe, S. Filizadeh, and L. Wang, "A dynamic phasor model of an MMC with extended frequency range for EMT simulations," *IEEE Journal of Emerging and Selected Topics in Power Electronics*, vol. 7, no. 1, pp. 30–40, 2019.

[6] T. Yang, "Development of dynamic phasors for the modelling of aircraft electrical power systems," Ph.D. dissertation, The University of Nottingham, 2013.

[7] Y. Amran, F. Huliehel, and S. Ben-Yaakov, "A unified SPICE compatible average model of PWM converters," *IEEE Transactions on Power Electronics*, vol. 6, no. 4, pp. 585–594, 1991.

[8] M. Klein, G. Rogers, and P. Kundur, "A fundamental study of inter-area oscillations in power systems," *IEEE Transactions on Power Systems*, vol. 6, no. 3, pp. 914–921, 1991.

[9] L. Ding, X. Lu, and J. Tan, "Comparative small-signal stability analysis of grid-forming and grid-following inverters in low-inertia power systems," in *47th Annual Conference of the IEEE Industrial Electronics Society*, 2021, pp. 1–6.

[10] L. Harnefors, M. Bongiorno, and S. Lundberg, "Input-admittance calculation and shaping for controlled voltage-source converters," *IEEE Transactions on Industrial Electronics*, vol. 54, no. 6, pp. 3323–3334, 2007.

[11] X. Wang, L. Harnefors, and F. Blaabjerg, "Unified impedance model of grid-connected voltage-source converters," *IEEE Transactions on Power Electronics*, vol. 33, no. 2, pp. 1775–1787, 2018.

[12] B. Wen, D. Boroyevich, R. Burgos, P. Mattavelli, and Z. Shen, "Analysis of d-q small-signal impedance of grid-tied inverters," *IEEE Transactions on Power Electronics*, vol. 31, no. 1, pp. 675–687, 2016.

[13] C. Yang, L. Huang, H. Xin, and P. Ju, "Placing grid-forming converters to enhance small signal stability of PLL-integrated power systems," *IEEE Transactions on Power Systems*, vol. 36, no. 4, pp. 3563–3573, 2011.

[14] A. Tayyebi, D. Groß, A. Anta, F. Kupzog, and F. Dörfler, "Frequency stability of synchronous machines and grid-forming power converters," *IEEE Journal of Emerging and Selected Topics in Power Electronics*, vol. 8, no. 2, pp. 1004–1018, 2020.

[15] R. Rosso, X. Wang, M. Liserre, X. Lu, and S. Engelken, "Grid-forming converters: Control approaches, grid-synchronization, and future trends—a review," *IEEE Open Journal of Industry Applications*, vol. 2, pp. 93–109, 2021.

[16] T. Qorai, F. Gruson, F. Colas, X. Guillaud, M.-S. Debry, and T. Prevost, "Tuning of cascaded controllers for robust grid-forming voltage source converter," in *IEEE Power Systems Computation Conference (PSCC)*, 2018.

Part II

Grid Supporting Controllers for Enabling 100% Penetration of Inverter Based Resources

Sakis A. P. Meliopoulos
George J. Cokkinides
Siyao Cai, Graduate Student
Kaiyu Liu, Graduate Student
Syed Sohail Feroz Syed Afroz, Graduate Student

Georgia Institute of Technology

For information about this project, contact:

Sakis A.P. Meliopoulos
Georgia Power Distinguished Professor
Georgia Institute of Technology
School of Electrical and Computer Engineering
Atlanta, Georgia 30332-0250
Phone: 404-894-2926
E-mail: sakis.m@gatech.edu

Power Systems Engineering Research Center

The Power Systems Engineering Research Center (PSERC) is a multi-university Center conducting research on challenges facing the electric power industry and educating the next generation of power engineers. More information about PSERC can be found at the Center's website: http://www.pserc.wisc.edu.

For additional information, contact:

Power Systems Engineering Research Center
Arizona State University
527 Engineering Research Center
Tempe, Arizona 85287-5706
Phone: 480-965-1643
Fax: 480-965-0745

Notice Concerning Copyright Material

Table of Contents

List of Figures

List of Tables

1. Introduction

The electric power system is undergoing a transformation as more and more inverter interfaced resources are added to the system. The trend will result in future power systems that transition to significant amount of renewable energy. For example, California has mandated 100% renewable energy supply by 2045 and Minnesota has passed laws to move to full renewable energy supply by 2050. New technologies such as HVDC systems will also be integrated into the conventional AC systems forging hybrid AC-DC systems. To assure reliable integration of such a massive amount of renewable inverter-based resources (IBRs), the IBRs should be augmented with grid support capabilities and compatibility features. To this end, this project proposes a multi-pronged research effort as follows: i) Grid Firming Converters: proposing methods to achieve desired voltage and frequency supports from IBRs such as wind and PV farms in the future grid, ii) Grid Forming Converters: developing controls to enable cold start capability of a system with high penetration of renewables, and iii) Resilient Converters: Designing fault ride through capability and post-fault recovery control strategies to avoid massive dropouts of renewables following a disturbance such as what happened in the Western system.

This report addresses the issues associated with Grid Forming Converters: developing controls to enable cold start capability of a system with high penetration of renewables.

In legacy power systems, synchronous machines automatically provide load start-up support within their capability by virtue of their inherent inertia and generated voltage. In a system with large penetration of IBRs, the converters should have this capability as well. We discuss the development of controllers that will enable a converter to control the frequency and transient response of the grid in such a way that the grid will be steered to operate near nominal frequency and voltage, minimize transients and ensure the correct operation of all inverters in the system. This is the essence of grid forming inverters. We will demonstrate the controller performance for the basic problem of starting a dynamic load, such as an air-conditioner, with a 100% inverter interfaced resources system. This basic problem will generate a plethora of knowledge that will provide the size (ratings) required by a converter to start a specific load of known dynamics. This information is necessary to define and provide design guidance for the cold start capabilities of an IBR dominated power system.

Cold start of a typical large coal power plant takes several hours. Converters have the potential to be loaded quickly as load as the power source is available (wind, PV, battery) with the appropriate controller. Therefore, each generation unit in an IBR-based power system can quickly start operating. However, in a system with many IBRs, devising a coordinated cold start for the out-of-service resources is necessary. The proposed method will enable cold start capability of each IBR and more importantly, each converter is equipped with a supplementary controller, which is automatically activated when a cold start condition is detected. The supplementary controller ensures that full power of the renewable energy resource is brought into service as quickly as possible. In this task, we will study the performance and effectiveness of the proposed method by quasi-dynamic domain simulation studies on a test system.

The report is organized as follows. We first review the existing control strategies for GFM inverters. Section 3 introduces the model development and simulation method we used in this project. Section 5 presents the simulation results of the proposed control strategy. Section 6 presents a comparison of results between the quadratized modeling approach results and the PSCAD results. Future works of this project will be presented in section 7.

2. Literature Review

There is much work on grid forming inverters as they are considered an essential solution for the challenges facing the power systems of the future. This section provides a small glimpse of the research work in this area.

2.1 Inverter-Dominated Power System

Electric power resources that may operate at other than AC near nominal frequency, may need to be interfaced to the electric power system via power electronics, primarily inverters. These systems are referred to as Inverter Based Resources, or IBRs. IBRs convert electric power in these resources to AC power of frequency equal to the frequency of the power grid. Power systems with over 50% of its rated installed power is IBRs are classified as inverter-dominated power grid [1]. The level of generation from IBRs at any instant of time varies from the installed power. We can define the concept of operating penetration level, which is defined as the percentage of generation via IBRs. It is important to note that in the US, the penetration measured in terms of installed capacities is relatively small, less than 30%, the operating penetration level has reached 100% for some system for short periods of time. The operating penetration level is more important for the stability of the power system.

The stability of conventional power system has three major categories: rotor angle stability, frequency stability and voltage stability [2]. The rotor angle stability measures the ability of the synchronous generator to remain in synchronism after disturbances. In inverter-dominated power systems, as the number of synchronous generators decreases significantly, the fault ride-through capabilities become one of the key factors of power system stability [3]. The requirements for frequency and voltage stability remain the same for inverter-dominated power systems. Traditionally, the normal operation range for frequency is ±0.2 Hz. The normal operation voltage range for North American power systems depends on the sector of end users. For residential is ±5% of the nominal voltage [4].

It is important to recognize that grid forming inverters should provide the same performance as the historical performance of legacy power systems.

2.2 Grid-Following (GFL) Inverters –and their Controllers

The performance of inverters primarily depends on the design of their controllers. There are two classes of inverter controllers, grid-following (GFL) controller and grid-forming (GFM) controller. GFL controllers represent the most popular control strategy of IBR connected to the grid now [5]. GFL controllers have two major components: a phase-locked loop (PLL) that estimates the frequency and phase angle of the sinusoidal voltage at the terminals of the inverter and a current-control loop that regulates the AC current output frequency and phase angle [6]. As a result, grid following inverters, follow the frequency and the phase angle of the power system. PLL was originally introduced by Appleton in 1923 and Bellescize in 1932. It was first used for synchronous reception of radio signals and later used in communication systems and motor control systems [7]. Recently, PLL has been used for synchronization between inverters and the grid [8].

The fundamental of GFL control strategies is measuring the instantaneous phase angle of the AC voltage. In general, it works well when the system exhibits minimal amplitudes of frequency deviations. The original PLL design contains a phase detector (PD), a loop filter (LP) and a voltage-controlled oscillator (VCO). PD measures the difference between the phase angles of the input and output signals. LP in PLL is typically a low-pass filter that suppresses the noise and high-frequency signals from the PD. VCO is an electronic device that generates waveforms, where the frequencies of the generated waveforms are determined by the input voltages. The output signal tracks the input signal and minimizes the phase error with the input signal [9].

Although PLL and its variations are widely used in GFL inverter controllers, the low system inertia of inverter dominated systems and the resulting high rate of change of frequency (ROCOF) requires the PLL to respond to fast changes in frequency and voltage transients. In general, it is difficult for the PLL to respond fast enough. Specifically, the PLL requires a period of time to change the frequency during fast system frequency changes [10]. This slow response will affect the firings of the inverter valves and the operation of the inverter may deviate from synchronization with the power grid and possible mis-operations of valve firings. This is a main drawback of GFL inverters. This poor performance of GFL inverters during transients can be corrected by replacing PLLs with digital controllers that are more flexible and can respond faster. The appropriate use of digital controllers and improved controllability leads to grid forming inverters to be discussed next.

2.3 Grid-Forming (GFM) Inverters and Their Controllers

Over the past years, many researchers have devoted efforts to developing Grid-forming control strategies. GFM inverters do not use PLLs for the reasons discussed earlier. Also, GFM inverter can work independently from external voltage measurements. It actively controls the frequency and magnitude of the output voltage. Therefore, the control strategy can incorporate voltage and frequency regulation to the local power system [11].

In an inverter dominated power system, the amount of generation from synchronous machines decreases. The ability to provide the required transient power following an outage is reduced since the inverters are limited in providing required transient power. In legacy power systems, the cold-start capability is provided by self-energized devices that can provide the active and reactive power to accommodate the required high inrush currents by transformers and the high starting currents of induction motors [12]. GFL inverters require a stable power system with minimal transients to operate normally. Therefore, GFL inverters cannot provide cold-start capability to the power system. Whereas GFM inverters with battery energy storage system (BESS) can provide the cold-start capability to the power system as GFM inverters can operate independently from the external grid.

There are several existing GFM controllers that have been widely used and investigated. In this section, we will review some of the popular GFM controllers including Droop Control, Virtual Synchronous Machine, Power-Synchronization Control and Virtual Oscillator Controller. These controllers will be analyzed from three aspects, frequency control, voltage control and black start capabilities.

2.4 Droop Control

Droop control was first introduced in 1993 by *Chandorkar et al*. [13]. The author presented a control scheme for parallel-connected inverters in a standalone AC supply system without reference of system frequency and voltage. Instead, the inverter is controlled based on feedback measured locally at the inverter. The inverter controls the real and reactive power fed into the AC system by controlling the time integral of the inverter output voltage space vector [14]. The real power (P) is controlled by the power angle and the reactive power (Q) is controlled by the inverter flux vectors. The difference between the set point and the measure value of P and Q are fed into a proportional-integral (P-I) regulator, where the set points of the control parameters were generated for the control loop.

The frequency control of the droop controller is implemented by a PI controller of the difference between the actual and reference angle position of the AC system voltage vector. The voltage is controlled by the voltage amplitude of the measured AC system voltage vector. *Ogbonnaya et al* analyzed the black start capability of islanded droop-controlled microgrids [15]. The author developed a systematic black start formulation that simulates the sequential restoration of an islanded droop-controlled microgrid. In the simulation, two GFM inverters were used to provide voltage reference to the system during the restoration process. The soft black-start capabilities of droop control were also evaluated by *Alassi et al*. where they developed a test system with a 2-level, 3-phase VSC based GFM inverter connected to an AC system [16]. Several GFM inverter control techniques including droop control and virtual synchronous machine were tested under AC and DC disturbances and black starts. A 35 MW and 5 MVAr loads were connected to an islanded network at the PCC to evaluate the soft black-start capability of the control schemes. The results show that droop control was able to follow the reference voltage and frequency while instantaneously providing the required real and reactive power during the soft black-start process.

The key advantages of droop control are that it enables the proportional power sharing between parallel connected GFM inverters in the system and it does not require communication channels between the parallel connected inverters to achieve system-wide synchronization. Droop control operates like a conventional synchronous machine, which exhibits a linear trade-off between frequency and voltage versus real and reactive power [17]. Typically, the droop control has P-Omega (real power-frequency) control mode and Q-V (reactive power-voltage) control mode. In P-Omega control model allows the frequency of each inverter to decrease slightly and increase the real power as the load in the system increases. Similarly, a linearly proportional relationship exists between the reactive power and the voltage output of the inverter.

2.5 Virtual Synchronous Machine

Another popular approach in the design of GFM inverter controllers is to make the inverters behave as synchronous machines. The objectives of this approach are apparent. The Virtual Synchronous Machine (VSM) control strategy was first introduced by Beck et al in 2007 [18]. The working principle of VSM is to control the operation of the inverter in such way that it acts like a synchronous machine between DC voltage source and the grid. The mechanical system of an electromechanical machine is represented by a control strategy in VSM. A virtual rotating mass is created in the model to be electrically effective in relation to the grid with adjustable model parameters [19]. For this approach to work properly, it is required that the inverter has an available power source at the DC bus, and it is designed to deliver currents that need to be much higher than the typical rated currents of inverters (i.e., the inverter must be properly over-rated).

The VSM model has two classes of components, power electronic components and computational components. Power electronic components contain highly dynamic IGBT inverter and phase current controller. The computational components include algorithmic model of synchronous machine and a DSP model. The VSM takes instantaneous grid voltage measurements as inputs to determine the instantaneous current of the virtual machine. *Miguel et al* presented the frequency control of VSM, where the controller monitors the frequency of the grid and compares it to the reference frequency that the system needs to reach in steady state [20]. Once a frequency deviation is detected, the model that emulates the inertial response starts to inject power to the grid or absorb power from the grid to regulate the frequency of the system. Another method by which the VSM controls the frequency is through the damping coefficient and the damping power.

To control the voltage output of VSM, *Chen et al* presented an updated control scheme for VSM, where the inputs are grid currents measured at the PCC and the outputs are the reference voltage of the PWM [21]. In [16], the author also evaluated the performance of the VSM scheme in soft black-start scenarios, where the results showed that VSM has the capability to support a soft black-start. But the proposed test system in the paper does not include transformers and induction motors, which is unrealistic for a real-world cold start scenario.

In general, the approach to design inverter controllers to make inverters behave as virtual synchronous machines is costly. On the other hand, it is an effective way to make the inverters Grid Forming.

2.6 Power-Synchronization Control

The power-synchronization control (PSC) is a control method that is being widely used in renewable energy systems and microgrids to coordinate and regulate the power flow between multiple power sources and IBRs in the power system to achieve synchronization. In power-synchronization control for VSC, unlike PLL, phase angle and voltage magnitude are directly used to control the active power and reactive power. [22] A reference value of active power is fed into the power-synchronization controller and the output is the change in phase angle.

The frequency control of PSC is implemented with a power-synchronization control loop, which maintains the synchronism between the VSC and the AC system. The input of the control loop is the error between the real power and the reference real power. The power error is converted into a frequency deviation and then integrated to provide the phase angle. Therefore, the frequency regulation of PSC is mainly maintaining the frequency of the VSC output at the frequency of the AC system [23].

However, there are limitations of this control mechanism. *Zhang et al* [24] presented some limitations of the PSC approach, including uncontrolled current at fundamental frequency in AC system and the stability limitation of PSC in both alternating-voltage control mode and the reactive-power control mode. The performance of this control mechanism is not desired in VSC-

HVDC connected to strong AC systems due to the relatively higher load angles. The frequency regulation capability and black-start capability of this control scheme is not proved in reported research.

3. Model Development and Simulations

In this project, GFM inverter models were developed using a quadratized modeling approach and PSCAD. GFM inverter is a type of inverter that actively controls its frequency and voltage output with fast response during transients. It can establish and maintain the voltage and frequency of a power system and can work well as a grid connected inverter or as a standalone inverter. In a system with a high penetration of RES, GFM inverters can provide synchronization, stability and resilience to the power grid.

In the following section, we will introduce the modeling development of the GFM inverter.

3.1 Grid-Forming (GFM) Inverter Model

The design and modeling of the GFM inverter is inspired by [25]-[27]. Figure 3-1 shows the overall configuration of the GFM inverter model. The model consists of 3 parts, Voltage Source Converter (VSC), VSC Controller and Digital Signal Processor (DSP). The inputs and outputs of the three model components are listed in Table 3-1. The model development of the three components is shown in sections 3.1.1, 3.1.2 and section 3.1.3.

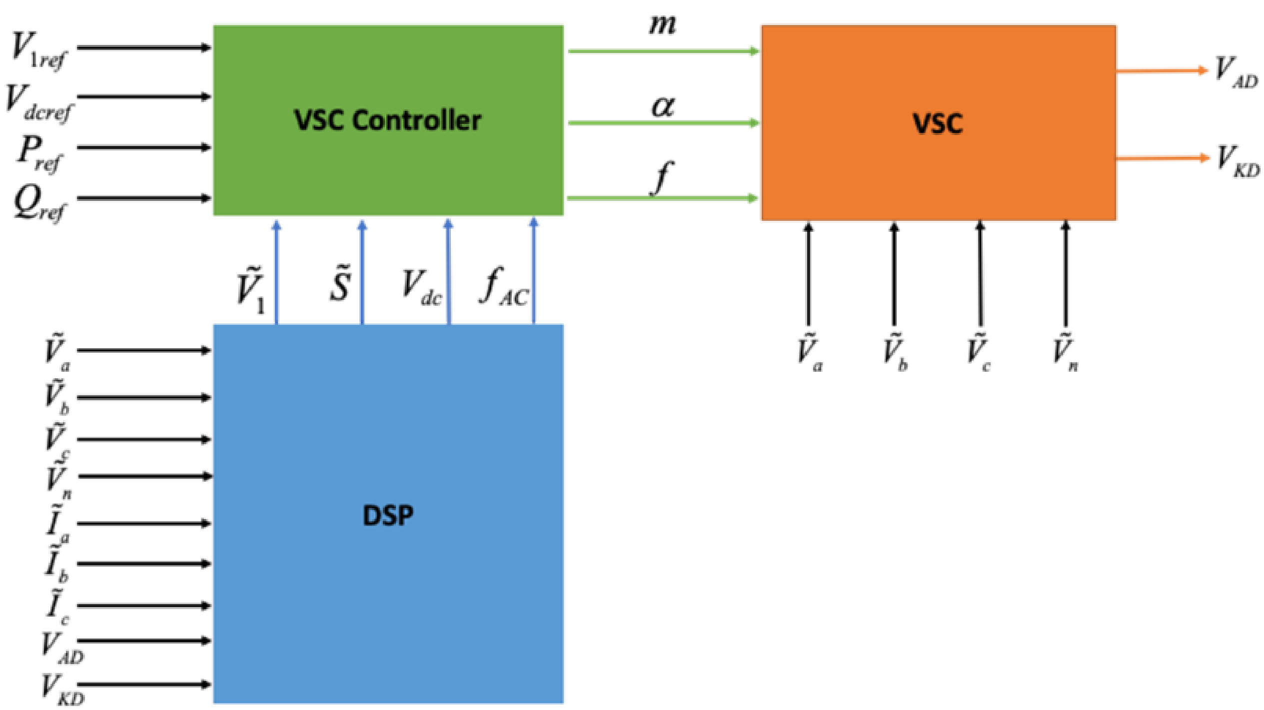

Figure 3-1. Block Diagram of the VSC Model

Table 3-1. List of Parameters in GFM Inverter Model

Parameter	Description
$\tilde{V}_{a,b,c,n}$	AC voltage phasor in phase A, B, C, N
$V_{AD,KD}$	Voltage at DC terminal AD, KD
$\tilde{I}_{a,b,c}$	AC current phasor in phase A, B, C
$\tilde{V}_1$	Positive sequence voltage phasor
$\tilde{S}$	Three-pha se total complex power
V_{dc}	DC voltage
f_{ac}	Fundamental frequency of AC voltages
V_{1ref}	Target value of the magnitude of
V_{dcref}	Target value of DC voltage
P_{ref}	Target value of real power at AC side
Q_{ref}	Target value of reactive power at AC side
m	Modulation Index
α	Delay angle
f	Fundamental frequency of AC side

3.1.1 Compact Voltage Source Converter (VSC) Model

For the VSC model, we present a three-phase two-level pulse width modulation (PWM) converter. The circuit diagram of the VSC is shown in Figure 3-2, in which the black boxes in the diagram represent power electronic valves. Figure 3-3 shows the detailed circuit diagram of the power electronic valves, where each valve consists of parasitic conductance and parasitic capacitance of IGBT, IGBT conductance, a snubber circuit, and a current limiter circuit. By adding these parts in the valve, the fidelity of the model is improved. The model becomes a realistic representation of the inverter.

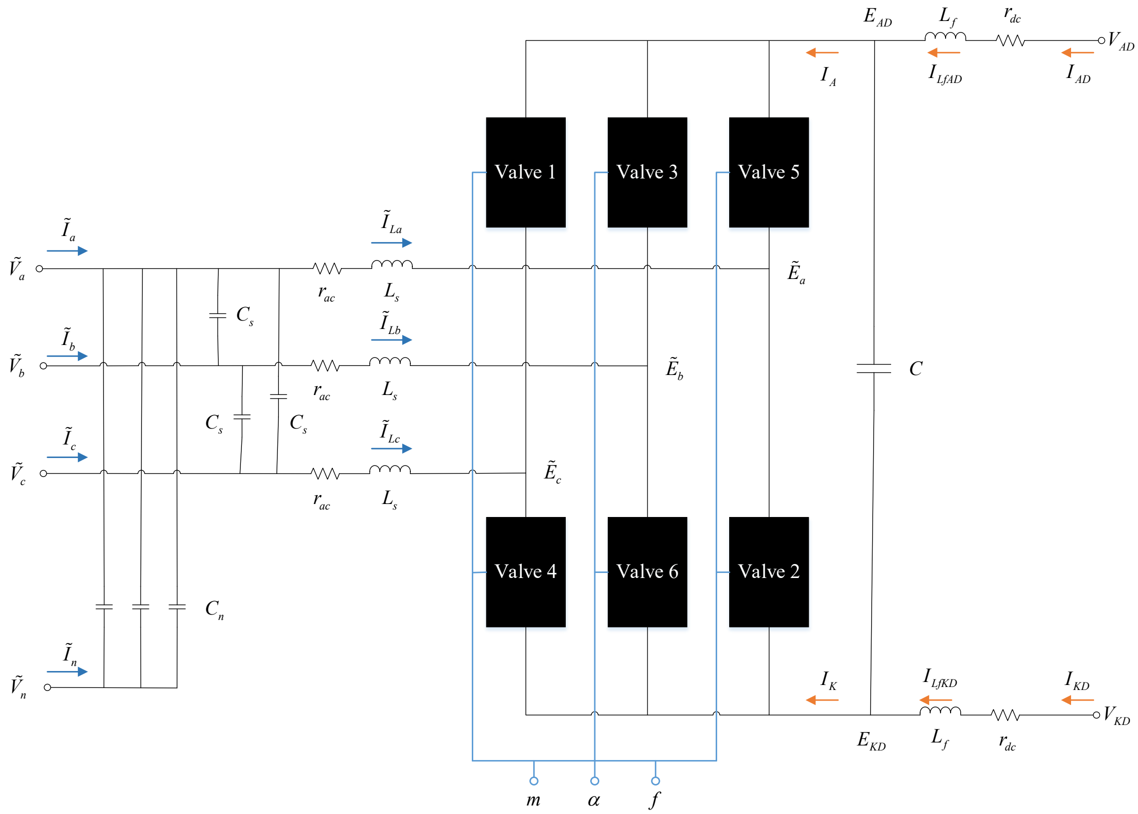

Figure 3-2. Circuit Diagram of Full VSC Model

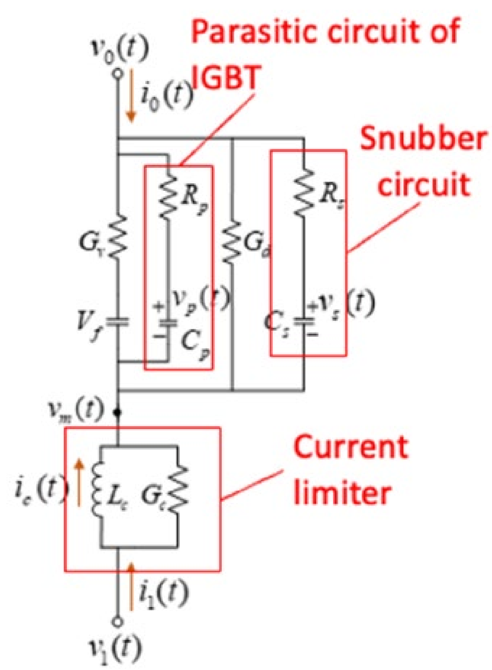

Figure 3-3. Detailed Circuit Diagram of Power Electronic Valve

A mathematical model of the VSC was developed based on the circuit diagram shown in Figures 3-2 and 3-3. The model is listed below:

$$I_{AD} = I_{LfAD} \tag{3.1.1}$$

$$I_{KD} = I_{LfKD} \tag{3.1.2}$$

$$\tilde{I}_a = \tilde{I}_{La} + j4\pi fC_s\tilde{V}_a - j2\pi fC_s\tilde{V}_b - j2\pi fC_s\tilde{V}_c + j2\pi fC_n\tilde{V}_a - j2\pi fC_n\tilde{V}_n \tag{3.1.3}$$

$$\tilde{I}_b = \tilde{I}_{Lb} + j4\pi fC_s\tilde{V}_b - j2\pi fC_s\tilde{V}_a - j2\pi fC_s\tilde{V}_c + j2\pi fC_n\tilde{V}_b - j2\pi fC_n\tilde{V}_n \tag{3.1.4}$$

$$\tilde{I}_c = \tilde{I}_{Lc} + j4\pi fC_s\tilde{V}_c - j2\pi fC_s\tilde{V}_a - j2\pi fC_s\tilde{V}_b + j2\pi fC_n\tilde{V}_c - j2\pi fC_n\tilde{V}_n \tag{3.1.5}$$

$$\tilde{I}_n = j6\pi fC_n\tilde{V}_n - j2\pi fC_n\tilde{V}_a - j2\pi fC_n\tilde{V}_b - j2\pi fC_n\tilde{V}_c \tag{3.1.6}$$

$$I_m = 0 \quad \text{(terminal m)} \tag{3.1.7}$$

$$I_\alpha = 0 \quad \text{(terminal a)} \tag{3.1.8}$$

$$I_f = 0 \quad \text{(terminal f)} \tag{3.1.9}$$

$$0 = \tilde{V}_a - \tilde{E}_a - j2\pi fL_s\tilde{I}_{La} - L_s\frac{d\tilde{I}_{La}}{dt} - r_{ac}\tilde{I}_{La} \tag{3.1.10}$$

$$0 = \tilde{V}_b - \tilde{E}_b - j2\pi fL_s\tilde{I}_{Lb} - L_s\frac{d\tilde{I}_{Lb}}{dt} - r_{ac}\tilde{I}_{Lb} \tag{3.1.11}$$

$$0 = \tilde{V}_c - \tilde{E}_c - j2\pi fL_s\tilde{I}_{Lc} - L_s\frac{d\tilde{I}_{Lc}}{dt} - r_{ac}\tilde{I}_{Lc} \tag{3.1.12}$$

$$0 = V_{AD} - E_{AD} - L_f\frac{dI_{LfAD}}{dt} - r_{dc}I_{LfAD} \tag{3.1.13}$$

$$0 = V_{KD} - E_{KD} - L_f\frac{dI_{LfKD}}{dt} - r_{dc}I_{LfKD} \tag{3.1.14}$$

$$0 = \frac{m}{2\sqrt{2}}\left(E_{AD} - E_{KD}\right)e^{j\alpha} - j2\pi fL_s\tilde{I}_{La} - L_s\frac{d\tilde{I}_{La}}{dt} - \tilde{E}_a \tag{3.1.15}$$

$$0 = \frac{m}{2\sqrt{2}}\left(E_{AD} - E_{KD}\right)e^{j\left(\alpha-\frac{2\pi}{3}\right)} - j2\pi fL_s\tilde{I}_{Lb} - L_s\frac{d\tilde{I}_{Lb}}{dt} - \tilde{E}_b \tag{3.1.16}$$

$$0 = \frac{m}{2\sqrt{2}}\left(E_{AD} - E_{KD}\right)e^{j\left(\alpha+\frac{2\pi}{3}\right)} - j2\pi fL_s\tilde{I}_{Lc} - L_s\frac{d\tilde{I}_{Lc}}{dt} - \tilde{E}_c \tag{3.1.17}$$

$$0 = C\frac{dE_{AD}}{dt} - C\frac{dE_{KD}}{dt} + I_A - I_{LfAD} \tag{3.1.18}$$

$$0 = -C\frac{dE_{AD}}{dt} + C\frac{dE_{KD}}{dt} + I_K - I_{LfKD} \tag{3.1.19}$$

$$0 = I_{Lar} + I_{Lbr} + I_{Lcr} + I_A + I_k \tag{3.1.20}$$

$$0 = \underbrace{\operatorname{Re}\left(\tilde{E}_a\tilde{I}_{La}^* + \tilde{E}_b\tilde{I}_{Lb}^* + \tilde{E}_c\tilde{I}_{Lc}^*\right)}_{AC\ \text{Power}} + \underbrace{E_{AD}I_A}_{DC\ \text{Power}} + \underbrace{E_{KD}I_K}_{DC\ \text{Power}} \tag{3.1.21}$$

where the through variables of this models are:

$$i^T = \begin{bmatrix} I_{AD} & I_{KD} & \tilde{I}_a & \tilde{I}_b & \tilde{I}_c & \tilde{I}_n & I_m & I_\alpha & I_f \end{bmatrix}^T$$

And the state variables of this model are:

$$x^T = \begin{bmatrix} V_{AD} & V_{KD} & \tilde{V}_a & \tilde{V}_b & \tilde{V}_c & \tilde{V}_n & m & \alpha & f & \tilde{E}_a & \tilde{E}_b & \tilde{E}_c & E_{AD} & E_{KD} & \tilde{I}_{La} & \tilde{I}_{Lb} & \tilde{I}_{Lc} & I_{LfAD} & I_{LfKD} & I_A & I_K \end{bmatrix}$$

Subsequently, the mathematical model is integrated using the quadratic integration method. The quadratic integration method is described in [28]. After the quadratic integration, the state and control algebraic companion form of the VSC (SCAQCF) is obtained. Details of the SCAQCF model of the VSC are shown in appendix B. Once obtained the SCAQCF model, the VSC model is developed in C++. Figure 3-4 shows the user interface of the VSC model. A test case of the VSC model was also constructed as shown in Figure 3-5.

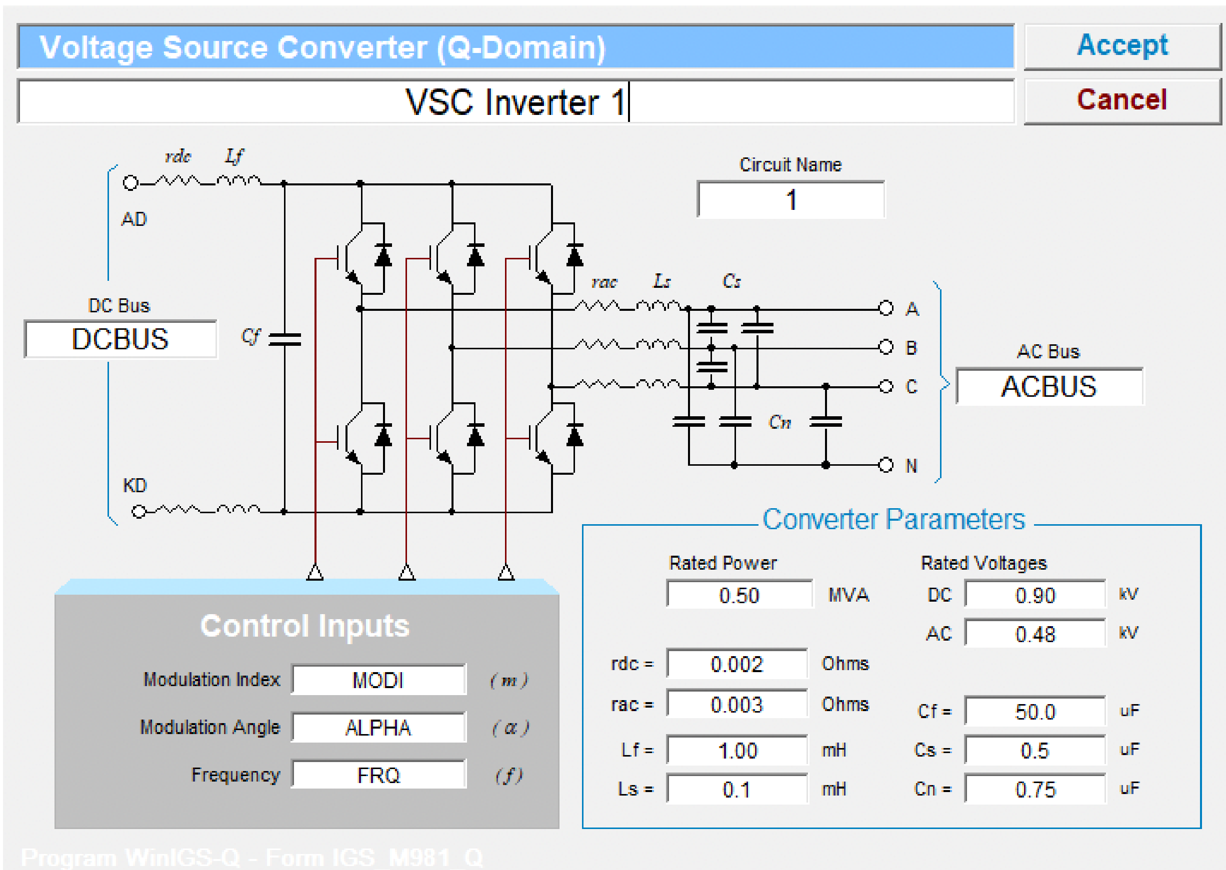

Figure 3-4. User Interface of VSC Model

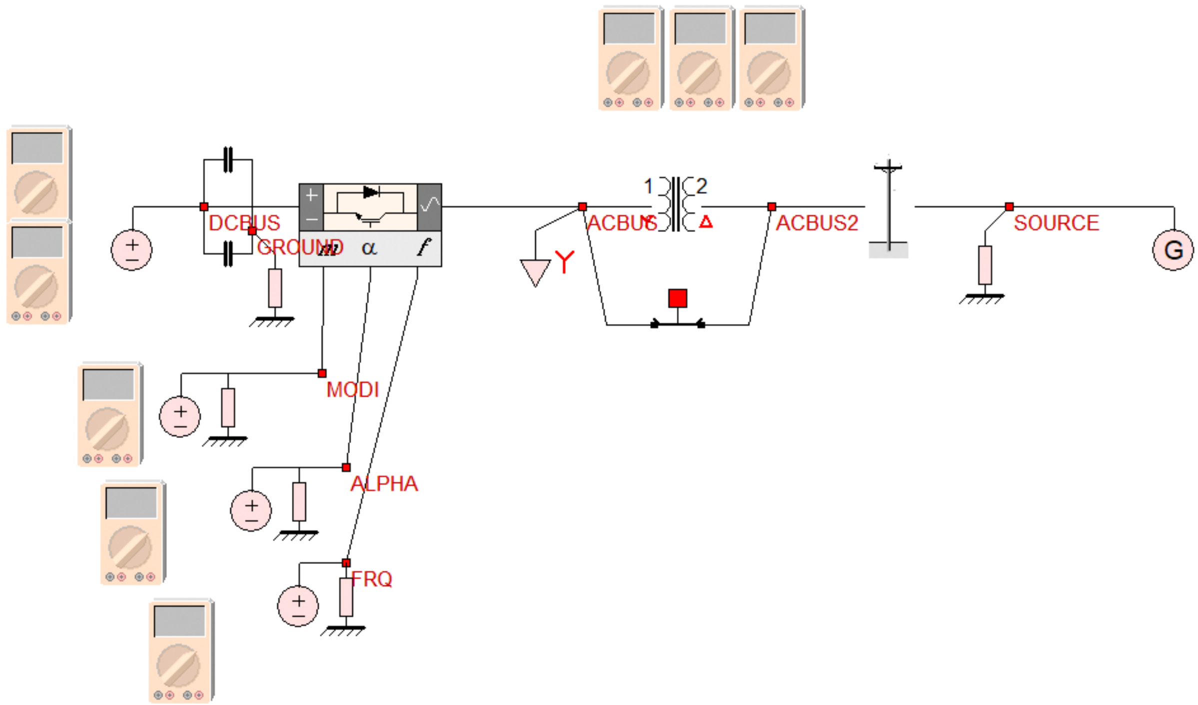

Figure 3-5. Test Case of VSC Model

3.1.2 Quadratized Voltage Source Converter (VSC) Model

The compact device model is quadratized to provide the quadratized device model (QDM). For the quasi-dynamic domain, the phasor quantities are split into real and imaginary components. Any terms that have nonlinearities greater than two, they are converted into quadratic terms by the introduction of additional state variables.

Once this task has been completed, the resulting equations are cast into the SCQDM standard syntax. Note that in this form, all the interface equations form Group 1; the remaining equations (internal equations) are split into linear and nonlinear, the linear form Group 2 and the nonlinear form Group 3. Note also that group 3 contains only algebraic equations.

The SCQDM standard syntax:

Group 1: interface equations

$$i(t) = Y_{eqx1}\mathbf{x}(t) + Y_{equ1}\mathbf{u}(t) + D_{eqxd1}\frac{d\mathbf{x}(t)}{dt} + C_{eqc1}$$

Group 2: internal linear equations

$$0 = Y_{eqx2}\mathbf{x}(t) + Y_{equ2}\mathbf{u}(t) + D_{eqxd2}\frac{d\tilde{\mathbf{x}}(t)}{dt} + C_{eqc2}$$

Group 3: internal non-linear equations

$$0 = Y_{eqx3}\mathbf{x}(t) + Y_{equ3}\mathbf{u}(t) + \begin{Bmatrix} \vdots \\ \mathbf{x}(t)^T \left\langle F^i_{eqxx3} \right\rangle \mathbf{x}(t) \\ \vdots \end{Bmatrix} + \begin{Bmatrix} \vdots \\ \mathbf{u}(t)^T \left\langle F^i_{equu3} \right\rangle \mathbf{u}(t) \\ \vdots \end{Bmatrix} + C_{eqc3}$$

Additional model variables

Connectivity: *TerminalNodeName*

Normalization Factor: StateNormFactor, ThroughNormFactor, ControlNormFactor

Note: All the above variables are in the metric system.

Note that equation sets 1 and 2 must be linear. This means that it may be necessary to introduce additional variables to meet this requirement. In this case, equation set 1 includes nonlinear equations. The following additional state variables are introduced to convert these equations into linear.

$$\tilde{Y}_1(t) = f(t)\tilde{V}_a(t)$$
$$\tilde{Y}_2(t) = f(t)\tilde{V}_b(t)$$
$$\tilde{Y}_3(t) = f(t)\tilde{V}_c(t)$$
$$\tilde{Y}_4(t) = f(t)\tilde{V}_n(t)$$
$$\tilde{Z}_1(t) = f(t)\tilde{I}_{La}(t)$$
$$\tilde{Z}_2(t) = f(t)\tilde{I}_{Lb}(t)$$
$$\tilde{Z}_3(t) = f(t)\tilde{I}_{Lc}(t)$$

Upon substitution of above, equation set 1 becomes linear.

Subsequently, all the complex equations in the resulting model are split into real and imaginary.

Any remaining nonlinear equations are quadratized. For this model the following equation needs to be quadratized (3.20), (3.21) and (3.22). Consider equation (3.20):

$$0 = \frac{m}{2\sqrt{2}}\left(E_{AD} - E_{KD}\right)e^{j\alpha} - j2\pi f L_s \tilde{I}_{La} - L_s\frac{d\tilde{I}_{La}}{dt} - \tilde{E}_a$$

First, the equation is split into real and imaginary parts.

$$0 = \frac{m}{2\sqrt{2}}\left(E_{AD} - E_{KD}\right)\cos\alpha + 2\pi f L_s I_{Lai} - L_s\frac{dI_{Lar}}{dt} - E_{ar}$$

$$0 = \frac{m}{2\sqrt{2}}\left(E_{AD} - E_{KD}\right)\sin\alpha - 2\pi f L_s I_{Lar} - L_s\frac{dI_{Lai}}{dt} - E_{ai}$$

Subsequently, we introduce eight new variables.

$$cs = \cos\alpha \quad \rightarrow \quad \frac{dcs}{dt} = -ss\frac{d\alpha}{dt}$$

$$ss = \sin\alpha \quad \rightarrow \quad \frac{dss}{dt} = cs\frac{d\alpha}{dt}$$

$$x_1 = \left(E_{AD} - E_{KD}\right)cs$$

$$x_2 = \left(E_{AD} - E_{KD}\right)ss$$

$$x_3 = \frac{d\alpha}{dt}$$

$$x_4 = \frac{dcs}{dt}$$

$$x_5 = \frac{1}{2\sqrt{2}}mx_1$$

$$x_6 = \frac{1}{2\sqrt{2}}mx_2$$

Using the new variables, the quadratized equation becomes

$$0 = x_5 + 2\pi fL_s I_{Lai} - L_s\frac{dI_{Lar}}{dt} - E_{ar}$$

$$0 = x_6 - 2\pi fL_s I_{Lar} - L_s\frac{dI_{Lai}}{dt} - E_{ai}$$

$$0 = x_1 - \left(E_{AD} - E_{KD}\right)cs$$

$$0 = x_2 - \left(E_{AD} - E_{KD}\right)ss$$

$$0 = x_3 - \frac{d\alpha}{dt}$$

$$0 = x_4 - \frac{dcs}{dt}$$

$$0 = x_4 + ss.x_3$$

$$0 = cs^2 + ss^2 - 1$$

$$0 = x_5 - \frac{1}{2\sqrt{2}}mx_1$$

$$0 = x_6 - \frac{1}{2\sqrt{2}}mx_2$$

Similarly, the equations for phase b and phase c become:

$$0 = -\frac{1}{2}x_5 + \frac{\sqrt{3}}{2}x_6 + 2\pi f L_s I_{Lbi} - L_s \frac{dI_{Lbr}}{dt} - E_{br}$$
$$0 = -\frac{\sqrt{3}}{2}x_5 - \frac{1}{2}x_6 - 2\pi f L_s I_{Lbr} - L_s \frac{dI_{Lbi}}{dt} - E_{bi}$$
$$0 = -\frac{1}{2}x_5 - \frac{\sqrt{3}}{2}x_6 + 2\pi f L_s I_{Lci} - L_s \frac{dI_{Lcr}}{dt} - E_{cr}$$
$$0 = \frac{\sqrt{3}}{2}x_5 - \frac{1}{2}x_6 - 2\pi f L_s I_{Lcr} - L_s \frac{dI_{Lci}}{dt} - E_{ci}$$

Note that the quadratization has introduced a number of new variables and an equal number of additional equations. This way mathematical consistency is maintained.

The quadratized equations are listed as follows:

Equation Set 1:

$$I_{AD} = I_{LfAD}$$
$$I_{KD} = I_{LfKD}$$
$$I_{ar} = I_{Lar} - 2\pi\left(2C_s + C_n\right)Y_{1i} + 2\pi C_s Y_{2i} + 2\pi C_s Y_{3i} + 2\pi C_n Y_{4i}$$
$$I_{ai} = I_{Lai} + 2\pi\left(2C_s + C_n\right)Y_{1r} - 2\pi C_s Y_{2r} - 2\pi C_s Y_{3r} - 2\pi C_n Y_{4r}$$
$$I_{br} = I_{Lbr} - 2\pi\left(2C_s + C_n\right)Y_{2i} + 2\pi C_s Y_{1i} + 2\pi C_s Y_{3i} + 2\pi C_n Y_{4i}$$
$$I_{bi} = I_{Lbi} + 2\pi\left(2C_s + C_n\right)Y_{2r} - 2\pi C_s Y_{1r} - 2\pi C_s Y_{3r} - 2\pi C_n Y_{4r}$$
$$I_{cr} = I_{Lcr} - 2\pi\left(2C_s + C_n\right)Y_{3i} + 2\pi C_s Y_{1i} + 2\pi C_s Y_{2i} + 2\pi C_n Y_{4i}$$
$$I_{ci} = I_{Lci} + 2\pi\left(2C_s + C_n\right)Y_{3r} - 2\pi C_s Y_{1r} - 2\pi C_s Y_{2r} - 2\pi C_n Y_{4r}$$
$$I_{nr} = -6\pi C_n Y_{4i} + 2\pi C_n Y_{1i} + 2\pi C_n Y_{2i} + 2\pi C_n Y_{3i}$$
$$I_{ni} = 6\pi C_n Y_{4r} - 2\pi C_n Y_{1r} - 2\pi C_n Y_{2r} - 2\pi C_n Y_{3r}$$
$$I_m = 0 \text{ (Terminal m)}$$
$$I_\alpha = 0 \text{ (Terminal } \alpha\text{)}$$
$$I_f = 0 \text{ (Terminal } f\text{)}$$

Equation Set 2:

$$0 = V_{ar} - E_{ar} + 2\pi L_s Z_{1i} - L_s \frac{dI_{Lar}}{dt} - r_{ac} I_{Lar}$$
$$0 = V_{ai} - E_{ai} - 2\pi L_s Z_{1r} - L_s \frac{dI_{Lai}}{dt} - r_{ac} I_{Lai}$$

$$0 = V_{br} - E_{br} + 2\pi L_s Z_{2i} - L_s \frac{dI_{Lbr}}{dt} - r_{ac} I_{Lbr}$$

$$0 = V_{bi} - E_{bi} - 2\pi L_s Z_{2r} - L_s \frac{dI_{Lbi}}{dt} - r_{ac} I_{Lbi}$$

$$0 = V_{cr} - E_{cr} + 2\pi L_s Z_{3i} - L_s \frac{dI_{Lcr}}{dt} - r_{ac} I_{Lcr}$$

$$0 = V_{ci} - E_{ci} - 2\pi L_s Z_{3r} - L_s \frac{dI_{Lci}}{dt} - r_{ac} I_{Lci}$$

$$0 = V_{AD} - E_{AD} - L_f \frac{dI_{LfAD}}{dt} - r_{dc} I_{LfAD}$$

$$0 = V_{KD} - E_{KD} - L_f \frac{dI_{LfKD}}{dt} - r_{dc} I_{LfKD}$$

$$0 = x_5 + 2\pi L_s Z_{1i} - L_s \frac{dI_{Lar}}{dt} - E_{ar}$$

$$0 = x_6 - 2\pi L_s Z_{1r} - L_s \frac{dI_{Lai}}{dt} - E_{ai}$$

$$0 = -\frac{1}{2} x_5 + \frac{\sqrt{3}}{2} x_6 + 2\pi L_s Z_{2i} - L_s \frac{dI_{Lbr}}{dt} - E_{br}$$

$$0 = -\frac{\sqrt{3}}{2} x_5 - \frac{1}{2} x_6 - 2\pi L_s Z_{2r} - L_s \frac{dI_{Lbi}}{dt} - E_{bi}$$

$$0 = -\frac{1}{2} x_5 - \frac{\sqrt{3}}{2} x_6 + 2\pi L_s Z_{3i} - L_s \frac{dI_{Lcr}}{dt} - E_{cr}$$

$$0 = \frac{\sqrt{3}}{2} x_5 - \frac{1}{2} x_6 - 2\pi L_s Z_{3r} - L_s \frac{dI_{Lci}}{dt} - E_{ci}$$

$$0 = C \frac{dE_{AD}}{dt} - C \frac{dE_{KD}}{dt} + I_A - I_{LfAD}$$

$$0 = -C \frac{dE_{AD}}{dt} + C \frac{dE_{KD}}{dt} + I_K - I_{LfKD}$$

$$0 = I_{Lar} + I_{Lbr} + I_{Lcr} + I_A + I_k$$

$$0 = x_3 - \frac{d\alpha}{dt}$$

$$0 = x_4 - \frac{dcs}{dt}$$

Equation Set 3:

$$0 = Y_{1r} - fV_{ar}$$

$$0 = Y_{1i} - fV_{ai}$$

$$0 = Y_{2r} - fV_{br}$$

$$0 = Y_{2i} - fV_{bi}$$

$$0 = Y_{3r} - fV_{cr}$$

$$0 = Y_{3i} - fV_{ci}$$

$$0 = Y_{4r} - fV_{nr}$$

$$0 = Y_{4i} - fV_{ni}$$

$$0 = Z_{1r} - fI_{Lar}$$

$$0 = Z_{1i} - fI_{Lai}$$

$$0 = Z_{2r} - fI_{Lbr}$$

$$0 = Z_{2i} - fI_{Lbi}$$

$$0 = Z_{3r} - fI_{Lcr}$$

$$0 = Z_{3i} - fI_{Lci}$$

$$0 = x_1 - \left(E_{AD} - E_{KD}\right) cs$$
$$0 = x_2 - \left(E_{AD} - E_{KD}\right) ss$$
$$0 = x_4 + ss \cdot x_3$$
$$0 = cs^2 + ss^2 - 1$$
$$0 = x_5 - \frac{1}{2\sqrt{2}} m x_1$$
$$0 = x_6 - \frac{1}{2\sqrt{2}} m x_2$$

$$0 = E_{ar} I_{Lar} + E_{ai} I_{Lai} + E_{br} I_{Lbr} + E_{bi} I_{Lbi} + E_{cr} I_{Lcr} + E_{ci} I_{Lci} + E_{AD} I_A + E_{KD} I_K$$

Note, the SCQDM has 53 states, and 53 equations as follows: 13 through equations, 19 internal linear equations and 21 internal non-linear equations.

The through variables are:

$$i^T = \left[I_{AD},\ I_{KD},\ I_{ar},\ I_{ai},\ I_{br},\ I_{bi},\ I_{cr},\ I_{ci},\ I_{nr},\ I_{ni},\ I_m,\ I_\alpha,\ I_f \right]$$

The states are:

$$x^T = [\ \ V_{AD},\ V_{KD},\ V_{ar}, V_{ai},\ V_{br}, V_{bi},\ \ V_{cr}, V_{ci},\ V_{nr}, V_{ni},\ m,\ \alpha,\ f,$$

$$E_{ar}, E_{ai}, E_{br}, E_{bi}, E_{cr}, E_{ci}, \quad E_{AD}, E_{KD}, \quad I_{Lar}, I_{Lai}, I_{Lbr}, I_{Lbi}, I_{Lcr}, I_{Lci} \quad I_{LfAD}, I_{LfKD}, I_A, I_K,$$

$$x_3, x_4, Y_{1r}, Y_{1i}, Y_{2r}, Y_{2i}, Y_{3r}, Y_{3i}, Y_{4r}, Y_{4i}, Z_{1r}, Z_{1i}, Z_{2r}, Z_{2i}, Z_{3r}, Z_{3i}, \quad x_1, x_2, cs, ss, x_5, x_6]$$

3.1.3 Digital Signal Processor (DSP) Model

The inputs and outputs of the DSP model are shown in Figure 3-6. The inputs of the DSP are (1) DC voltage, (2) three-phase AC voltage phasors and (3) three-phase AC current phasors.

The DSP model calculates the following outputs: (1) positive sequence voltage phasor, (2) the three-phase complex power, (3) the DC voltage magnitude, and (4) the fundamental frequency from the AC voltages.

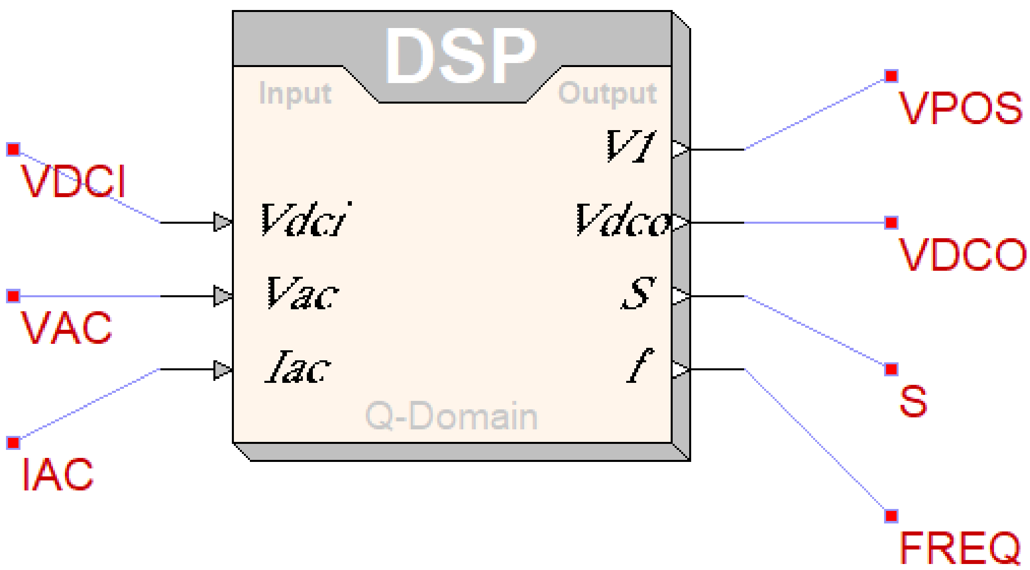

Figure 3-6. Block Diagram of the DSP Model

The following mathematical model is developed for the DSP. The model consists of four parts, interface equations, positive sequence voltage phasor computation, DC voltage output computation, total complex power computation, and frequency computation.

$$i_{Vdci} = 0 \tag{3.2.1}$$

$$i_{Vac} = 0 \tag{3.2.2}$$

$$i_{Iac} = 0 \tag{3.2.3}$$

$$i_{V_1}(t) = V_1(t) - V_{1out}(t) \tag{3.2.4}$$

$$i_{Vdco}(t) = V_{dc}(t) - V_{DCout}(t) \tag{3.2.5}$$

$$i_{Sr}(t) = S_r(t) - P(t) \tag{3.2.6}$$

$$i_{Si}(t) = S_i(t) - Q(t) \tag{3.2.7}$$

$$i_f(t) = f(t) - \frac{f_a(t) + f_b(t) + f_c(t)}{3} \tag{3.2.8}$$

$$\tilde{V}_1 = \frac{\tilde{V}_{an} + e^{j120^\circ}\tilde{V}_{bn} + e^{j240^\circ}\tilde{V}_{cn}}{3} \tag{3.2.9}$$

$$V_{DCout}(t) = \frac{1}{5}V_{DCin}(t) + \frac{1}{5}\sum_{k=1}^{4} V_{DCin}(t-kh) \tag{3.2.10}$$

$$S = \tilde{V}_{an}\tilde{I}_a^* + \tilde{V}_{bn}\tilde{I}_b^* + \tilde{V}_{cn}\tilde{I}_c^* \tag{3.2.11}$$

$$i_f(t) = f_{sys}(t) - f(t) \tag{3.2.12}$$

$$x_1^2(t) = \frac{\left|\tilde{V}(t)\right|^2}{\left|\tilde{V}(t-h)\right|^2} \tag{3.2.13}$$

$$\frac{\tilde{V}(t) - x_1(t)\tilde{V}(t-h)}{\tilde{V}(t)} = d\delta e^{j\left(90^\circ + \frac{d\delta}{2}\right)} \tag{3.2.14}$$

$$\frac{d\delta(t)}{dt} = f(t) - f(t-h) \tag{3.2.15}$$

$$x_1(t)\tilde{V}(t-h) = x_1(t)V(t-h)e^{j\delta(t-h)} \tag{3.2.16}$$

$$\tilde{V}(t) = V(t)e^{j\delta(t)} \tag{3.2.17}$$

where the through variables of this models are:

$$i^T = \begin{bmatrix} i_{Vdci} & i_{Vac} & i_{Iac} & i_{V_1} & i_{Vdco} & i_{Sr} & i_{Si} & i_f \end{bmatrix}$$

And the state variables of this model are:

$$x^T = \begin{bmatrix} V_{DCin} & V_{DCout} & \tilde{V}_{an} & \tilde{V}_{bn} & \tilde{V}_{cn} & \tilde{I}_a & \tilde{I}_b & \tilde{I}_c & \tilde{V}_1 & S & f & f_{sys} & x_1 & \tilde{V} & \delta \end{bmatrix}$$

The DSP model was integrated using the quadratic integration method [6]. After the quadratic integration, the state and control algebraic companion form (SCAQCF) of the DSP is obtained. The user interface and test case of the DSP model is shown as follows. Where the parameters of the DSP model can be set in the user interface.

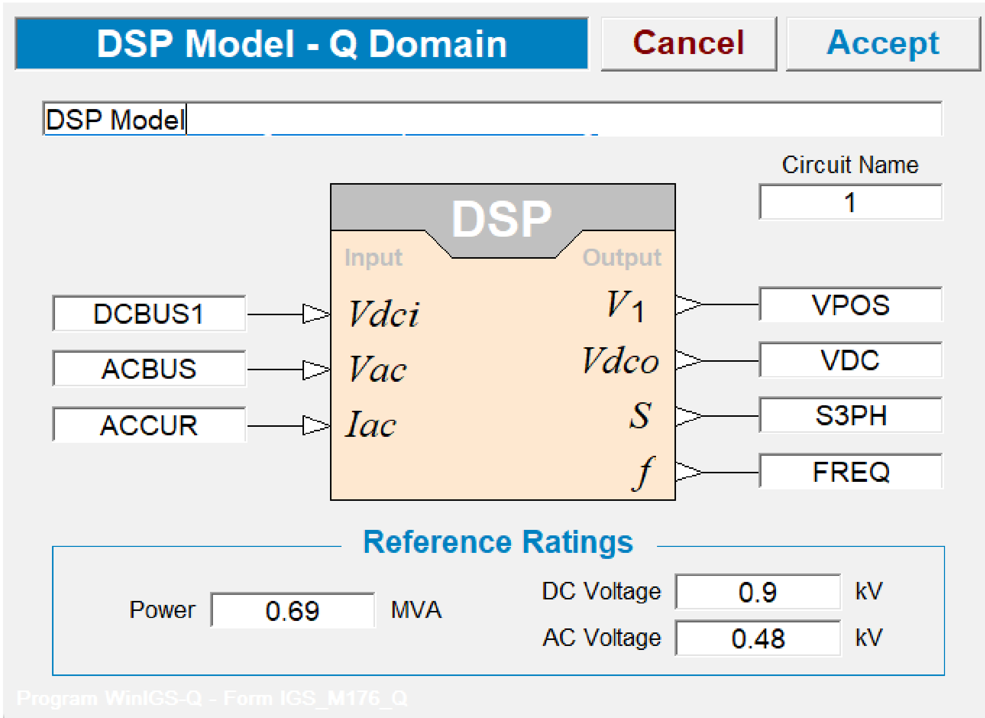

Figure 3-7. User Interface of the DSP Model

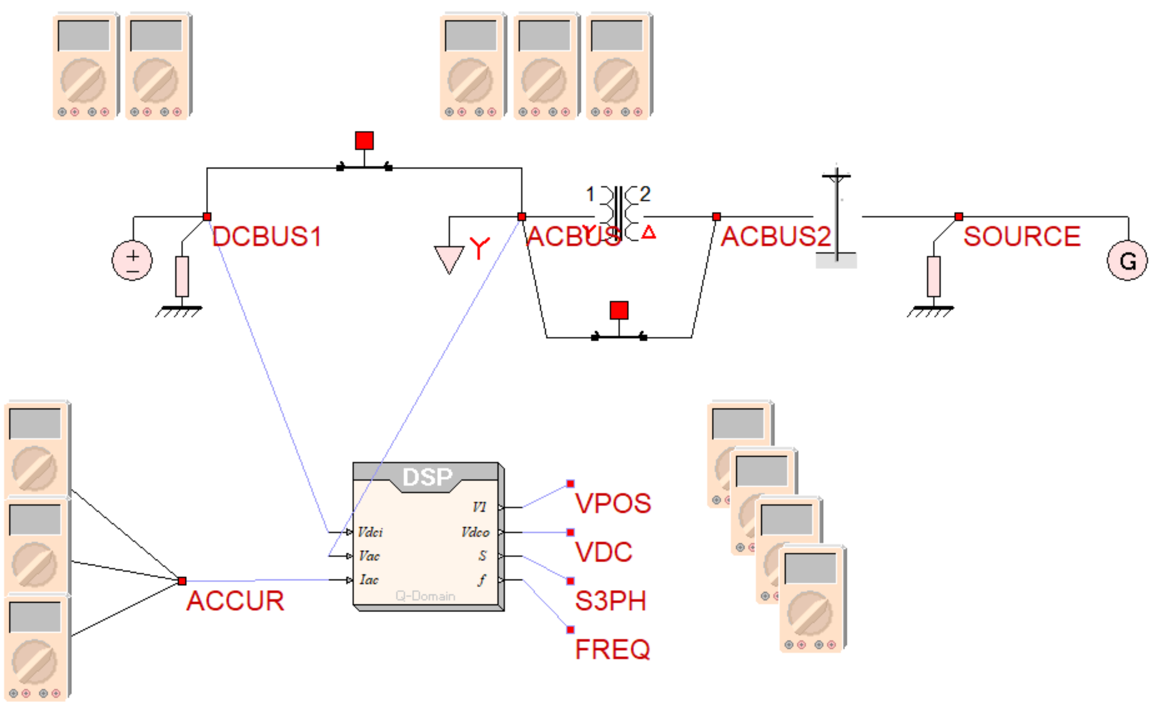

Figure 3-8. Test Case of the DSP Model

3.1.4 VSC Controller Model

To achieve the cold start task and maintain the frequency and voltage during the operation of the system, a digital VSC controller is proposed in this project to avoid the pitfalls of standard PLL-based controllers. A digital model of PWM was constructed to generate firing sequence signals for the valves in the converter model to create the desirable AC waveforms. The inputs and outputs of the VSC controller are shown in Figure 3-9. The VSC controller takes the outputs from the DSP as inputs. It also takes the reference value of the magnitude of positive sequence voltage phasor (V_{1ref}), reference value of magnitude of DC voltage (V_{dcref}), reference value of real power (P_{ref}) and reactive power (Q_{ref}). The outputs of the VSC controller are modulation index (m), delay angle (α) and frequency (f). The outputs are fed into the VSC model as controller parameters.

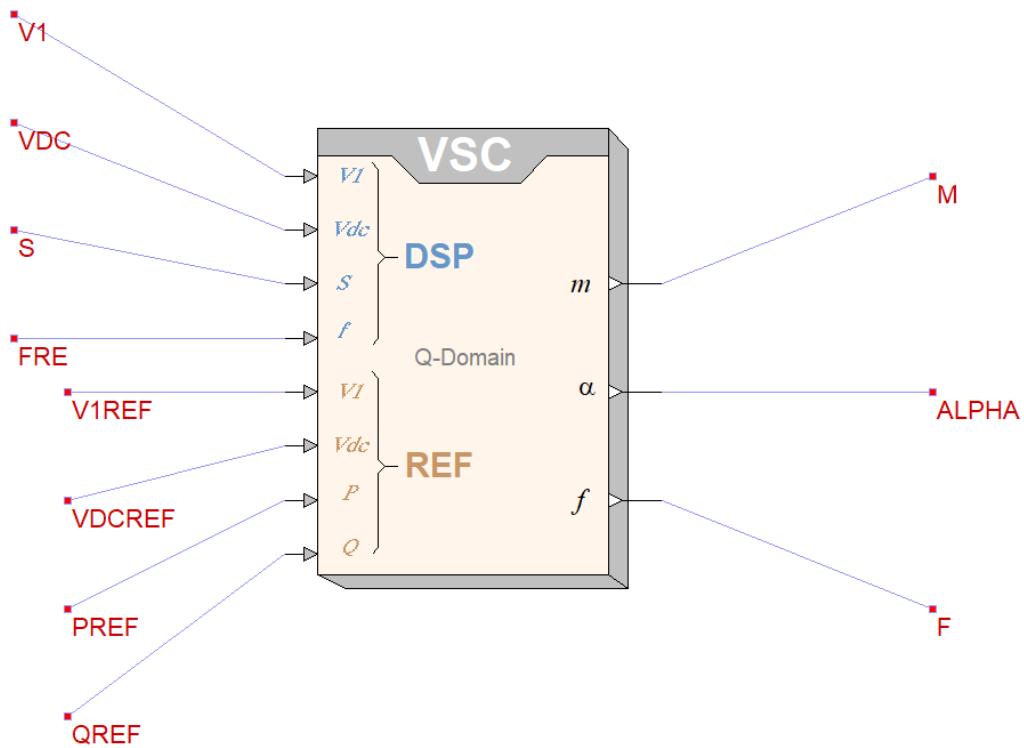

Figure 3-9. Block Diagram of the VSC Controller Model

The concept of Proportional Integral (PI) control was implemented in the VSC controller model. The controller has two operation modes, Vac-Vdc mode and Q-Vdc mode. The control diagram of the Vac-Vdc mode is shown as Figure 3-10, where the DC voltage is controlled by the modulation index and the magnitude of positive sequence voltage phasor is controlled by the modulation index.

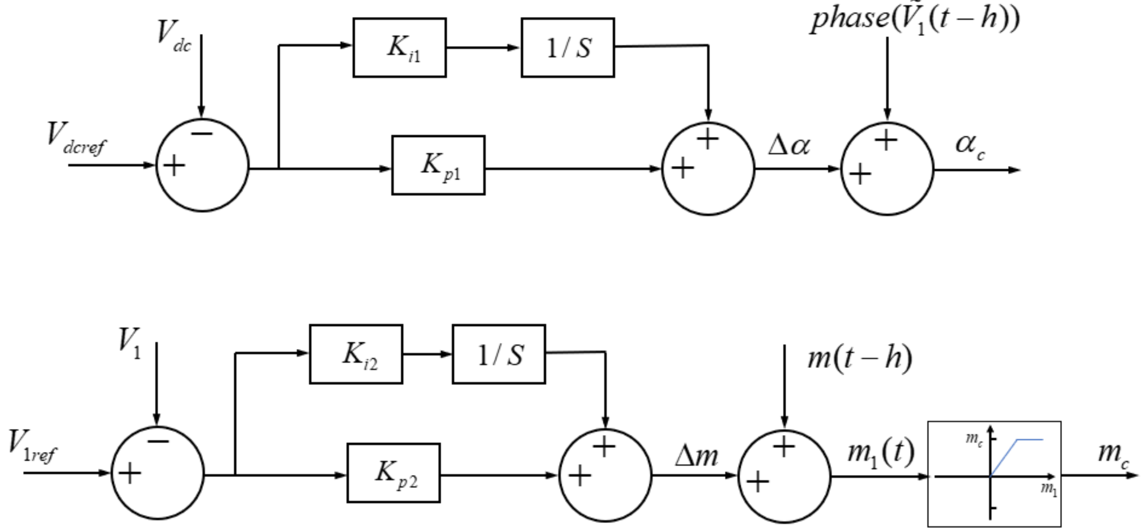

Figure 3-10. Control Diagram of the VSC Controller in Vac-Vdc Mode

From the control diagram, we can derive the following equations sets of the VSC controller:

$$\Delta\alpha(t) = k_{p1}\left(V_{dcref}(t) - V_{dc}(t)\right) + k_{i1}\int_{-\infty}^{t}\left(V_{dcref}(\tau) - V_{dc}(\tau)\right)d\tau \tag{3.3.1}$$

$$\alpha_c = phase(\tilde{V}_1(t-h)) + \Delta\alpha \tag{3.3.2}$$

$$\Delta m(t) = k_{p2}\left(V_{1ref}(t) - V_1(t)\right) + k_{i2}\int_{-\infty}^{t}\left(V_{1ref}(\tau) - V_1(\tau)\right)d\tau \tag{3.3.3}$$

$$m_1(t) = \Delta m + m(t-h) \tag{3.3.4}$$

$$m_c(t) = \begin{cases} m_1(t) & m_1(t) < 1.0 \\ 1.0 & m_1(t) \geq 1.0 \\ 0.0 & m_1(t) = 0.0 \end{cases} \tag{3.3.5}$$

These equations were written into the following mathematical model:

$$I_m(t) = m(t) - m_c(t) \tag{3.3.6}$$

$$I_\alpha(t) = \alpha(t) - \alpha_c(t) \tag{3.3.7}$$

$$I_f(t) = f(t) - f_c(t) \tag{3.3.8}$$

$$\tilde{I}_{V_1}(t) = 0 \quad (\text{Terminal } \tilde{\mathrm{V}}_1) \tag{3.3.9}$$

$$\tilde{I}_{S_1}(t) = 0 \quad (\text{Terminal } \tilde{\mathrm{S}}_1) \tag{3.3.10}$$

$$I_{V_{dc}}(t) = 0 \quad (\text{Terminal } V_{dc}) \tag{3.3.11}$$

$$I_{f_{AC}}(t) = 0 \quad (\text{Terminal } f_{AC}) \tag{3.3.12}$$

$$I_{V_{1ref}}(t) = 0 \quad (\text{Terminal } V_{1ref}) \tag{3.3.13}$$

$$I_{V_{dcref}}(t) = 0 \quad (\text{Terminal } V_{dcref}) \tag{3.3.14}$$

$$I_{P_{ref}}(t)=0 \quad \text{(Terminal } P_{ref}\text{)} \tag{3.3.15}$$

$$I_{Q_{ref}}(t)=0 \quad \text{(Terminal } Q_{ref}\text{)} \tag{3.3.16}$$

$$0=k_{p1}\frac{d\left(V_{dcref}(t)-V_{dc}(t)\right)}{dt}+k_{i1}\left(V_{dcref}(t)-V_{dc}(t)\right)-\frac{d\Delta\alpha(t)}{dt} \tag{3.3.17}$$

$$0=\alpha_c(t)-phase\left(\tilde{V}_1(t-h)\right)-\Delta\alpha(t) \tag{3.3.18}$$

$$0=k_{p2}\frac{d\left(V_{1ref}(t)-V_1(t)\right)}{dt}+k_{i2}\left(V_{1ref}(t)-V_1(t)\right)-\frac{d\Delta m(t)}{dt} \tag{3.3.19}$$

$$0=\Delta m(t)+m(t-h)-m_1(t) \tag{3.3.20}$$

$$m_c(t)=m_1(t)-\left(m_1(t)-1.0\right)u\left(m_1(t)-1.0\right) \tag{3.3.21}$$

where the through variables of this models are:

$i^T(t)=\left[I_m(t), I_\alpha(t), I_f(t), \tilde{I}_{V_1}(t), \tilde{I}_{S_1}(t), I_{V_{dc}}, I_{fp}, I_{V_{1ref}}, I_{V_{dcref}}, I_{P_{ref}}, I_{Q_{ref}}\right]$

And the state variables of this model are:

$x^T(t)=\left[m, \alpha, f, \tilde{V}_1, V_{dc}, \Delta\alpha, \alpha_c, \Delta m, m_1, m_c, f_c, V_{dcref}, V_{1ref}\right]$

The control diagram of Q-Vdc control mode is shown in Figure 3-11, where the DC voltage is controlled by the modulation index and the reactive power is controlled by the modulation index.

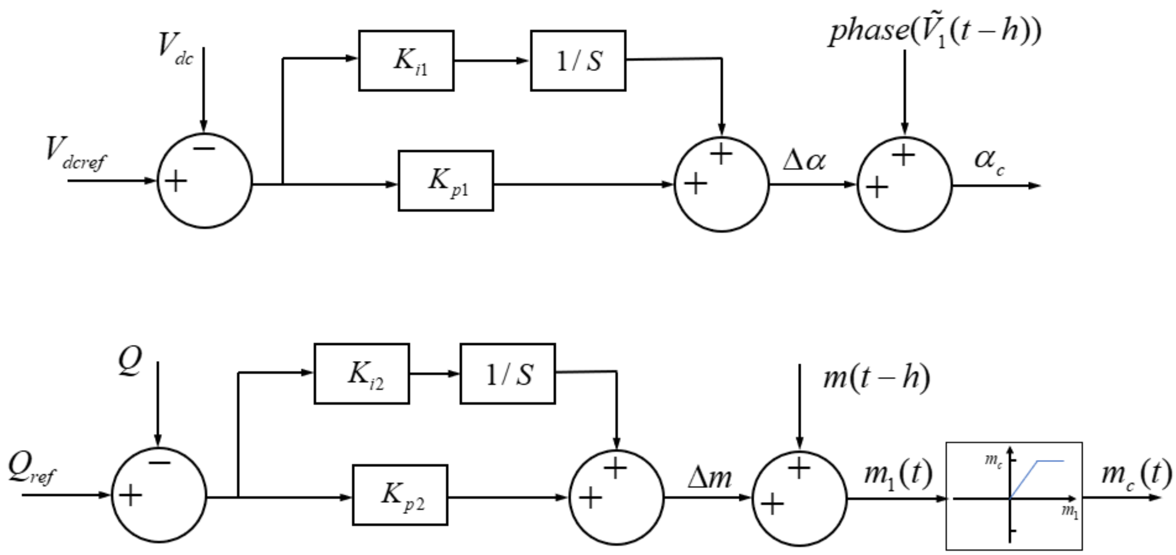

Figure 3-11. Control Diagram of the VSC Controller in Q-Vdc Mode

From the control diagram, we can derive the following equations sets of the VSC controller:

$$\Delta\alpha(t)=k_{p1}\left(V_{dcref}(t)-V_{dc}(t)\right)+k_{i1}\int_{-\infty}^{t}\left(V_{dcref}(\tau)-V_{dc}(\tau)\right)d\tau \tag{3.3.22}$$

$$\alpha_c=phase(\tilde{V}_1(t-h))+\Delta\alpha \tag{3.3.23}$$

$$\Delta m(t) = K_{p2}\left(Q_{ref}(t) - Q(t)\right) + K_{i2}\int_{-\infty}^{t}\left(Q_{ref}(\tau) - Q(\tau)\right)d\tau \tag{3.3.24}$$

$$m_1(t) = \Delta m + m(t-h) \tag{3.3.25}$$

$$m_c(t) = \begin{cases} m_1(t) & m_1(t) < 1.0 \\ 1.0 & m_1(t) \geq 1.0 \\ 0.0 & m_1(t) = 0.0 \end{cases} \tag{3.3.26}$$

These equations were written into the following mathematical model:

$$I_m(t) = m(t) - m_c(t) \tag{3.3.27}$$

$$I_\alpha(t) = \alpha(t) - \alpha_c(t) \tag{3.3.28}$$

$$I_f(t) = f(t) - f_c(t) \tag{3.3.29}$$

$$\tilde{I}_{V_1}(t) = 0 \quad (\text{Terminal } \tilde{\mathrm{V}}_1) \tag{3.3.30}$$

$$\tilde{I}_{S_1}(t) = 0 \quad (\text{Terminal } \tilde{\mathrm{S}}_1) \tag{3.3.31}$$

$$I_{V_{dc}}(t) = 0 \quad (\text{Terminal } V_{dc}) \tag{3.3.32}$$

$$I_{f_{AC}}(t) = 0 \quad (\text{Terminal } f_{AC}) \tag{3.3.33}$$

$$I_{V_{1ref}}(t) = 0 \quad (\text{Terminal } V_{1ref}) \tag{3.3.34}$$

$$I_{V_{dcref}}(t) = 0 \quad (\text{Terminal } V_{dcref}) \tag{3.3.35}$$

$$I_{P_{ref}}(t) = 0 \quad (\text{Terminal } P_{ref}) \tag{3.3.36}$$

$$I_{Q_{ref}}(t) = 0 \quad (\text{Terminal } Q_{ref}) \tag{3.3.37}$$

$$0 = k_{p1}\frac{d\left(V_{dcref}(t) - V_{dc}(t)\right)}{dt} + k_{i1}\left(V_{dcref}(t) - V_{dc}(t)\right) - \frac{d\Delta\alpha(t)}{dt} \tag{3.3.38}$$

$$0 = \alpha_c(t) - phase\left(\tilde{V}_1(t-h)\right) - \Delta\alpha(t) \tag{3.3.39}$$

$$0 = K_{p2}\frac{d\left(Q_{ref} - Q\right)}{dt} + K_{i2}\left(Q_{ref} - Q\right) - \frac{d\Delta m(t)}{dt} \tag{3.3.40}$$

$$0 = \Delta m(t) + m(t-h) - m_1(t) \tag{3.3.41}$$

$$m_c(t) = m_1(t) - \left(m_1(t) - 1.0\right)u\left(m_1(t) - 1.0\right) \tag{3.3.42}$$

where the through variables of this models are:

$$i^T(t) = \left[I_m(t), I_\alpha(t), I_f(t), \tilde{I}_{V_1}(t), \tilde{I}_{S_1}(t), I_{V_{dc}}, I_{fp}, I_{V_{1ref}}, I_{V_{dcref}}, I_{P_{ref}}, I_{Q_{ref}}\right]$$

And the state variables of this model are:

$$x^T(t) = \left[m, \alpha, f, \tilde{V}_1, V_{dc}, Q, \Delta\alpha, \alpha_c, \Delta m, m_1, m_c, f_c, V_{dcref}, Q_{ref}\right]$$

The user interface and test case of the VSC controller model are shown in Figure 3-12 and Figure 3-13. Please note that the test case shows a full GFM inverter model contains all three models.

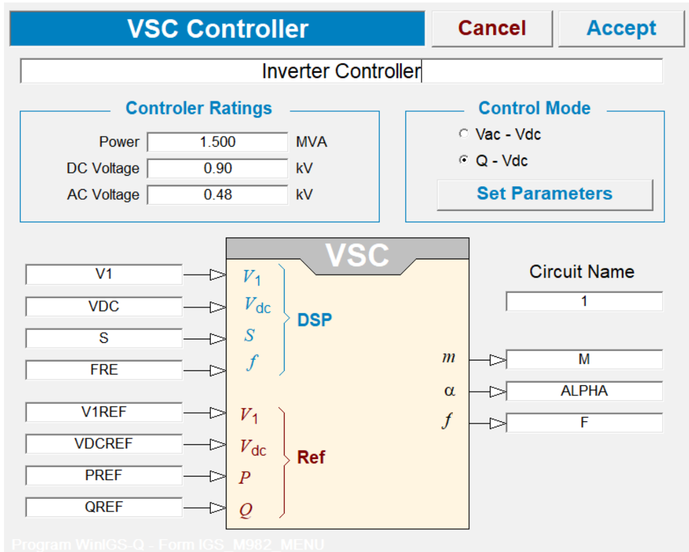

Figure 3-12. User Interface of the VSC Controller Model

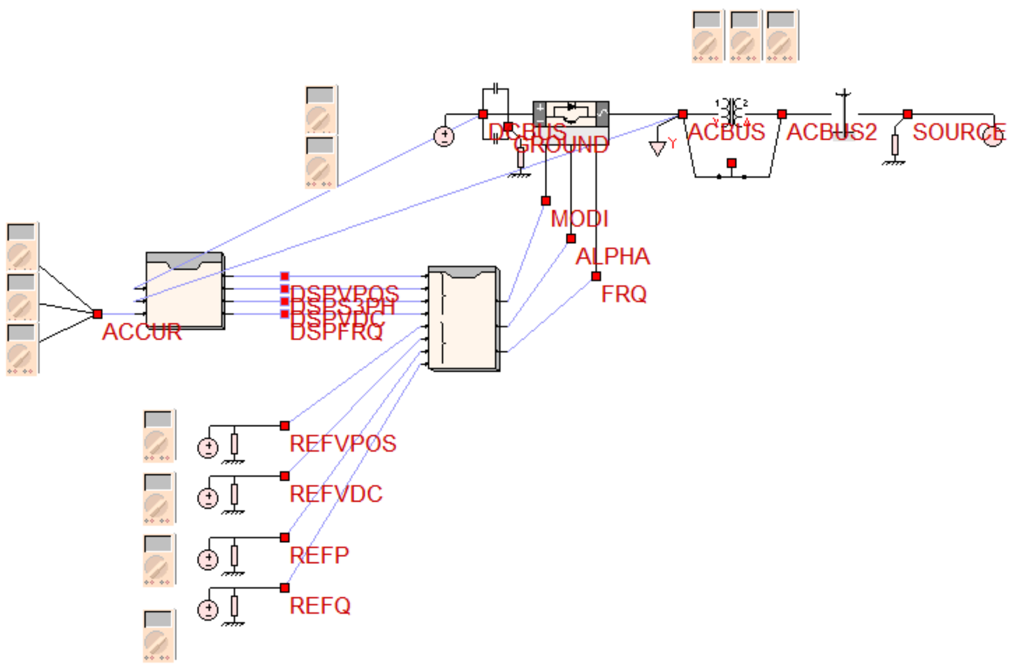

Figure 3-13. Test Case of the VSC Controller Model

3.2 Example Results

To demonstrate the effectiveness of the proposed model, compare the computational efficiency and check the scalability, the example test system with PVs is modeled as a 7.5MW PV farm with 15 inverters. Figure 3-14 shows the example system model. The model has 5 PV subsystems, and each subsystem contains three inverters. Each inverter has different solar insolation inputs in the case. The simulation results of two selected inverters are compared in Figures 3-15, 3-16 and 3-17. These results verify that under normal, near steady state conditions, the two software provide similar results.

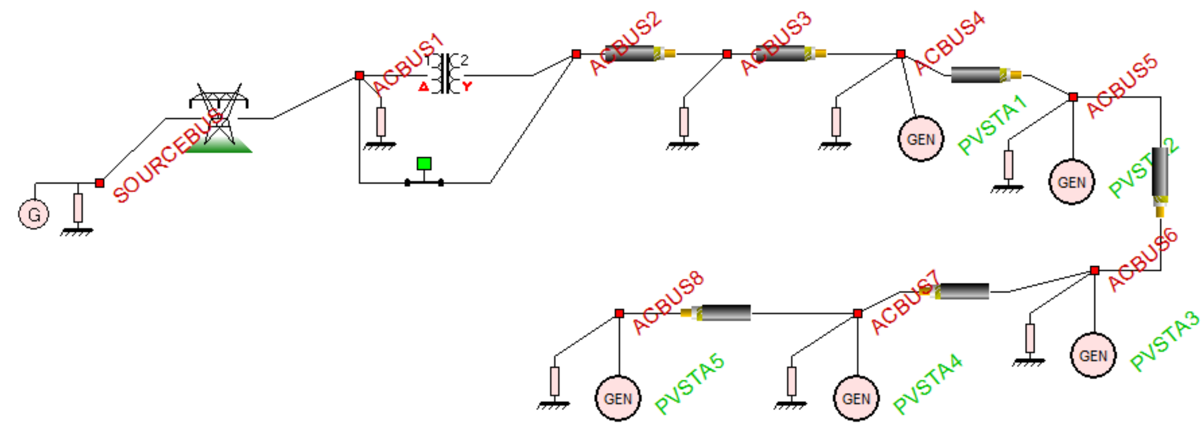

Figure 3-14. Baseline System Model

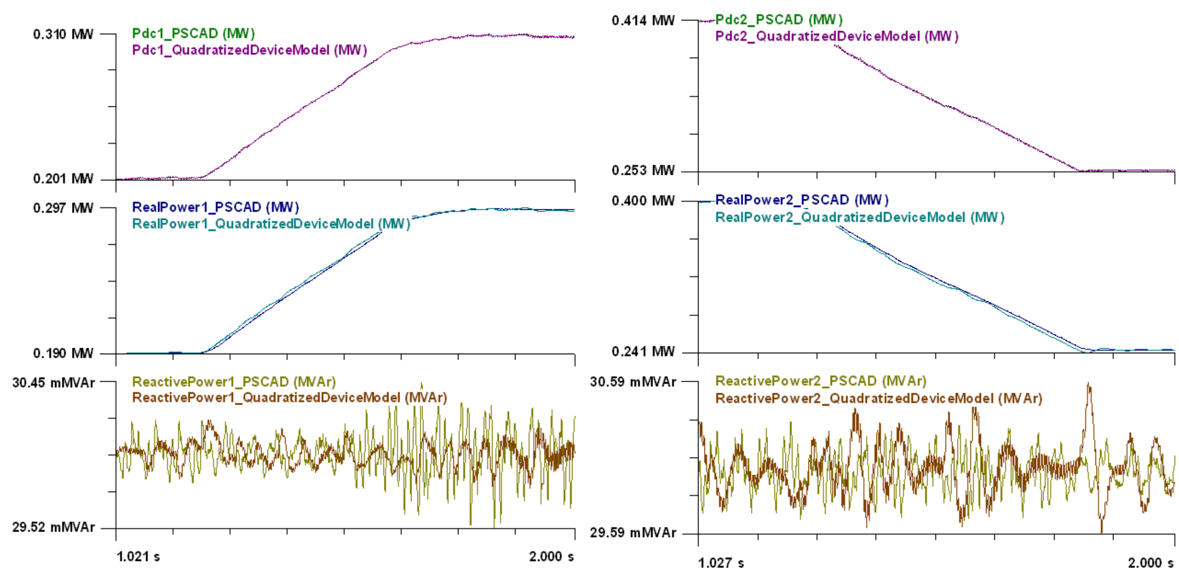

Figure 3-15. Power Simulation Results of PSCAD Simulation and Quasi-Dynamic Domain Simulation

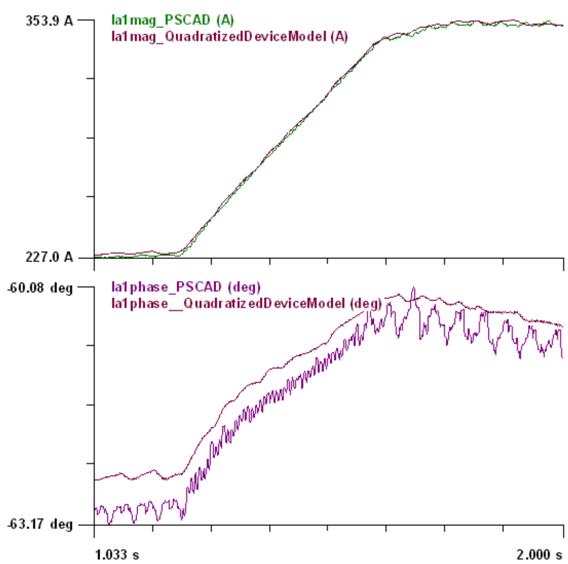

Figure 3-16. Current Simulation Results of PSCAD simulation and Quasi-dynamic Domain Simulation

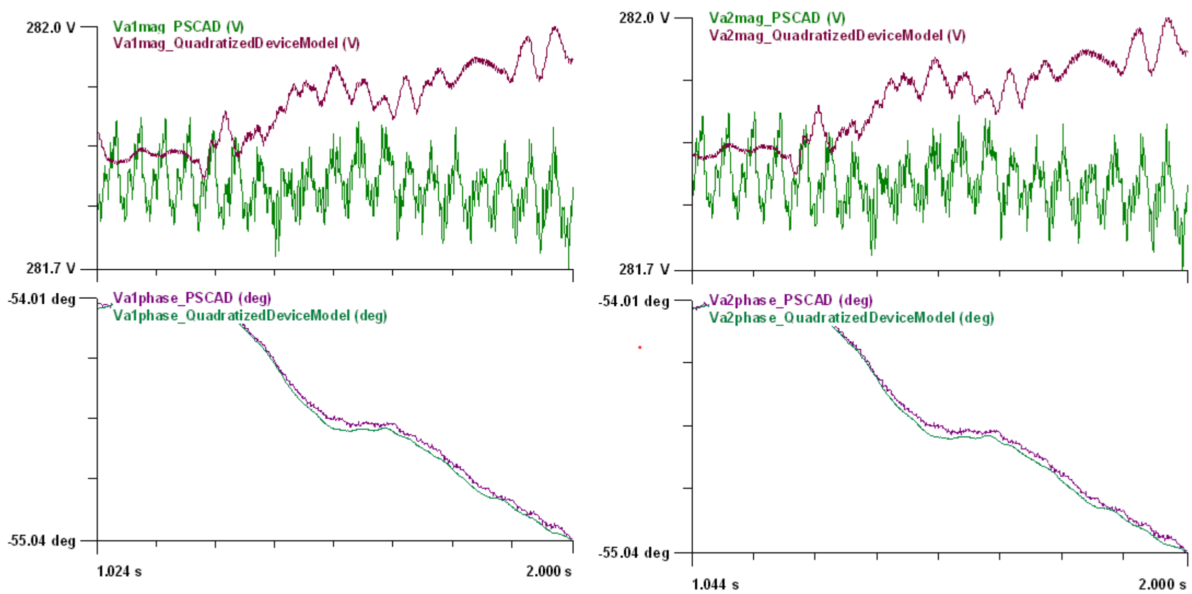

Figure 3-17. Voltage Simulation Results of PSCAD simulation and Quasi-dynamic Domain Simulation

4. DSE Enabled Supplementary Predictive Inverter Control

Grid Forming Inverters must have controls for the smooth riding disturbances that exhibit fast frequency and voltage changes. Smooth riding through these disturbances is facilitated by information about the system oscillations and future evolution of frequency. Similarly, abrupt changes may alter the voltage phase abruptly. Inverter controls should provide smooth transitions from one condition to another. To address these problems, a predictive inverter control approach is helpful. This section presents this approach. In the implementation of this approach it is necessary to rely only on local measurements as it is known that using telemetering may result in an unreliable system due to possible communication failures as well as communication delays.

4.1 Overall Design

The supplementary predictive inverter control is achieved by feeding appropriate signals to modulate the switching-signal generator of the inverter. The supplementary predictive inverter control approach is based on obtaining information about system oscillations, prediction of frequency evolution and any abrupt changes in phase angles. This information is translated into signals that are fed into the controller, such as frequency modulation, modulation index, and phase angle modulation controls as shown in Figure 4-1. This additional control scheme supervises the inverter controller and guarantees synchronization and stability of the inverters.

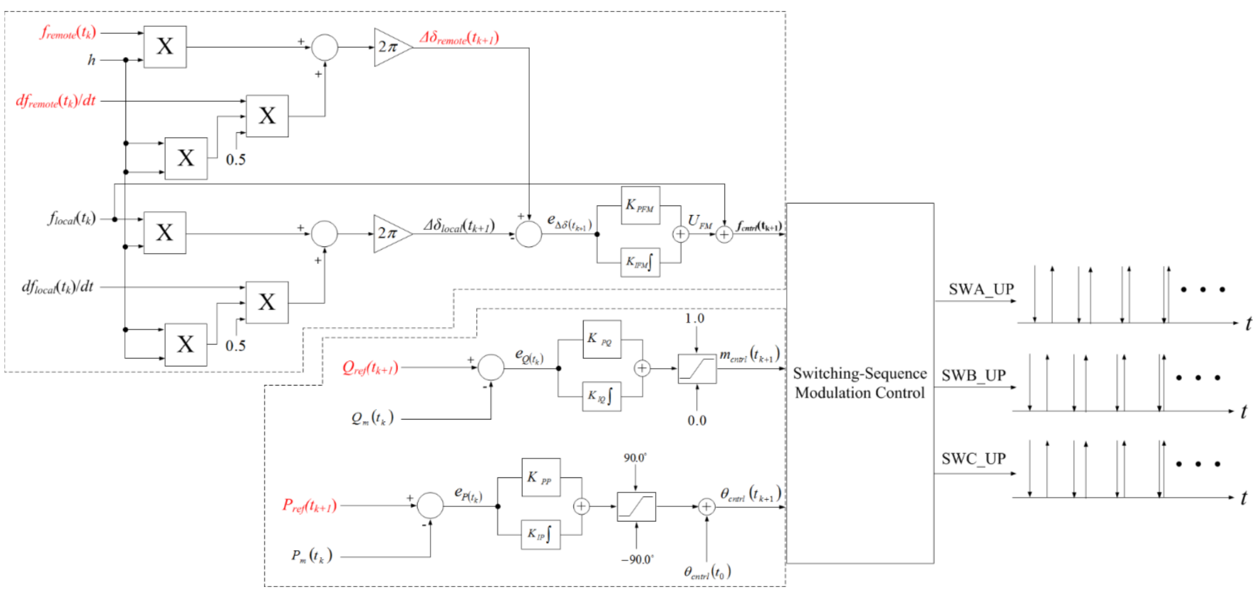

Figure 4-1. Block Diagram of the Supplementary Predictive Inverter Control

The supplementary control scheme feeds two signals into the inverter controller. One signal is the target frequency for the operation of the inverter and the other signal is the target phase angle of the inverter. Both signals are computed from information obtained via a dynamic state estimator that uses only local measurements. The output of the dynamic state estimation provides the future trajectory of frequency and phase angles. Using this information, the controller computes target values of frequency and phase angles for the next time step of firing signals for the inverter valves.

Here we discuss the way this information is used to control the inverter operation. Later in this chapter we discuss the problem of how this information is obtained from dynamic state estimation using local measurements only.

The target frequency signal causes a compression or expansion in time of the switching signal generated by the inverter controller while the phase angle signal causes a translation in time of the switching sequences generated by the inverter. Both the compression/expansion and translation in time are applied smoothly causing a gradual shifting towards the operation of the inverter at the target values.

4.2 Frequency-Modulation Control

In the frequency-modulation control, the first task is to predict the rate of phase-angle changes at both local and remote side, shown as follows:

$$t_{k+1} = t_k + h \tag{4.2.1}$$

$$\Delta\delta_{local}(t_{k+1}) = 2\pi \cdot \left(f_{local}(t_k) \cdot h + \frac{1}{2} \cdot \frac{df_{local}(t_k)}{dt} \cdot h^2 \right) \tag{4.2.2}$$

$$\Delta\delta_{remote}(t_{k+1}) = 2\pi \cdot \left(f_{remote}(t_k) \cdot h + \frac{1}{2} \cdot \frac{df_{remote}(t_k)}{dt} \cdot h^2 \right) \tag{4.2.3}$$

A closed-loop feedforward control was implemented to generate frequency-modulation control commands. The frequency-modulation control with respect to the one-step forward-predicted rates of phase angle changes of two inverters are shown as follows:

$$X(t_{k+1}) = \left(\Delta\delta_{remote}(t_k) - \Delta\delta_{local}(t_k)\right) + \left(\Delta\delta_{remote}(t_{k+1}) - \Delta\delta_{local}(t_{k+1}) - \Delta\delta_{remote}(t_k) + \Delta\delta_{local}(t_k)\right) \cdot h \tag{4.2.4}$$

$$\dot{X}(t_{k+1}) = -\frac{K_{IFM}}{K_{PFM}} X(t_{k+1}) + \frac{1}{K_{PFM}} U_{FM}(t_{k+1}) \tag{4.2.5}$$

$$f_{control}(t_{k+1}) = f_{local}(t_k) + U_{FM}(t_{k+1}) \tag{4.2.6}$$

4.3 Modulation-Index and Phase-Angle Modulation Control

The modulation-index and Phase-Angle Modulation Control using real and reactive power reference and real and reactive power measurements from the digital signal processor (DSP). By sending/receiving more reactive power to a power system, we can increase/decrease the voltage of a power system as described in equation 4.3.1. Furthermore, we can directly control the voltage of a converter-interfaced power system by controlling the modulation index m of the sinusoidal pulse width modulation (SPWM) of the switching-signal generator on behalf of the inverter control. Therefore, we can control the flow of the reactive power between the inverter and the power system by controlling the modulation index. Using the relation between the modulation index and flow of reactive power, we develop the proportional and integral (PI) control-based reactive-power control as follows:

$$V_{local} = \frac{Q \cdot X_s + V_{remote}^2}{V_{remote} \cdot \cos(\theta_{local} - \theta_{remote})} \tag{4.3.1}$$

$$X(t_{k+1}) = \left(Q_{ref}(t_{k+1}) - Q_m(t_k)\right) + \left(Q_{ref}(t_{k+1}) - Q_m(t_{k+1}) - Q_{ref}(t_k) + Q_m(t_k)\right) \cdot h \tag{4.3.2}$$

$$\dot{X}(t_{k+1}) = -\frac{K_{IQ}}{K_{PQ}} X(t_{k+1}) + \frac{1}{K_{PQ}} m_{cntrl}(t_{k+1}) \tag{4.3.3}$$

$$0.0 \le m_{cntrl} \le 1.0 \tag{4.3.4}$$

By controlling the phase angle of the SPWM of the switching-signal generator, we can adjust the phase-angle difference between an inverter and the power system. Therefore, we can control the flow of the real power between an inverter and the power system by controlling the phase angle θ_{local} of the SPWM. Using the relation between the phase angle of the SPWM and flow of the real power, we develop the proportional and integral (PI) real-power control. The real power reference is determined by the V_{dc}/P droop control. The phase angle control equations are shown as follows.

$$P = \frac{V_{local} V_{remote} \sin(\theta_{local} - \theta_{remote})}{X_s} \tag{4.3.5}$$

$$S_{ref} = m(t_k) \cdot \cos(2\pi \cdot f_{cntrl}(t_k) \cdot t_k + \theta_{cntrl}(t_k)) \tag{4.3.6}$$

$$P_{ref}(t_{k+1}) = P_{set} + k(V_{dc\_m}(t_k) - V_{dc\_set}) \tag{4.3.7}$$

$$X(t_{k+1}) = \left(P_{ref}(t_{k+1}) - P_m(t_k)\right) + \left(P_{ref}(t_{k+1}) - P_m(t_{k+1}) - P_{ref}(t_k) + P_m(t_k)\right) \cdot h \tag{4.3.8}$$

$$\dot{X}(t_{k+1}) = -\frac{K_{IP}}{K_{PP}} X(t_{k+1}) + \frac{1}{K_{PP}} \theta_{cntrl}(t_{k+1}) \tag{4.3.9}$$

$$-\frac{\pi}{2} \le \theta_{cntrl} \le \frac{\pi}{2} \tag{4.3.10}$$

4.4 Switching-Sequence Modulation Control

Switching-sequence modulation control is applied to generate the switching sequence for the three upper switches of the inverter by using the three control inputs $f_{cntrl}(t_{k+1}), m_{cntrl}(t_{k+1}), \theta_{cntrl}(t_{k+1})$ from the previous sections. First, the initial operation time for the switching-sequence modulation control is calculated with the zero-crossing time. The equations are shown as follows:

$$t_{\text{int}} = t_{ZX}(t_0) + \frac{\frac{\pi}{2} + \theta_{v1}(t_0)}{2\pi \cdot f_{local}(t_0)} \tag{4.4.1}$$

$$t_k = t_{\text{int}} + k \cdot h \tag{4.4.2}$$

The three-phase base switching sequence for a period was calculated based on a base frequency of 60 Hz and a switching frequency of 1260 Hz are shown as follows in Figure 4-2 to Figure 4-4.

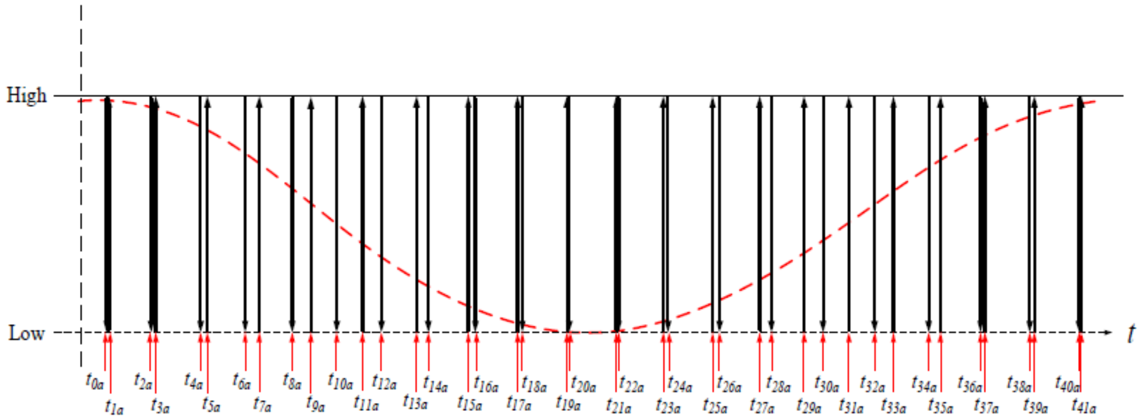

Figure 4-2. Base Switching Sequence of Phase A

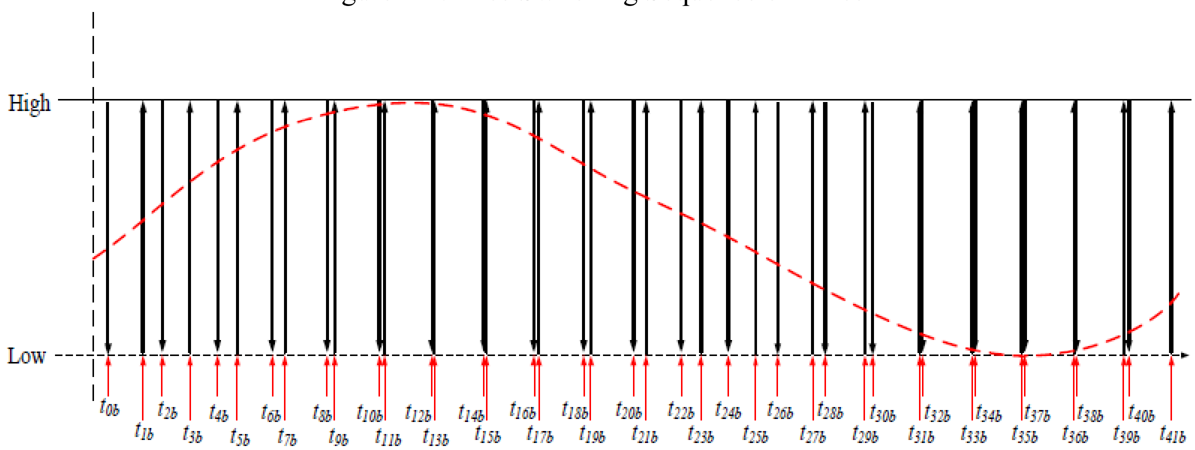

Figure 4-3. Base Switching Sequence of Phase B

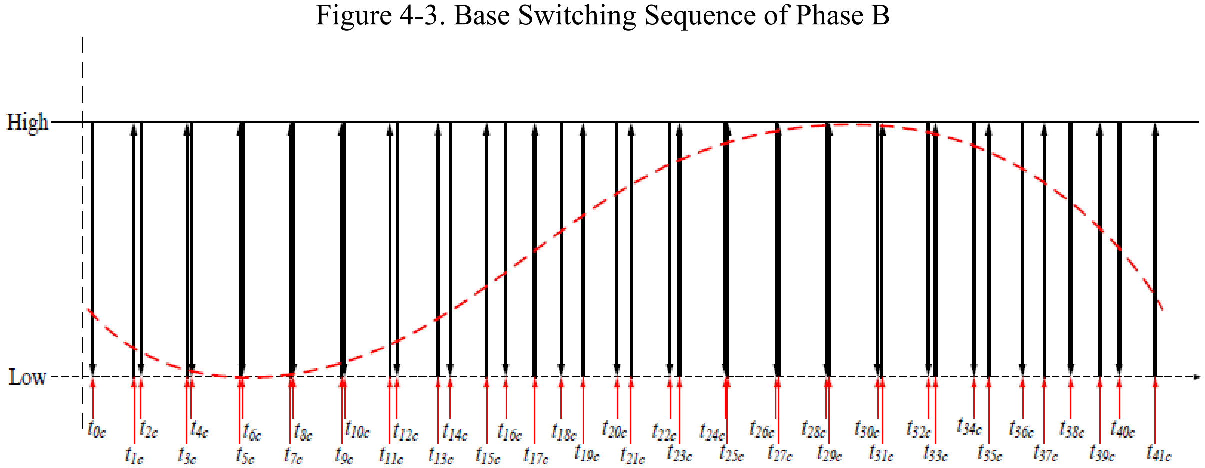

Figure 4-4. Base Switching Sequence of Phase C

By modulating the above base switching sequences with the supplementary predictive inverter control, the proposed switching-signal generator can control real and reactive power flows of the system as follows:

$$SWA\_UP = \{ct_{0a}, \quad ct_{1a}, \quad ct_{2a}, \quad \cdots \quad ct_{39a}, \quad ct_{40a}, \quad ct_{41a}\} \tag{4.4.1}$$

$$SWB\_UP = \{ct_{0b}, \quad ct_{1b}, \quad ct_{2b}, \quad \cdots \quad ct_{39b}, \quad ct_{40b}, \quad ct_{41b}\} \tag{4.4.2}$$

$$SWC\_UP = \{ct_{0c}, \quad ct_{1c}, \quad ct_{2c}, \quad \cdots \quad ct_{39c}, \quad ct_{40c}, \quad ct_{41c}\} \tag{4.4.2}$$

Figure 4-5 to figure 4-7 shows the three-phase modulated switching sequence for a full period.

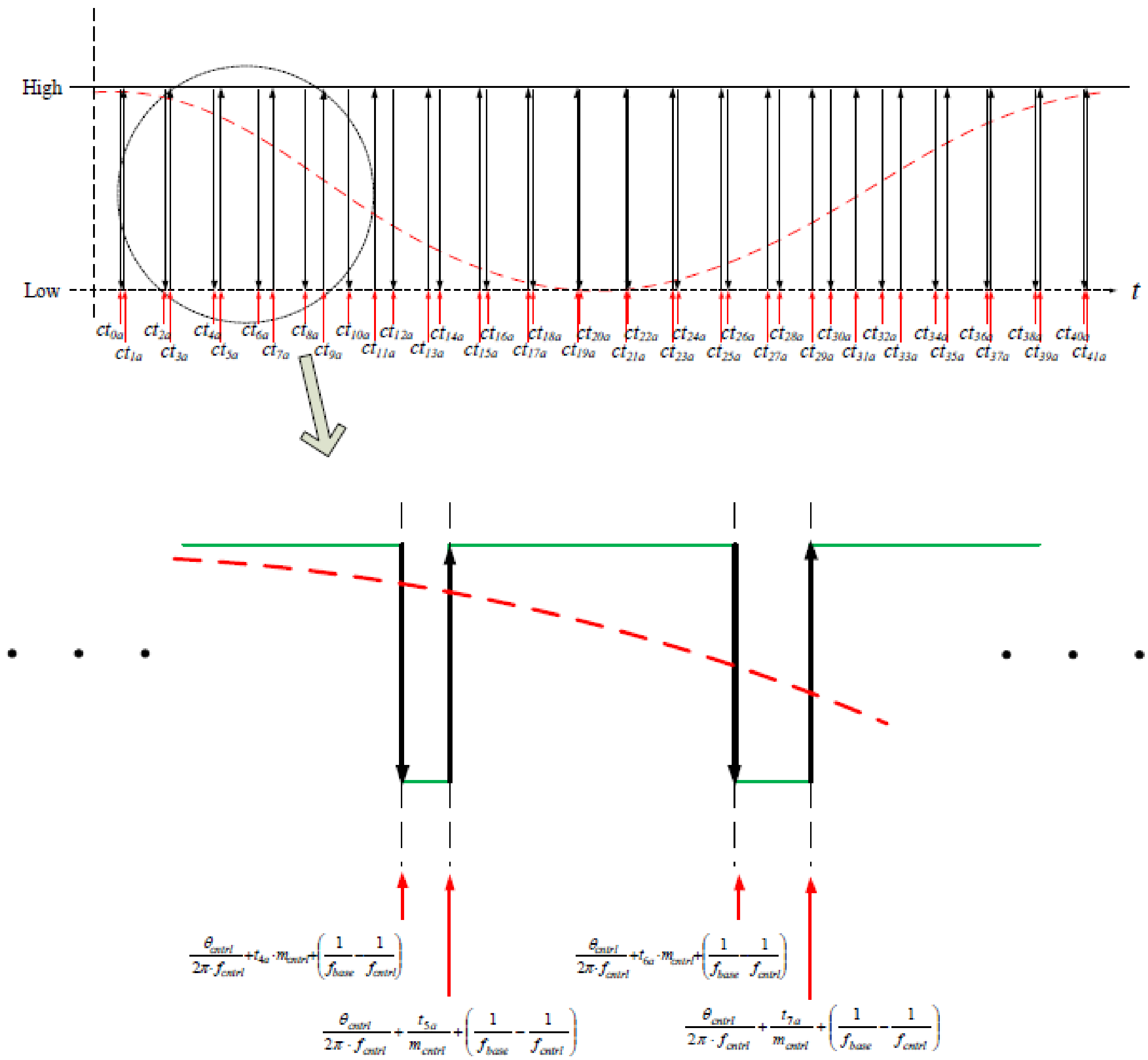

Figure 4-5. Modulated Switching-Signal Sequence of the Phase A (SWA_UP)

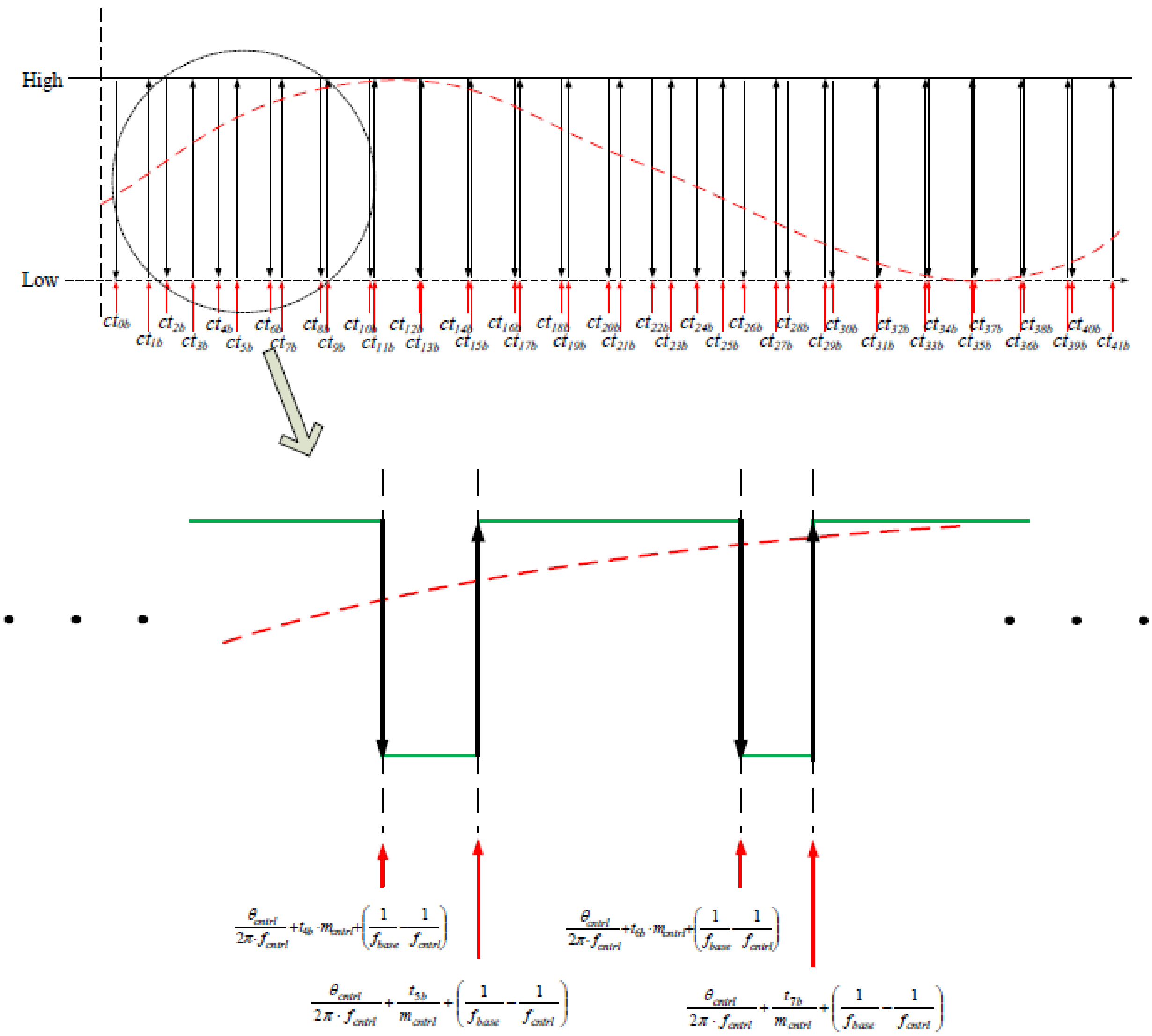

Figure 4-6. Modulated Switching-Signal Sequence of the Phase B (SWB_UP)

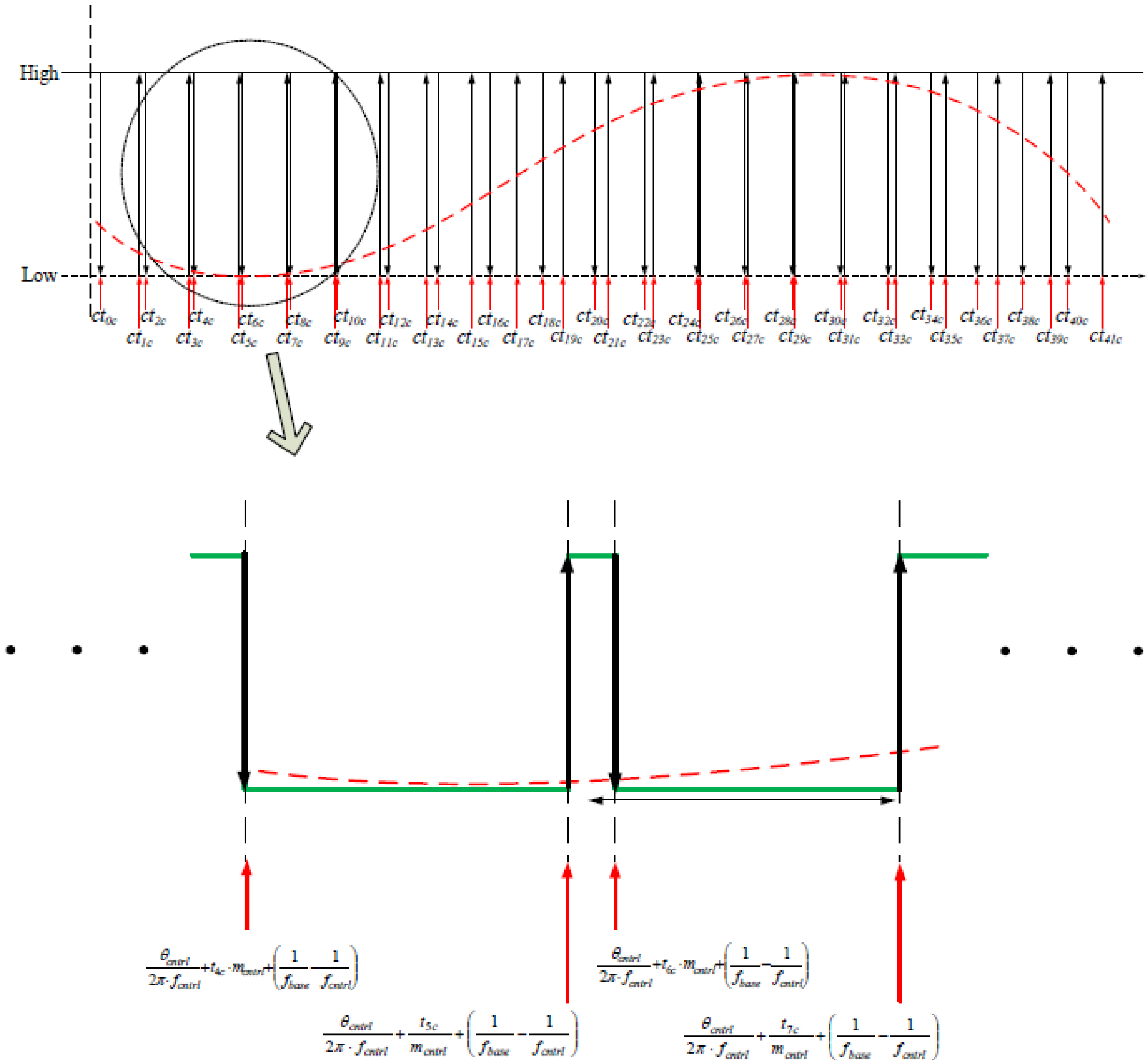

Figure 4-7. Modulated Switching-Signal Sequence of the Phase C (SWC_UP)

4.5 Performance Evaluation of Dynamic State Estimation (DSE)

This section presents a series of simulation that tests the accuracy by which the dynamic state estimator can determine frequency and rate of change of frequency of the power grid while it uses only local measurements at the inverter location. The simulation results indicate that the accuracy of the dynamic stat estimator is excellent.

Figure 4-8 shows the test system used in the simulation, which evaluates the performance of estimating the frequency and rate of frequency change locally at the inverter as well as at the system with only local measurements. The system consists of a wind turbine system (WTS) that operates at 50 Hz. The WTS is connected to two converters and a 690V to 34.5 kV transformer. A transmission line at 34.5 kV is used to connect the local side and remote side in the test system. The grid side is assumed to have a generator that oscillates in such a way that the frequency varies as follows: 60 ± 0.1 Hz. The source is connected to the power grid via a step-up transformer and the 1.5-mile-long line.

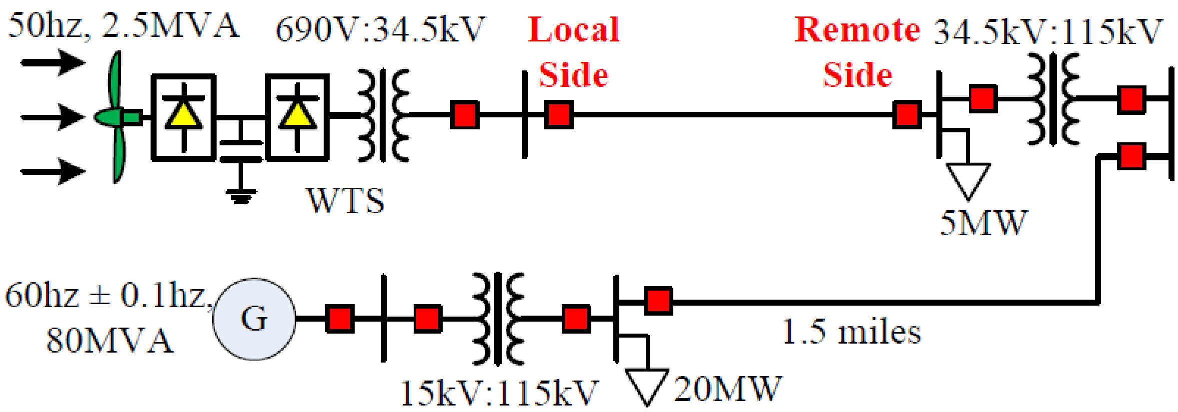

Figure 4-8. Simulation System for Frequency Estimation

One of the objectives of the dynamic state estimator is to provide the best estimate of the frequency and the rate of frequency change at the local (inverter location) and remote side (34.5kV/115kV transformer). Numerical experiments have been performed with different lengths of lines.

Figure 4-9 shows the results of the frequency and rate of frequency change estimation. At the local side (inverter side) of the 1.5-mile transmission line. The first two channels show instantaneous values of three-phase measured and DSE estimated voltages. The third and fourth channel shows the actual and estimated frequency, and the fourth channel shows the difference between the estimated and measured frequency. The maximum absolute error is 18.87 μHz. The fifth channel shows the actual and estimated rate of frequency change, and the sixth channel shows the difference between the estimated and measured rate of frequency change. The error of the estimated rate of frequency change is 0.124 mHz/s.

Figure 4-10 shows the results of the frequency and rate of frequency change, at the remote side of the 1.5-mile transmission line. The first two channels show instantaneous values of three phase measured and DSE estimated voltages. The third and fourth channel shows the actual and estimated frequency, and the fourth channel shows the difference between the estimated and measured value. The maximum absolute error is 0.177 mHz. The fifth channel shows the actual and estimated rate of frequency change, and the sixth channel shows the difference between the estimated and measured rate of frequency change. The error of the estimated rate of frequency change is 1.144 mHz/s.

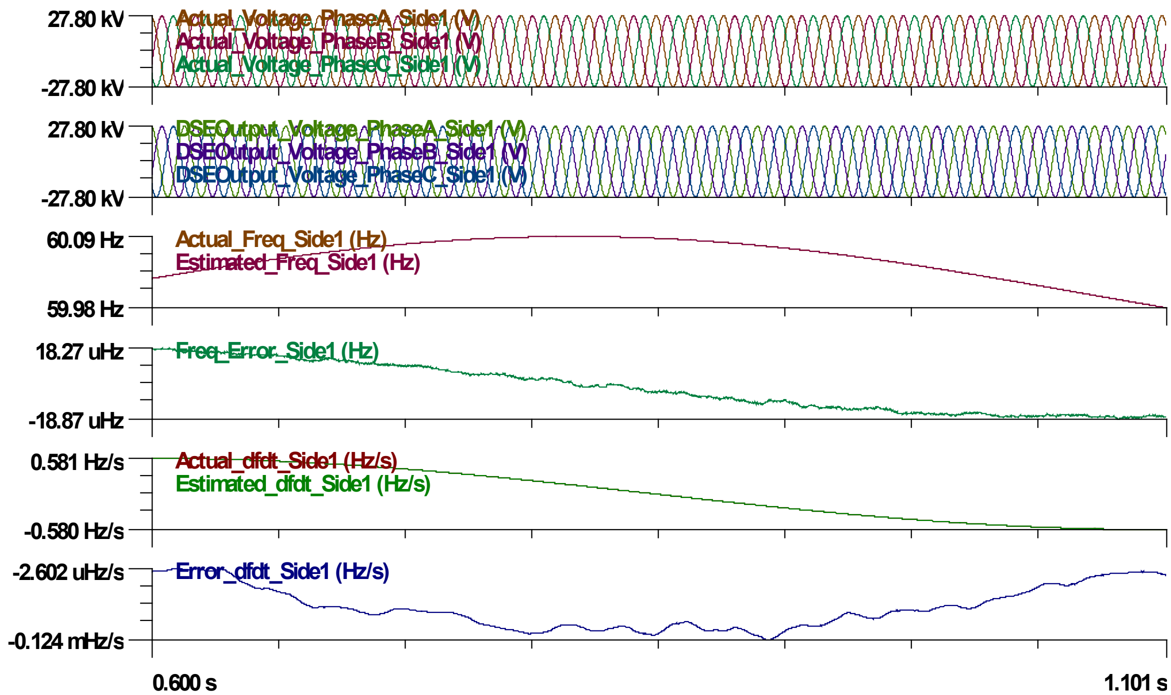

Figure 4-9. Simulation Results, 1.5-Mile Line, Local Side

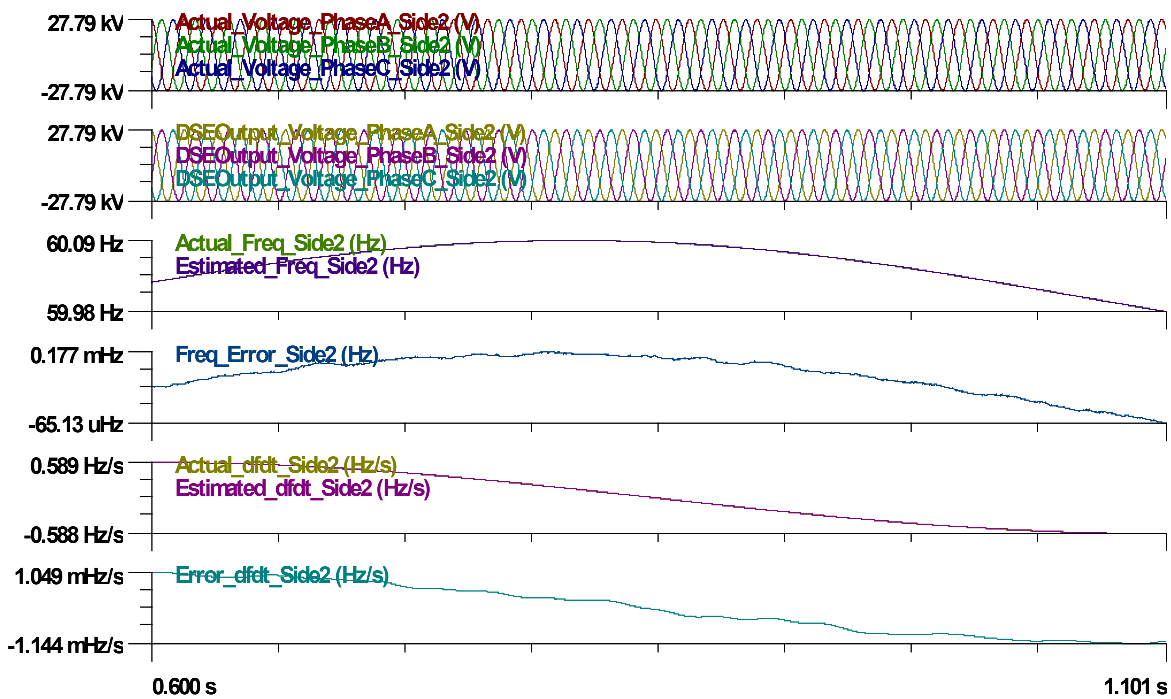

Figure 4-10. Simulation Results, 1.5-Mile Line, Remote Side

Figure 4-11 shows the results of the frequency and rate of frequency change estimation. At the local side (inverter side) of the 2.5-mile transmission line. The first two channels show instantaneous values of three-phase measured and DSE estimated voltages. The third and fourth channel shows the actual and estimated frequency, and the fourth channel shows the difference between the estimated and measured frequency. The maximum absolute error is 20.05 μHz. The fifth channel shows the actual and estimated rate of frequency change, and the sixth channel shows the difference between the estimated and measured rate of frequency change. The error of the estimated rate of frequency change is 0.128 mHz/s.

Figure 4-12 shows the results of the frequency and rate of frequency change, at the remote side of the 2.5-mile transmission line. The first two channels show instantaneous values of three phase measured and DSE estimated voltages. The third and fourth channel shows the actual and estimated frequency, and the fourth channel shows the difference between the estimated and measured value. The maximum absolute error is 0.282 mHz. The fifth channel shows the actual and estimated rate of frequency change, and the sixth channel shows the difference between the estimated and measured rate of frequency change. The error of the estimated rate of frequency change is 1.906 mHz/s.

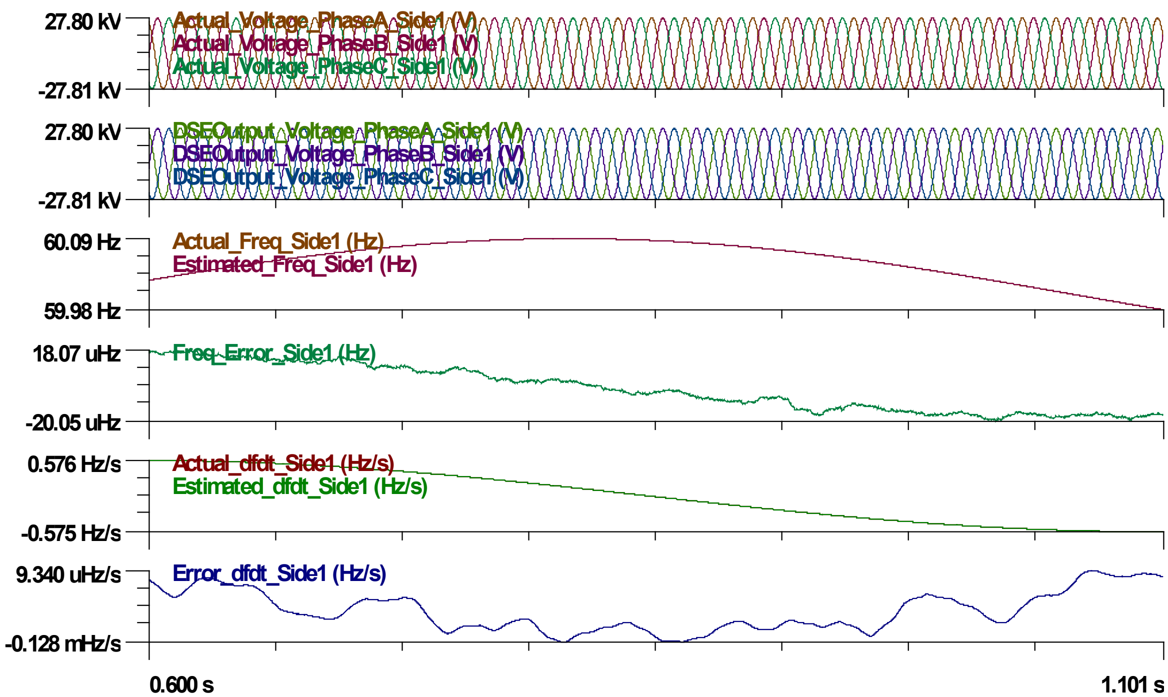

Figure 4-11. Simulation Results, 2.5-Mile Line, Local Side

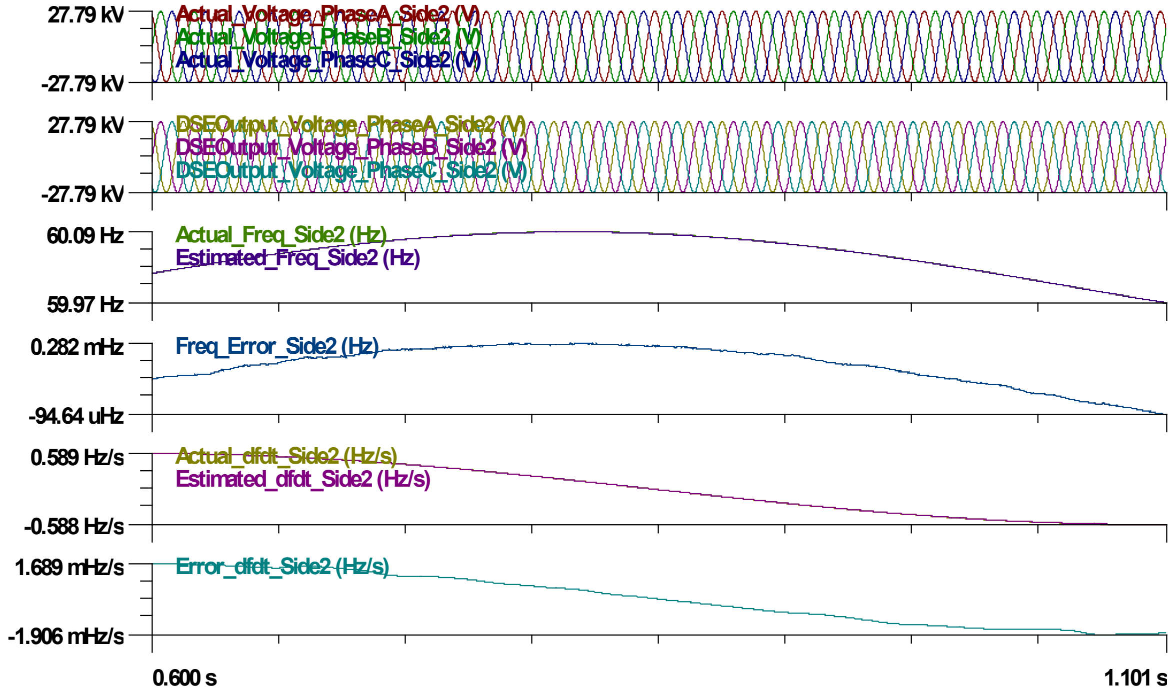

Figure 4-12. Simulation Results, 2.5-Mile Line, Remote Side

Figure 4-13 shows the results of the frequency and rate of frequency change estimation. At the local side (inverter side) of the 4.0-mile transmission line. The first two channels show instantaneous values of three-phase measured and DSE estimated voltages. The third and fourth channel shows the actual and estimated frequency, and the fourth channel shows the difference between the estimated and measured frequency. The maximum absolute error is 18.53 µHz. The fifth channel shows the actual and estimated rate of frequency change, and the sixth channel shows the difference between the estimated and measured rate of frequency change. The error of the estimated rate of frequency change is 0.135 mHz/s.

Figure 4-14 shows the results of the frequency and rate of frequency change, at the remote side of the 4.0-mile transmission line. The first two channels show instantaneous values of three phase measured and DSE estimated voltages. The third and fourth channel shows the actual and estimated frequency, and the fourth channel shows the difference between the estimated and measured value. The maximum absolute error is 0.451 mHz. The fifth channel shows the actual and estimated rate of frequency change, and the sixth channel shows the difference between the estimated and measured rate of frequency change. The error of the estimated rate of frequency change is 2.896 mHz/s.

All results are summarized in Table 4-1 and Table 4-2. The frequency varies from 59.98~60.09 Hz, and the rate of frequency change varies from -0.6 ~ 0.6 Hz/s. From the two tables below, the maximum absolute error is within 0.001% for frequency and 0.5% for rate of frequency change. We can conclude that the proposed method can accurately estimate the local and remote side frequency as well as rate of frequency change with local information only.

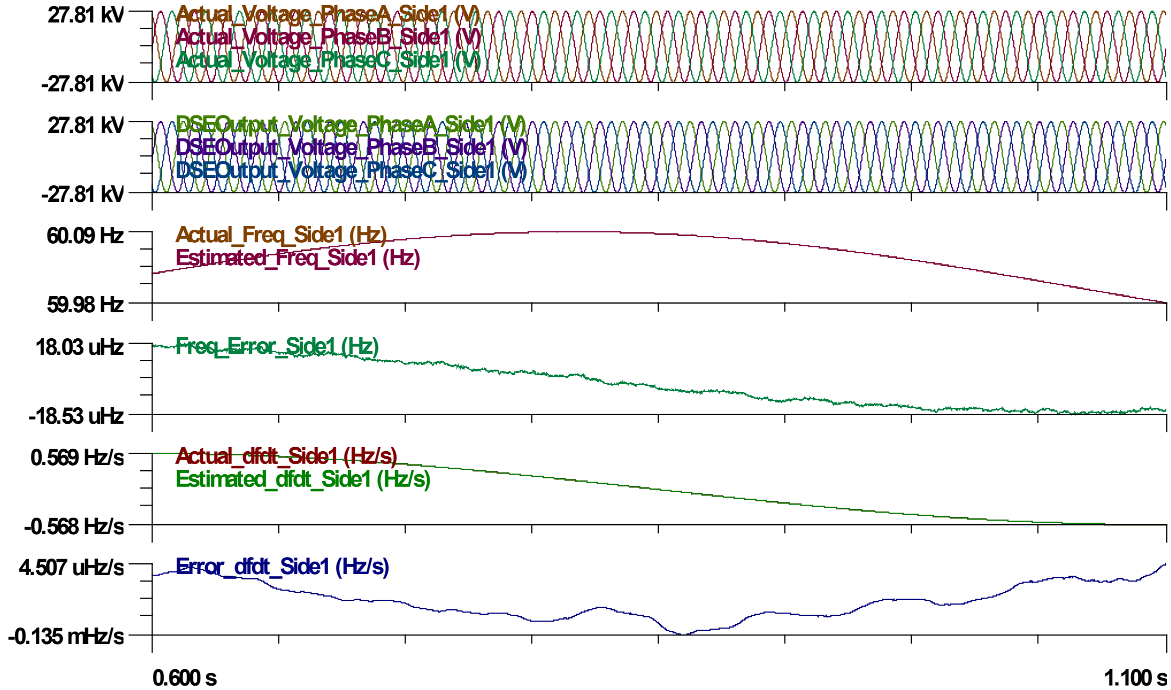

Figure 4-13. Simulation Results, 4.0-Mile Line, Local Side

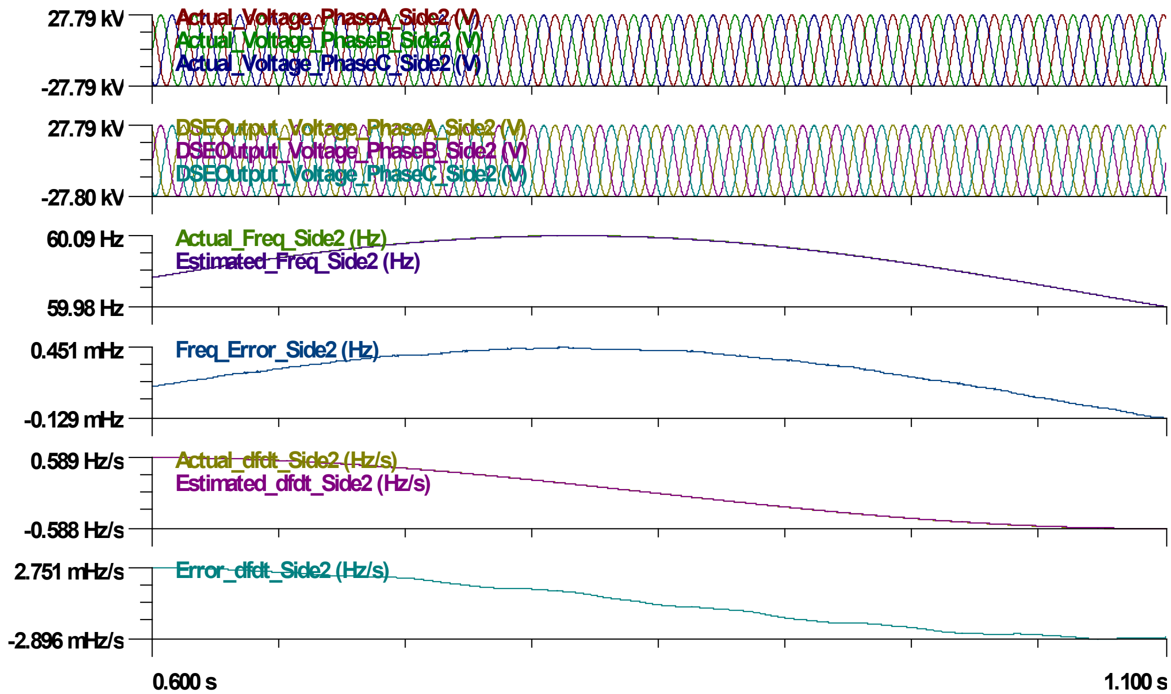

Figure 4-14. Simulation Results, 4.0-Mile Line, Remote Side

Table 4-1. Simulation Results of Local Side

Case Number	Line length	Frequency Error	dFreq/dt error
1	1.5 miles	$-1.887\times10^{-5} \sim 1.827\times10^{-5}$ Hz	$-1.24\times10^{-4} \sim -2.602\times10^{-6}$ Hz/s
2	2.5 miles	$-2.005\times10^{-5} \sim 1.807\times10^{-5}$ Hz	$-1.28\times10^{-4} \sim 9.340\times10^{-6}$ Hz/s
3	4 miles	$-1.853\times10^{-5} \sim 1.803\times10^{-5}$ Hz	$-1.35\times10^{-4} \sim 4.507\times10^{-6}$ Hz/s

Table 4-2. Simulation Results of Remote Side

Case Number	Line length	Frequency Error	dFreq/dt error
1	1.5 miles	$-6.513\times10^{-5} \sim 1.77\times10^{-4}$ Hz	$-1.144\times10^{-3} \sim 1.049\times10^{-3}$ Hz/s
2	2.5 miles	$-9.464\times10^{-5} \sim 2.82\times10^{-4}$Hz	$-1.906\times10^{-3} \sim 1.689\times10^{-3}$ Hz/s
3	4 miles	$-1.29\times10^{-4} \sim 4.51\times10^{-4}$ Hz	$-2.896\times10^{-3} \sim 2.751\times10^{-3}$ Hz/s

4.6 Performance Evaluation of Supplementary Predictive Inverter Control Enabled by Dynamic State Estimation (DSE)

Numerical experiments were conducted to evaluate the performance of the supplementary predictive inverter control. Each numerical experiment investigated two scenarios: scenario 1: the proposed supplementary control is disabled; scenario 2: the proposed supplementary control is enabled while keeping the system conditions the same (same set of disturbances).

The numerical experiments were performed using the test system of Figure 4-15. The system consists of a type 4 wind turbine system connected to a step-up transformer, a 35 kV transmission circuit, connecting to a collector substation. The key components of the test system are listed in Table 4-3. By enabling supplementary inverter control, the proposed control practically eliminates valve mis-operations in the inverter when disturbances occur in the system. We present two example cases in the following subsections.

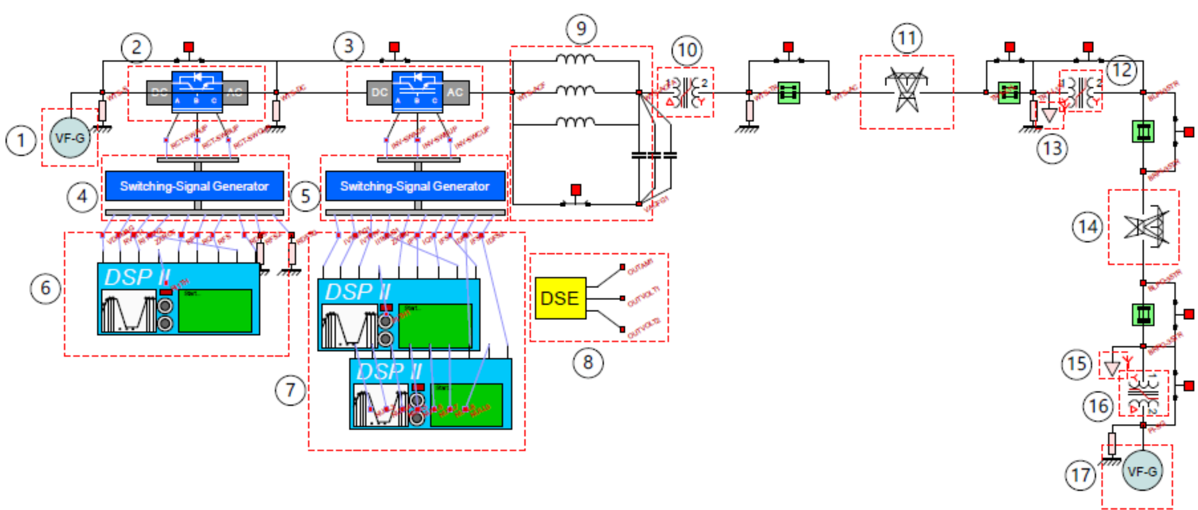

Figure 4-15. Test Bed for the Supplementary Predictive Inverter Control

Table 4-3. List of Components in Test Bed for the Supplementary Predictive Inverter Control

Index	Component
1	Variable-Speed Wind Turbine (0.690 kV / 2.5 MVA)
2	Wind Turbine-Side Converter (0.690 kV / 2.5 MVA)
3	Grid-Side Inverter (0.690 kV / 2.5 MVA)
4	Wind Turbine-Side Converter Controller
5	Grid-Side Inverter Controller
6	Digital Signal Processor (DSP) for Wind Turbine-Side Converter Control
7	DSPs for Grid-Side Inverter Control
8	Dynamic State Estimator (DSE)
9	L-C Filter
10	Delta-Wye Transformer (0.670 kV / 34.5 kV)
11	1.5-Mile Transmission Line (34.5 kV)
12	Wye-Wye Transformer (34.5 kV / 115 kV)
13	Three-Phase Load (34.5 kV / 5 MVA)
14	1.5-Mile Transmission Line (115 kV)
15	Three-Phase Load (115 kV / 20 MVA)
16	Wye-Delta Transformer (115 kV / 15 kV)
17	Variable-Frequency Three-Phase Equivalent Voltage Source (15 kV / 80 MVA)

4.6.1 Case 1: Performance without Supplementary Predictive Inverter Control

The system of Figure 4-15 was simulated with the following event: 1, the grid-side inverter operates under its own controller. The wind power results in rotor speed corresponding to 50 Hz and the wind has a 10% variability. The power grid experiences an oscillation. At the remote generator, the frequency oscillation is $60+0.1\sin(2\pi \cdot t)$ Hz. The grid-side inverter control is set to operate at 2 MW/0.8 Kv_{DC} and 0.5 MVar (P-Q mode). Power imbalances in the system are absorbed by the conventional generation.

Simulation results are shown in Figure 4-16 over a period of 2 seconds. The first two traces show the voltages and currents at the output of the inverter. Traces 3 and 4 show the real and reactive power output of the inverter. Note the variability caused by the oscillating conditions of the power grid. Traces 5 shows the local and remote frequencies of the phase A voltage. Traces 6 shows the local and remote phase angles.

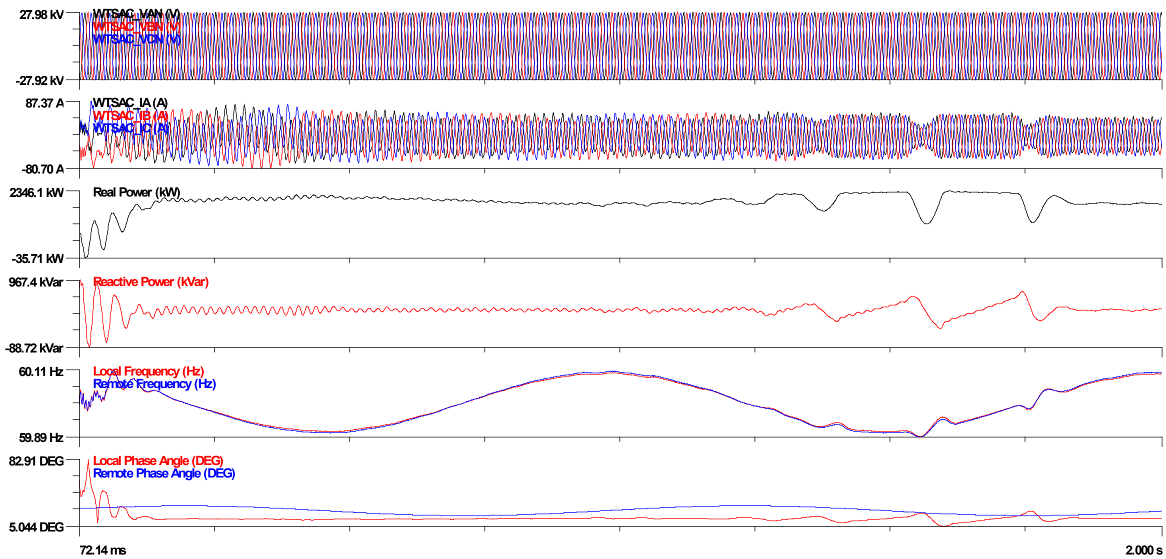

Figure 4-16. Simulation Result when Supplementary Predictive Inverter Control Is Disabled

4.6.2 Case 2: Performance with Supplementary Predictive Inverter Control

The system of Figure 4-15 was simulated with the following event: 2, the grid-side inverter operates with the supplementary control. The wind power results in rotor speed corresponding to 50 Hz and the wind has a 10% variability. The power grid experiences an oscillation. At the remote generator, the frequency oscillation is $60 + 0.1\sin(2\pi \cdot t)$ Hz. The grid-side inverter control is set to operate at 2 MW/0.8 Kv_{DC} and 0.5 MVar (P-Q mode). Power imbalances in the system are absorbed by the conventional generation.

Simulation results are shown in Figure 4-17 over a period of 2 seconds. The first two traces show the voltages and currents at the output of the inverter. Traces 3 and 4 show the real and reactive power output of the inverter. Note the variability caused by the oscillating conditions of the power grid. Traces 5 shows the local and remote frequencies of the phase A voltage. Traces 6 shows the local and remote phase angles.

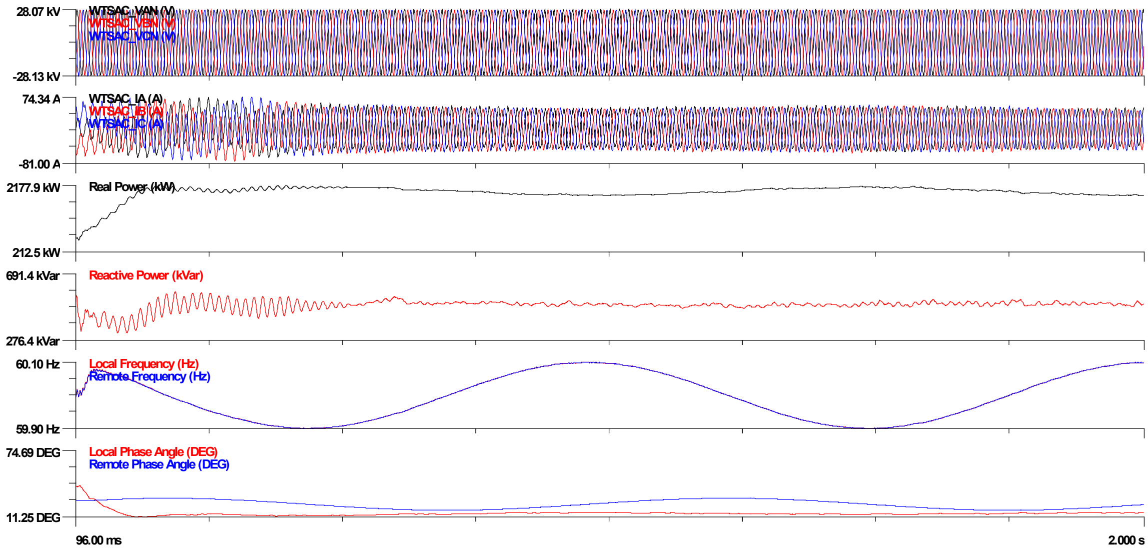

Figure 4-17. Simulation Result when Supplementary Predictive Inverter Control Is Enabled

5. Simulation Results of GFM Inverters

Simulation results with GFM inverters are presented in this section.

5.1 Example Test Systems to assess performance of GFM Inverter

The target system for validating the performance of the model as a grid forming inverter is shown in Figure 5-1. The example test system contains two major parts, legacy AC system and 100% inverter-based system. Note that the system can be configured to operate in parallel with the grid or in isolation as a 100% inverter-based system when the breaker at XFMR-H is open. A battery energy storage system (BESS) is connected to the system via a GFM inverter. The isolated 100% inverter-based system has heavy motor-based loads and represents an excellent system to quantify the performance of the grid forming inverters.

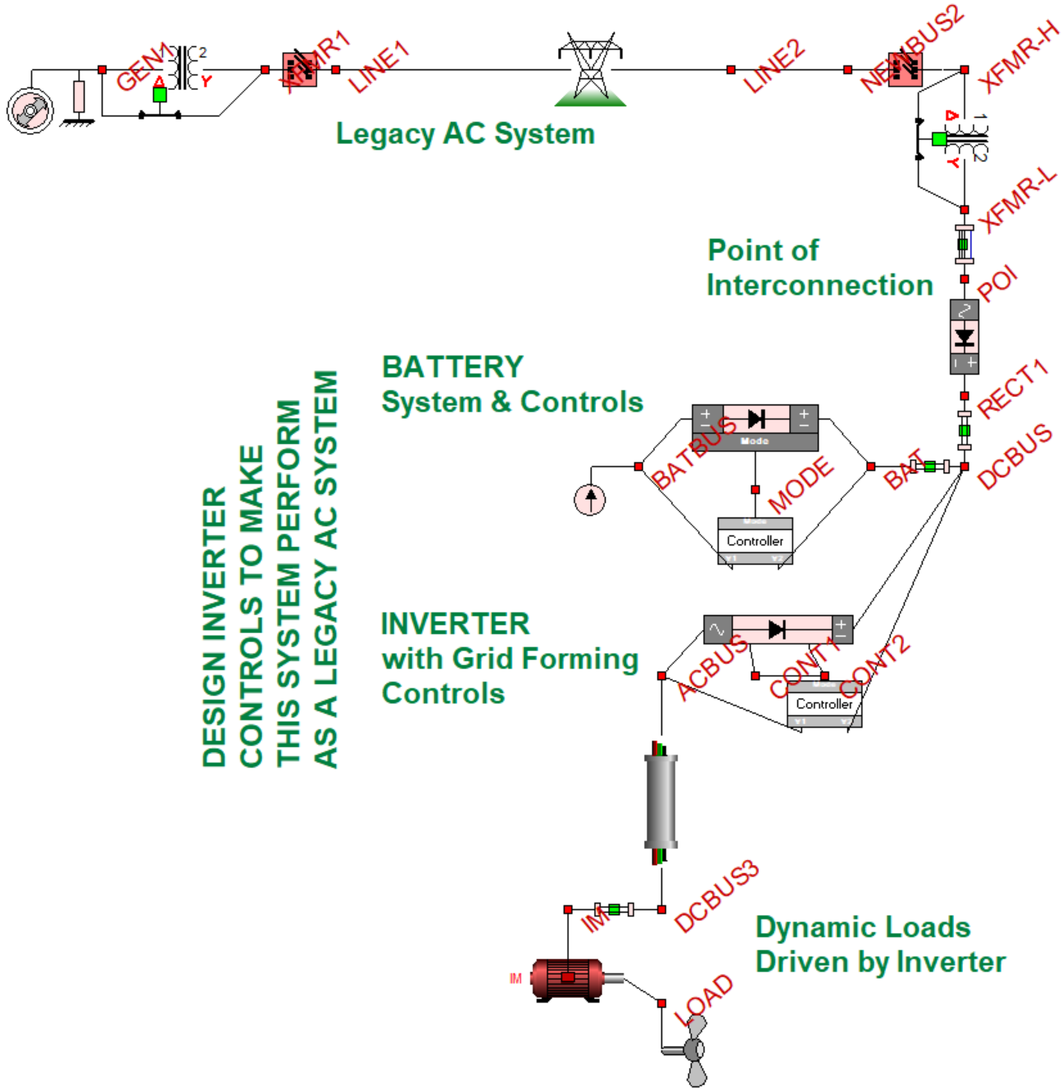

Figure 5-1. Example Test System

5.2 Performance Evaluation of GFM Inverter

In this section, we will present the simulation results obtained from the example test system in two different use cases. The simulation results will be analyzed to evaluate the performance of the proposed GFM Inverter control scheme.

The simulation contains two use cases. Use case 1 tests the performance of the GFM inverter during the loss of the synchronous generator, where the synchronous generator in the example test system disconnects at 2 seconds of the simulation. Therefore, the system operates under a 100% inverter-based condition after the loss of synchronous generator. Use case 2 tests the cold start capability of the proposed GFM inverter. In use case 2, the system operates purely on GFM inverters after 1.5 seconds of the simulation and the induction-motor based load starts at 2.5 seconds of the simulation. So that the cold start of the induction motor-based load is purely supported by the GFM inverter.

The simulation length was 5.0 seconds with a step size of 41.667 microseconds as shown in Figure 5-2. The simulation results from both use cases are presented in the next section.

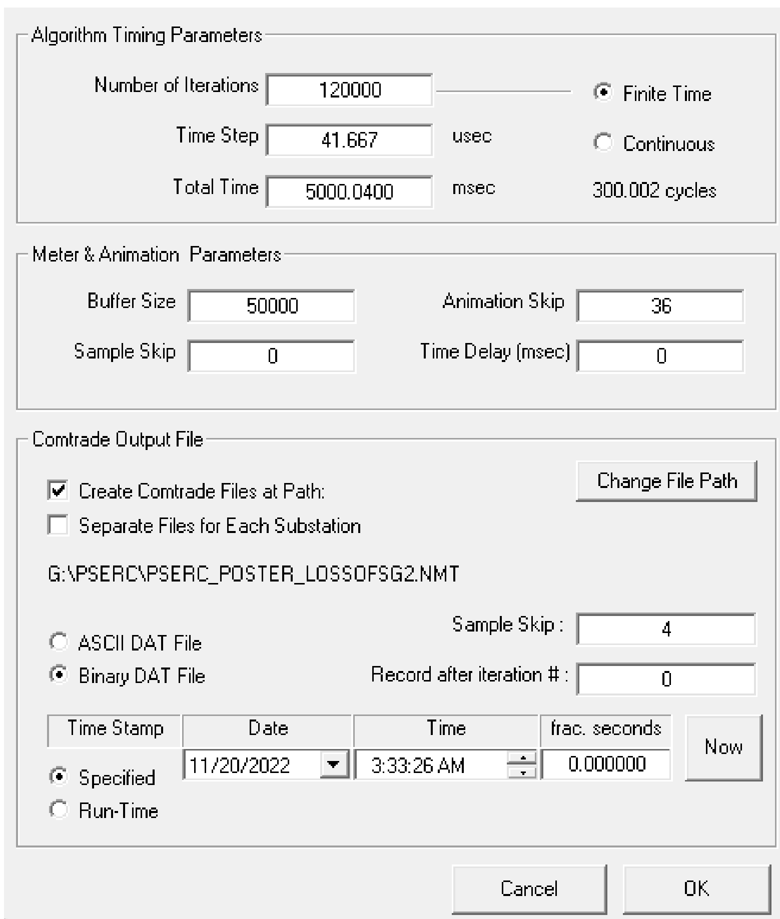

Figure 5-2. Parameter Settings of Simulation

5.3 Simulation Results – Loss of Synchronous Generator

This simulation studies the performance of the GFM inverter during the loss of synchronous generators in the example test system. The parameters of the components in the example test system are presented in Appendix C. Waveforms and phasors of voltages and currents measured at different locations of the test system were collected during the simulation.

Figure 5-3 shows the detailed view of selected waveforms measured from 1.882 seconds to 2.256 seconds of the simulation with high induction motor load output, where the disconnection of the synchronous generator occurred at 2 seconds. In Figure 5-3, 6 selected groups of waveforms are presented. The first two groups of waveforms are the three-phase voltage and three-phase current waveforms measured at ACBUS in Figure 5-1. The third and fourth group of waveforms display the three-phase voltage and three-phase current waveforms measured at the induction motor-based load at bus LOAD in Figure 5-1. The fifth and sixth group of waveforms are the three-phase voltage and three-phase current waveforms measured at the high-voltage side of transformer XFMR-H.

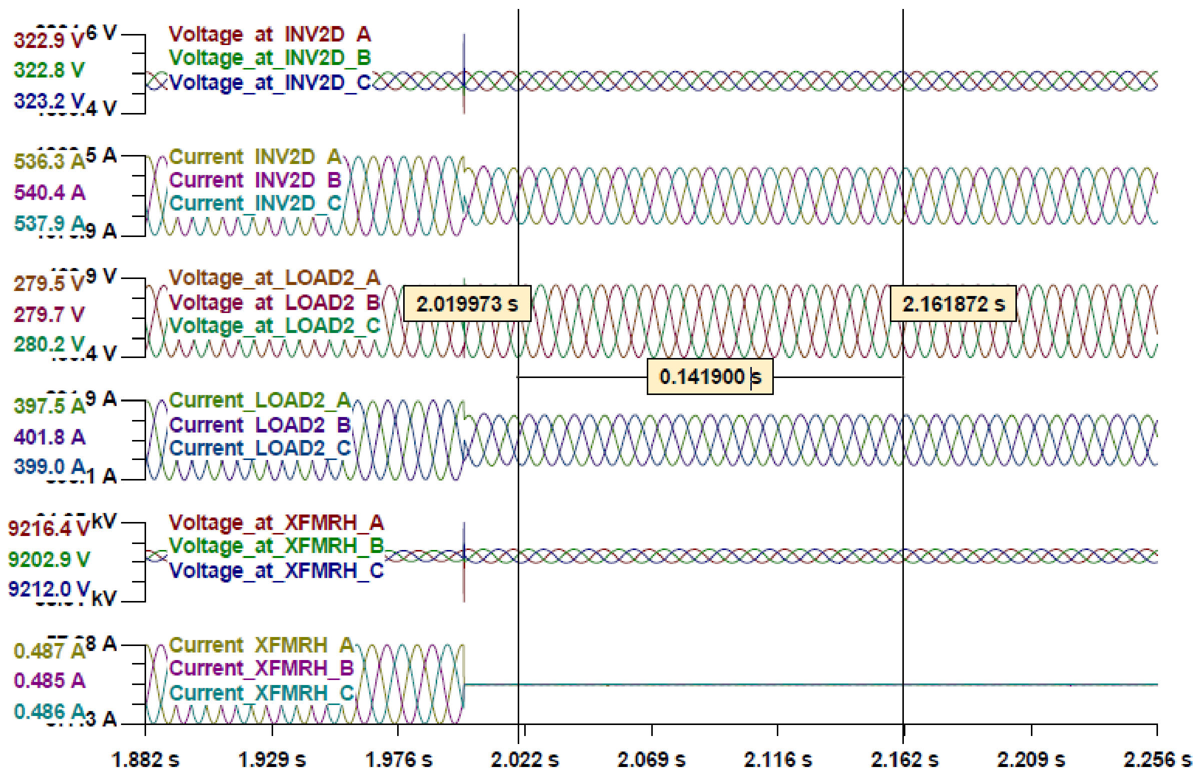

Figure 5-3. Selected Waveforms of Use Case 1 with High Induction Motor Output Power

Similarly, Figure 5-4 shows the detailed view of selected waveforms measured from 1.857 seconds to 2.277 seconds of the simulation with low induction motor load output, where the disconnection of the synchronous generator occurred at 2 seconds. The same groups of waveforms are presented in Figure 5-3 and Figure 5-4.

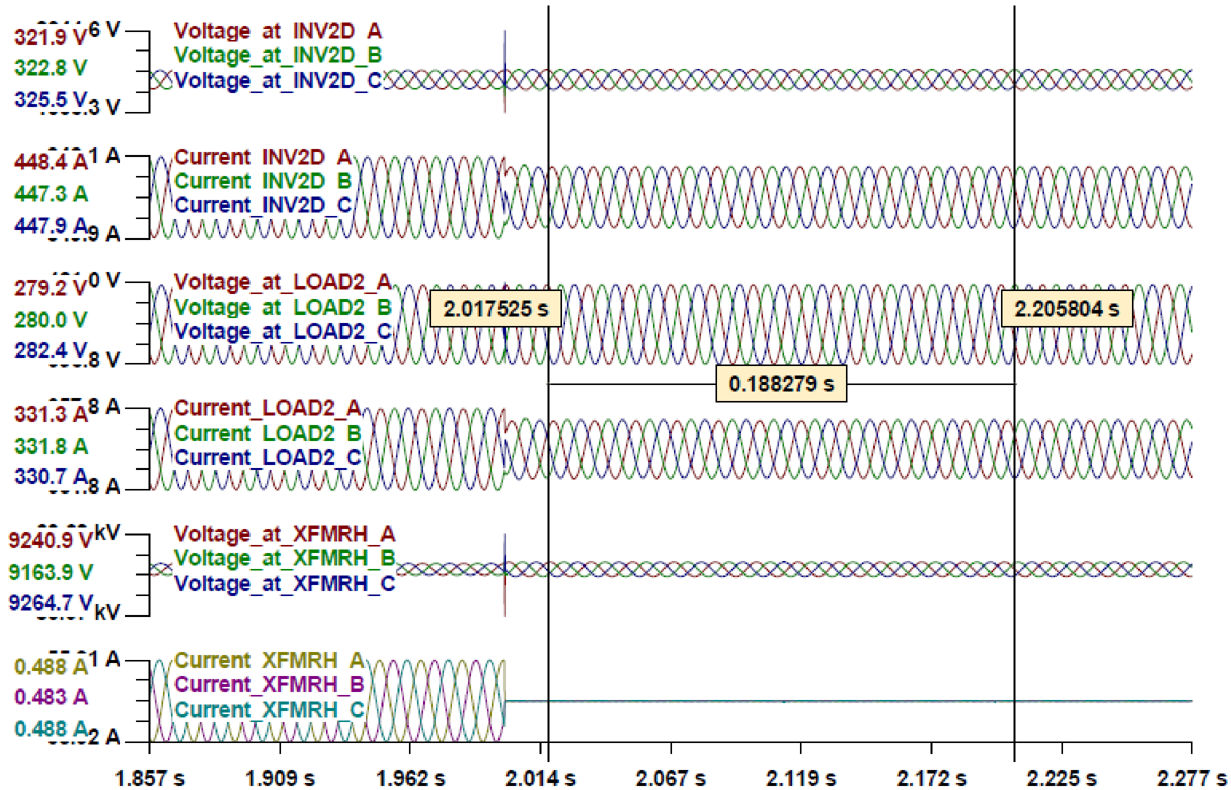

Figure 5-4. Selected Waveforms of Use Case 1 with Low Induction Motor Output Power

Figure 5-5 and Figure 5-6 present the phasor plot generated from Figure 5-3 and Figure 5-4, respectively. Figure 5-5 shows the detailed view of selected phasor plots from 1.733 seconds to 2.423 seconds of the simulation. Figure 5-18 shows the detailed view of selected phasor plots from 1.847 seconds to 2.268 seconds of the simulation.

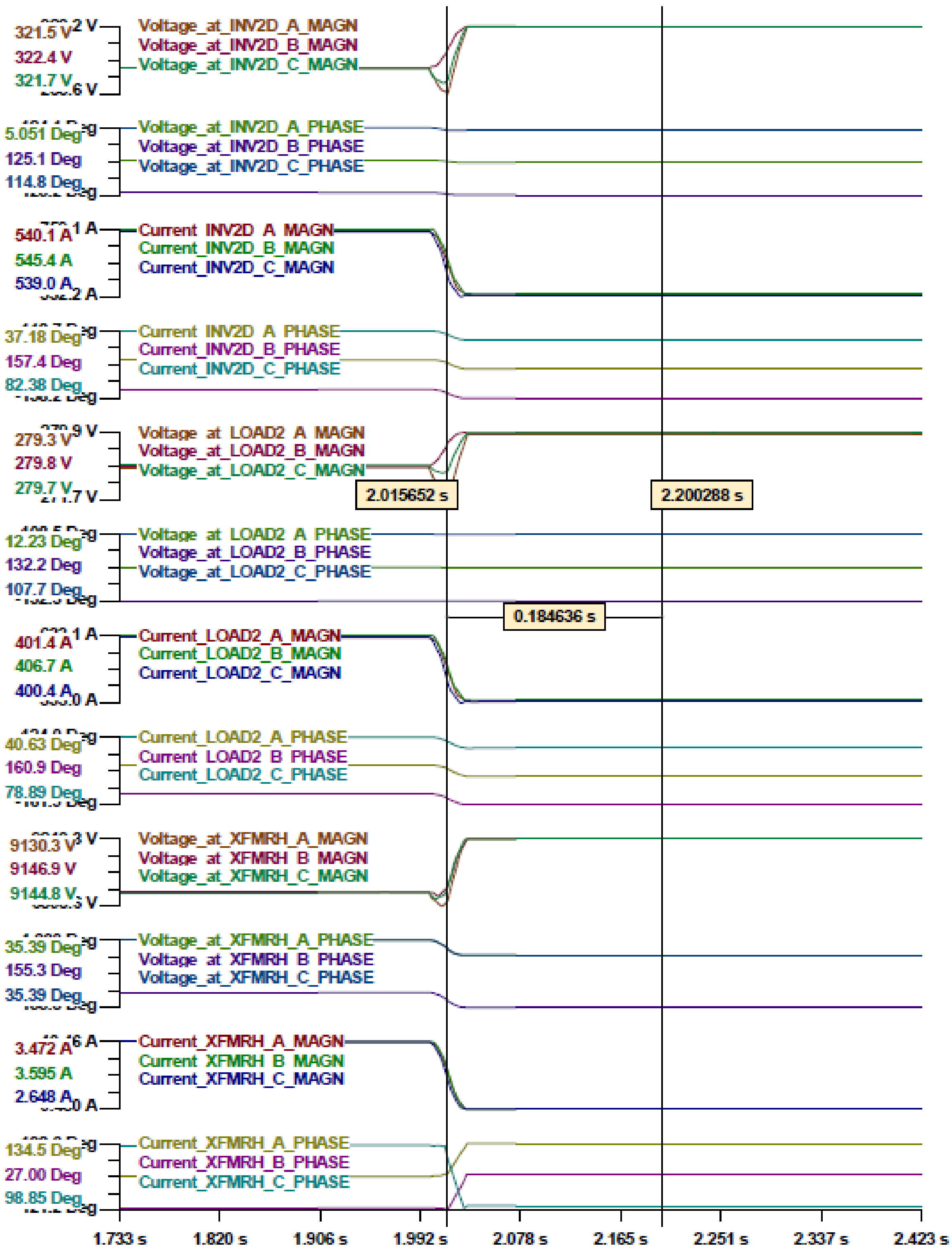

Figure 5-5. Phasor Plot of Selected Channels of Use Case 1 with High Induction Motor Output Power

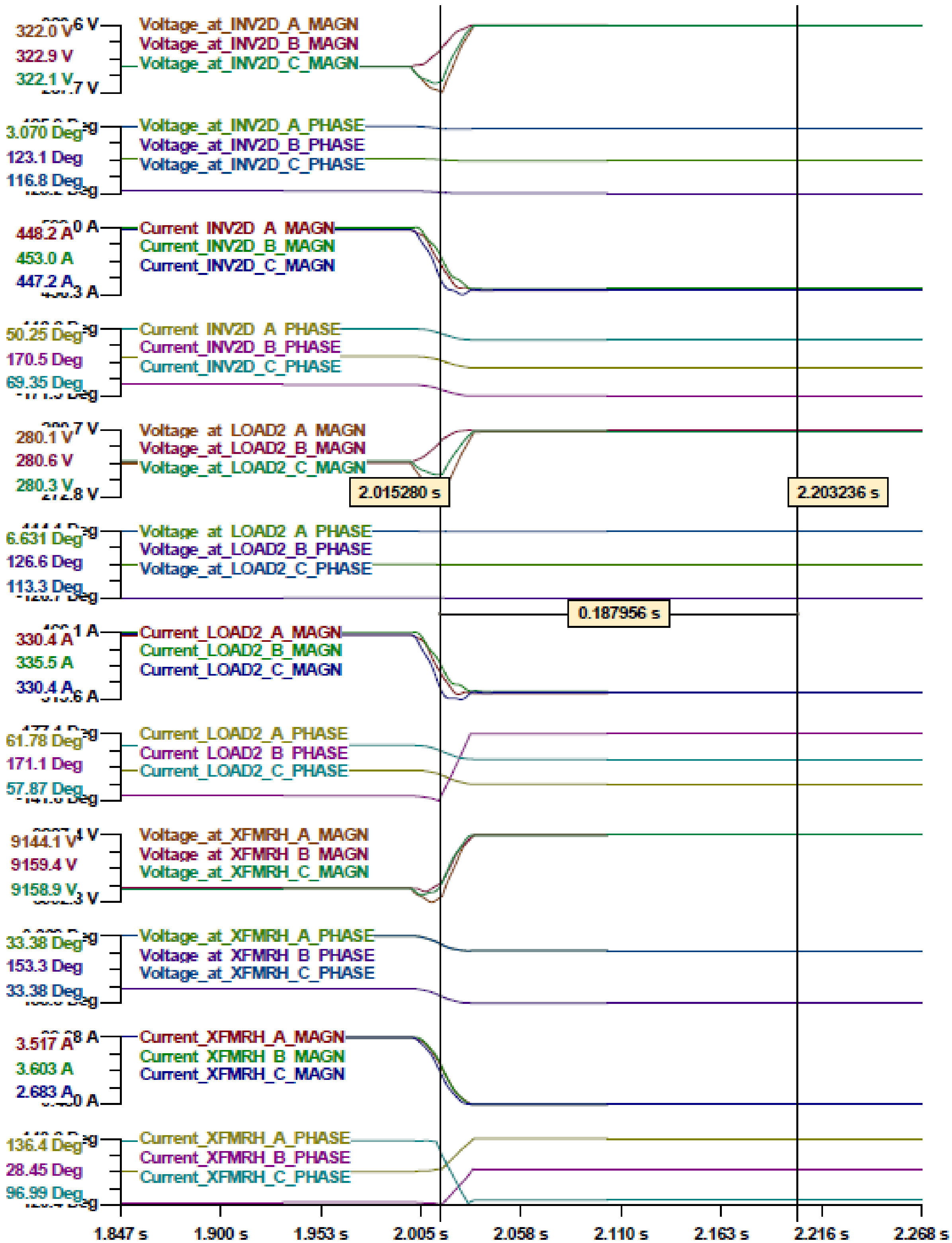

Figure 5-6. Phasor Plot of Selected Channels of Use Case 1 with Low Induction Motor Output Power

From the figures shown above, the voltage at the load remained stable during the loss of the synchronous generator. However, a 10% drop in the magnitude of the current at induction motor-based load can be observed. This is caused by the limitation of the BESS power setting used in this simulation (0.5 MW). The load currents remained in the normal range and the motor operated normally after the disconnection of the synchronous generator in both high and low output conditions. The phasor plots indicate good stability in voltage and current at the induction motor-based load during the transition around 2 seconds. No abrupt changes were observed during the transition from a hybrid power system to a 100% inverter-based system.

5.4 Simulation Results – Cold Start of Induction Motor-based Load.

This simulation studies the performance of the GFM inverter during the cold start of induction motor-based load in the example test system. The cold start of the load occurred at 2.5 seconds of the simulation, when the power system is purely supported by the GFM inverters. Waveforms and phasors of voltages and currents measured at different locations of the test system were collected during the simulation.

Figure 5-7 shows the detailed view of selected waveforms measured from 2.279 seconds to 2.894 seconds of the simulation with high induction motor load output. In Figure 5-19, 6 selected groups of waveforms are presented. The first two groups of waveforms are the three-phase voltage and three-phase current waveforms measured at bus POI in Figure 5-1. The third and fourth group of waveforms display the three-phase voltage and three-phase current waveforms measured at the bus ACBUS in Figure 5-1. The fifth and sixth group of waveforms are the three-phase voltage and three-phase current waveforms measured at the induction motor-based load.

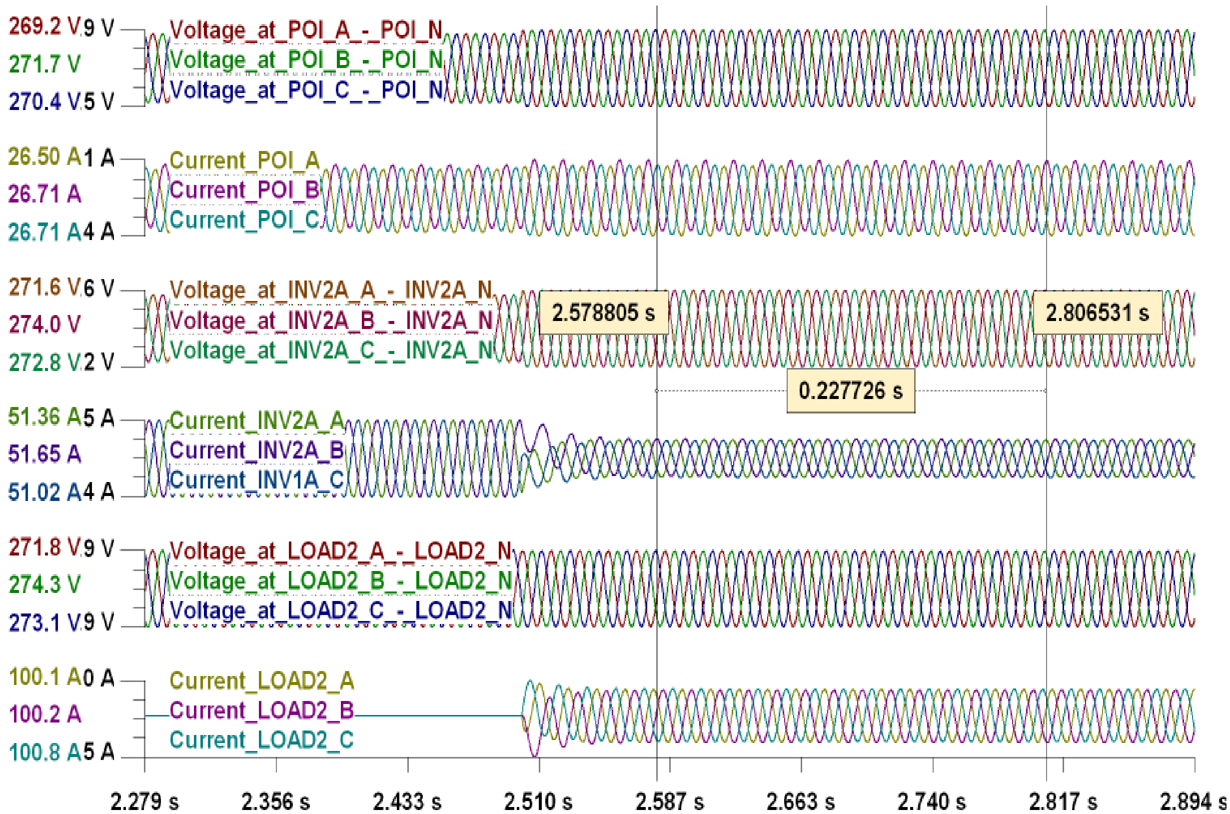

Figure 5-7. Selected Waveforms of Use Case 2 with High Induction Motor Output Power

Figure 5-8 shows the detailed view of selected waveforms measured from 2.264 seconds to 2.921 seconds of the simulation with low induction motor load output, where the cold start of the induction motor-based load occurs at 2.5 seconds. The same groups of waveforms are presented in Figure 5-7 and Figure 5-8.

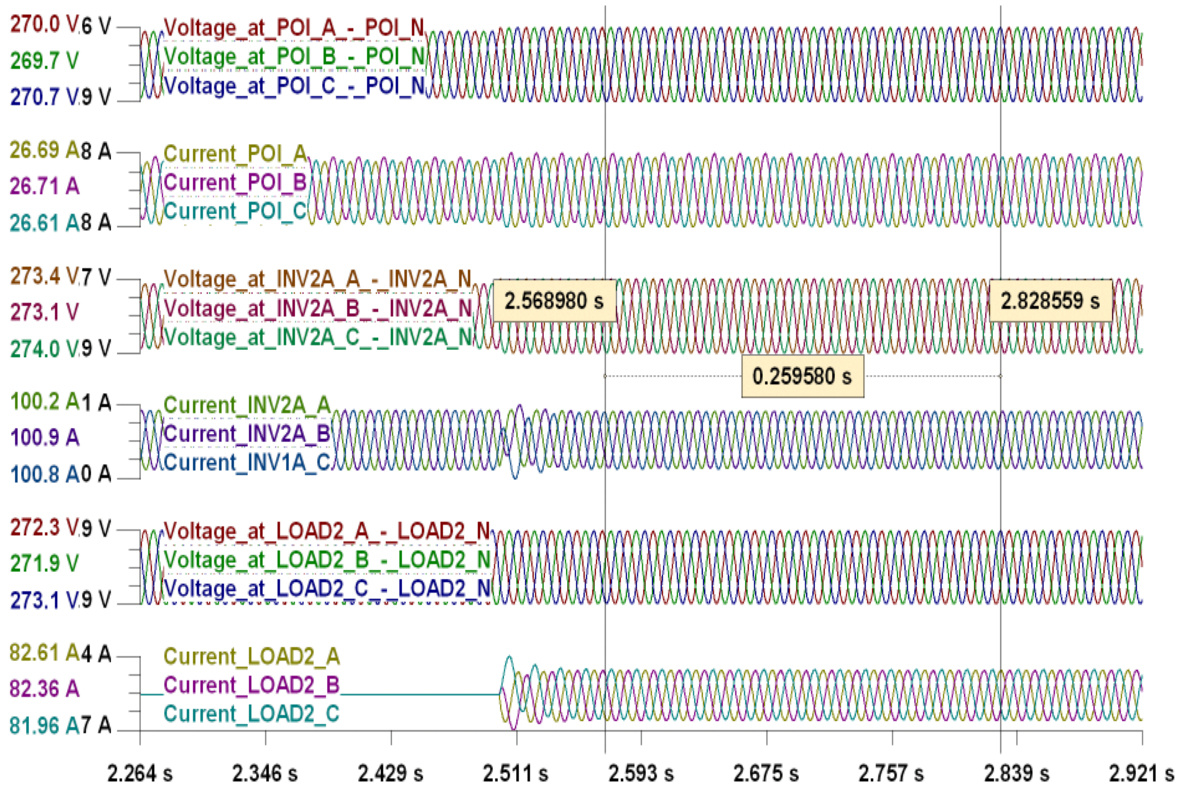

Figure 5-8. Selected Waveforms of Use Case 2 with Low Induction Motor Output Power

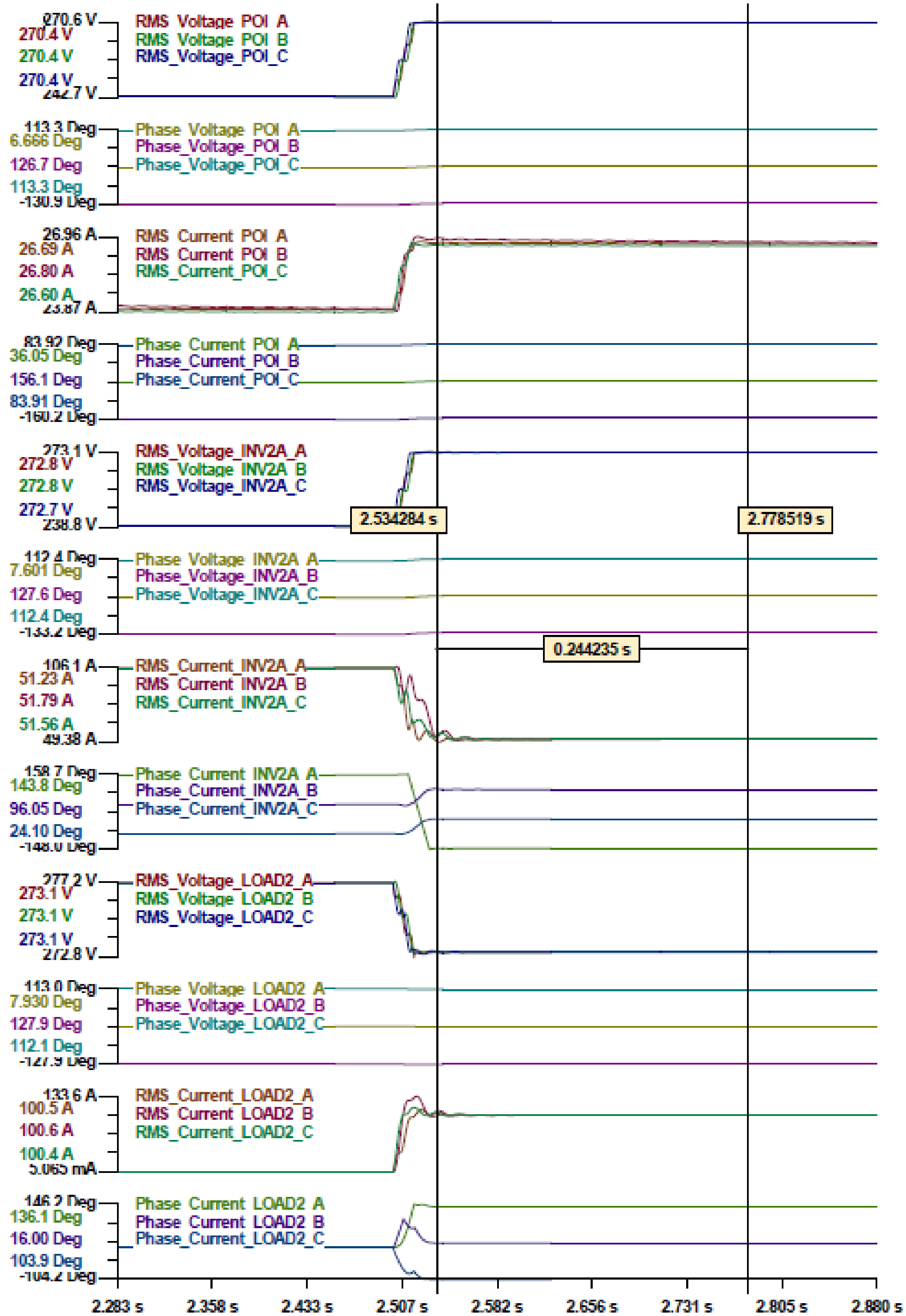

Figure 5-9. Phasor Plot of Selected Channels of Use Case 2 with High Induction Motor Output Power

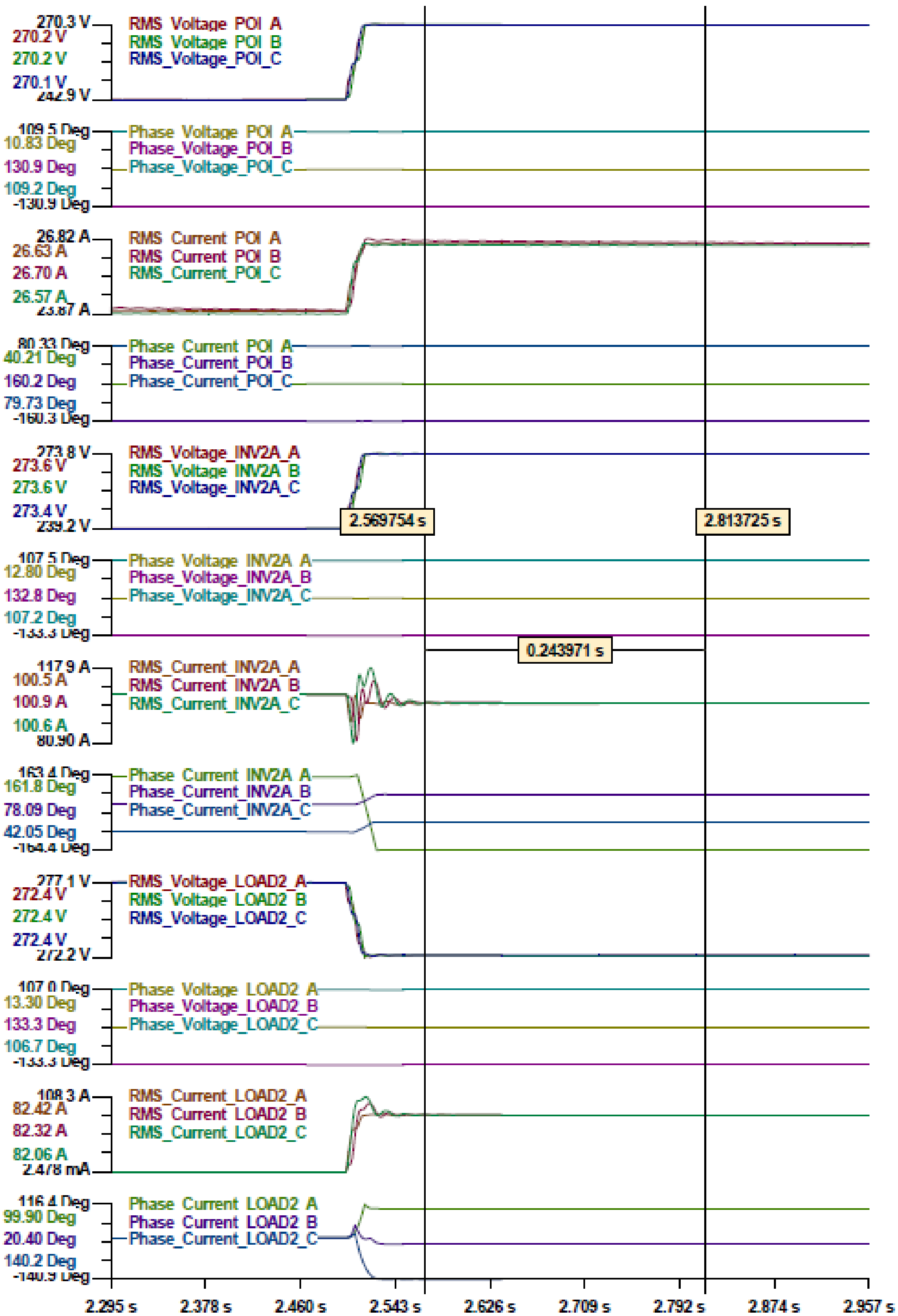

Figure 5-10. Phasor Plot of Selected Channels of Use Case 2 with Low Induction Motor Output Power

Figure 5-9 and Figure 5-10 present the phasor plot generated from Figure 5-7 and Figure 5-8, respectively. Figure 5-9 shows the detailed view of selected phasor plots from 2.283 seconds to 2.880 seconds of the simulation. Figure 5-10 shows the detailed view of selected phasor plots from 2.295 seconds to 2.957 seconds of the simulation.

As shown in the figures above, voltage at the load remained stable at around 273 V during the cold start of the induction motor. The RMS value of the current at the load increased from zero to around 100 A and 82 A respectively for the high and low induction motor output. From the phasor plots, the transients and inrush currents during the cold start of the induction motor-based load were contained well with the proposed control strategy. This proves the capability of the GFM inverter in providing support to the power system during cold start.

6. Comparison of GFM Inverter Performance to PSCAD Models

To validate the results of the quadratized model software in the previous section, an identical test system was built in PSCAD. The model development process in PSCAD is introduced in section 6.1.

6.1 Test System Development in PSCAD

Figure 6-1 shows the test system developed in PSCAD, which is identical to the test system shown in Figure 5-13. The system consists of two major parts, (1) the legacy AC system includes a synchronous generator, two transformers and a transmission line; and (2) 100% IBR system that includes 2 GFM inverters, a BESS and an induction motor-based load. Breakers were placed in the test system to disconnect the legacy AC system from the 100% IBR system. Details about the parameters in the test system can be found in Appendix D.

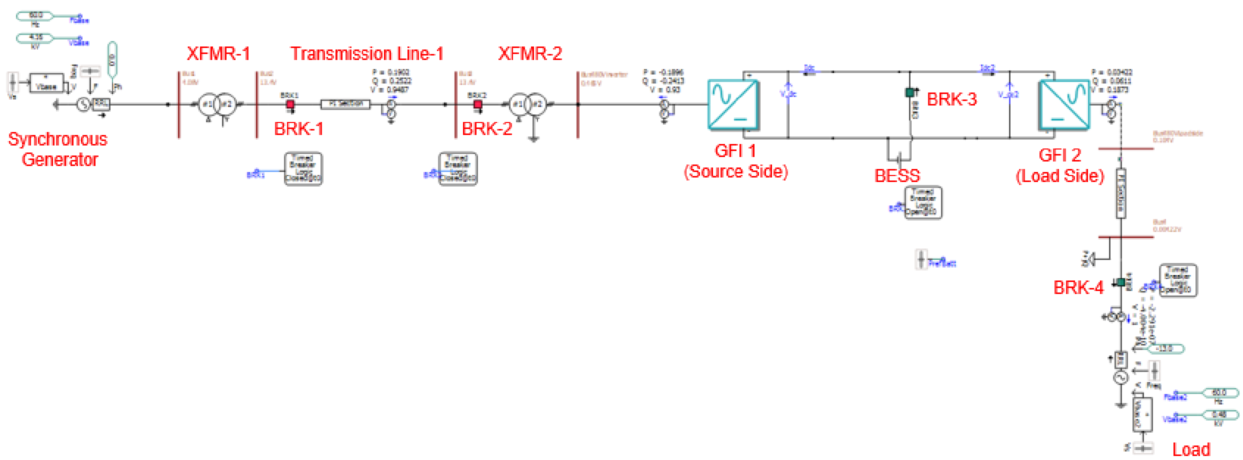

Figure 6-1. Example Test System in PSCAD

Instead of using existing inverter models in PSCAD, self-defined models of GFM inverters were used in this model. The VSC model in PSCAD is shown in Figure 6-2. As shown in Figure 6-2, the valves in the VSC model consist of IGBTs and diode. The IGBTs have the snubber circuit enabled. In the PSCAD model, the current limiter was not added to the valve. Other than the difference in valve design, the overall VSC configuration in PSCAD is identical with the model in Appendix A.

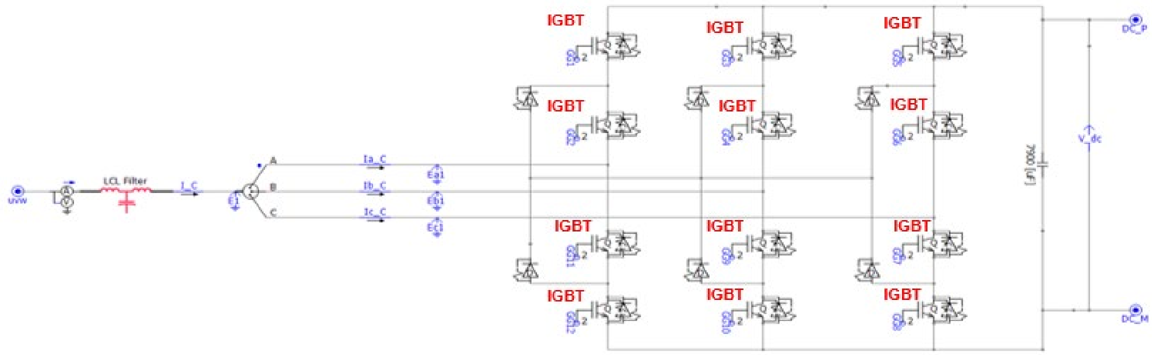

Figure 6-2. Voltage Source Converter (3-level) Model in PSCAD

The VSC controller model in PSCAD is presented in Figure 6-2, where the Q-Vdc control mode was implemented with a PI controller, which follows the same control diagram in Figure 4-10.

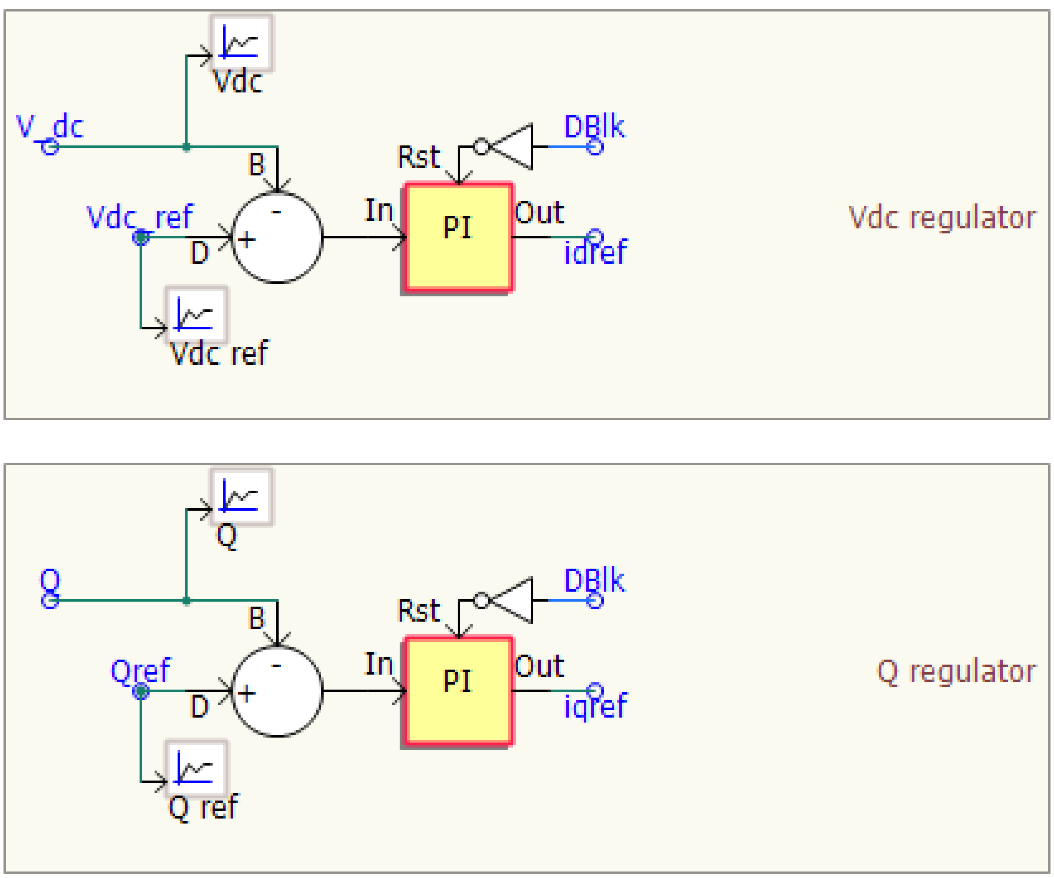

Figure 6-3. Control Diagram of the VSC Controller in PSCAD (Q-Vdc Mode)

A PWM model was also constructed in PSCAD to generate the firing sequences for the IGBTs in the VSC model. The PWM model is shown in Figure 6-4. A 5000 Hz carrier frequency was used in the PWM model.

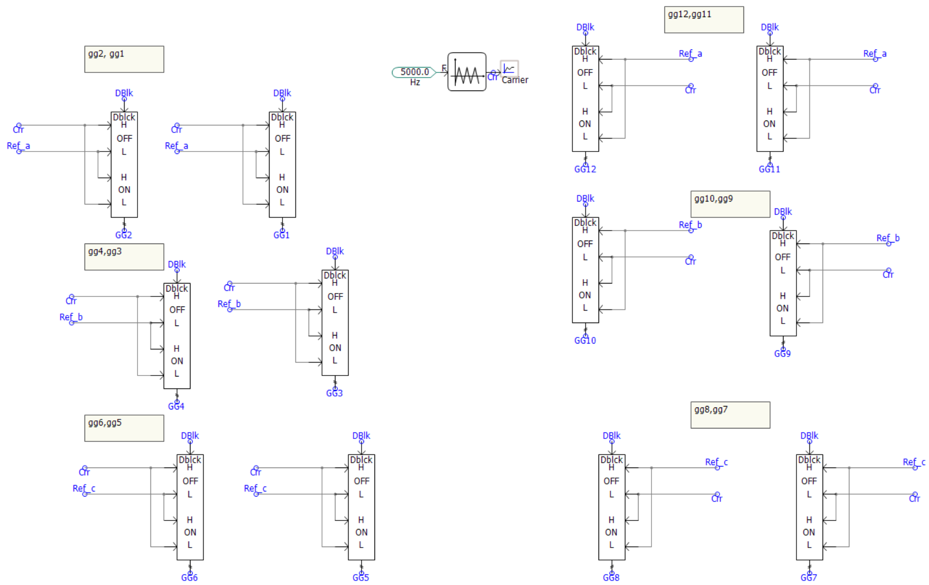

Figure 6-4. PWM Model of VSC in PSCAD

6.2 Performance Evaluation of GFM Inverter in PSCAD

In this section, the simulation results from the test system in PSCAD will be presented. Two use cases were tested in the PSCAD test system. The simulation results will be analyzed to evaluate the performance of the proposed GFM Inverter control scheme and to verify the results with the model of Appendix A. The total simulation time is 5 seconds with a step of 50 microseconds.

Figure 6-5 and Figure 6-6 present the voltage and current waveforms measured at load and low-side of transformer XFMR-2 in the test system. In use case 1, the synchronous generator disconnects at 2.0 seconds of the simulation. The following figures show the detailed view of selected waveforms measured from 1.80 seconds to 2.20 seconds of the simulation.

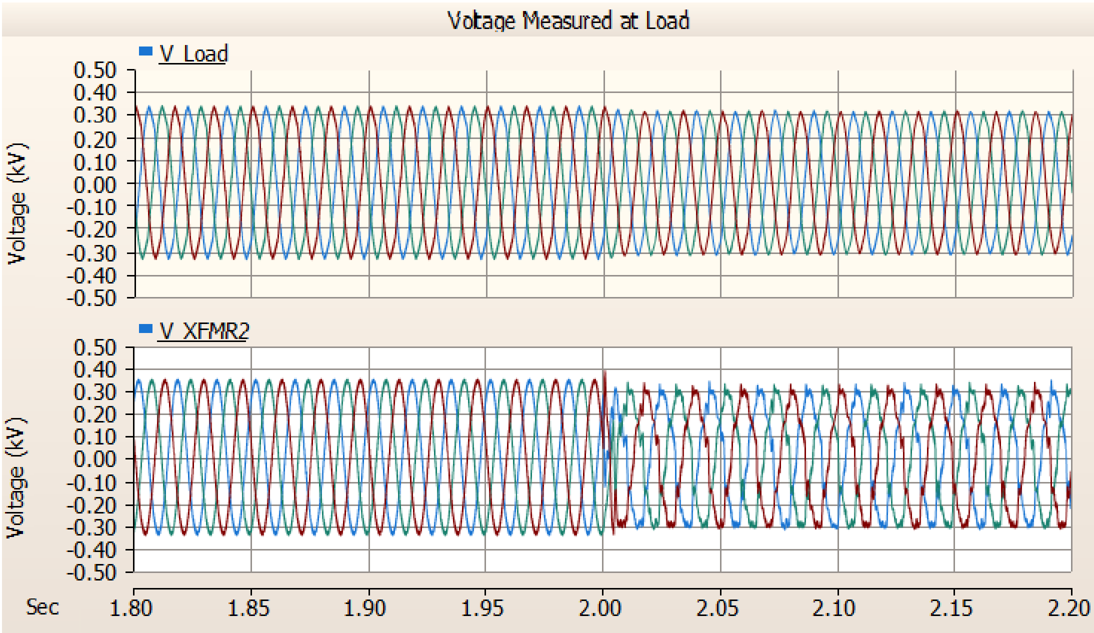

Figure 6-5. Voltage Waveforms measured at Load and XFMR 2 in Use Case 1

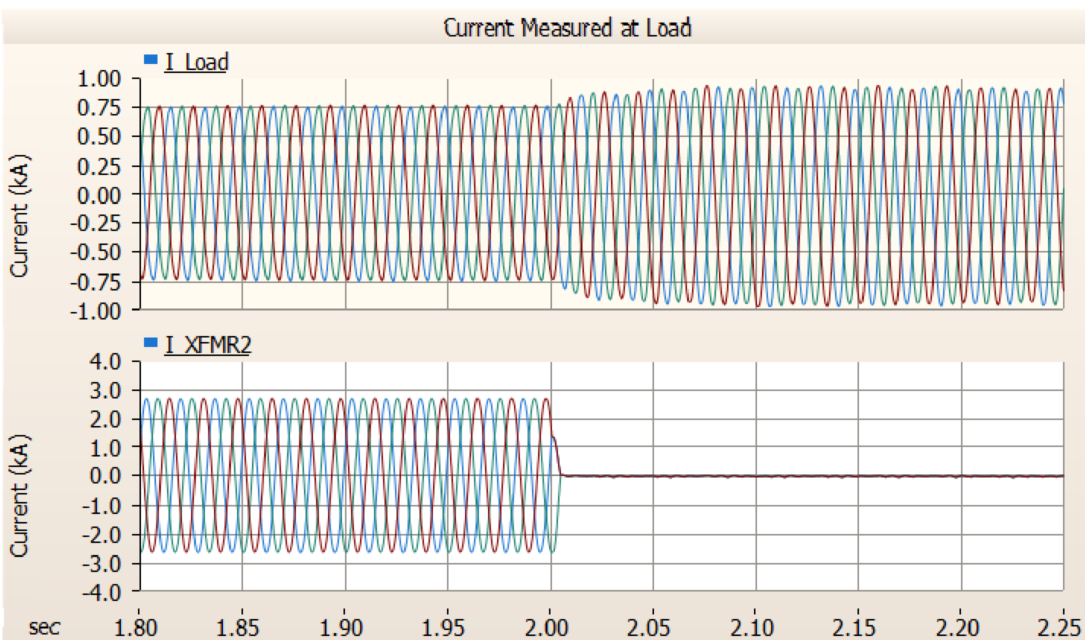

Figure 6-6. Current Waveforms measured at Load and XFMR 2 in Use Case 1

As shown in the above figures, the voltage at load remains stable after the loss of synchronous generator. However, a 10% increase in current was observed after 2 seconds of the simulation. From the current measured at the low side of transformer XFMR-2, we can confirm the disconnection of the legacy AC system after 2 seconds. From the PSCAD simulation results for use case 1, the proposed GFM inverter control scheme can support the normal operation of induction motor-based load in a 100% IBR system.

In use case 2, we studied the GFM inverter performance in cold start of the load at 2.5 seconds. Figure 6-7 below shows the detailed view of selected voltage waveforms measured from 2.375 seconds to 2.625 seconds of the simulation. Figure 6-8 shows the detailed view of selected current waveforms measured from 2.425 seconds to 2.650 seconds of the simulation. During the cold start, a drop in load voltage was observed between 2.500 to 2.525 seconds. After 2.525 seconds, the RMS value of the load voltage remained stable at about 212 V. In the load current waveform, we can see the load current stabilized from the in-rush current of the cold start after 2.525 seconds. The PSCAD simulation result for use case 2 proves the cold start capabilities of the proposed control scheme in a 100% IBR system.

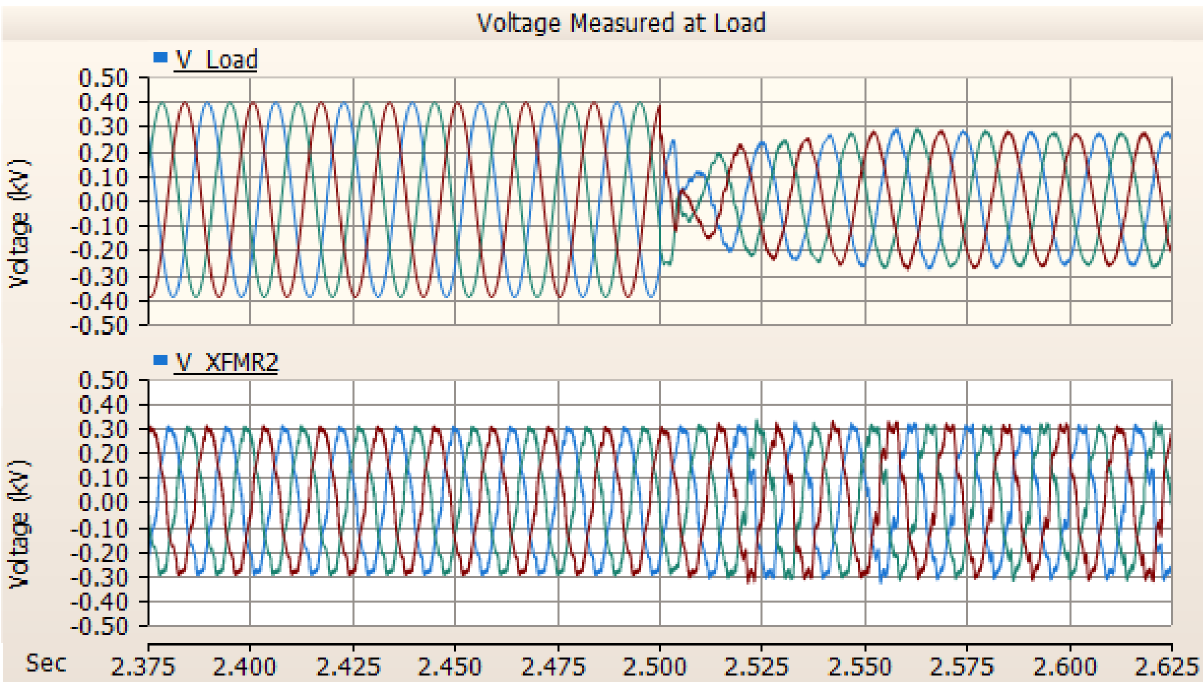

Figure 6-7. Voltage Waveforms measured at Load and XFMR 2 in Use Case 2

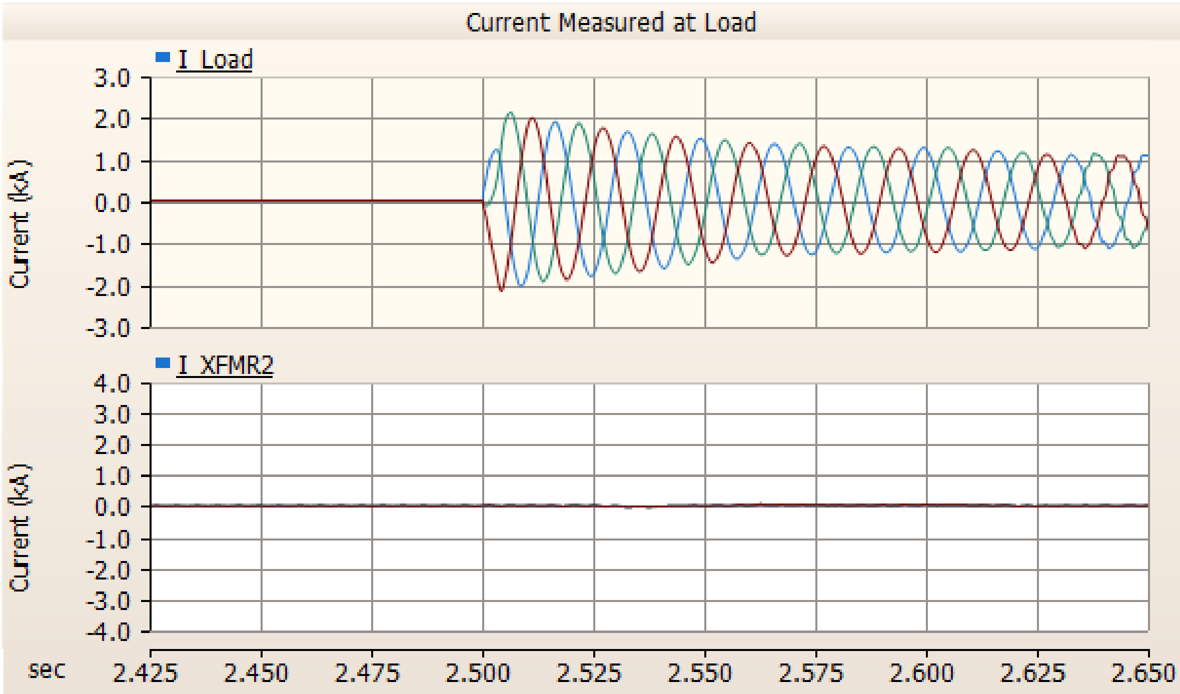

Figure 6-8. Current Waveforms measured at Load and XFMR 2 in Use Case 2

6.3 Comparison of the GFM Inverter Performance

Comparing the simulation results of use case 1 and 2 for the systems in Appendices A and B, we can conclude that the proposed GFM inverter control scheme can provide support for the 100% IBR system during loss of synchronous generator and cold start of induction motor. The differences between the load voltages and currents are caused by the differences in the two platforms and slight differences in modeling. (See Appendices A and B)

For comparison, the parameters of the key components in the test system are shown in Tables 6-1 and 6-2.

Table 6-1. Parameters of Legacy AC Section of Appendices A and B Test Systems

Device	Parameter	See Appendix A	See Appendix B
Synchronous Generator	Rated Voltage (L-L)	4.16 kV	4.16 kV
	Base Power	3.5 MVA	3.5 MVA
	Pos. Sequence Resistance	0.12821 Ohms	0.12820 Ohms
	Pos. Sequence Reactance	1.2821 Ohms	1.2820 Ohms

	Zero. Sequence Resistance	0.041286 Ohms	0.17364 Ohms (Fixed)
	Zero. Sequence Reactance	0.41286 Ohms	0.9848 Ohms (Fixed)
Transformer 1	Rating	3.5 MVA	3.5 MVA
	Side 1 Voltage	4.16 kV (Delta)	4.16 kV (Delta)
	Side 2 Voltage	13.8 kV (Wye)	13.8 kV (Wye)
	Pos. Seq Leakage Reactance	0.1 pu	0.1 pu
	Copper Loss	0.005 pu	0.005 pu
	Eddy Current Loss	0.005 pu	0.005 pu
Transmission Line	Length	2.5 mi	4 km
	Pos. Sequence Resistance	0.292 Ohms	0.73E-4 Ohm/m
	Pos. Sequence Inductive Reactance	1.384 Ohms	0.346E-3 Ohm/m
	Pos. Sequence Capacitive Reactance	103102.2 Ohms	412.408E6 Ohm*m
	Zero. Sequence Resistance	1.408 Ohms	3.52E-4 Ohm/m
	Zero. Sequence Inductive Reactance	7.131 Ohms	1.7E-3 Ohm/m
	Zero. Sequence Capacitive Reactance	282197.9 Ohms	1128.788E6 Ohm*m
Transformer 2	Rating	2.0 MVA	2.0 MVA
	Side 1 Voltage	13.8 kV (Delta)	13.8 kV (Delta)
	Side 2 Voltage	0.48 kV (Wye)	0.48 kV (Wye)
	Pos. Seq Leakage Reactance	0.1 pu	0.1 pu
	Copper Loss	0.005 pu	0.005 pu
	Eddy Current Loss	0.005 pu	0.005 pu

Table 6-2. Parameters of 100% IBR Section of Appendices A and B Test Systems

Device	Parameter	See Appendix A	See Appendix B

Inverter 1	Rated Voltage (AC Side)	0.48 kV	0.48 kV
	Rated Voltage (DC Side)	0.6 kV	0.6 kV
	Rated Power	2.0 MVA	2.0 MVA
	DC Link Capacitance	50 uF	50 uF
	Control Parameter K_p_Q	0.5	0.5
	Control Parameter K_i_Q	0.02	0.02
	Control Parameter K_p_V_{dc}	0.35	0.35
	Control Parameter K_i_V_{dc}	0.03	0.03
Inverter 2	Rated Voltage (AC Side)	0.48 kV	0.48 kV
	Rated Voltage (DC Side)	0.6 kV	0.6 kV
	Rated Power	2.5 MVA	2.5 MVA
	DC Link Capacitance	50 uF	50 uF
	Control Parameter K_p_Q	0.5	0.5
	Control Parameter K_i_Q	0.08	0.08
	Control Parameter K_p_V_{dc}	0.4	0.4
	Control Parameter K_i_V_{dc}	0.02	0.02
Battery	Nominal Voltage	0.6 kV	0.6 kV
	Rated Capacity	1 kA*hr	1 kA*hr
Load	Real Power	0.5 MVA	0.5 MVA
	Reactive Power	0.15 MVAr	0.15 MVAr
	Rated Voltage	0.48 kV	0.48 kV

Figure 6-9 below shows the comparison of the results measured at Load 2 of the test system in use case 1. The RMS value of voltages measured at the load are 21% higher in the model of Appendix A compared to the voltages measured in the model of Appendix B after the loss of the synchronous generator. The RMS value of the currents measured at the load are 35% higher in the model of

Appendix B compared to the currents measured in the model of Appendix A after the loss of the synchronous generator. No harmonics or distortions were observed in the voltage and current waveforms in the model of Appendix B and in the model of Appendix A results for use case 1.

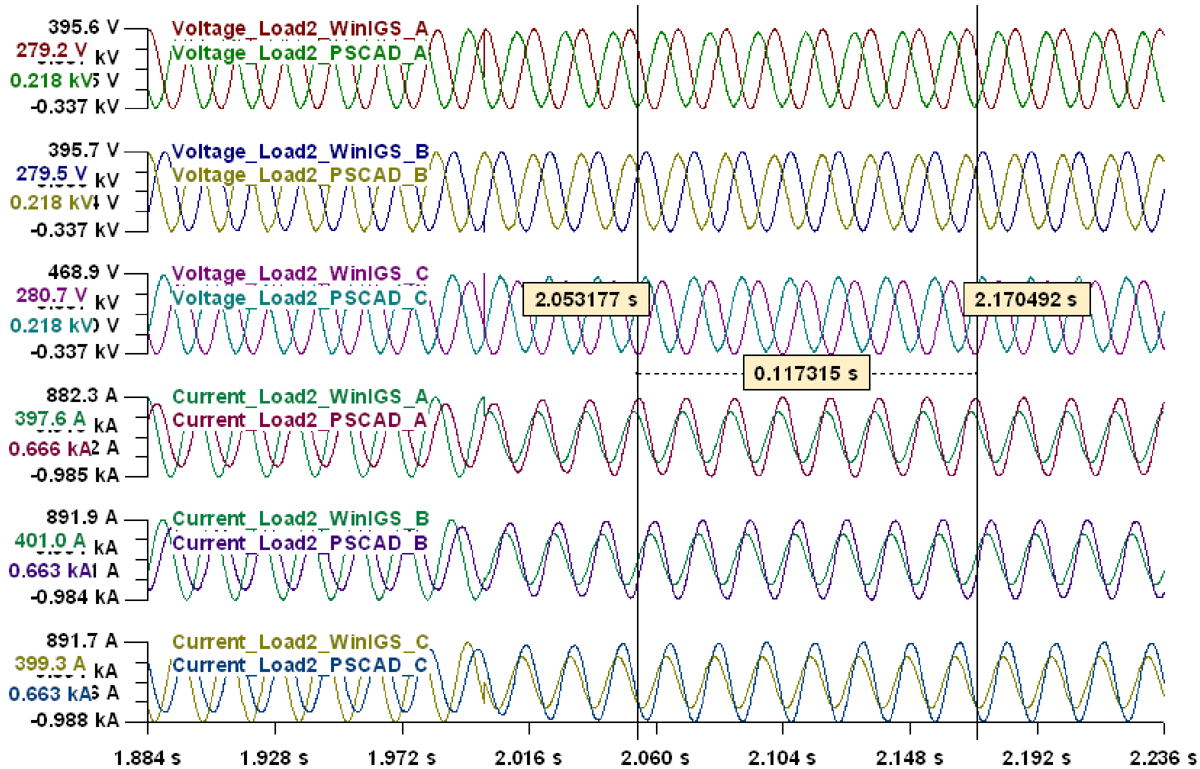

Figure 6-9. Comparison of Simulation Results at Load2 in Use Case 1

Figure 6-10 shows the comparison of the results measured at Load 2 of the test system in use case 2. The RMS value of the voltages measured at the load are 25% higher in the model of Appendix A compared to the voltages measured in the model of Appendix B after the cold start of the induction motor-based load. It is worth noticing that the RMS value of the currents measured at the load are significantly (800%) higher in the model of Appendix B compared to the currents measured in the model of Appendix A after the cold start of the induction motor-based load. Harmonics were also observed in the voltage and current waveforms in the model of Appendix B after the cold start of the load. The root cause of the differences between the simulation results of models of Appendices A and B still needs investigation.

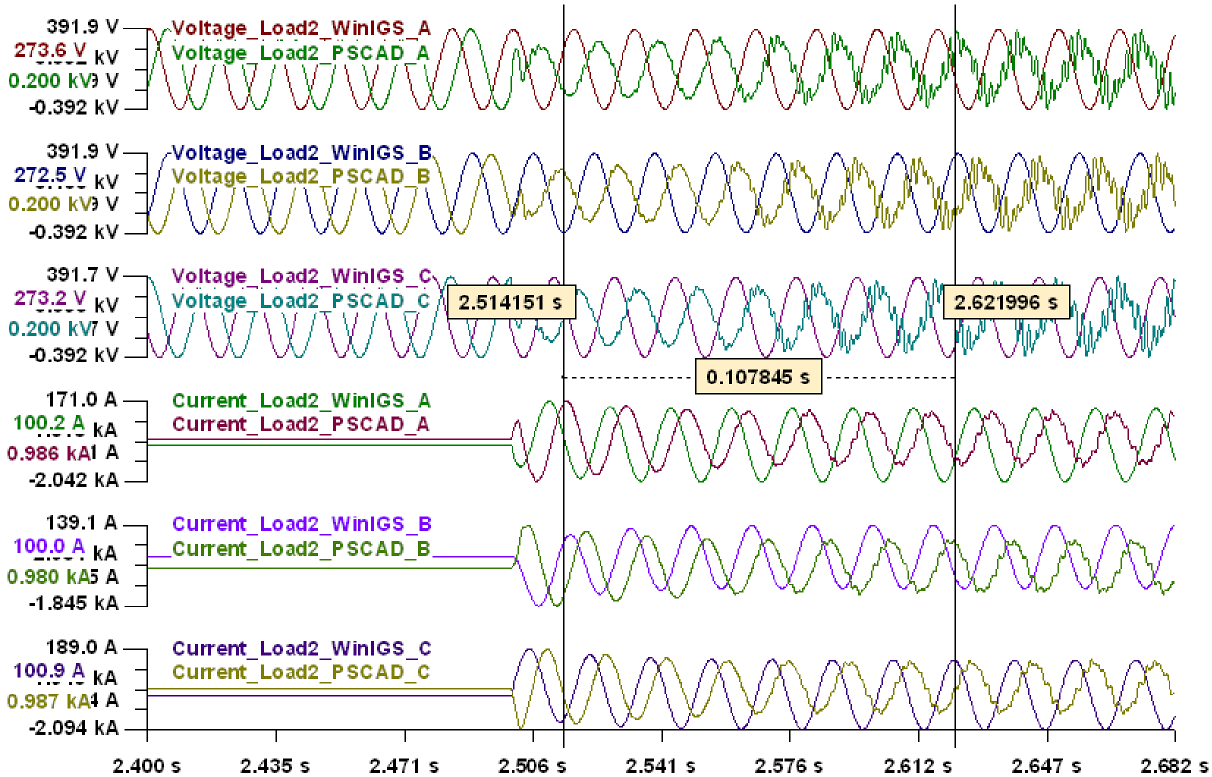

Figure 6-10. Comparison of Simulation Results at Load2 in Use Case 2

7. Conclusions and Future Work

In this project, we proposed a GFM inverter control scheme that enables 100% penetration of IBR in power system. Simulations were conducted to prove the effectiveness of the proposed controller design. In the model of Appendix A, we developed a GFM inverter model that contains three parts, VSC, DSP, and VSC controller. The digital VSC controller uses PI control. An example test system was constructed and presented in Appendix A to evaluate the performance of the GFM inverter in two use cases, (1) loss of synchronous generator and (2) cold start of induction motor-based load in a 100% IBR powered system. The simulation results showed that the proposed control scheme successfully sustained the transients and maintained the operation of the 100% IBR system after the loss of the synchronous generator and provided cold start capability to the 100% IBR system.

An identical test system was constructed and presented in Appendix B to validate the results from the model of Appendix A. The model in Appendix B has been developed for PSCAD so that the proposed models can be compared with PSCAD. The simulation results from the model of Appendix B matches the results from the model of Appendix A despite minor differences in the RMS value of the current and voltage at the load caused by the different parameter settings.

The future plans of this project will be (1) find the root cause of the differences between the described simulation results, i.e. between the proposed models and methods and the industry established PSCAD; (2) compare the proposed GFM inverter control methods with other control schemes from reports from other researchers; (3) build a larger and more complex test system and test the validity of the proposed method in complex test systems.

References

[1] T. Mai *et al.*, “Renewable Electricity Futures Study. Volume 1: Exploration of High-Penetration Renewable Electricity Futures,” *www.osti.gov*, Jun. 01, 2012. https://www.osti.gov/biblio/1046880 (accessed Aug. 27, 2023).

[2] S. Perera and S. Elphick, *Applied Power Quality*. Elsevier, 2022.

[3] N. G. Hingorani, “Power electronics in electric utilities: role of power electronics in future power systems,” *Proceedings of the IEEE*, vol. 76, no. 4, pp. 481–482, Apr. 1988, doi: https://doi.org/10.1109/5.4432.

[4] A. Monti, F. Milano, Ettore Bompard, and X. Guillaud, *Converter-Based Dynamics and Control of Modern Power Systems*. Academic Press, 2020.

[5] F. Blaabjerg and D. M. Ionel, “Renewable Energy Devices and Systems – State-of-the-Art Technology, Research and Development, Challenges and Future Trends,” *Electric Power Components and Systems*, vol. 43, no. 12, pp. 1319–1328, Jul. 2015, doi: https://doi.org/10.1080/15325008.2015.1062819.

[6] Y. Li, Y. Gu, and T. Green, “Revisiting Grid-Forming and Grid-Following Inverters: A Duality Theory,” *IEEE Transactions on Power Systems*, vol. 37, no. 6, pp. 1–1, 2022, doi: https://doi.org/10.1109/tpwrs.2022.3151851.

[7] G.-C. Hsieh and J. C. Hung, “Phase-locked loop techniques. A survey,” *IEEE Transactions on Industrial Electronics*, vol. 43, no. 6, pp. 609–615, Dec. 1996, doi: https://doi.org/10.1109/41.544547.

[8] X. Guo, W. Wu, and H-R. Gu, “Phase locked loop and synchronization methods for grid-interfaced converters: a review,” *Przegląd Elektrotechniczny*, vol. 87, no. 4, pp. 182–187, Jan. 2011.

[9] S. C. Gupta, “Phase-locked loops,” *Proceedings of the IEEE*, vol. 63, no. 2, pp. 291–306, 1975, doi: https://doi.org/10.1109/proc.1975.9735.

[10] G. A. Leonov, N. T. Kuznetsov, M. V. Yuldashev, and R. V. Yuldashev, “Hold-In, Pull-In, and Lock-In Ranges of PLL Circuits: Rigorous Mathematical Definitions and Limitations of Classical Theory,” *IEEE Transactions on Circuits and Systems I-regular Papers*, vol. 62, no. 10, pp. 2454–2464, May 2015, doi: https://doi.org/10.1109/tcsi.2015.2476295.

[11] Y. Lin *et al.*, “Research Roadmap on Grid-Forming Inverters,” *www.osti.gov*, Nov. 11, 2020. https://www.osti.gov/biblio/1721727

[12] R. Hamilton, “Analysis of Transformer Inrush Current and Comparison of Harmonic Restraint Methods in Transformer Protection,” *IEEE Transactions on Industry Applications*, vol. 49, no. 4, pp. 1890–1899, Jul. 2013, doi: https://doi.org/10.1109/tia.2013.2257155.

[13] M. C. Chandorkar, D. M. Divan, and R. Adapa, “Control of parallel connected inverters in standalone AC supply systems,” *IEEE Transactions on Industry Applications*, vol. 29, no. 1, pp. 136–143, 1993, doi: https://doi.org/10.1109/28.195899.

[14] Z. Lin and H. Ma, “Modeling and Analysis of Three-phase Inverter based on Generalized State Space Averaging Method,” in *39th Annual Conference of the IEEE Industrial Electronics Society*, Jan. 2014.

[15] O. Bassey and K. L. Butler-Purry, “Black Start Restoration of Islanded Droop-Controlled Microgrids,” *Energies*, vol. 13, no. 22, p. 5996, Nov. 2020, doi: https://doi.org/10.3390/en13225996.

[16] A. Alassi, K. Ahmed, A. Egea-Alvarez and O. Ellabban, "Performance Evaluation of Four Grid-Forming Control Techniques with Soft Black-Start Capabilities," *2020 9th International Conference on Renewable Energy Research and Application (ICRERA)*, Glasgow, UK, 2020, pp. 221-226, doi: 10.1109/ICRERA49962.2020.9242758.
[17] H. Zhang, W. Xiang, W. Lin, and J. Wen, "Grid Forming Converters in Renewable Energy Sources Dominated Power Grid: Control Strategy, Stability, Application, and Challenges," *Journal of Modern Power Systems and Clean Energy*, vol. 9, no. 6, pp. 1239–1256, 2021, doi: https://doi.org/10.35833/mpce.2021.000257.
[18] H. -P. Beck and R. Hesse, "Virtual synchronous machine," 2007 9th International Conference on Electrical Power Quality and Utilisation, Barcelona, Spain, 2007, pp. 1-6, doi: 10.1109/EPQU.2007.4424220
[19] Y. Chen, R. Hesse, D. Turschner, and H. P. Beck, "Dynamic properties of the virtual synchronous machine (VISMA)," *Renewable Energy and Power Quality Journal*, vol. 1, no. 9, pp. 755–759, May 2011, doi: https://doi.org/10.24084/repqj09.444.
[20] M. Torres and L. A. C. Lopes, "Virtual Synchronous Generator: A Control Strategy to Improve Dynamic Frequency Control in Autonomous Power Systems," *Energy and Power Engineering*, vol. 05, no. 02, pp. 32–38, 2013, doi: https://doi.org/10.4236/epe.2013.52a005.
[21] Y. Chen, R. Hesse, D. Turschner, and H.-P. Beck, "Comparison of methods for implementing virtual synchronous machine on inverters," *Renewable Energy and Power Quality Journal*, vol. 1, no. 10, pp. 734–739, Apr. 2012, doi: https://doi.org/10.24084/repqj10.453.
[22] L. Zhang, L. Harnefors, and H.-P. Nee, "Power-Synchronization Control of Grid-Connected Voltage-Source Converters," *IEEE Transactions on Power Systems*, vol. 25, no. 2, pp. 809–820, May 2010, doi: https://doi.org/10.1109/tpwrs.2009.2032231.
[23] L. Harnefors, M. Hinkkanen, U. Riaz, F. M. M. Rahman, and L. Zhang, "Robust Analytic Design of Power-Synchronization Control," *IEEE Transactions on Industrial Electronics*, vol. 66, no. 8, pp. 5810–5819, Aug. 2019, doi: https://doi.org/10.1109/TIE.2018.2874584.
[24] L. Zhang, H.-P. Nee, and L. Harnefors, "Analysis of Stability Limitations of a VSC-HVDC Link Using Power-Synchronization Control," *IEEE Transactions on Power Systems*, vol. 26, no. 3, pp. 1326–1337, Aug. 2011, doi: https://doi.org/10.1109/tpwrs.2010.2085052.
[25] Wei Yao, Jinyu Wen, Haibo He and Shijie Cheng, "Modeling and simulation of VSC-HVDC with dynamic phasors," 2008 Third International Conference on Electric Utility Deregulation and Restructuring and Power Technologies, Nanjing, 2008, pp. 1416-1421, doi: 10.1109/DRPT.2008.4523628.
[26] X. Jiang, J. H. Chow, A. -A. Edris, B. Fardanesh and E. Uzunovic, "Dynamic control modes of unified power flow controllers for transmission reinforcement," 2008 IEEE/PES Transmission and Distribution Conference and Exposition, Chicago, IL, USA, 2008, pp. 1-8, doi: 10.1109/TDC.2008.4517207.
[27] R. Pan, G. Tang, S. Liu and Z. He, "Impedance Analysis of Grid Forming Control Based Modular Multilevel Converters," in Journal of Modern Power Systems and Clean Energy, vol. 11, no. 3, pp. 967-979, May 2023, doi: 10.35833/MPCE.2021.000649.
[28] A. P. Meliopoulos, G. Cokkinides, and G. Stefopoulos, "Quadratic Integration Method," in *International Conference on Power Systems Transients*, Jun. 2005.

Appendix A: Example Test System Parameters – Quadratized Modeling

This section introduces the parameters settings used in the example test system using the quadratized modeling approach.

The legacy AC system consists of a synchronous generator, a transmission line, 2 transformers and 2 breakers. The parameters of the synchronous generator are shown in Figure A-1.

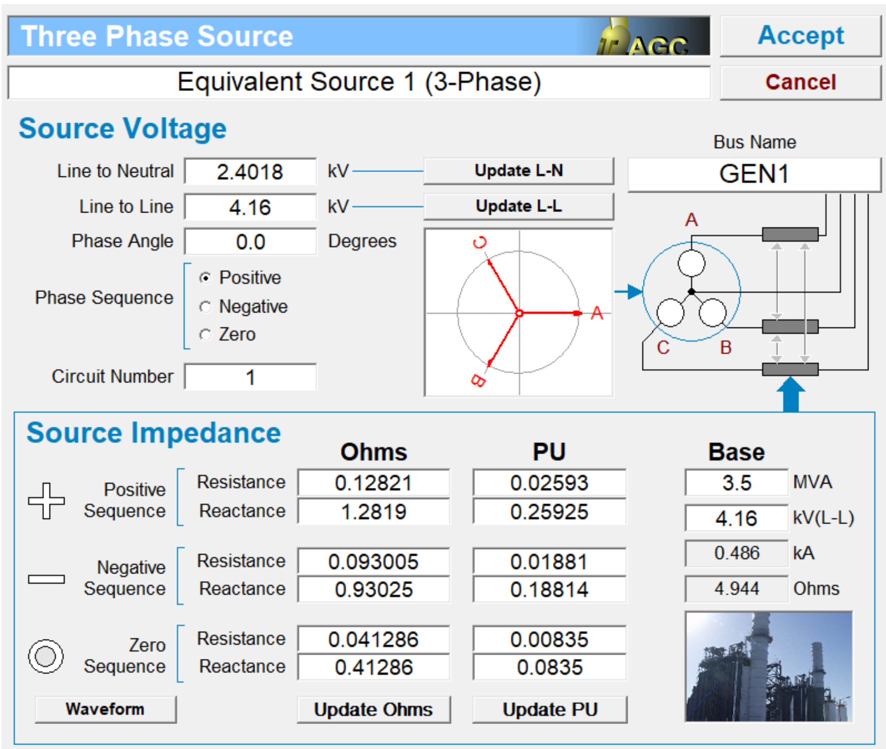

Figure A-1. Parameters of Synchronous Generator in Test System

The synchronous generator has a rated power of 3.5 MVA at a rated voltage of 4.16 kV (L-L). The positive sequence impedance is shown in Figure A-1. The parameters of transformer at the generator side are shown in Figure A-2, where the low side (delta) of the transformer is rated at 4.16 kV and the high side (wye) is rated at 13.8 kV. The transformer is rated at 3.5 MVA with winding resistance and leakage reactance of 0.01 and 0.1 p.u. respectively.

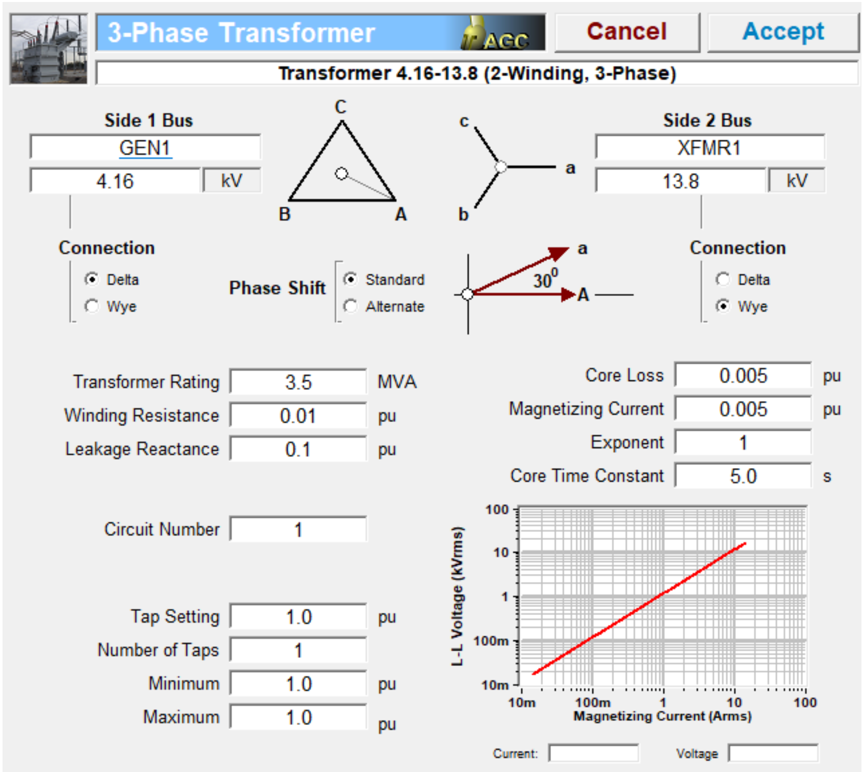

Figure A-2. Parameters of Transformer 1

The parameters of the transmission line in the test system are shown in Figure A-3. The conductor, shield and tower type are shown in the figure. The length of the transmission line is 2.5 miles.

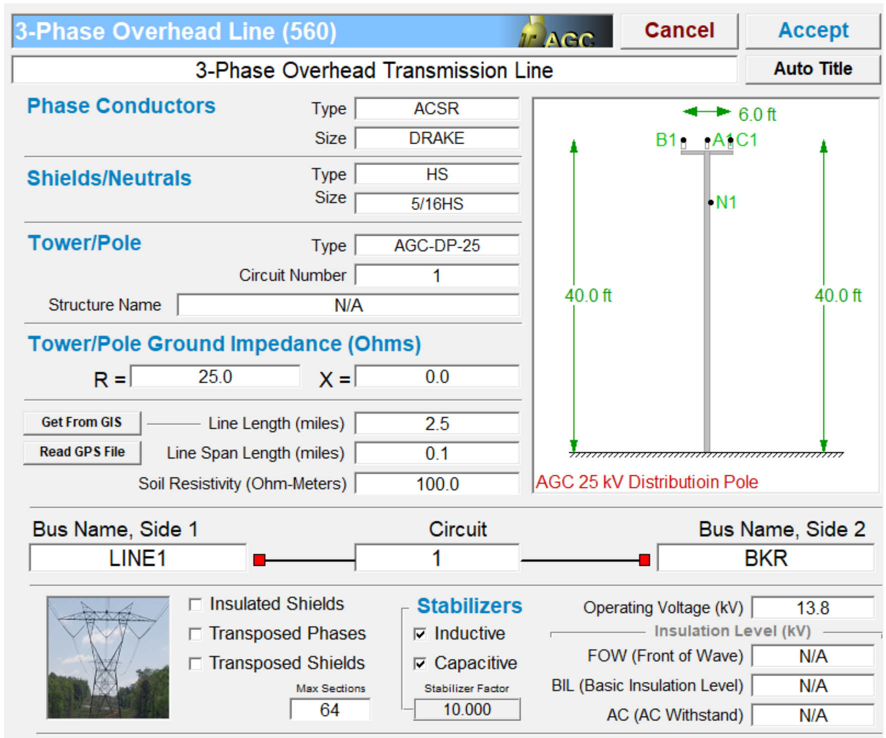

Figure A-3. Parameters of Transmission Line 1

The parameters of transformer 2 at the point of interaction are shown as follows. The high side (delta) of the transformer is rated at 13.8 kV and the low side (wye) is rated at 0.48 kV. The transformer has a power rating of 2 MVA with winding resistance and leakage reactance of 0.01 and 0.1 p.u. respectively.

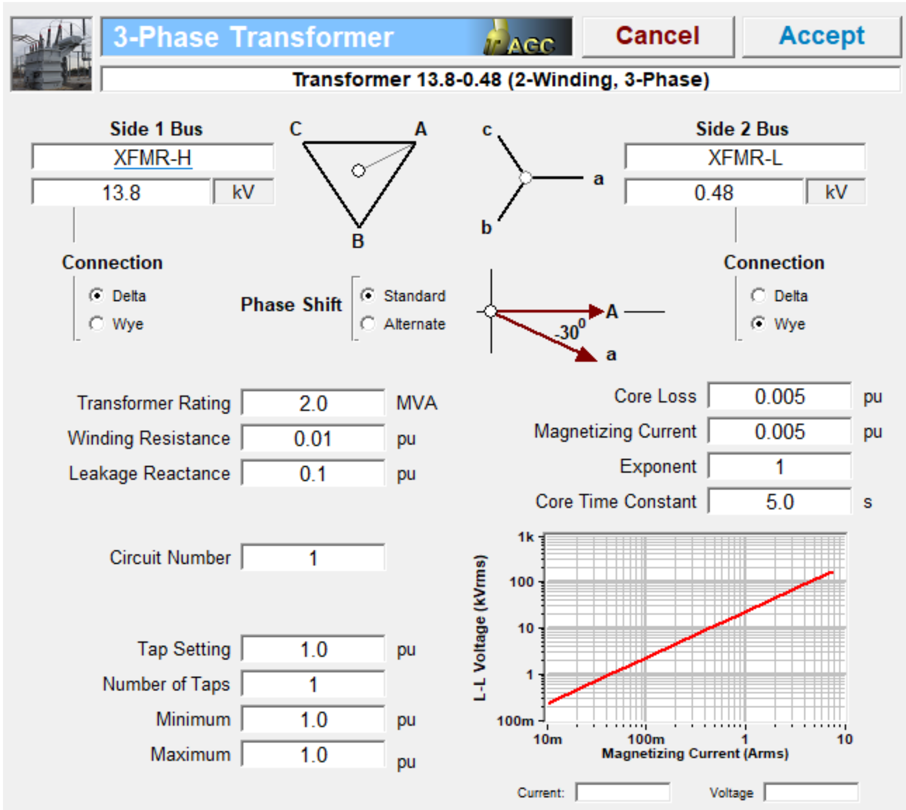

Figure A-4. Parameters of Transformer 2

The parameters of the components in the 100% IBR system are shown as follows. Figure A-5 and Figure A-6 show the parameters of VSC 1 and VSC 2 in the test system, respectively. The AC side of the VSC is rated at 0.48 kV and the DC side of the VSC is rated at 0.6 kV. Other parameters of the VSCs are shown in the figures.

The battery energy storage system (BESS) model in the test system is represented by a synchronous generator connected to a VSC. The battery has a rated power of 0.5 MW and a rated voltage of 0.48 kV. The model impedance was reduced to mimic the impedance of a BESS model. The VSC connected to BESS is rated at 0.48 kV on the AC side and 0.6 kV on the DC side. Detailed parameters of the BESS and VSC are shown in Figure A-7 and Figure A-8, respectively.

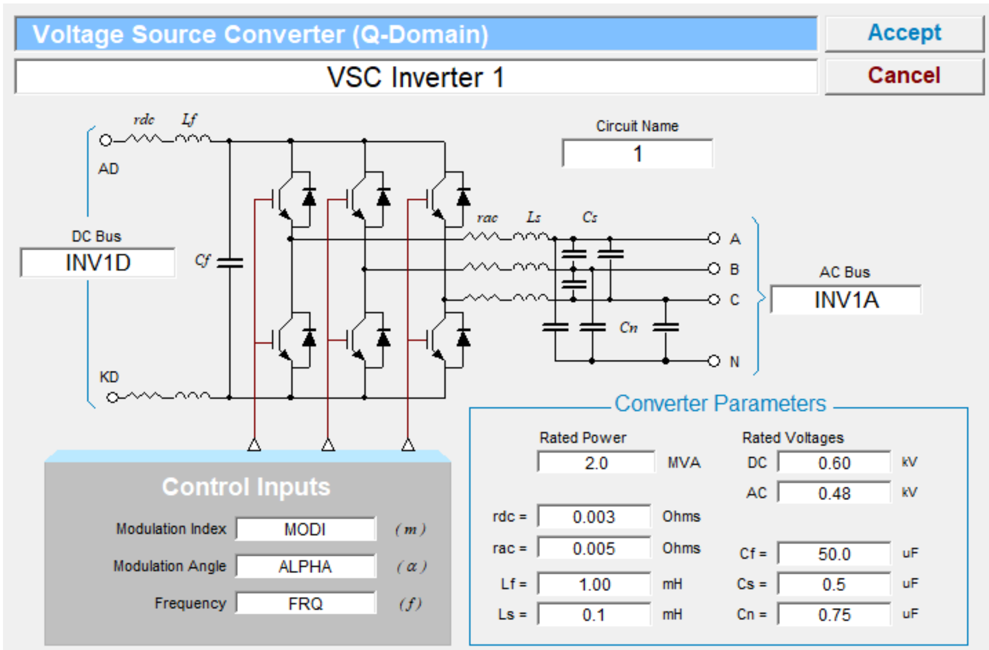

Figure A-5. Parameters of VSC 1

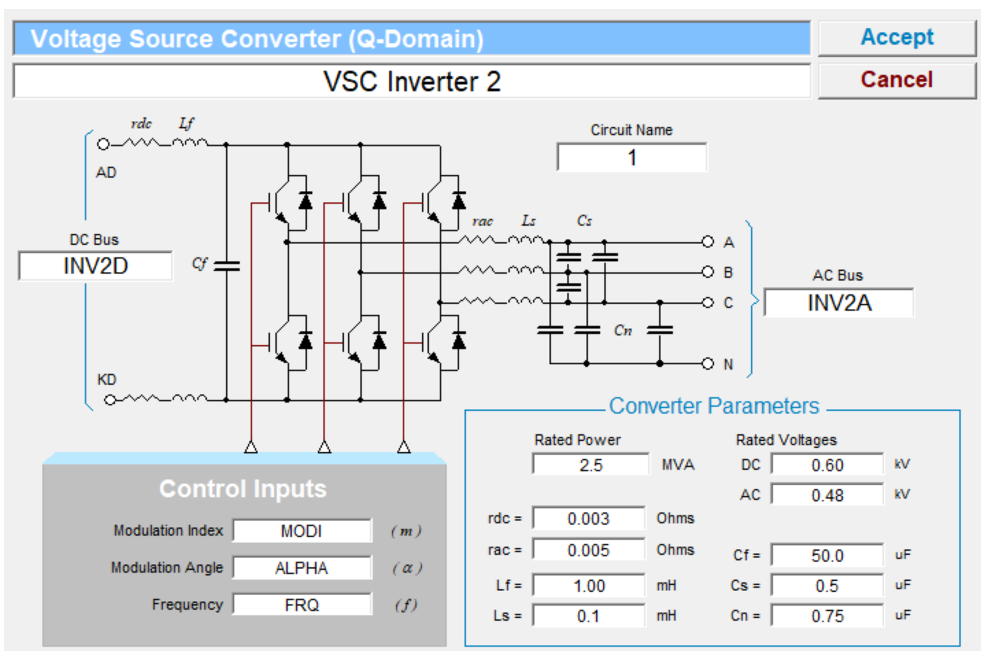

Figure A-6. Parameters of VSC 2

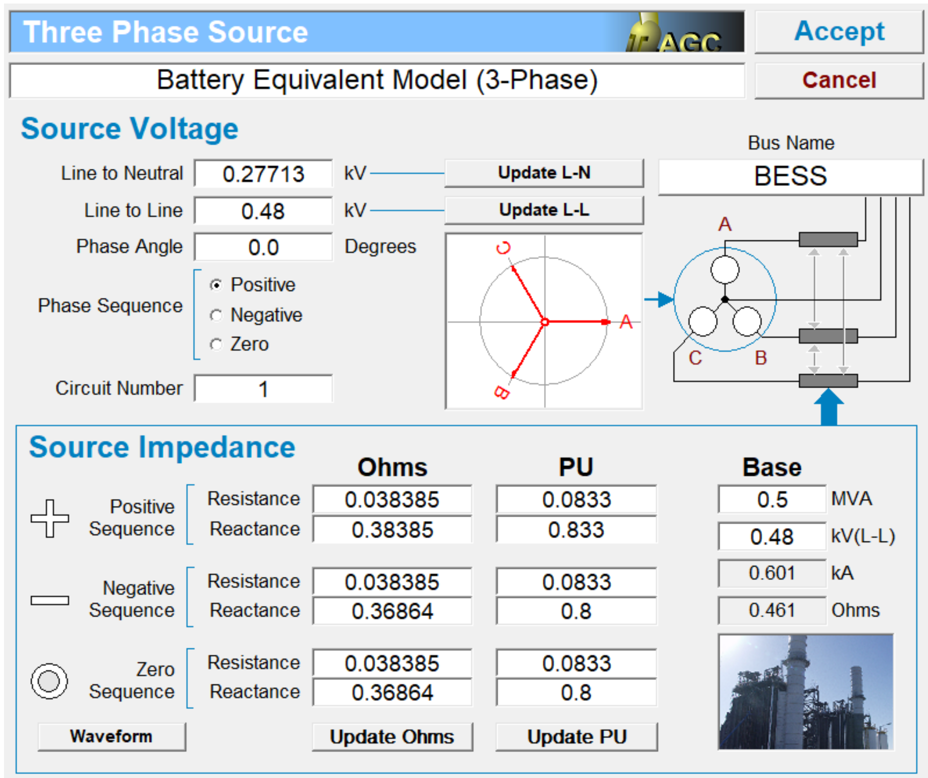

Figure A-7. Parameters of Approximated BESS Model

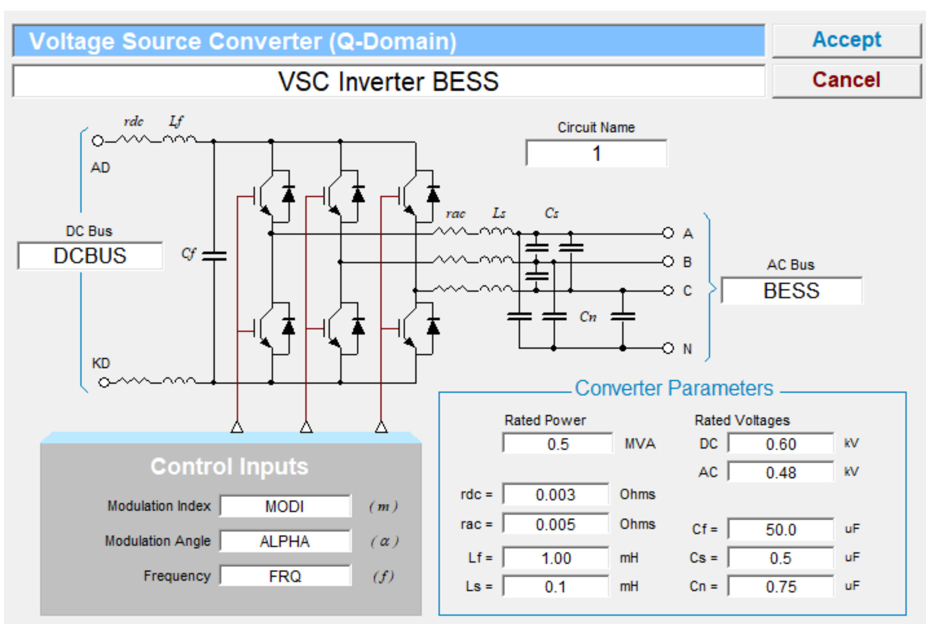

Figure A-8. Parameters of VSC_BESS

The parameters of the VSC controller in the test system are shown as Figure A-9 below. The induction motor-based load has a power of 0.5 MW at a rated voltage of 0.48 kV.

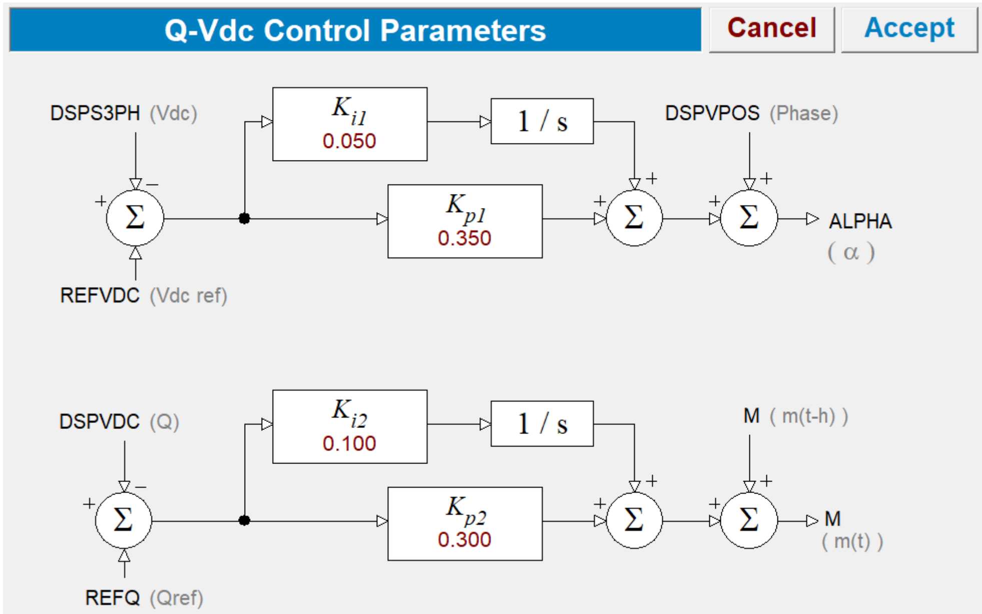

Figure A-9. Parameters of VSC Controller

Appendix B: Example Test System Parameters - PSCAD

This section introduces the parameters settings used in the test system in PSCAD.

The synchronous generator in the legacy AC system has a rated voltage of 4.16 kV and a base power of 3.5 MVA. To be consistent with the synchronous generator model in the model of Appendix A, the impedance settings of the synchronous generator model are the same and are shown in Figure B-1.

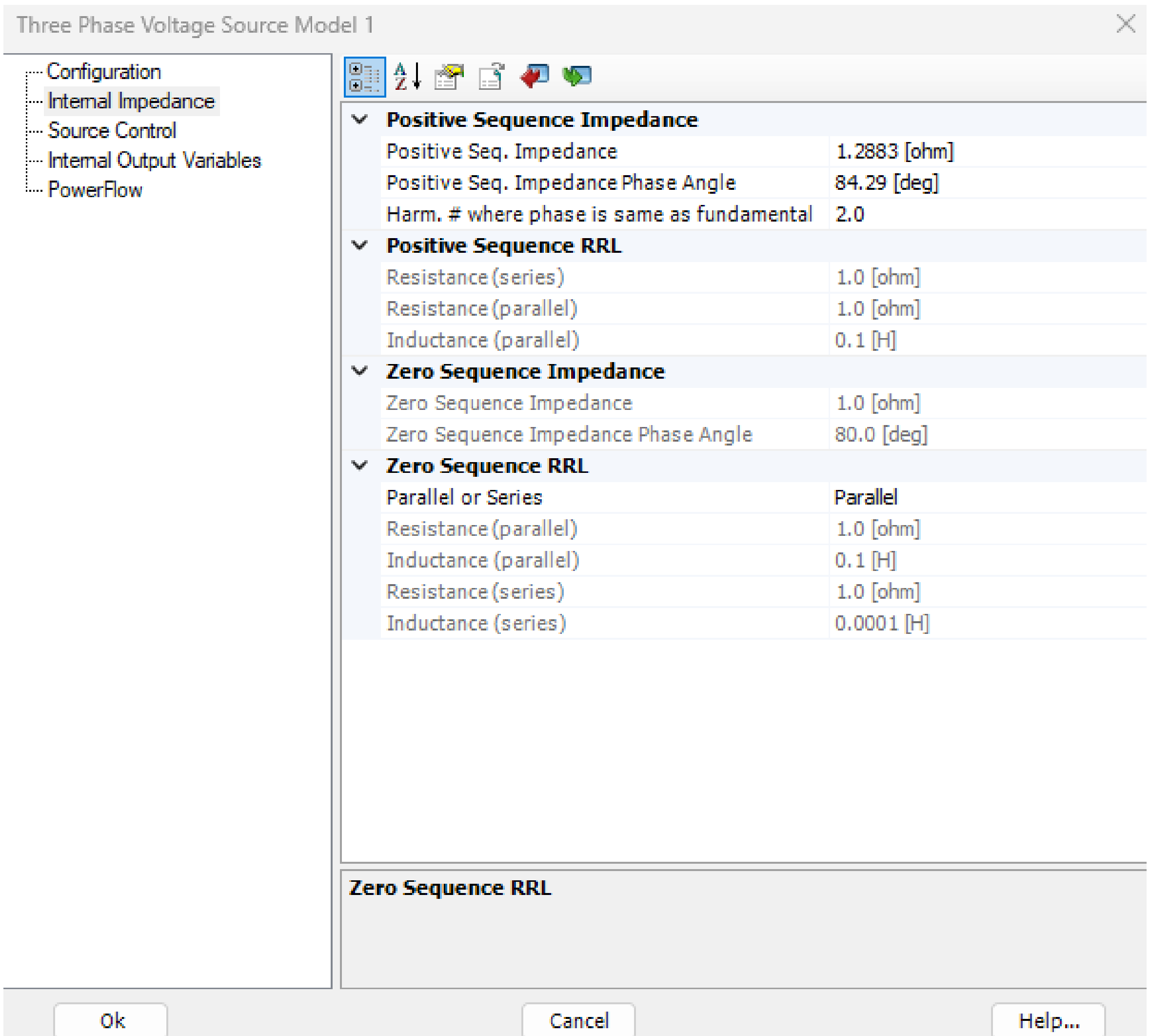

Figure B-1. Synchronous Generator Model Parameters in PSCAD

The parameters of transformer at the generator side are shown in Figure B-2, where the low side (delta) of the transformer is rated at 4.16 kV and the high side (wye) is rated at 13.8 kV. The transformer is rated at 3.5 MVA with a positive sequence leakage reactance of 0.1 p.u.

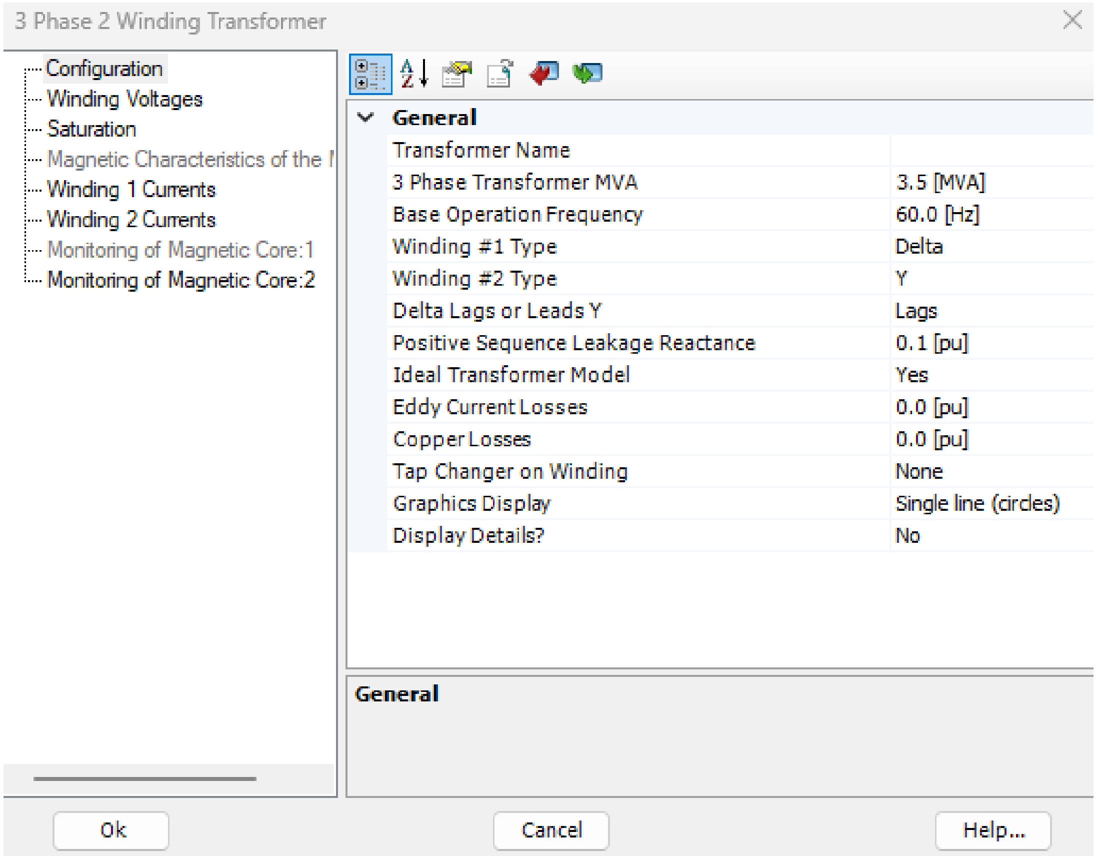

Figure B-2. Parameters of Transformer 1 in PSCAD Test System

The positive sequence and zero sequence parameters of the transmission line in the test system are shown below in Figure B-3. The length of the transmission line is 4 kms (2.5 miles).

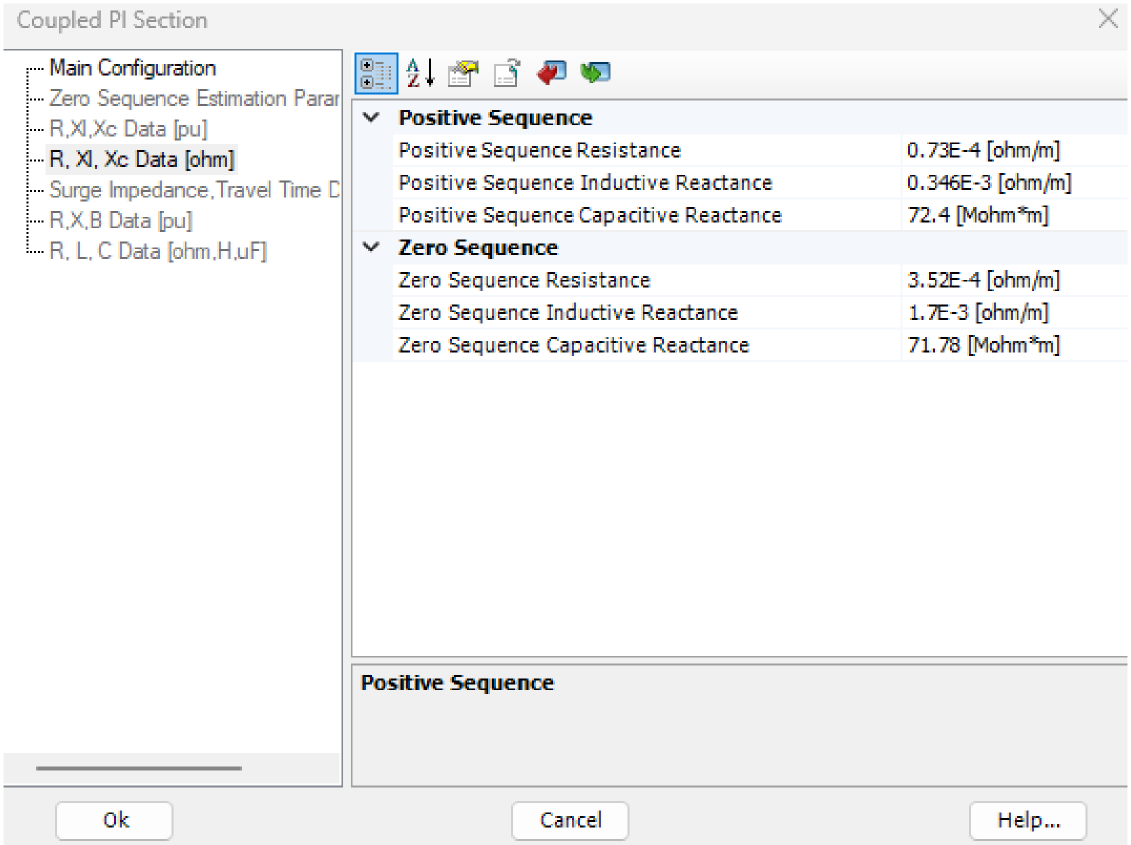

Figure B-3. Parameters of Transmission Line in PSCAD Test System

The parameters of transformer 2 at the point of interaction are shown as follows. The high side (delta) of the transformer is rated at 13.8 kV and the low side (wye) is rated at 0.48 kV. The transformer has a power rating of 2 MVA with a positive sequence leakage reactance of 0.1 p.u.

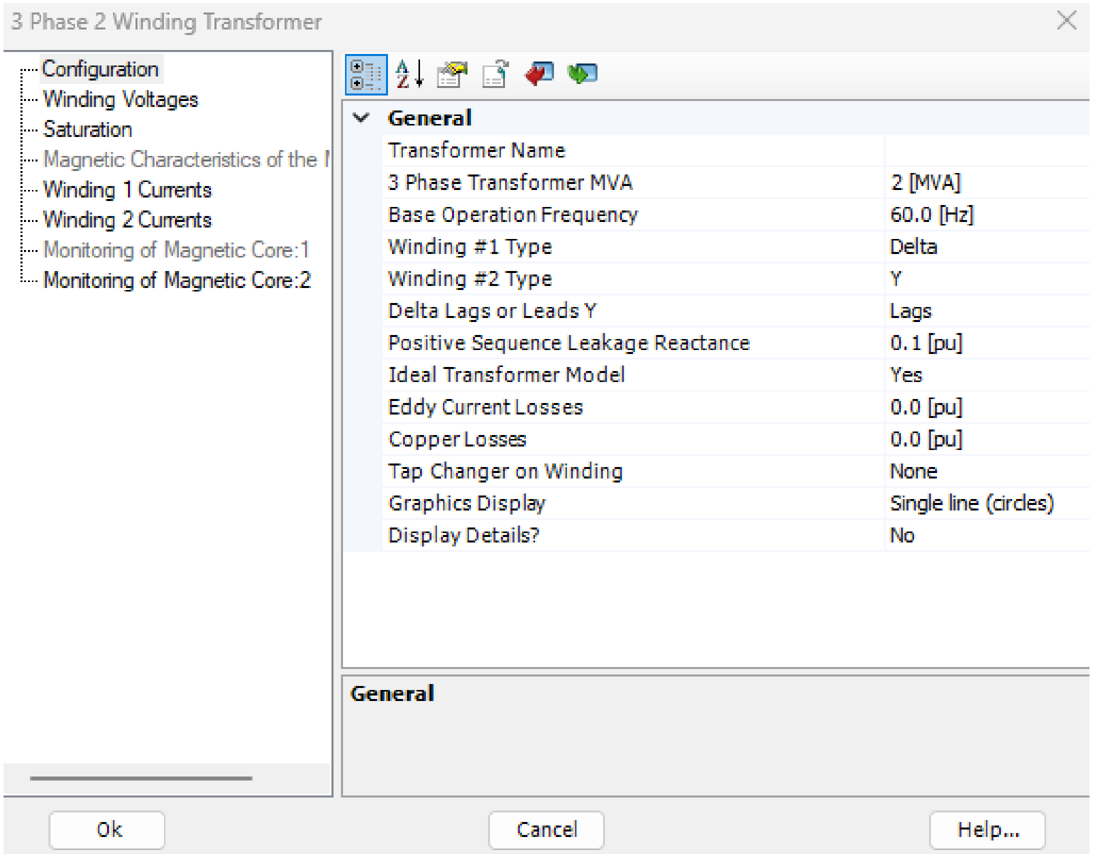

Figure B-4. Parameters of Transformer 2 in PSCAD Test System

The parameters of the components in the 100% IBR system are shown as follows: VSC 1 and VSC 2 are rated at 2.0 MW and 2.5 MW, respectively. The AC side of the VSC 1 and VSC 2 are rated at 0.48 kV and the DC side of the VSC is rated at 0.6 kV. The DC capacitor in the VSC has a capacitance of 50 µF. The parameters of the VSC controller are shown in Figure B-5 below.

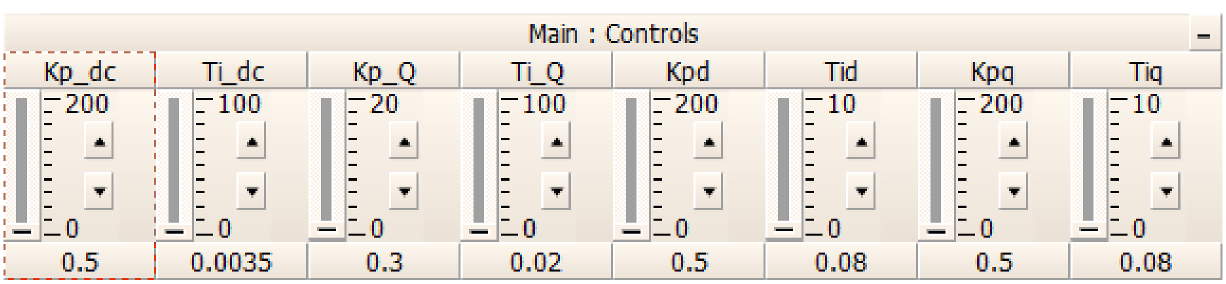

Figure B-5. Parameters of VSC Controller in PSCAD Test System

The battery model used in PSCAD has a rated voltage of 0.6 kV and a rated capacity of 1.0 kA*hr. The parameters of the battery model are shown in Figure B-6. The induction motor-based load has a power of 0.5 MW at a rated voltage of 0.48 kV.

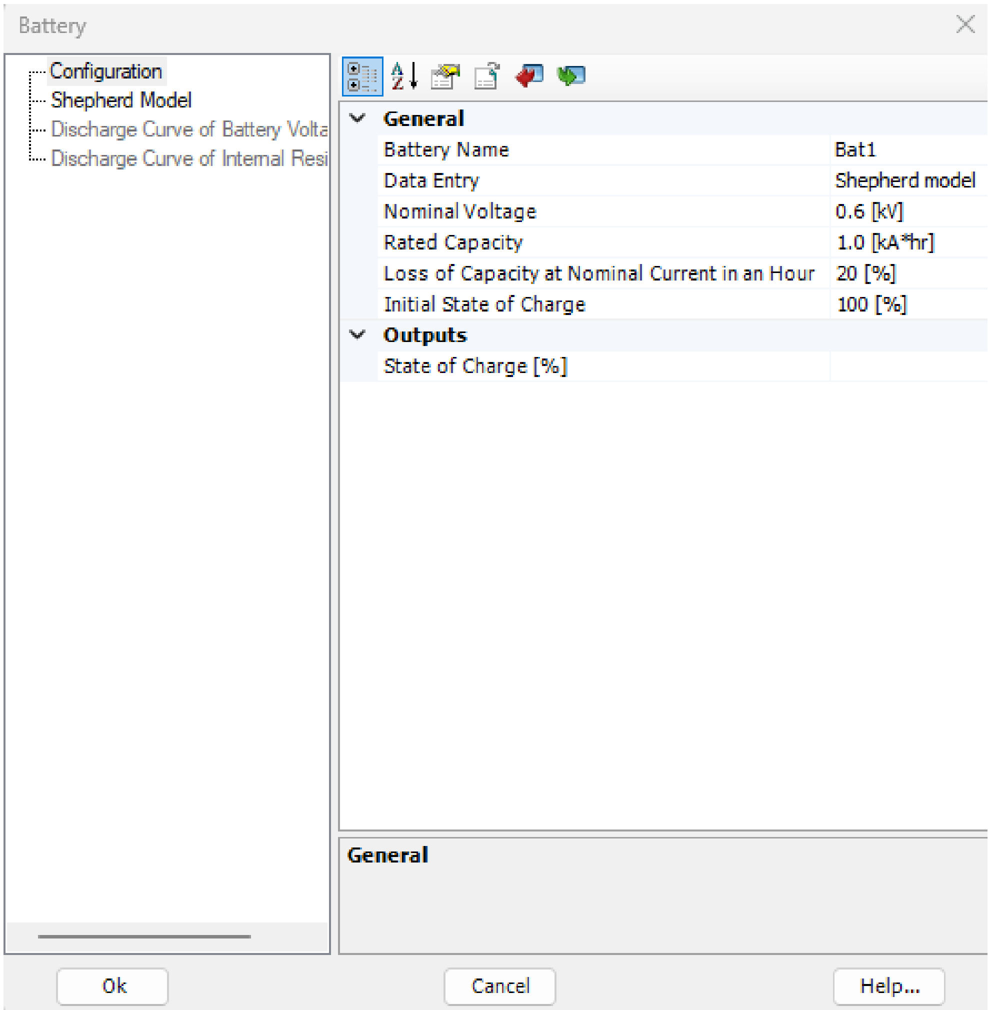

Figure B-6. Parameters of Battery Model in PSCAD Test System

Part III

Fault Ride Through and Post-Fault Recovery of Inverter Based Resources

Saeed Lotfifard
Ali Maleki, Graduate Student

Washington State University

For information about this project, contact

Saeed Lotfifard
Washington State University
School of Electrical Engineering and Computer Science
Pullman, Washington 99164-2752
Phone: 509-335-0903
Email: s.lotfifard@wsu.edu

Power Systems Engineering Research Center

The Power Systems Engineering Research Center (PSERC) is a multi-university Center conducting research on challenges facing the electric power industry and educating the next generation of power engineers. More information about PSERC can be found at the Center's website: http://www.pserc.wisc.edu.

For additional information, contact:

Power Systems Engineering Research Center
Arizona State University
527 Engineering Research Center
Tempe, Arizona 85287-5706
Phone: 480-965-1643
Fax: 480-727-2052

Table of Contents

List of Figures

NOMENCLATURE

IBR	Inverter base resources
FRT	Fault ride-through
PV	Photovoltaic
AW	Anti-windup
PBSMC	Proxy Based Sliding Mode Controller
SMC	Sliding Mode Controller
PLL	Phase-locked loop
DDSRF PLL	Decoupled double synchronous reference frame-PLL
Iref-q	Reference value of current in q frame
Iref-d	Reference value of current in d frame
$\mathrm{v_{id}}, \mathrm{i_d}, \mathrm{v_{iq,}} \mathrm{i_q}$	Current, and voltage of inverter, in dq0 reference frame.
C	Capacitor of the dc link
U	Modulation control signal determined by the MPPT algorithm
$\mathrm{I_{max}}$	Maximum current of the inverter
$\mathrm{I_{nominal}}$	Nominal current of the inverter
$\mathrm{V_{max}}$	Maximum voltage of the inverter
$\mathrm{V_{di-no\,limit}}, \mathrm{V_{qi-no\,limit}}$	Voltage of inverter in d and q frame without considering V_{max} limit
$\mathrm{V_{di-modified}}$ and $\mathrm{V_{qi-modified}}$	Voltage of inverter in d and q frame considering V_{max} limit
$\mathrm{v_{d+}},\mathrm{v_{q+}},\mathrm{v_{d-}},\mathrm{v_{q-}}$	Positive and negative sequence voltage at inverter terminal in dq frame
$\mathrm{i_d^+}, \mathrm{i_q^+}, \mathrm{i_d^-}, \mathrm{i_q^-}$	Positive and negative sequence current flows in the inverter in dq frame.
$\mathrm{i_{ref-d}^+}, \mathrm{i_{ref-q}^+}, \mathrm{i_{ref-d}^-}, \mathrm{i_{ref-q}^-}$	Positive and negative sequence reference current in dq reference frame
$\mathrm{k_p}$, $\mathrm{k_i}$ and $\mathrm{k_d}$	Proportional, integral and derivative gains of PID controller
x and $\mathrm{x_p}$	Position of controlled object and position of the proxy
$\mathrm{x_d}$	Desired position of the controlled object
λ	Gain of SMC
m	Mass of the proxy
$\mathrm{f_{smc}}, \mathrm{f_{PID}}$	Force produced by SMC, PID
$\mathrm{S_{PBSMC}}$	Sliding surface of PBSMC

ω	Angular velocity
φ_a^+, φ_a^-	Phase angle of positive and negative sequence
$v_{d+}^*, v_{d-}^*, v_{q+,}^* v_{q-}^*$	Positive and negative sequence voltage at the inverter terminal in dq reference frame.
$i_{d+}^*, i_{d-}^*, i_{q+,}^* i_{q-}^*$	Reference value of positive and negative sequence current flow in the inverter in dq reference frame.
P_0, Q_0	Average values of the instantaneous active and reactive powers respectively
P_c, P_s, Q_c, Q_s	Oscillatory terms of instantaneous power in unbalanced situation
P_{ref}, Q_{ref}	Reference values for the active and reactive power

1. Fault Ride Through and Post-Fault Recovery of Inverter Based Resources

1.1 Background

In modern power grids, the integration and deployment of inverter base resources (IBRs) increase. Ensuring the fault ride-through (FRT) capability of grid-connected IBRs is of special importance. Upon occurrence of faults, IBRs should remain connected to the grid and support the grid by injecting reactive currents. Moreover, once the fault is cleared, IBRs should seamlessly transition into the post-fault condition. One of the main challenges in realizing this feature for IBRs is addressing the saturation of controllers of IBRs.

This project specifically focuses on analyzing the performance of controllers of IBRs in facing saturations. Different methods that are used for coping with the saturation of controllers are studied. Different anti-windup (AW) methods are implemented, and their performances are analyzed. A controller called Proxy Based Sliding Mode Controller (PBSMC) is implemented. PBSMC combines conventional PID controllers with nonlinear controller SMC to take advantage of both methods. It provides a systematic approach for addressing the saturation of PI controllers in facing large disturbances such as faults.

In the following sections the response of PV power plants in facing balanced and unbalanced faults are studied. The simulation results demonstrate utilizing appropriate methods for addressing the saturation of the controllers play an important role in enhancing PV power plants fault ride-through (FRT) capability and smoother transition into post-fault condition.

1.2 Fault Response of Inverter Based Resources

The fault response of conventional synchronous generators has been studied extensively in the literature and well-established models are developed as shown in Figure 1.1 (a) [1][2]. As Figure 1.1 (a) shows conventional synchronous generators are modeled in positive sequence networks by a voltage source behind the positive sequence impedance. In the negative and zero sequence networks, positive and negative sequence impedances are used to model synchronous generators fault response. In contrast to conventional synchronous generators, the fault response of inverter-based resources varies depending on the utilized technologies. Figure 1.1 (b). shows a generic model of IBRs with the current limiting feature. Before the fault occurrence, IBRs, according to their controllers, may inject a certain amount of active and reactive powers into the grid. During the fault, the controller reduces the output current such that the peak current value does not exceed the maximum tolerable overcurrent value.

Different grid codes define different requirements for IBRs fault responses. In [3][4] review of different grid codes is provided. Figure 1.2 [3] shows a typical grid code. As shown in Figure 1.2 (a) depending on the severity of the fault (i.e. percentage of voltage sag at the terminal of the inverter) different grid codes require inverters to remain connected to the grid with different durations. Moreover, inverters should inject reactive current into the grid. Figure 1.2 (b) indicates for every percent of the voltage drop, inverters should at least inject two percents of reactive currents if the voltage drop is between 50% to 90% of the nominal value of the terminal voltage.

For voltage drops more than 50% of the nominal value of the terminal voltage, all nominal capacity of the inverter should be used to provide reactive current.

Faults in power grids could be balanced or unbalanced. In the following sections responses of inverters to balanced and unbalanced faults are discussed.

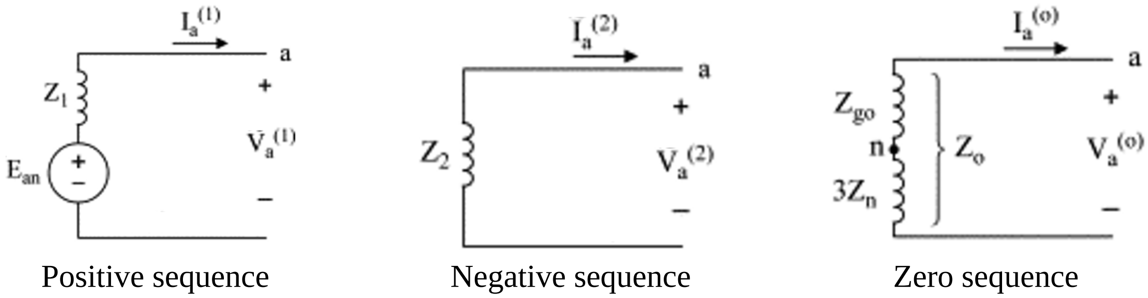

(a)

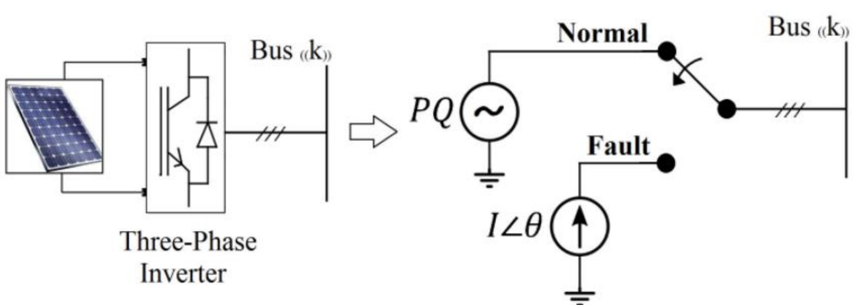

(b)

Figure 1.1 (a) Model of conventional synchronous generators in sequence domain [1] (b) Generic equivalent model of IBRs [2]

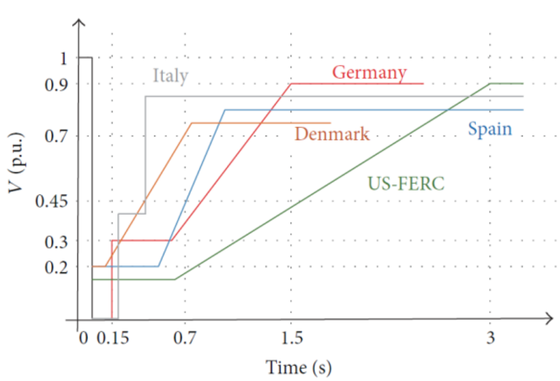

(a)

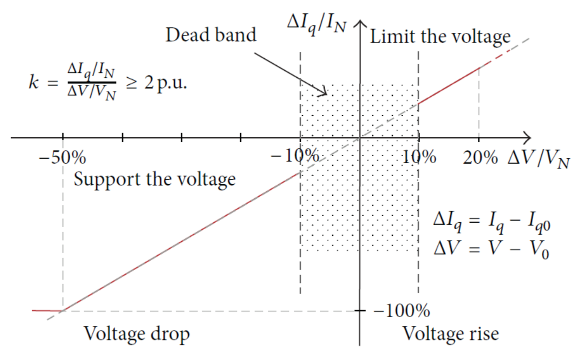

(b)

Figure 1.2 Grid codes requirements for fault ride through capability [3]

1.3 Fault Response of Inverters in Facing Balanced Faults

Figure 1.3 shows the implemented PV power plant. In this section it is assumed the fault is a symmetrical fault. The implemented controller has two control channels in d and q frames. It also has an inner current controller which controls the output current of the inverter. The outer controller provides the reference values to the inner current controller. Typically, in non-faulty condition, Iref-q =0 to allocate all capacity of the inverter to active power generated by the PV arrays. Iref-d is determined based on the voltage controller of the DC capacitor. At the DC side, by writing the KVL at the DC/DC converter the following holds [5]:

$$L\frac{di_b}{dt} = V_{in} - (1-U)V_{dc}) \tag{1.1}$$

Where U is the modulation control signal determined by the MPPT algorithm. L is the inductance in the dc link, i_b is the current flowing through the inductance, V_{in} is the voltage of the PV modules, V_{dc} is the voltage of the DC link capacitor.
The voltage dynamic at the capacitor is as follows:

$$C\frac{dV_{dc}}{dt} = (1-U)I_b - I_{dc} \tag{1.2}$$

Where C is capacitor in the dc link.
Also, by ignoring the power loss at the inverter

$$P_{ac} = P_{dc} \tag{1.3}$$

Where

$$P_{ac} = \frac{3}{2}(v_{id}i_d + v_{iq}i_q) \tag{1.4}$$

$$P_{dc} = V_{dc}I_{dc} \tag{1.5}$$

From (1.3) and (1.4), and (1.5):

$$I_{dc} = \frac{3}{2V_{dc}}(m_d\frac{V_{dc}}{2}i_d + m_q\frac{V_{dc}}{2}i_q) \tag{1.6}$$

By substituting (1.6) into (1.2), the following is derived:

$$C\frac{dV_{dc}}{dt} = (1-U)I_b - \frac{3}{4}(m_d i_d + m_q i_q) \tag{1.7}$$

Where P_{ac} and P_{dc} are power on the different side of inverters, P_{ac} is the power of inverter on the ac side of the system and P_{dc} is the power of inverter on the dc side of the system, $V_{dc}$is the voltage of the capacitor in the dc link and $i_{dc}$is the current flowing into the inverter from dc link. Also, m_d, $m_q$are modulating control signals for d and q channels.

According to (1.7), if the generated power by the PV arrays increases, the output current should be increased to ensure a fixed voltage value for the DC capacitor. Similarly, if the generated power by the PV arrays reduces, the output current should reduce too. This observation is used for generating Iref-d as shown in Figure 1.3 which utilizes a PI controller for this purpose.

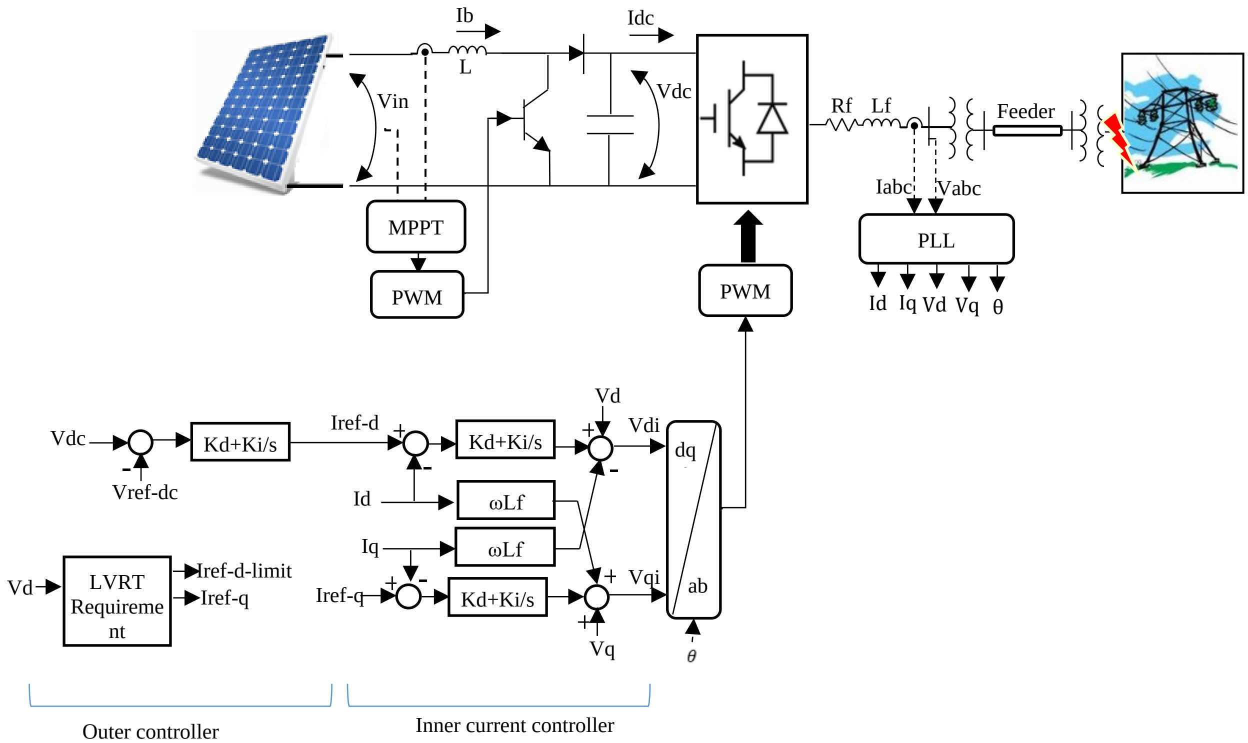

Figure 1.3 Schematic of PV power plant for symmetrical faults scenarios

1.3.1 Modeling of Constraints of Controllers

An important aspect of the controllers is controllers saturation when the control output is limited by the inverter limits. The following constraint holds for the inverter output current:

$$\sqrt{{I_d}^2 + {I_q}^2} \leq I_{max} \tag{1.8}$$

Where I_d and I_q are the current of the converter in d and q frame and I_{max} is the maximum current can flow in the inverter. Typically, $I_{max} = 1.2I_{nominal}$ which $I_{nominal}$ is the nominal current of the inverter. Also, the following holds for V_{di} and V_{qi} in Figure 1.3:

$$\sqrt{{V_{di}}^2 + {V_{qi}}^2} \leq V_{max} \tag{1.9}$$

Where V_d and V_q are the voltages of the inverter in d and q frames and V_{max} is the maximum voltage of the inverter.

As Figure 1.4 (a)[6] shows, equation (1.9) represents an area indie a circle with the radius of V_{max}. There are different methods for enforcing the limits. In [6] detailed discussions of the methods are provided. One common approach is rectangular approximation or boxed constraints.

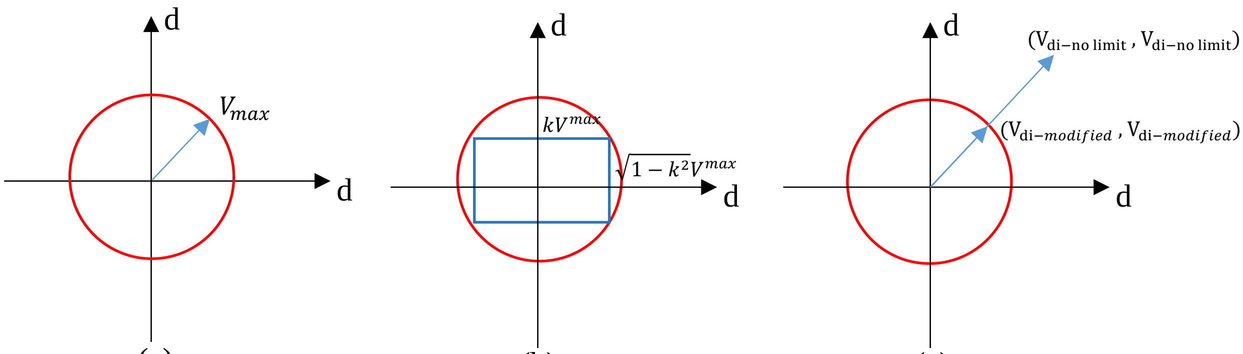

Figure 1.4 Different approaches for enforcing inverter constraints[6]

Figure 1.4 (b)[6] shows the structure of this approximation. It is assumed

$$V_{qi}{}^{max} = kV^{max} \tag{1.10}$$

Where k is a factor $0 \leq k \leq 1$. According to (1.9) and (1.10), the following holds:

$$V_{di}{}^{max} = \sqrt{1-k^2}V^{max} \tag{1.11}$$

Therefore, instead of (1.9) the following constraints are used:

$$\begin{gathered} -V_{qi}{}^{max} \leq V_{qi} \leq V_{qi}{}^{max} \\ -V_{di}{}^{max} \leq V_{di} \leq V_{di}{}^{max} \end{gathered} \tag{1.12}$$

The advantage of boxed constraints approximation is that the limits are fixed constant values. Therefore, the controller design and implementation are easier. However, it does not fully utilize the available capacity of the inverter as shown in Figure 1.4 (b)[6].

Another approach is Maintaining the Same Ratio approach. In this approach at first the control constraints are ignored, and control values of d and q channels are calculated as $V_{di-no\ limit}$ and $V_{qi-no\ limit}$. No further action is needed, if the following holds,

$$\sqrt{V_{di-no\ limit}{}^2 + V_{qi-no\ limit}{}^2} \leq V_{max} \tag{1.13}$$

However, if (1.13) does not hold, modified values of d and q channels should be calculated as $V_{di-modified}$ and $V_{qi-modified}$. In Maintaining Same Ratio approach, the following should hold:

$$\frac{V_{di-no\ limit}}{V_{qi-no\ limit}} = \frac{V_{qi-modified}}{V_{qi-modified}} \tag{1.14}$$

Equation (1.14) can be interpreted as Figure 1.4-(c)[6]. $V_{di-modified}$ and $V_{qi-modified}$ should satisfy the relationship in (1.14) and also the following relationship:

$$\sqrt{{V_{di-modified}}^2 + {V_{qi-modified}}^2} = V_{max} \tag{1.15}$$

One solution is as follows:

$$V_{di-modified} = \frac{V_{di-no\ limit}}{\sqrt{{V_{di-no\ limit}}^2 + {V_{qi-no\ limit}}^2}} V_{max} \tag{1.16}$$

$$V_{qi-modified} = \frac{V_{qi-no\ limit}}{\sqrt{{V_{di-no\ limit}}^2 + {V_{qi-no\ limit}}^2}} V_{max} \tag{1.17}$$

The advantage of the above approach is that the full capacity of the inverter is utilized. However, it requires changing the constraints in real-time which complicates the control design and implementation.

Another approach which is commonly used in IBRs, and is also implemented in this project, is assigning priority to one of the control channels. In this approach like the previous method, first the limits on the control channels are ignored and $V_{di-no\ limit}$ and $V_{qi-no\ limit}$ are calculated. Assuming q channel is the control channel with a higher priority, the following procedure is followed:

$$\begin{aligned}
&\text{If } V_{qi-no\ limit} \geq V_{max}, \text{ then} \\
&\quad V_{qi-modified} = V_{max} \text{ and } V_{di-modified} = 0 \\
&\text{If } V_{qi-no\ limit} < V_{max}, \text{ then} \\
&\quad V_{qi-modified} = V_{qi-no\ limit} \\
&\quad \text{If } V_{di-no\ limit} < \sqrt{V_{max}^2 - {V_{qi-no\ limit}}^2}, \text{ then} \\
&\qquad V_{di-modified} = V_{di-no\ limit} \\
&\quad \text{If } V_{di-no\ limit} \geq \sqrt{V_{max}^2 - {V_{qi-no\ limit}}^2}, \text{ then} \\
&\qquad V_{di-modified} = \sqrt{V_{max}^2 - {V_{qi-no\ limit}}^2}
\end{aligned} \tag{1.18}$$

Following similar approach, the grid code requirement in Figure 1.2 (b), and considering q channel has the higher priority, the following can be written:

$$
\begin{aligned}
& I_{q-check} = 2(1 - V_d) I_N \\
& \text{If} \quad V_d > 0.9, \quad \text{then} \\
& \qquad I_{q-modified} = I_{q0} \text{ and } I_{d-modified} = I_{d0} \\
& \text{If} \quad V_d \leq 0.9, \quad \text{then} \\
& \qquad \text{If} \quad I_{q-check} \geq I_{max}, \quad \text{then} \\
& \qquad\quad I_{q-modified} = I_{max}, \quad I_{d-modified} = 0 \\
& \qquad \text{If} \quad I_{q-check} < I_{max}, \quad \text{then} \\
& \qquad\quad I_{q-modified} = I_{q-check} \\
& \qquad\quad \text{If } I_{d-no\ limit} \geq \sqrt{I_{max}^2 - I_{q-check}^2} \\
& \qquad\qquad I_{d-modified} = \sqrt{I_{max}^2 - I_{q-check}^2} \\
& \qquad\quad \text{If } I_{d-no\ limit} < \sqrt{I_{max}^2 - I_{q-check}^2} \\
& \qquad\qquad I_{d-modified} = I_{d-no\ limit}
\end{aligned}
\tag{1.19}
$$

The common approach in facing constraints in the controllers channels is utilizing anti-windup (AW) strategies. When a PI controller faces limits, the integral part accumulates errors terms. If no approaches are used to address the problem, the time the controller remains in the saturation mode increases which degrades the response and even may lead to instability of the controller.

There are several AW approaches that are used in power systems such as PI conditional, Dead zone, tracking method, and track gain method which will be discussed in the later sections. These methods help to reduce the saturation effects on integral part of the controller. Saturation happens when the integral action accumulates error.

The proper tuning of AW methods is a challenging problem. Tuning AW parameters is a heuristic procedure. Therefore, methods that can address the saturation of PIs while can be tuned systematically is of special interest. Specifically in this project, a method called proxy-based sliding mode control (PBSMC) method is used which is developed in [7][8]. PBSMC interfaces nonlinear sliding mode control and PID control by using a virtual objective (proxy) so that the resulting control law has the advantages of each approach while addressing the saturation problem of PI controllers.

1.3.2 Methods for Handling Controllers Saturations

In the following section a brief review of the AW methods that have been implemented in power systems and presented in [9] are reviewed. The methods are implemented on a simulated PV power plant in Matlab Simulink which will be discussed in later sections.

Anti-windup PI with dead zone method

Figure 1.5 [9] shows the schematic of this method. The integral value is compared with the dead zone limit. If this value is larger than the limit, the value will be reduced, otherwise, no changes are made to the value.

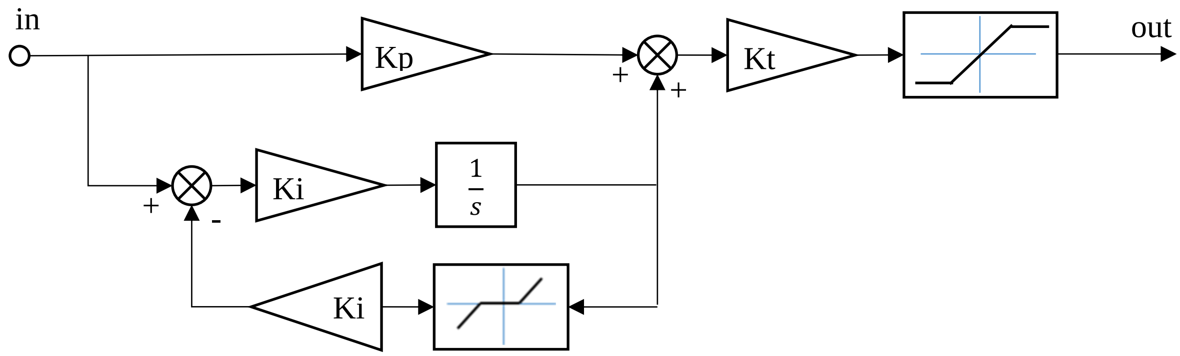

Figure 1.5 Anti-Windup PI with dead zone method

Anti-windup PI conditioned method

Figure 1.6 [9] shows the schematic of this method. In this scheme, if the values between the input and output of the saturation block are different, the integral value is held in the latest value to decrease the saturation effects by not letting the integral part accumulate the error. In this method, a switch is used to ensure that if any difference between the input and output of saturation block appears, the input of the integral part is set to zero. This method is used in IEEE Std. 421.5-2016. Although it has a simple structure and commonly used, there are applications that it does not operate properly, and alternative solutions have been proposed to address the shortcomings [10]

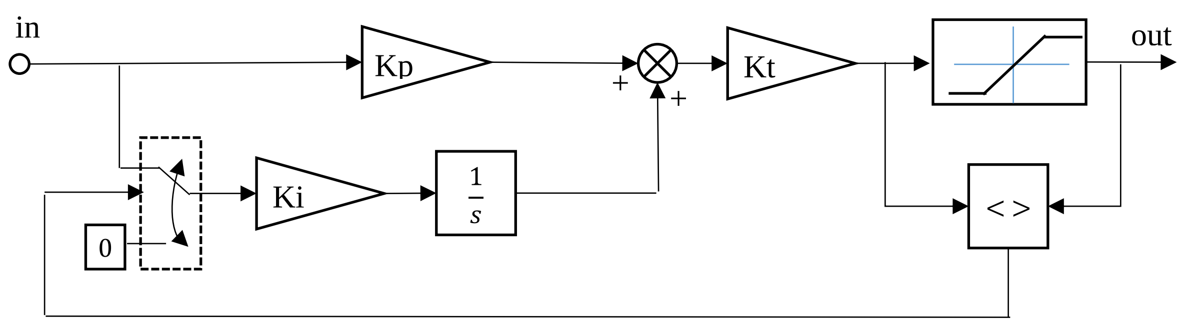

Figure 1.6 Anti Widup PI conditioned method

Anti-windup PI tracking method

Figure 1.7 [9] shows the schematic of this method. In this scheme, the difference between the input and output of the saturation block is used to reduce the effect of error accumulation in the integral part. In this method, typically overshoot in the response appears, but the time the system remains in the saturation decreases.

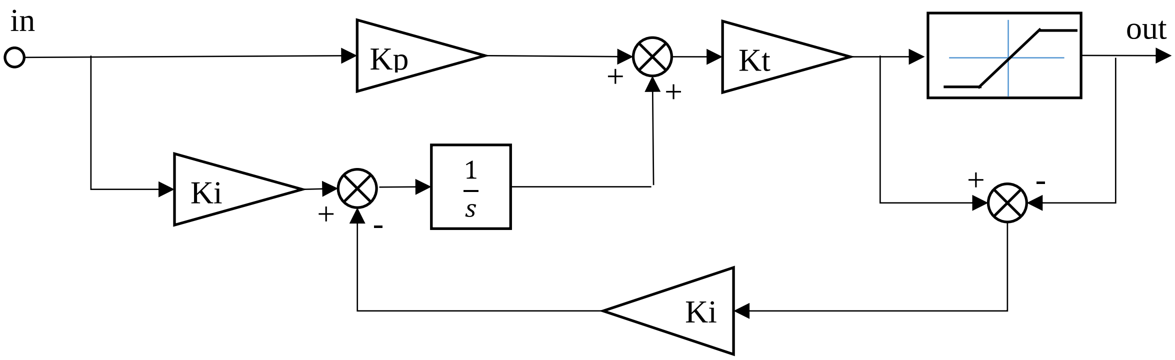

Figure 1.7 Anti-Windup PI tracking method

Anti-windup PI tracking with gain method

Figure 1.8 [9] shows the schematic of this method. This method is similar to the previous method but uses another gain in the feedback loop to improve the results. The gain G is between 1 and zero.

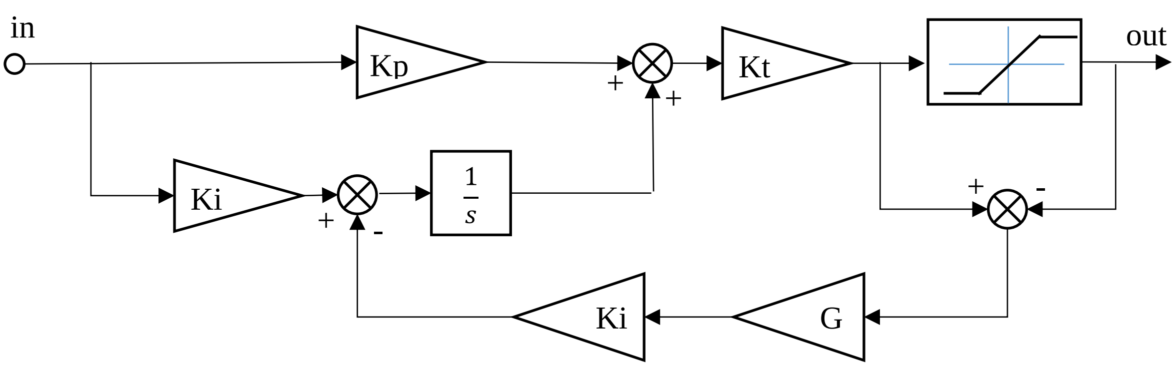

Figure 1.8 Anti-Windup PI tracking with gain method

Proxy-based sliding mode control (PBSMC)

In [7][8] a controller called PBSMC is proposed that combines PID controllers and SMC. PBSMC provides accurate and fast-tracking feature during normal condition while provides smooth resuming to the desired trajectory in facing large disturbances. Therefore, there is no need to make the PID controller unnecessarily slower. Moreover, compared to conventional AW methods that are heuristic approaches, PBSMC provides a more systematic approach for managing the post-saturation condition. Figure 1.9 shows the overall idea of the PBSMC. The PID controller interfaced to the SMC though a virtual object (proxy). The overall PID controller can be written as follows:

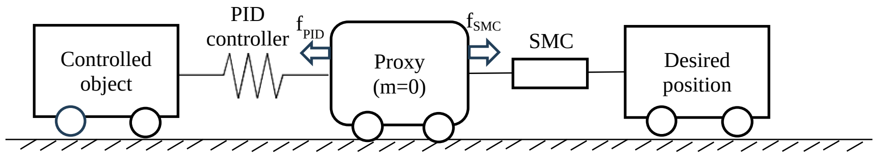

Figure 1.9 Schematic of PBSMC

$$f_{PID} = k_p.(x_p - x) + k_i.\int_0^t (x_p - x)\,dT + k_d.\frac{d}{dt}(x_p - x) \tag{1.20}$$

where, x and x_p denote the position of controlled object and position of the proxy, respectively. k_p, k_i and k_d are proportional, integral and derivative gains of PID controller, respectively. The objective of the SMC is to bring the position of the proxy to the desired position according to the sliding surface as follows:

$$S_{PBSMC} = K\frac{d}{dt}(x_d - x_p) + (x_d - x_p) \tag{1.21}$$

Where x_d is the desired position of the controlled object Therefore, the control law of the SMC becomes as follows:

$$f_{SMC} = F.sgn(S_{PBSMC}) = F.sgn(K\frac{d}{dt}(x_d - x_p) + (x_d - x_p)) \tag{1.22}$$

Where S_{PBSMC} is sliding surface of PBSMC
In Figure 1.9 , the motion equation for the proxy (i.e. virtual object) is as follows:

$$m.\frac{d^2x_p}{dt} = f_{smc} - f_{PID} \tag{1.23}$$

where, m is the mass of the proxy and is assumed to be zero. Therefore, the following holds:

$$f_{smc} = f_{PID} \tag{1.24}$$

In [11], the above equations are utilized and after using a series of mathematical relations, the PBSMC is developed as shown in Figure 1.10 [11]. The λ is a gain that can determine the speed of the response of the system.

.

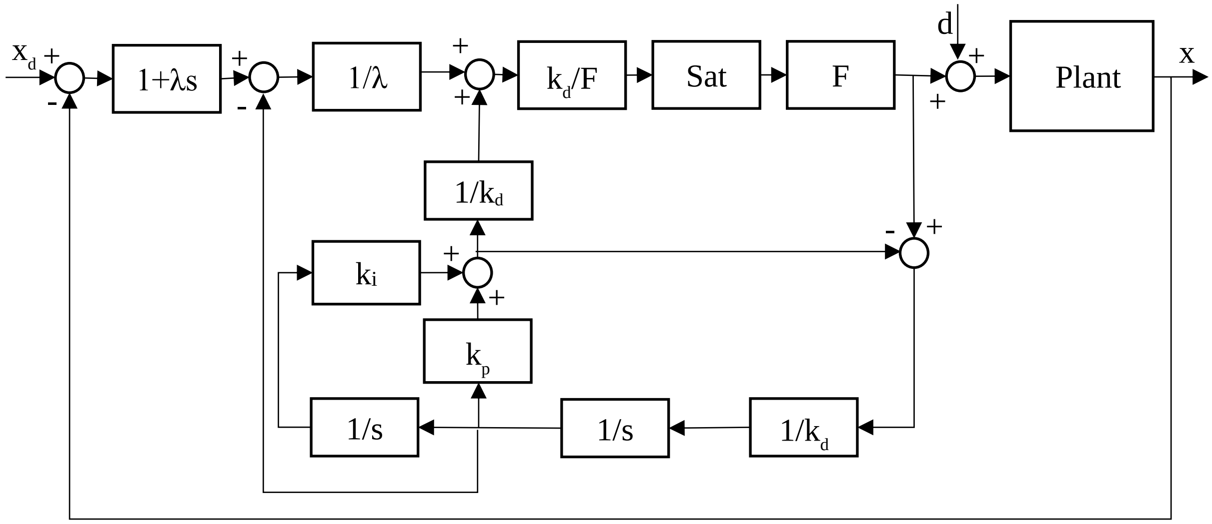

Figure 1.10 Proxy-based sliding mode control structure

1.3.3 Performance of Controllers in Different Hypothetical Plant Models

In this section to investigate the performance of different AW methods, several hypothetical plant models are considered. Then, the methods are applied to a PV power plant.

CASE 1: A plant model of $\frac{10}{s^2+10s+5}$ is considered and the PI parameters are K_p=10, K_i=4 and the plant input limit value is 14, and the reference is a step function from zero to five. The results are shown in Figure 1.11 and Figure 1.12. As can be seen in the simulated results, PBSMC has either similar or better response compared to other methods.

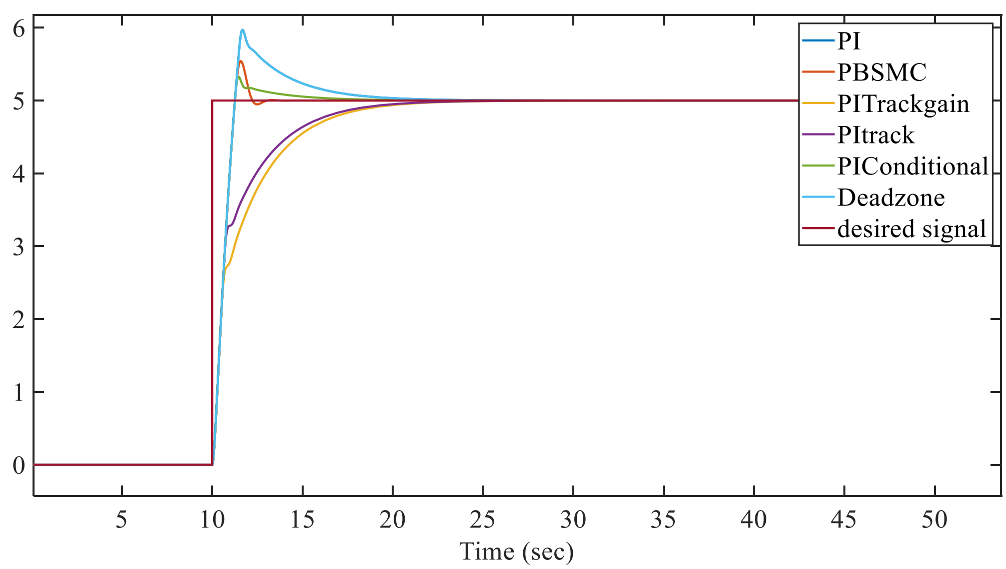

Figure 1.11 Comparison of different controllers in CASE 1

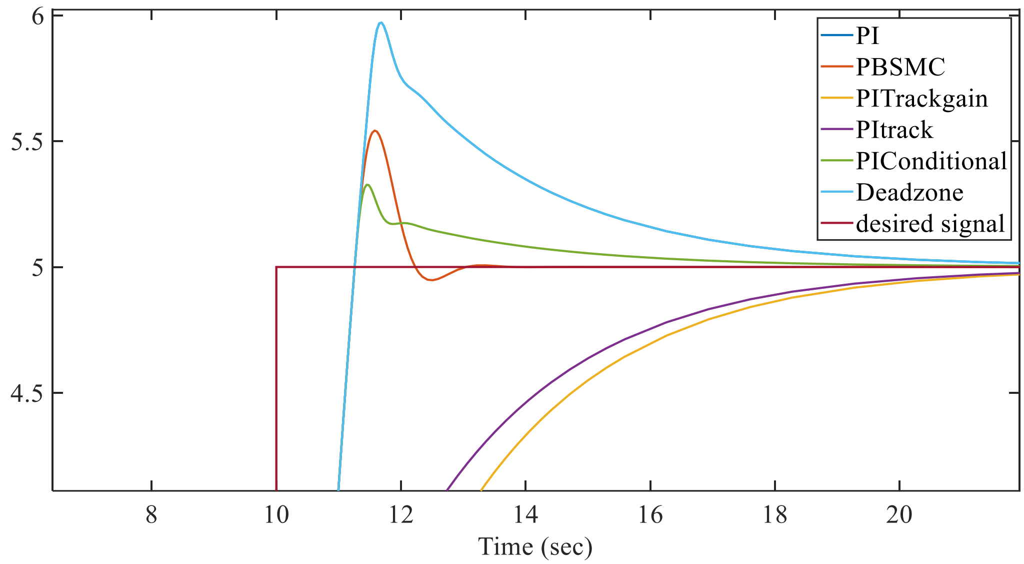

Figure 1.12 Comparison of different controllers in CASE 1, zoomed values

One advantage of the PBSMC is it has a systematic approach for the analysis of the impact of the controller parameters (i.e. λ) which makes the use of controller systematic.

CASE 2: The second considered plan model is $\frac{180}{s^2+14s+41}$. The controller parameters are K_p=30, K_i=20, Kd=0.6 and the input limit is 23 and the refrence is a step from 0 to 100 at t=10 second. The results are shown in Figure 1.13 and Figure 1.14. Similar to the previous case PBSMC controller has similar or better performance compared to other methods.

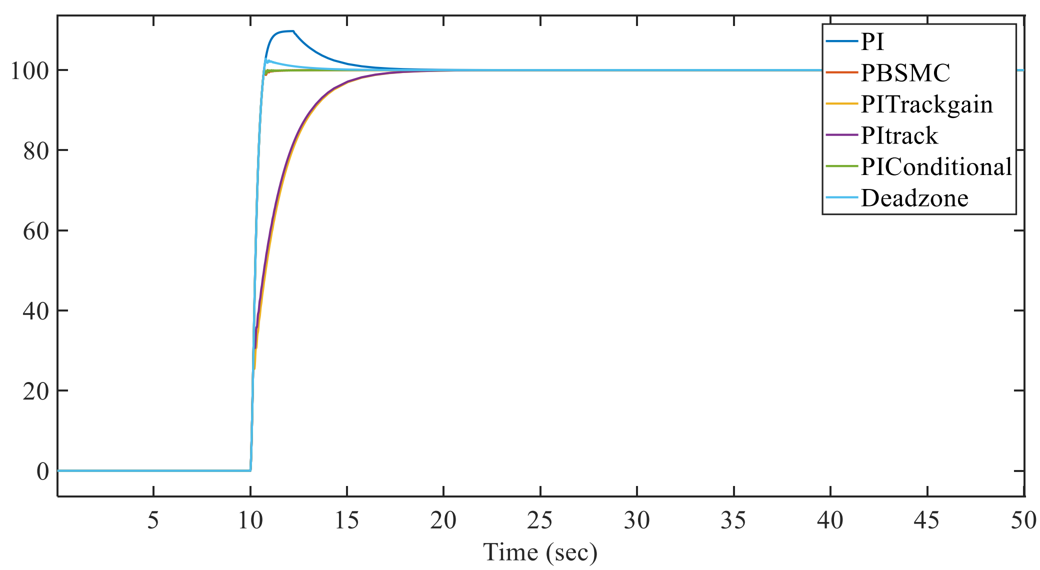

Figure 1.13 Comparison of different controllers in CASE 2

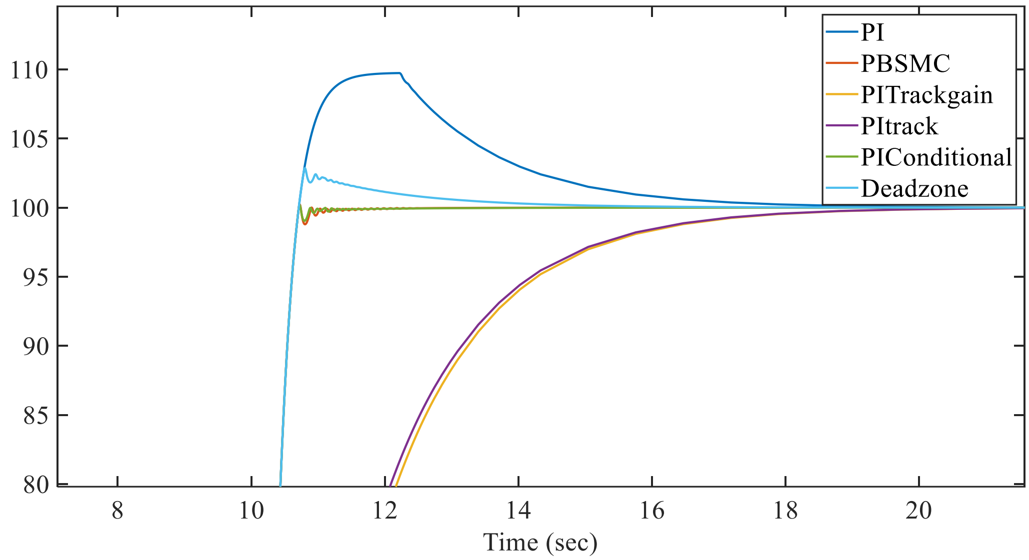

Figure 1.14 Comparison of different controllers in CASE 2, zoomed values

1.3.4 Performance of Controllers in PV Power Plant: Balanced Fault Cases

The power plan shown in Figure 1.3 is simulated in Matlab/Simulink and different AW methods are applied to the controller. According to the case study results, the limit on the PI controller of DC capacitor is influential. This is because during the fault, the controllers of the inverter follows the fault ride through requirements which requires injecting reactive current. This limits the available capacity for injecting Id which directly affects the voltage of the DC capacitor. To investigate the performance of different approaches, different fault scenarios are studies.

CASE 1: A three-phase fault occurs between 1.5 and 1.6667 seconds with a fault resistance of 0.001 ohms and a ground resistance of 0.01 ohms. This fault causes saturation in the Id channel because the Iq should be injected into the system. Figure 1.15 to Figure 1.17 show the results in this case. Note in the figures “PI” means no AW method is used which is not a realistic condition. It is only reported to show the impact of the saturation on the results.

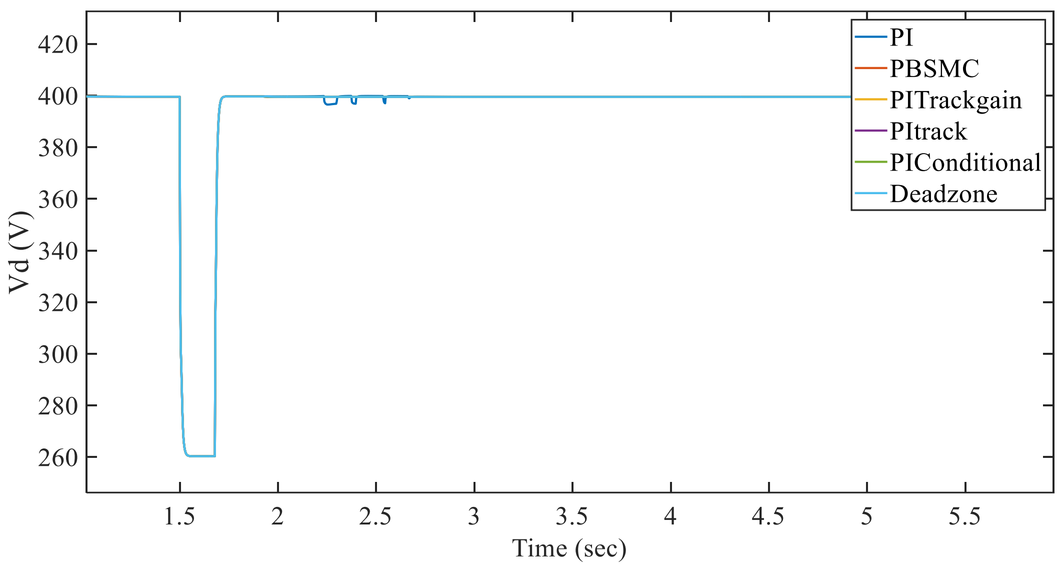

Figure 1.15 Vd for the balanced fault CASE 1

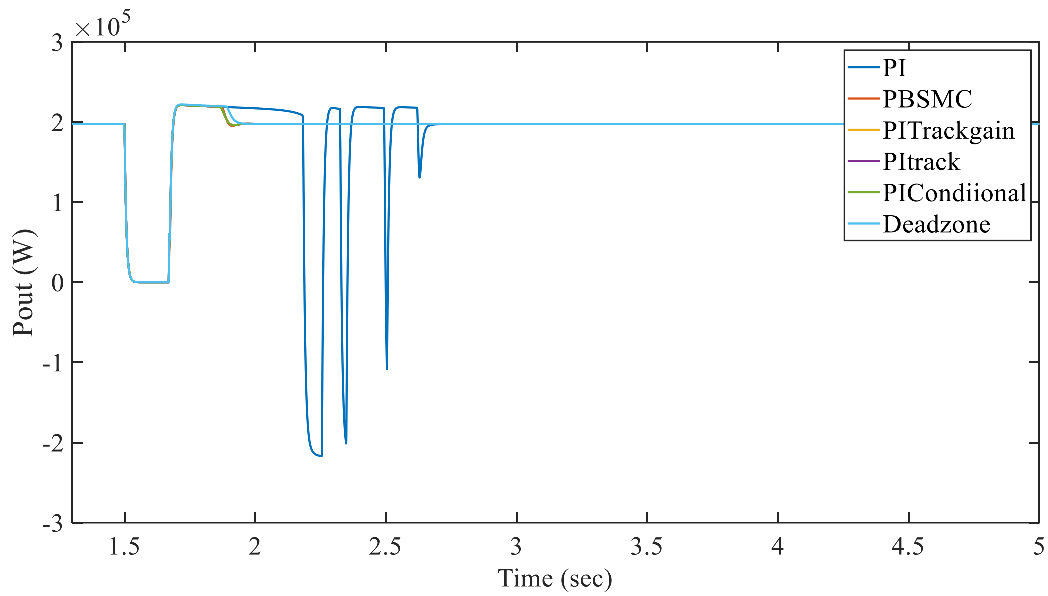

Figure 1.16 Pout for the balanced fault CASE 1

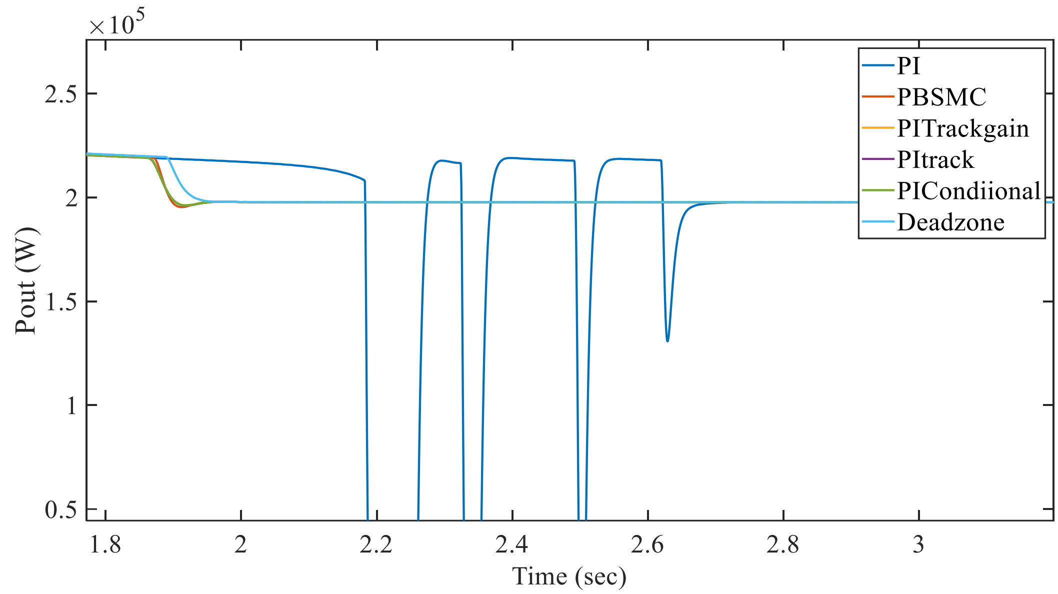

Figure 1.17 Pout zoomed on the saturation time for the balanced fault CASE 1

CASE 2: Compared to the previous case, the fault resistance is changed to 20 ohms. Figure 1.18 to Figure 1.20 show the results. In this case the voltage level does not drop like the previous case, and the controllers get out of saturation sooner than the previous case.

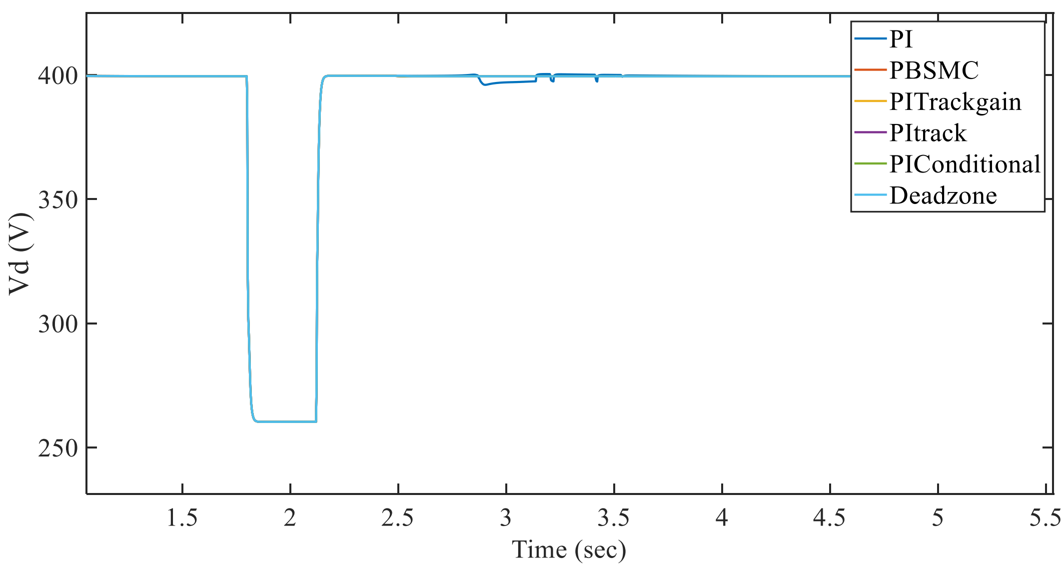

Figure 1.18 Vd for the balanced fault CASE 2

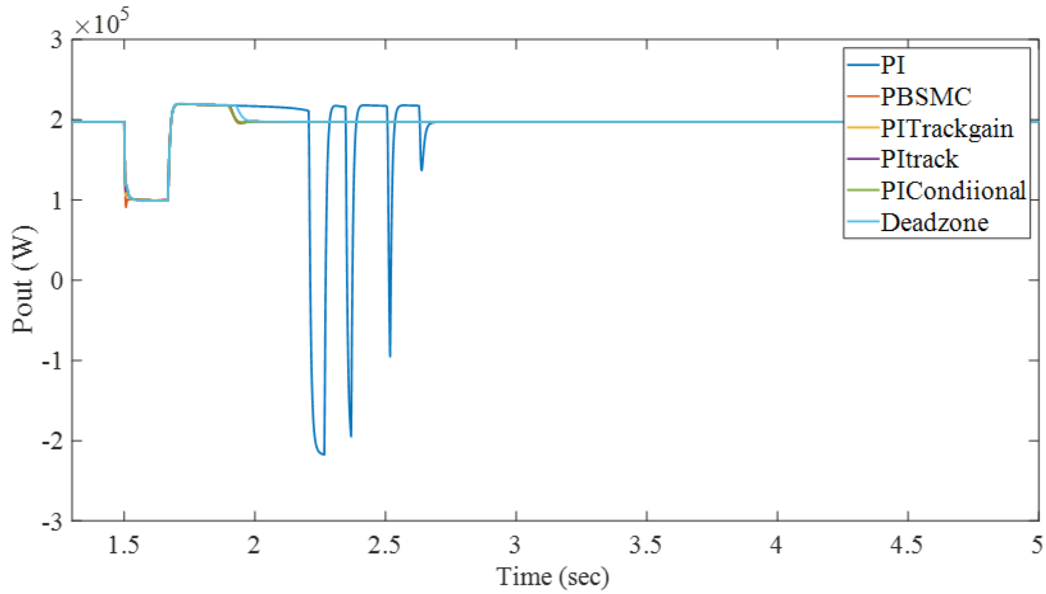

Figure 1.19 Pout for the balanced fault CASE 2

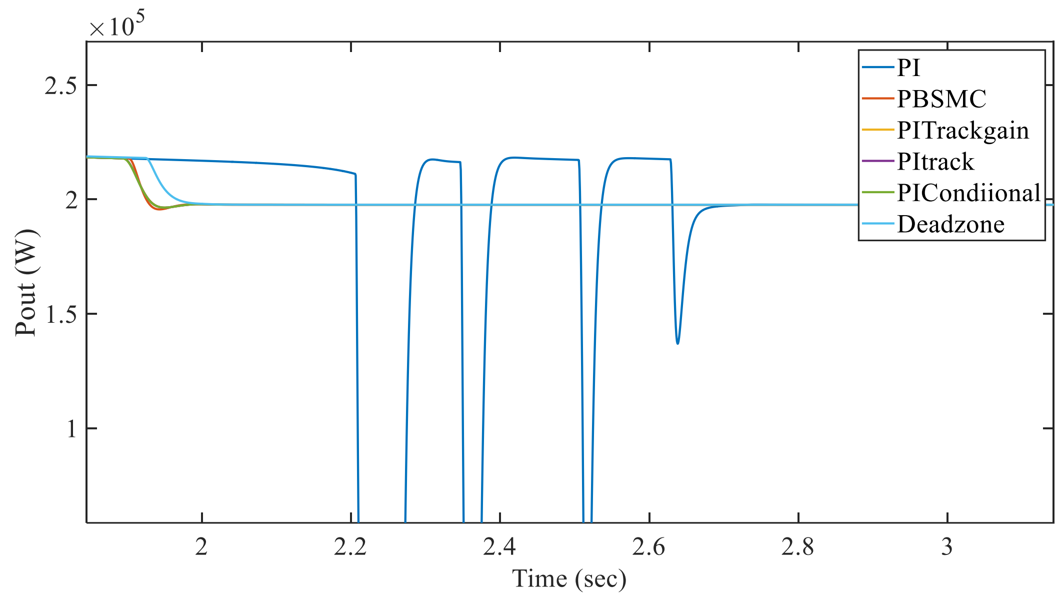

Figure 1.20 Pout zoomed on the saturation time for the balanced fault CASE 2

CASE 3: In this case, the fault starts at 1.8 seconds and lasts until 2.12 seconds, twice the duration of the previous scenario. Furthermore, the ground resistance is 0.01 ohms, and the fault resistance is 20 ohms. The simulation results are presented in Figure 1.21 to Figure 1.23.

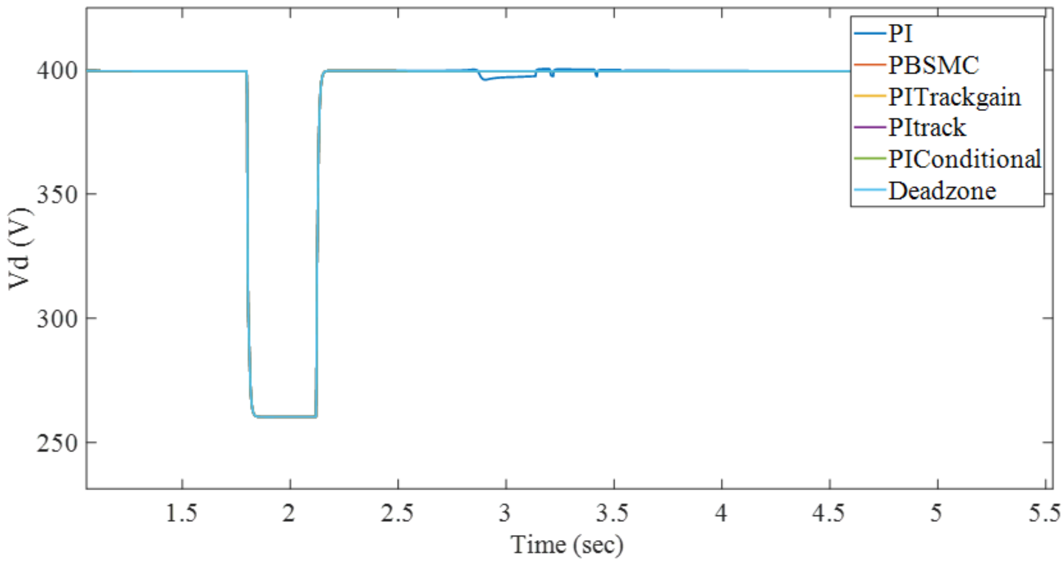

Figure 1.21 Vd for the balanced fault CASE 3

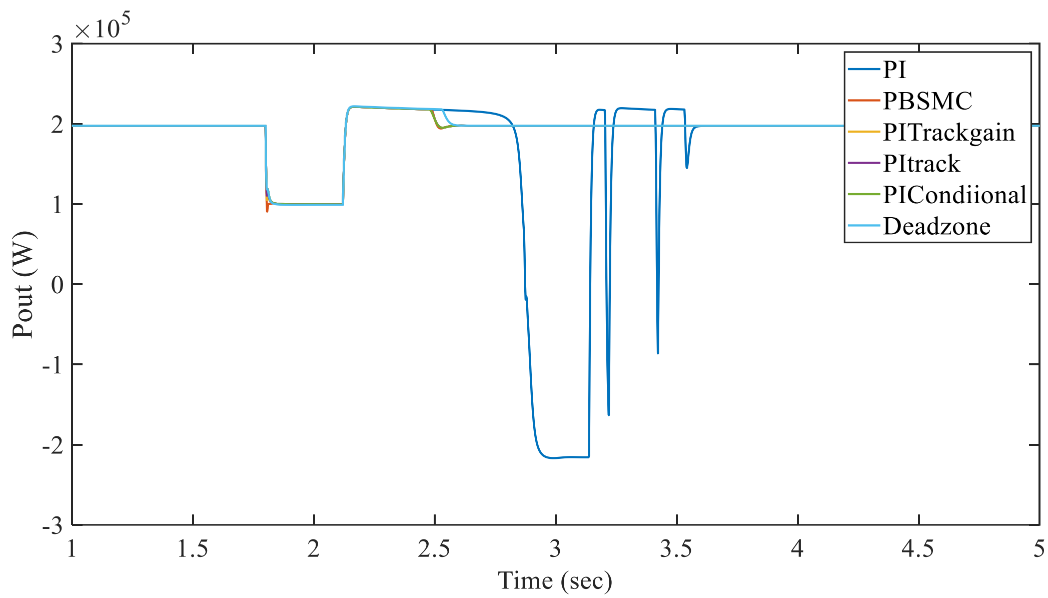

Figure 1.22 Pout for the balanced fault CASE 3

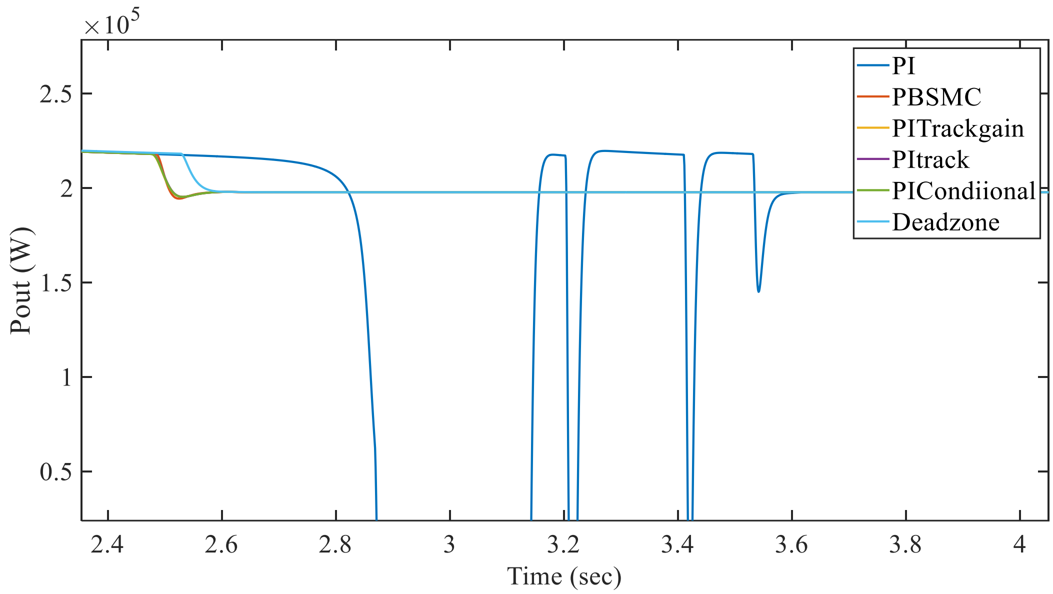

Figure 1.23 Pout zoomed on the saturation time for the balanced fault CASE 3

As the results show AW methods significantly improve the transitioning of the PV power plant to the post fault condition. Moreover, according to the simulation results, PBSMC method has either same or better performance compared to the AW methods. However, tuning the AW methods involves heuristic approaches. In contrast, tuning PBSMC is more systematic.

1.4 Fault Response of Inverters in Facing Unbalanced Faults

When an unbalanced fault occurs, the voltage and current signals become unbalanced. Therefore, the conventional synchronous reference frame phase-locked loop (SRF-PLL) becomes ineffective due to presence of double frequency oscillations. To explain this issue, Figure 1.24 and Figure 1.25 are used. In Figure 1.24 a three-phase balanced positive sequence voltage signals are applied to the SRF-PLL PLL. In Figure 1.25 a three-phase balanced negative sequence voltage signals are applied to the SRF-PLL PLL. As shown in Figure 1.24 and Figure 1.25 the vector derived by the Clarke transformation in Figure 1.24 rotates in the opposite direction of that of Figure 1.25. In the case of unbalanced fault, such as phase to phase or phase to ground faults, both positive and negative sequence components appear at the same time in the signals. Note that due to the configuration of the interfacing transformer, the zero-sequence component is not observed by the inverter controller.

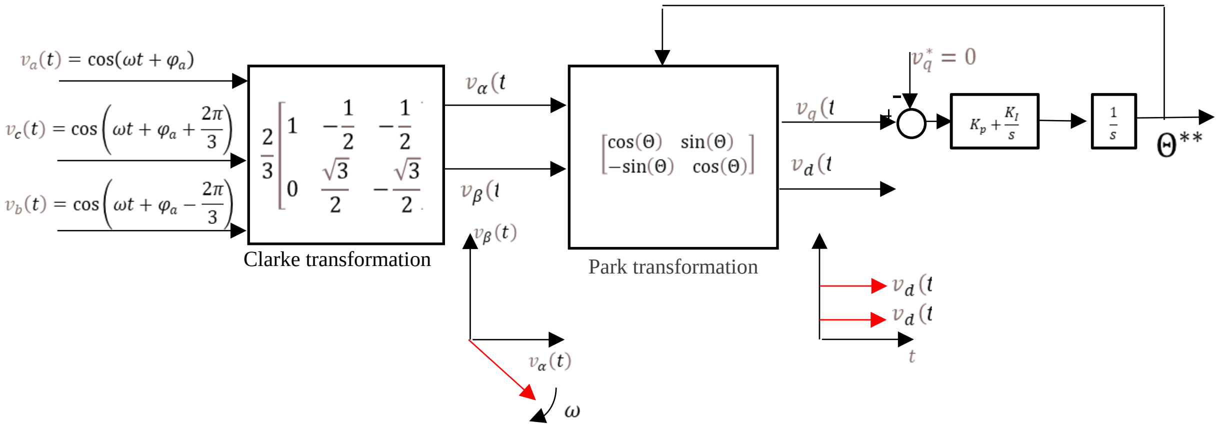

Figure 1.24 Three phase positive-sequence signal transformation to the dq frame

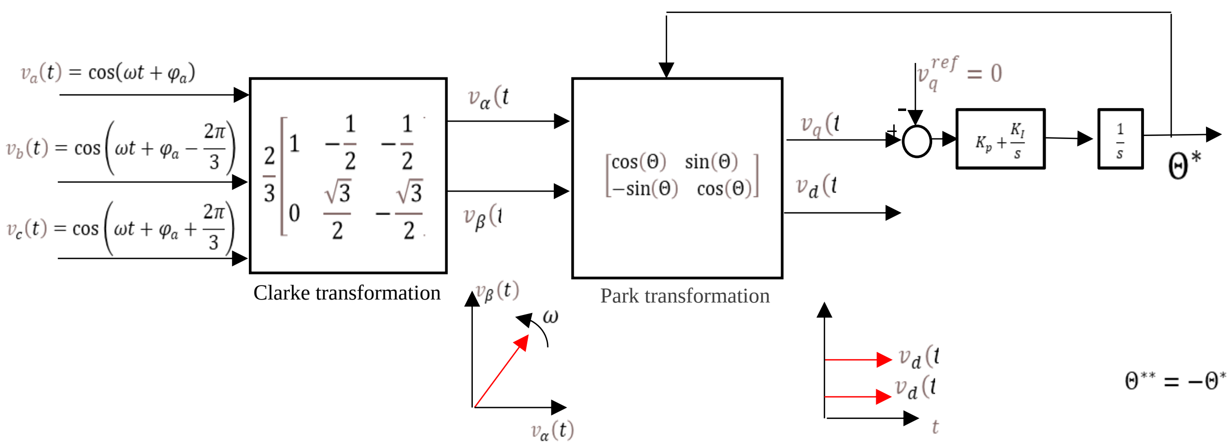

Figure 1.25 Three phase positive-sequence signal transformation to the dq frame

Therefore, the terminal voltage can be written as follows:

$$\begin{bmatrix} v_a(t) \\ v_b(t) \\ v_c(t) \end{bmatrix} = \begin{bmatrix} v_a^+(t) \\ v_b^+(t) \\ v_c^+(t) \end{bmatrix} + \begin{bmatrix} v_a^-(t) \\ v_b^-(t) \\ v_c^-(t) \end{bmatrix} = \begin{bmatrix} V_{max}cos(\omega t + \varphi_a^+) \\ V_{max}cos(\omega t + \varphi_a^+ - \frac{2\pi}{3}) \\ V_{max}cos(\omega t + \varphi_a^+ + \frac{2\pi}{3}) \end{bmatrix} + \begin{bmatrix} V_{max}cos(\omega t + \varphi_a^-) \\ V_{max}cos(\omega t + \varphi_a^- + \frac{2\pi}{3}) \\ V_{max}cos(\omega t + \varphi_a^- - \frac{2\pi}{3}) \end{bmatrix} \quad (1.25)$$

If the Park transformation with $\theta = \theta^*$is applied, the following is derived

$$\begin{bmatrix} v_{d+} \\ v_{q+} \end{bmatrix} = \begin{bmatrix} v_{d+}^* \\ v_{q+}^* \end{bmatrix} + \begin{bmatrix} \cos(2\theta^*) & \sin(2\theta^*) \\ -\sin(2\theta^*) & \cos(2\theta^*) \end{bmatrix} \begin{bmatrix} \bar{v}_{d-} \\ \bar{v}_{q-} \end{bmatrix} \quad (1.26)$$

If the Park transformation with $\theta = -\theta^*$is applied, the following is derived

$$\begin{bmatrix} v_{d-} \\ v_{q-} \end{bmatrix} = \begin{bmatrix} v_{d-}^* \\ v_{q-}^* \end{bmatrix} + \begin{bmatrix} \cos(-2\theta^*) & \sin(-2\theta^*) \\ -\sin(-2\theta^*) & \cos(-2\theta^*) \end{bmatrix} \begin{bmatrix} \bar{v}_{d+} \\ \bar{v}_{q+} \end{bmatrix} \tag{1.27}$$

Where $v_{d+}^*, v_{d-}^*, v_{q+,}^* v_{q-}^*$ are value of positive and negative sequence voltage at the inverter terminal in dq reference frame.

One way to extract $\begin{bmatrix} v_{d-}^* \\ v_{q-}^* \end{bmatrix}$ in (1.27) or $\begin{bmatrix} v_{d+}^* \\ v_{q+}^* \end{bmatrix}$ in (1.26), is using a low pass filter to eliminate the second harmonic components. However, it makes the PLL extremely slow which deteriorates its performance in tracking fast changing disturbances. To address this issue, decoupled double synchronous reference frame-PLL (DDSRF PLL) [12] is implemented. Figure 1.25 shows the overall structure of the DDSRF PLL. In DDSRF PLL the decupling is performed as follows:

According to (1.26) and (1.27)

$$\begin{bmatrix} v_{d+}^* \\ v_{q+}^* \end{bmatrix} = \begin{bmatrix} v_{d+} \\ v_{q+} \end{bmatrix} - \begin{bmatrix} \cos(2\theta^*) & \sin(2\theta^*) \\ -\sin(2\theta^*) & \cos(2\theta^*) \end{bmatrix} \begin{bmatrix} \bar{v}_{d-} \\ \bar{v}_{q-} \end{bmatrix} \tag{1.28}$$

And

$$\begin{bmatrix} v_{d-}^* \\ v_{q-}^* \end{bmatrix} = \begin{bmatrix} v_{d-} \\ v_{q-} \end{bmatrix} - \begin{bmatrix} \cos(-2\theta^*) & \sin(-2\theta^*) \\ -\sin(-2\theta^*) & \cos(-2\theta^*) \end{bmatrix} \begin{bmatrix} \bar{v}_{d+} \\ \bar{v}_{q+} \end{bmatrix} \tag{1.29}$$

Equations (1.28) and (1.29) can be represented in block diagrams as Figure 1.26[13]

When an unbalanced fault occurs, the active and power of inverter can be written as follows[14]:

$$\begin{gathered} P = P_0 + P_c \cos(2\omega t) + P_s sin\,(2\omega t) \\ Q = Q_0 + Q_c \cos(2\omega t) + Q_s sin\,(2\omega t) \end{gathered} \tag{1.30}$$

P_0 and Q_0 are the average values of instantaneous power and the P_c, P_s, Q_c, Q_s are oscillatory term of power in unbalanced situation.

$$\begin{aligned} P_0 &= 1.5 \times \left(v_d^+ i_d^+ + v_q^+ i_q^+ + v_d^- i_d^- + v_q^- i_q^-\right) \\ P_c &= 1.5 \times \left(v_d^+ i_d^- + v_q^+ i_q^- + v_d^- i_d^+ + v_q^- i_q^+\right) \\ P_s &= 1.5 \times \left(v_q^- i_d^+ - v_d^- i_q^+ - v_q^+ i_d^- + v_d^+ i_q^-\right) \\ Q_0 &= 1.5 \times \left(v_q^+ i_d^+ - v_d^+ i_q^+ + v_q^- i_d^- - v_d^- i_q^-\right) \\ Q_c &= 1.5 \times \left(v_q^+ i_d^- - v_d^+ i_q^- + v_q^- i_d^+ + v_d^- i_q^+\right) \\ Q_s &= 1.5 \times \left(v_d^+ i_d^- + v_q^+ i_q^- - v_d^- i_d^+ - v_q^- i_q^+\right) \end{aligned} \tag{1.31}$$

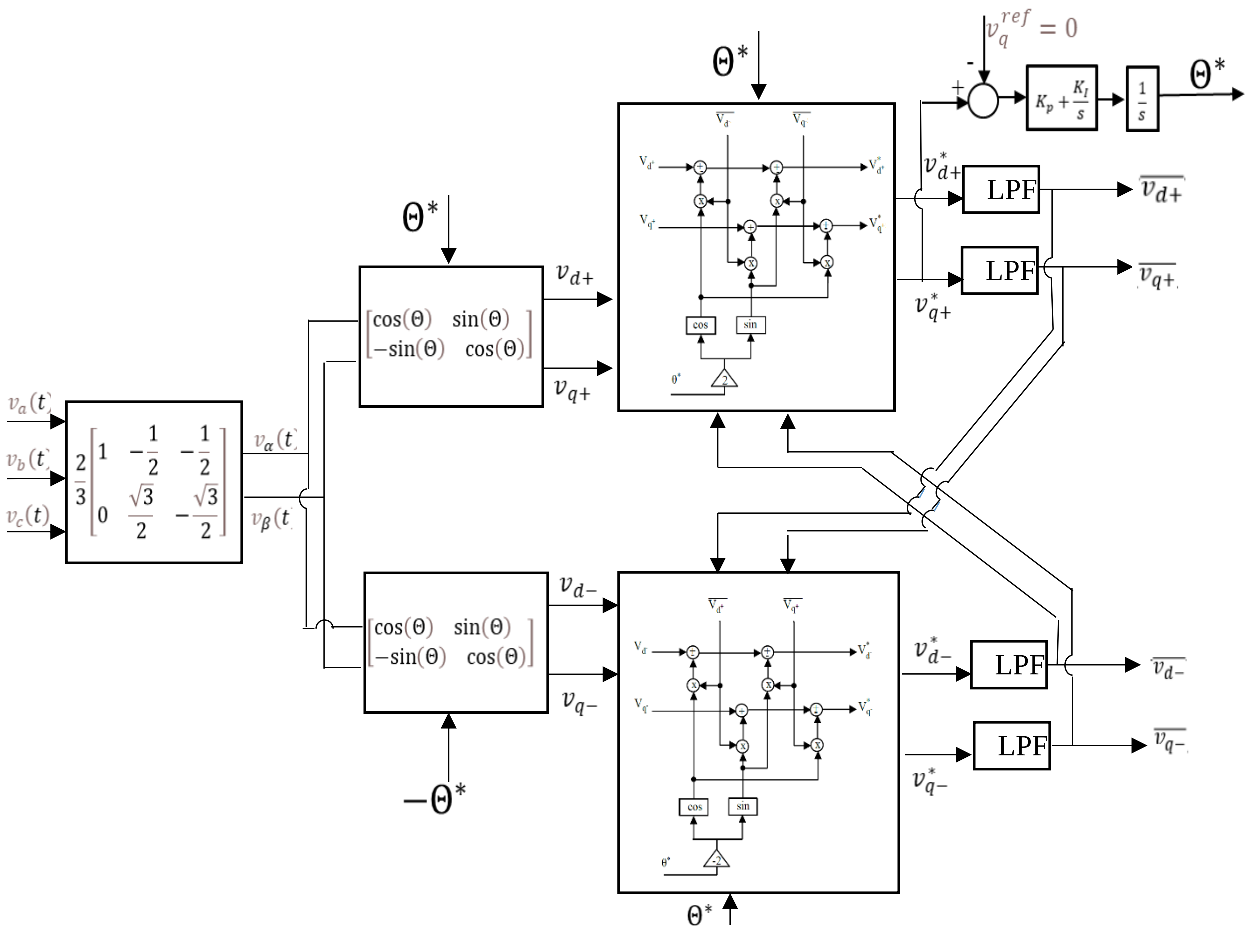

Figure 1.26 Schematic of decoupled double synchronous reference frame-PLL (DDSRF PLL)

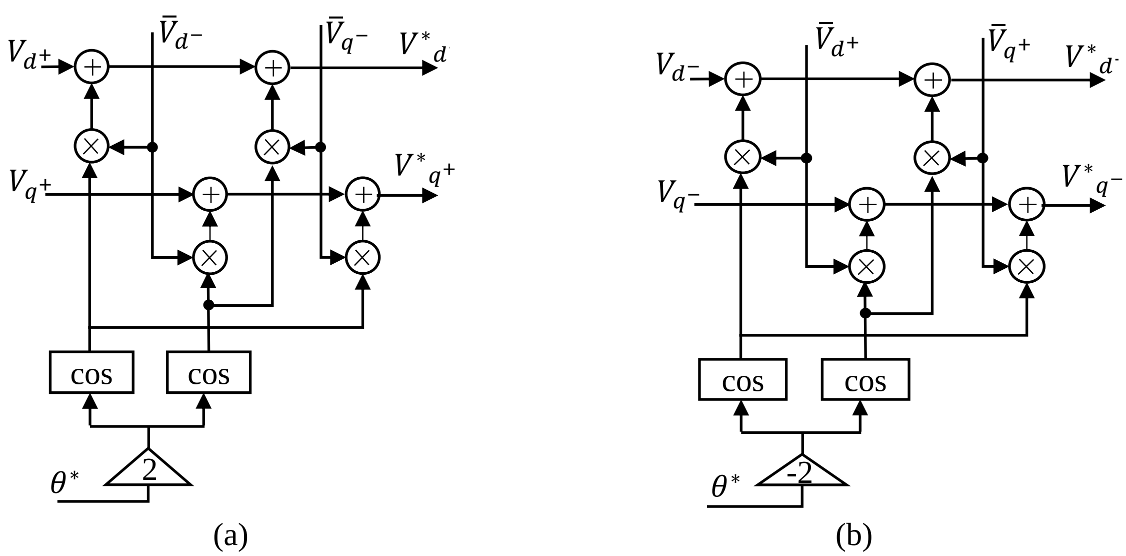

Figure 1.27 Block diagram of the decompiling process for extracting sequence component in DDSRF PLL [13]

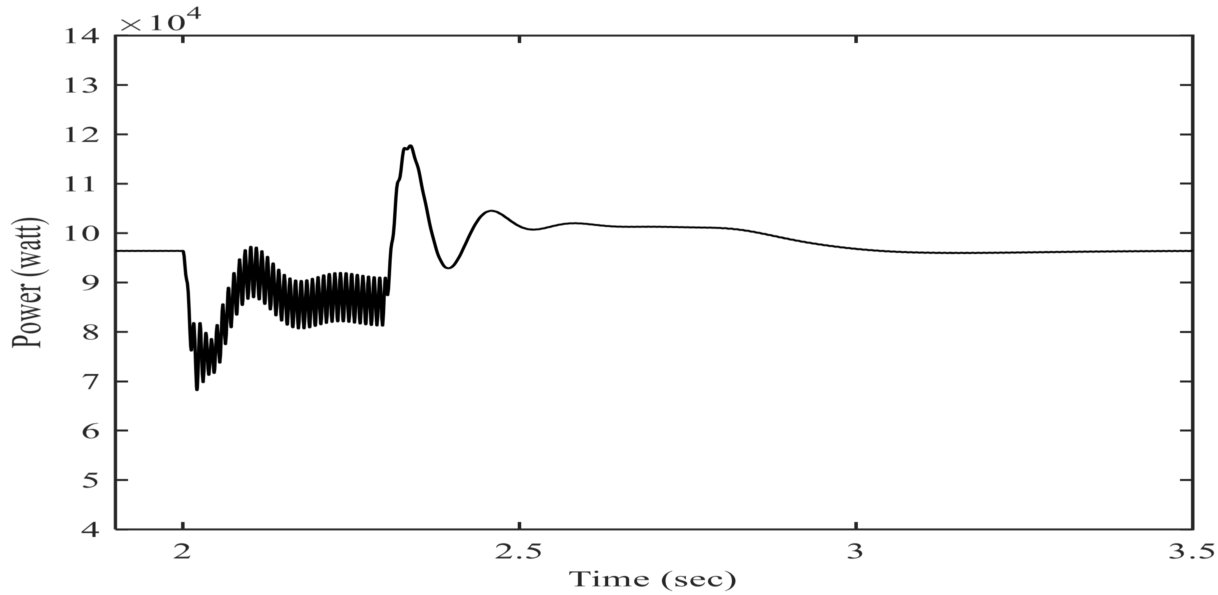

Figure 1.28 Pout having double-fundamental frequency oscillations during a-g fault in conventional positive sequence synchronous reference frame controller

In conventional positive sequence synchronous reference frame controllers double-fundamental frequency oscillations appear in output power. For instance, Figure 1.28 shows Pout having double-fundamental frequency oscillations during an a-g fault.

If dual current controller is used for the inverter, positive and negative sequence currents can be controlled simultaneously which means in (1.31), i_d^+, i_q^+, i_d^- *and* i_q^- can be controlled. The controller may have different objectives, such as suppression of negative sequence current, suppression of active power oscillations or suppression of reactive power oscillations. The controller for suppression of active power oscillations is one of the common methods that is also implemented in this project. The active power imbalance causes double-fundamental frequency oscillations in DC voltage as $P_c, and\ P_s$ are not zero. To eliminate $P_c, and\ P_s$ the references are calculated as follows [14][15]:

$$\begin{bmatrix} i_d^{+*} \\ i_q^{+*} \\ i_d^{-*} \\ i_q^{-*} \end{bmatrix} = \frac{2}{3} \begin{bmatrix} v_d^+ & v_q^+ & v_d^- & v_q^- \\ v_q^+ & -v_d^+ & v_q^- & -v_d^- \\ v_d^- & v_q^- & v_d^+ & v_q^+ \\ v_q^- & -v_d^- & -v_q^+ & v_d^+ \end{bmatrix}^{-1} \begin{bmatrix} P_0 \\ Q_0 \\ 0 \\ 0 \end{bmatrix} = \frac{2P_0}{3D} \begin{bmatrix} v_d^+ \\ v_q^+ \\ -v_d^- \\ -v_q^- \end{bmatrix} + \frac{2Q_0}{3F} \begin{bmatrix} v_q^+ \\ -v_d^+ \\ v_q^- \\ -v_d^- \end{bmatrix} \tag{1.32}$$

$$D = \left[(v_d^+)^2 + \left(v_q^+\right)^2\right] - \left[(v_d^-)^2 + \left(v_q^-\right)^2\right]$$
$$F = \left[(v_d^+)^2 + \left(v_q^+\right)^2\right] + \left[(v_d^-)^2 + \left(v_q^-\right)^2\right]$$

Where P_0 is determined by the PI controller of voltage of the DC capacitor.
Figure 1.29, shows the schematic of the implemented DDSRL-PLL and the dual current controller.

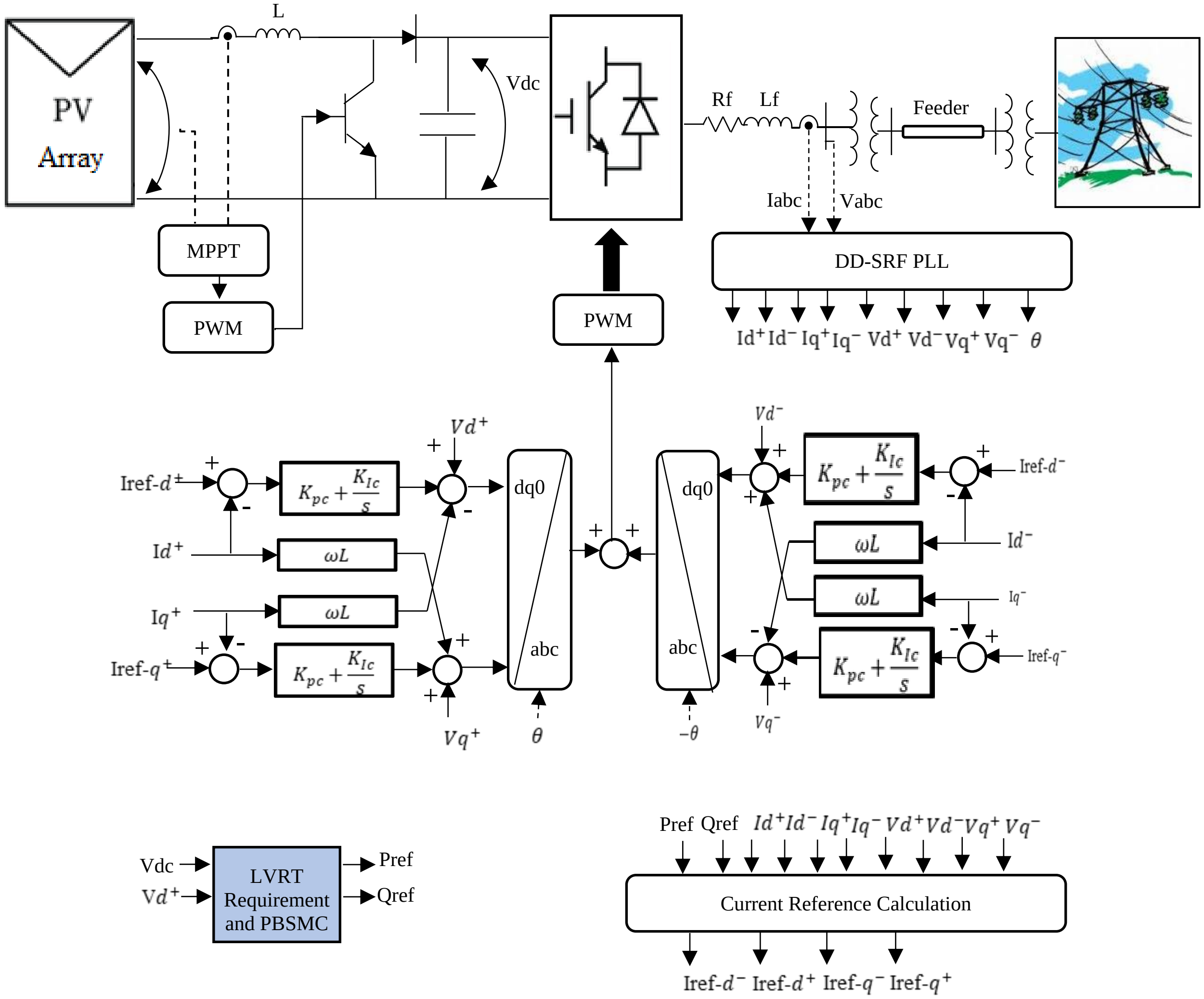

Figure 1.29 Schematic of the dual current controller for handling unbalanced faults.

1.4.1 Performance of Controllers in PV Power Plant: Unbalanced Fault Cases

To study the performance of different methods in facing unbalanced faults, different fault cases are simulated as follows.

CASE 1: A L-L-g fault (unbalanced fault) with a ground resistance of 2 ohms and a phase resistance of 2 ohms is applied. The fault occurs at 4.4 seconds and is cleared at 4.75 seconds. Figure 1.30 to Figure 1.32 show the results of different methods. As can be seen, the dual current controller eliminated double-fundamental frequency oscillations successfully. AW methods also enhance the transitioning of the inverter to the post fault condition. PBSMC method also provides similar or better results compared to other methods.

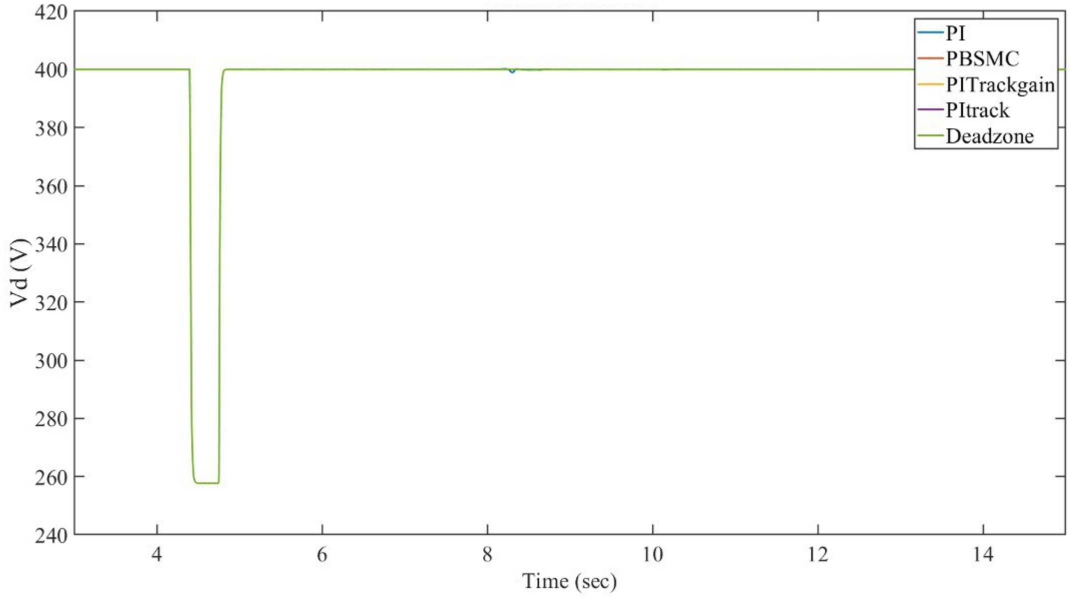

Figure 1.30 Vd in the unbalanced fault CASE 1

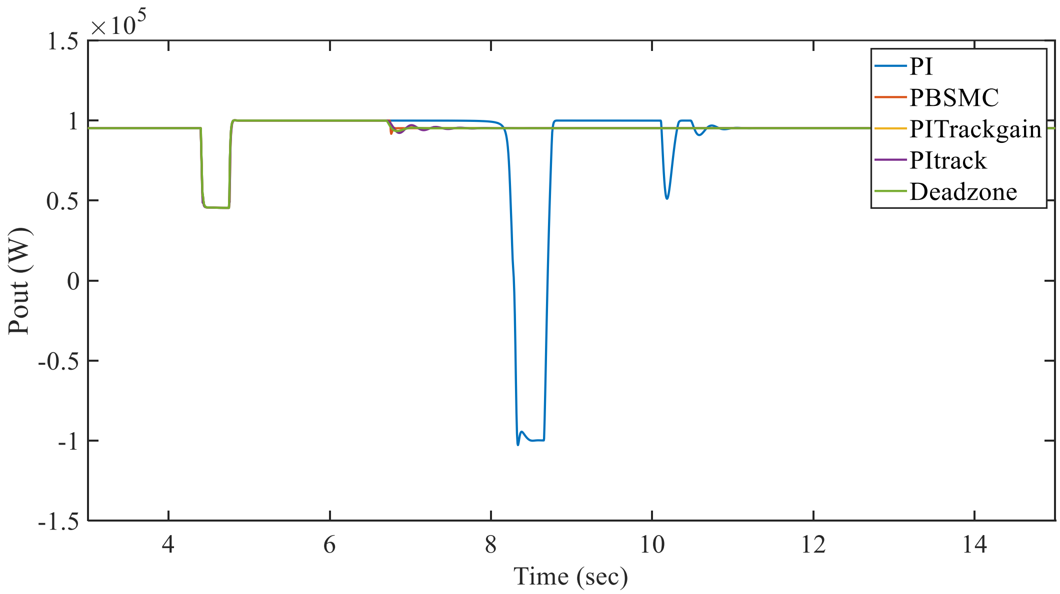

Figure 1.31 Pout for the unbalanced fault CASE 1

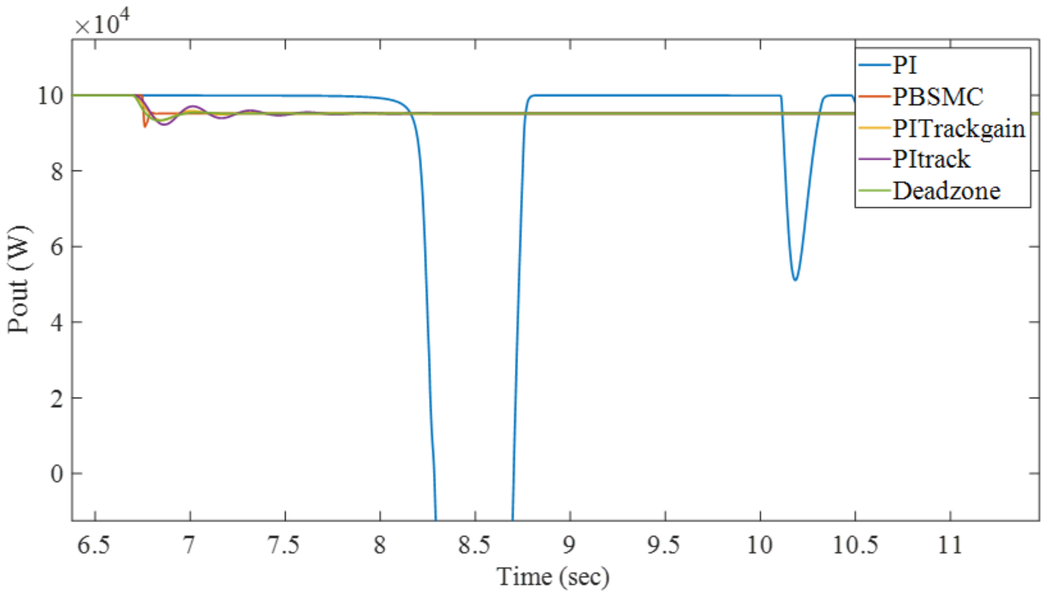

Figure 1.32 Pout zoomed on the saturation time for the unbalanced fault CASE 1

CASE 2: In this case a two-phase to ground fault is simulated that lasts for a longer duration compared to the previous case, starting at 3.4 seconds and continuing until 3.8 seconds Additionally, the ground resistance has been decreased to 2 ohms. Figure 1.33 to Figure 1.35 show the results in this case.

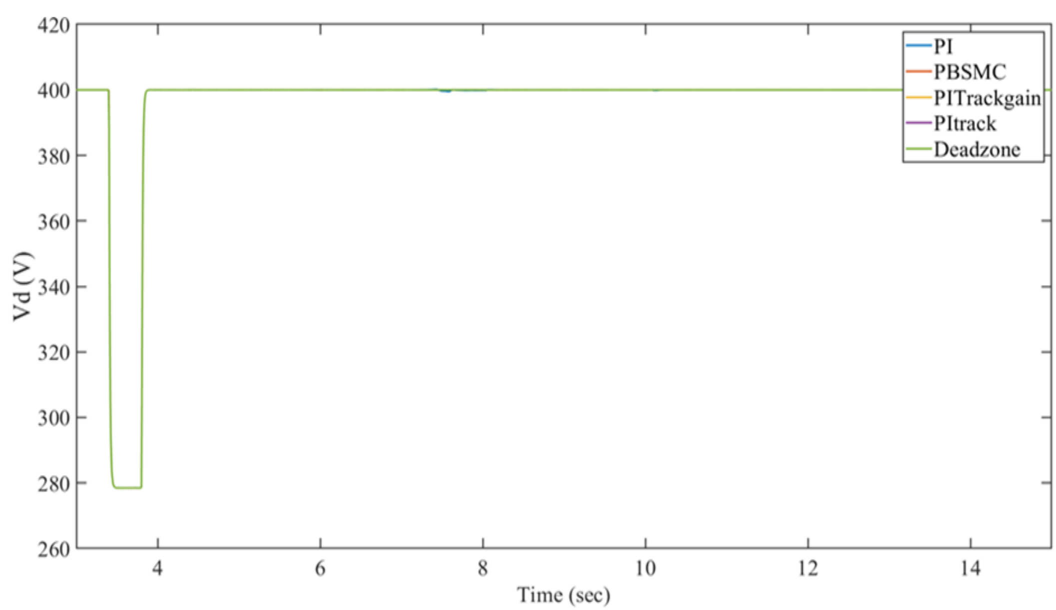

Figure 1.33 Vd in the unbalanced fault CASE 2

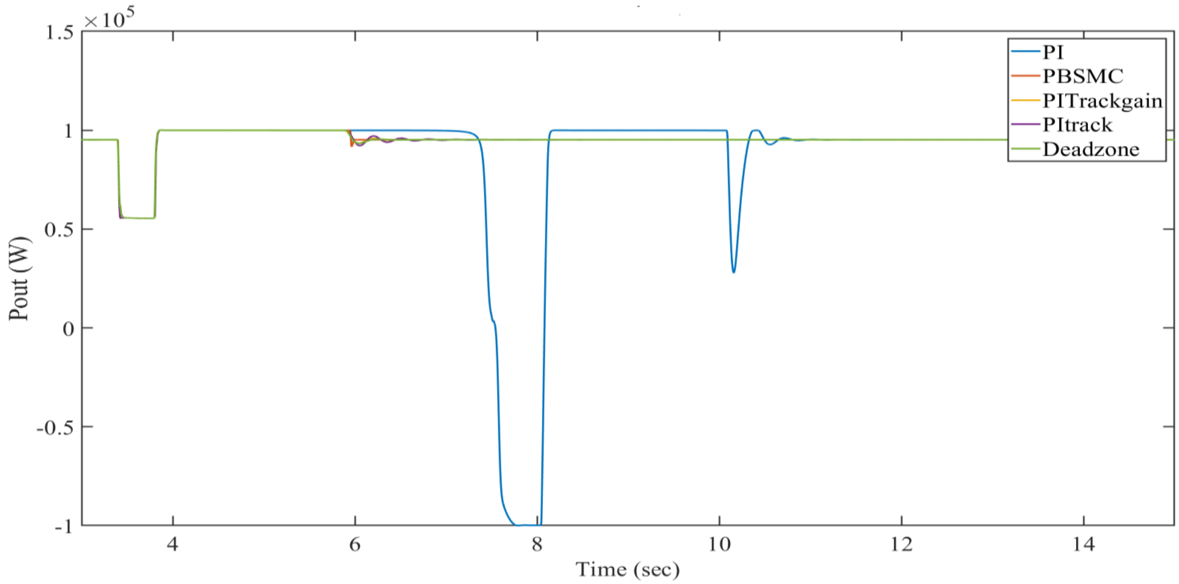

Figure 1.34 Pout in the unbalanced fault CASE 2

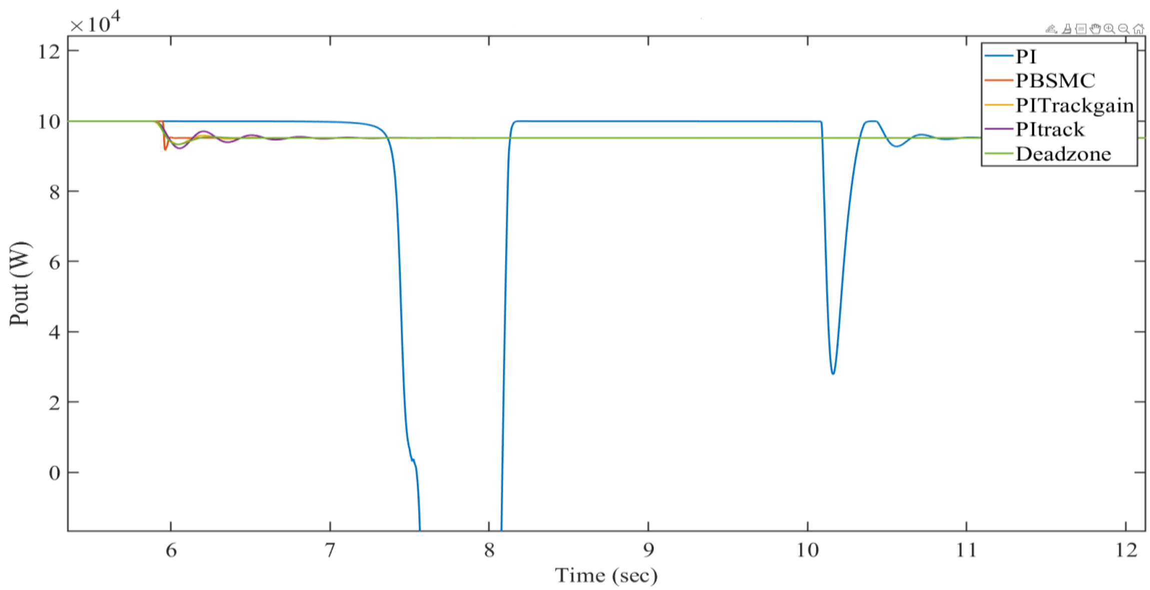

Figure 1.35 Pout zoomed on the saturation time for the unbalanced fault CASE 2

CASE 3: In this scenario, a line-to-line fault is simulated. The fault resistance is 2 ohms. The fault occurs at 4.4 sec and is cleared at 4.75 sec. Figure 1.36 to Figure 1.38 show the simulation results of different methods.

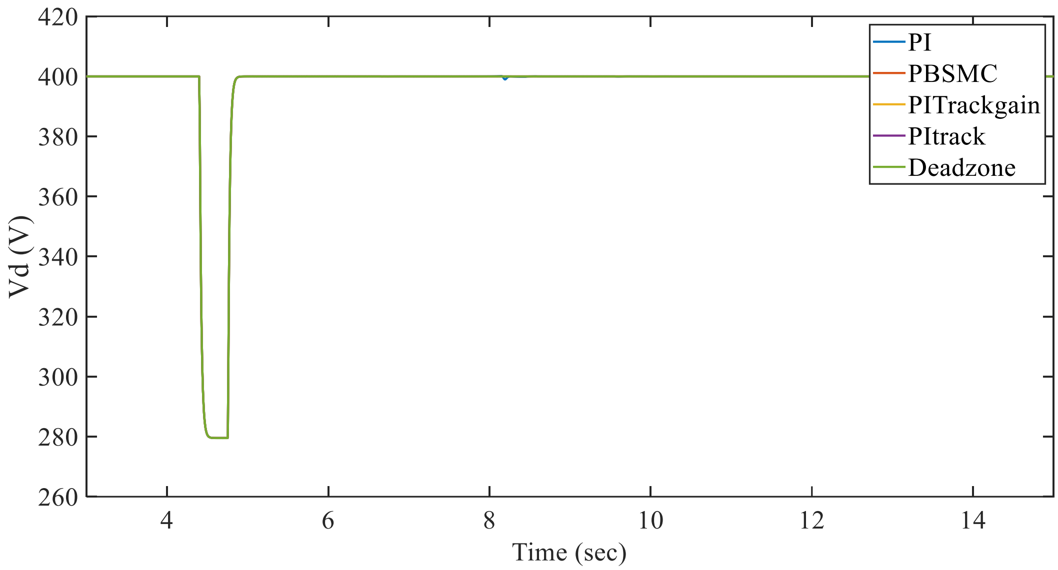

Figure 1.36 Vd in the unbalanced fault CASE 3

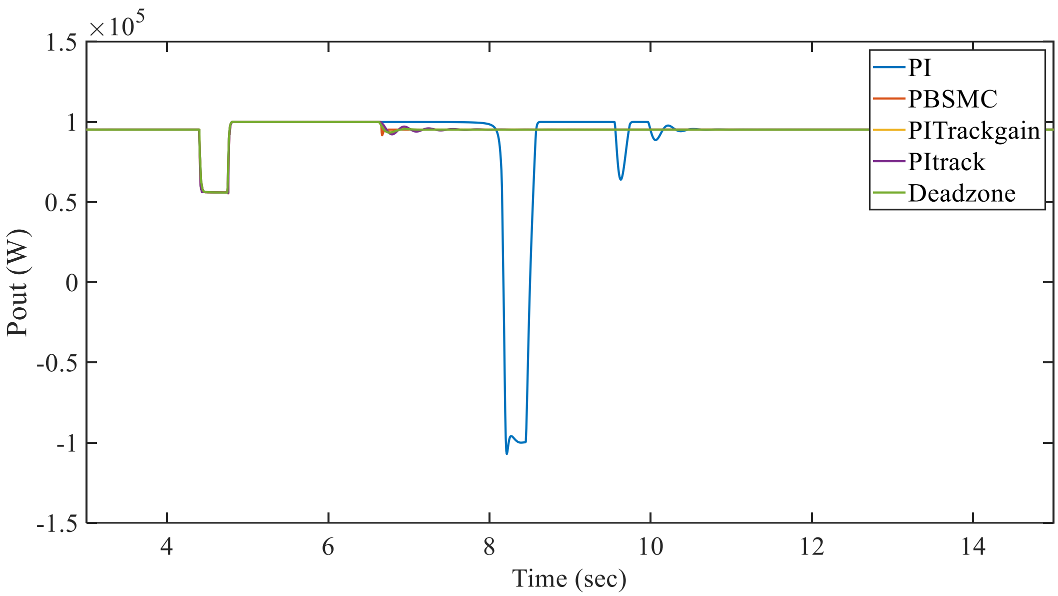

Figure 1.37 Pout in the unbalanced fault CASE 3

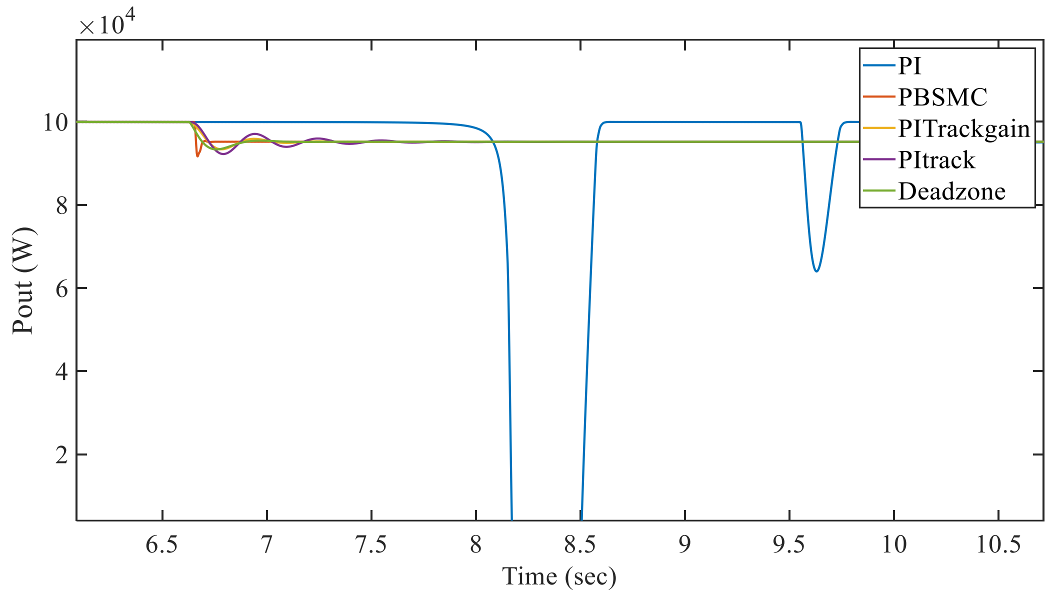

Figure 1.38 Pout zoomed on the saturation time for the unbalanced fault CASE 3

CASE 4: A line to-ground fault is considered in this case. The fault resistance is 2 ohms. The fault occurs at time 4.4 sec and is cleared at 4.75 sec. Figure 1.39 to Figure 1.41 show the simulation results. In this case also AW methods help the PI controller to have smooth transition to post-fault condition. Specifically, PBSMC has same or better performance compared to other methods.

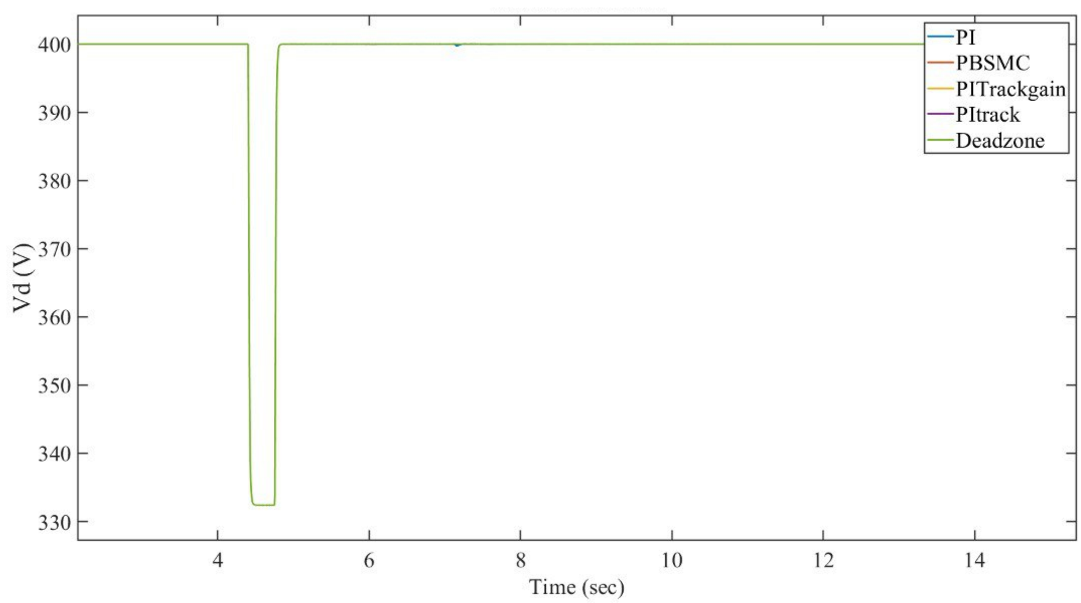

Figure 1.39 Vd in the unbalanced fault CASE 4

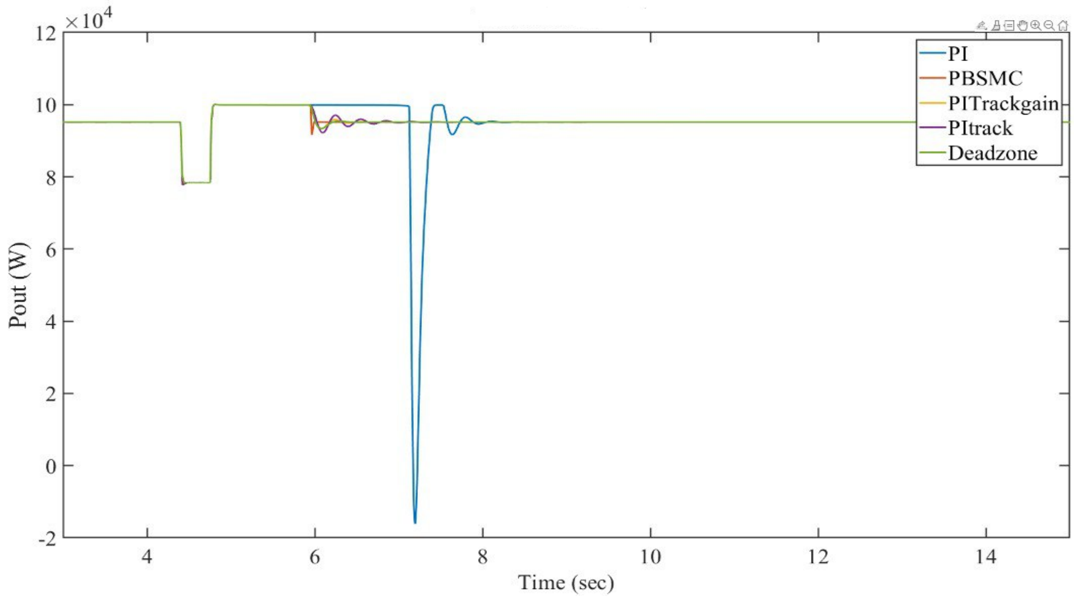

Figure 1.40 Pout in the unbalanced fault CASE 4

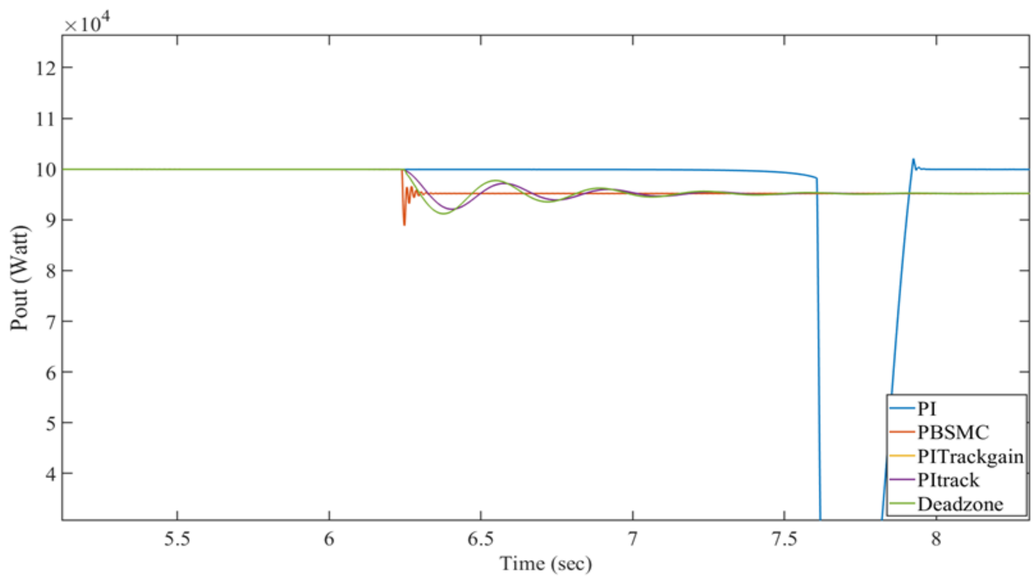

Figure 1.41 Pout zoomed on the saturation time for the unbalanced fault CASE 4

CASE 5: In this case a single phase to ground fault is simulated that lasts for a longer duration compared to previous case, starting at 3.4 seconds and continuing until 3.8 seconds. Additionally, the ground resistance is 0.2 ohms. Figure 1.42 to Figure 1.44 show the results of this case.

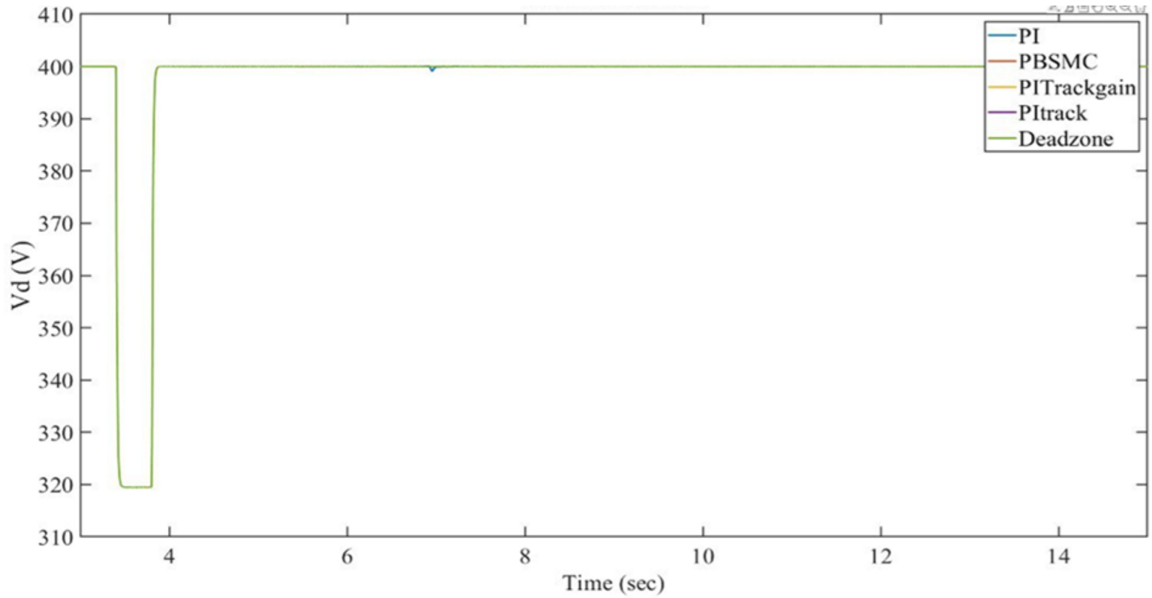

Figure 1.42 Vd in the unbalanced fault CASE 5

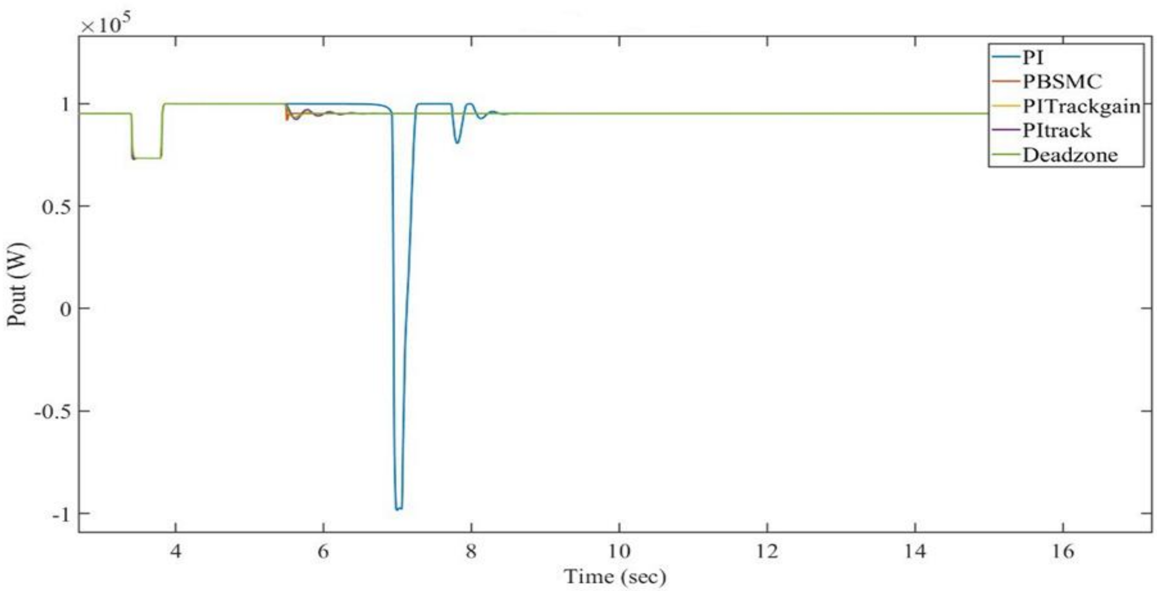

Figure 1.43 Pout in the unbalanced fault CASE 5

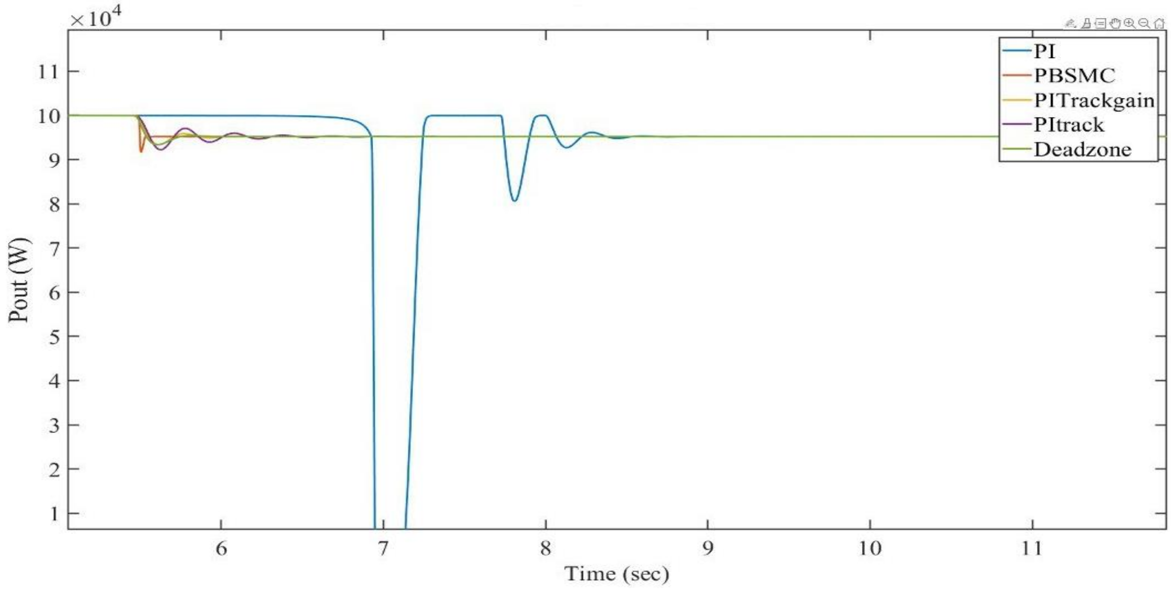

Figure 1.44 Pout zoomed on the saturation time for the unbalanced fault CASE 5

1.5 Conclusions

This project investigated the impacts of saturations of controllers due to different types of faults. Balanced and unbalanced faults, with different durations were simulated. Several anti-wide up methods were implemented. Moreover, a controller called proxy based sliding mode controller (PBSMC) was simulated. According to case study results, to enable seamless transition from during fault to post-fault condition addressing the saturation of controllers is essential. The results also showed PBSMC has similar or better results compared to several implemented anti-windup methods. Tuning AW methods is a heuristic process. In contrast, tuning the PBSMC parameter is a straightforward process which makes it suitable for practical application. The case study results showed the saturation of PI controller of the DC link voltage is influential on the outputs of inverter.

References

[1] J. Grainger, and W. Stevenson “Power System Analysis: Analysis and Design” McGraw Hill, 1994.

[2] M. Ghanatiaan, S. Lotfifard, "Sparsity Based Short Circuit Analysis of Power Distribution Systems with Inverter Interfaced Distributed Generators" IEEE Transactions on Power Systems, vol. 36, no. 6, pp. 4857-4868, 2019.

[3] Y. Yang, and Frede Blaabjerg ”Low-Voltage Ride-Through Capability of a Single-Stage Single-Phase Photovoltaic System Connected to the Low-Voltage Grid” International Journal of Photoenergy,pp.1-10, 2013.

[4] E. Buraimoh, and I. E. Davidson “Overview of Fault Ride-Through Requirements for Photovoltaic Grid Integration, Design and Grid Code Compliance” 9th International Conference on Renewable Energy Research and Applications, pp.1-5 ,2020.

[5] M. Azimi, S. Lotfifard, “A Nonlinear Controller Design for Power Conversion Units in Islanded Micro-grids using Interconnection and Damping Assignment tracking control” IEEE Transactions on Sustainable Energy, vol. 12, no.1, pp. 284-292, 2021.

[6] L. Wang, S. Chai, D. Yoo, L. Gan, and K. Ng “PID and Predictive Control of Electrical Drives and Power Converters Using MATLAB/Simulink” Wiley-IEEE Press, 2014.

[7] R. Kikuuwe and H. Fujimoto, "Proxy-based Sliding Mode Control for Accurate and Safe Position Control," IEEE International Conference on Robotics and Automation, 2006.

[8] R. Kikuuwe, S. Yasukouchi, H. Fujimoto, and M. Yamamoto, “Proxy Based Sliding Mode Control: A Safer Extension of PID Position Control,” IEEE Transactions on Robotics., vol. 26, no. 4, pp. 670–683, 2010.

[9] J. Espina, A. Arias, J. Balcells and C. Ortega, "Speed Anti-Windup PI Strategies Review for Field Oriented Control of Permanent Magnet Synchronous Machines," Compatibility and Power Electronics, pp. 279-285, 2009.

[10] H. Shin, and J. Park “Anti-Windup PID Controller with Integral State Predictor for Variable-Speed Motor Drives” IEEE Transactions on Industrial Electronics, vol. 59, no. 3, pp.1509-1516, 2012.

[11] G. Y. Gu, L. M. Zhu, C. Y. Su, H. Ding, and S. Fatikow, “Proxy-Based Sliding-Mode Tracking Control of Piezoelectric-Actuated Nanopositioning Stages” IEEE/ASME Transactions on Mechatronics, vol. 20, no. 4, pp.1956-1965 , 2015.

[12] P. Rodriguez, J. Pou, J. Bergas, J. I. Candela, R. P. Burgos, and D. Boroyevich, “Decoupled Double Synchronous Reference Frame PLL for Power Converters Control”, IEEE Transactions on Power Electronics, vol. 22, no. 2, pp. 584-592, 2007.

[13] F. Sevilmiş, and H. Karaca “Performance analysis of SRF-PLL and DDSRF-PLL Algorithms for Grid Interactive Inverters” International Advanced Researches, and Engineering Journal, vol. 3, no. 2, pp. 116-122, 2019.

[14] H. S. Song, and K. Nam “Dual Current Control Scheme for PWM Converter Under Unbalanced Input Voltage Conditions” IEEE Transactions on Industrial Electronics, vol. 46, no. 5, pp. 953 – 959, 1999.

[15] H. Ahuja, A. Singh, S. Sharma, G. Sharma, and P. N. Bokoro "Coordinated Control of Wind Energy Conversion System during Unsymmetrical Fault at Grid" Energies 15, no. 13: 4898. 2022.